

DEVELOPMENT OF A CELLULAR ANALYSIS PLATFORM  
FEATURING ARRAYS OF PATTERNED MICROWELLS  
FABRICATED ATOP PERMEABLE SUPPORTS

Douglas M. Ornoff

A dissertation submitted to the faculty at the University of North Carolina at Chapel Hill in  
partial fulfillment of the requirements for the degree of Doctor of Philosophy in the  
Department of Pharmacology in the School of Medicine.

Chapel Hill  
2014

Approved by:

Robert A. Nicholas

Nancy L. Allbritton

Scott H. Randell

Ashley G. Henderson

Anne M. Taylor

© 2014  
Douglas M. Ornoff  
ALL RIGHTS RESERVED

## **ABSTRACT**

Douglas M. Ornoff: Development of a cellular analysis platform featuring arrays of patterned microwells fabricated atop permeable supports  
(Under the direction of Nancy L. Allbritton)

Many human pulmonary diseases lead to accumulation of fluid in the alveoli, the air sacs located in the distal lung and at which gas exchange occurs. The most serious example of alveolar fluid buildup is in Acute Respiratory Distress Syndrome (ARDS), in which an insult to the lung results in injury to the cells lining the alveolus, leading to compromise of the alveolar capillary barrier and impaired gas exchange. Current ARDS mortality rates lie at 30-40%. Worsening this problem is the lack of disease-specific therapies for treating ARDS: the cornerstone of treatment is merely supportive respiratory care via mechanical ventilation.

Further investigations into treating ARDS have been hampered by unresolved questions about the normal physiology of alveolar fluid transport. Therefore, new insights are needed in order to develop more effective ARDS therapies. The alveolus is lined by two types of cells: squamous alveolar type 1 cells that cover 98% of the alveolar surface area and small cuboidal alveolar type 2 cells. While studies have examined AT2 cells, the ion transport properties of AT1 cells remain unknown. Recent attempts to culture AT1 cells in bulk monolayers for ion and fluid transport studies have been unsuccessful. It was therefore hypothesized that a microscale device to grow single AT1 cells in conditions that mimic the native lung would enable study of AT1 ion transport.

This dissertation describes the development of microfabricated devices that feature an array of microwells patterned atop a porous or otherwise permeable support. First, a method for fabricating 1002F photoresist into a freestanding microwell array is explored. Next, a strategy to co-fabricate freestanding 1002F films with the hydrogel chitosan to form microwells with a permeable support is described. Review of the literature suggests that this is the first reported co-fabrication of hydrogel and photoresist into a freestanding film. Lastly, an approach to micropattern commercially available permeable supports, etched with submicron-scale cylindrical pores, is presented. Together, these platforms offer potential for growth and analysis of not only primary alveolar cells, but a range of other cell types in a variety of research endeavors, pulmonary and otherwise.

*This work, being the longest block of prose I've ever written, is fittingly dedicated to the memory of Ms. Martha Woolery.*

*First, may this work be free of gross grammatical errors.*

*More importantly, may it be but one of many steps I take as I strive to "find a better way" for caring for the sick and afflicted.*

## ACKNOWLEDGEMENTS

I owe a great deal of thanks and appreciation to a number of people for their support, guidance, wisdom, and encouragement in getting me to where I am now. First, to my mentor Dr. Nancy Allbritton, I want to thank you for all your support throughout this process. Your patience, insight, and experience have been a true gem that I am glad and proud to have put my trust in. Dr. Chris Sims, your expertise and commitment to the lab have been invaluable to me. I also wish to thank everyone in the Allbritton Lab, past and present, for creating such an inspiring and lively place in which to train and learn. To the Microfabrication Team, I owe so much to your collective knowledge and experience. I would like to especially thank Dr. Wei Xu and Dr. Phil Gach for welcoming me into the lab and teaching me the ropes of microfabrication. I would also like to give special thanks to Dr. Yuli Wang for being so willing to share your vast amount of experience and always being willing to hear my questions and ideas. Drs. David Detwiler, Nick Dobes and Pavak Shah, as well as Pete Attayek, Asad Ahmad, Matt DiSalvo, I am grateful for all the assistance you've lent me, and all the fond memories. Lauren Westerhold, I have greatly enjoyed working with and training you and wish you all the best of success in your future endeavors. Joe Balowski and I have put in many hours of work in the dead of night, and I admire his dedication greatly. To the CE Team, each of you has done so much to make this lab such a great place in which to work. I would especially like to thank Dr. Angie Proctor, who is one of the most selfless people I have ever met, for your constant willingness to help out and offer guidance, and for your everyday outlook that is so positive and upbeat.

I would also like to thank my committee members and collaborators. Rob Nicholas, Tasha Blatt, Ross Dubose, Sam Wolff, and Ken Harden, thank you for all the help and assistance you've given me over these years. I count myself lucky that I have had people so willing to share their expertise and experience with me. Brian Button, Scott Randell, Leslie Fulcher, and Peter Bove, I thank you all for the outstanding insight and discussions on the nuances of respiratory epithelia, which have helped inspire so many of my ideas and so much of my creativity. Ashley Henderson, you have been such a great clinical mentor. Your patience and passion for teaching are a rare find, and I hope I get the chance to learn more from you in the future.

I would not be here today if it were not for several individuals who helped me take the plunge into the world of science. Foremost among these is Ric Boucher, who has been such an inspiration to me in my pursuits. If I end up being even half as successful as you, I will consider myself greatly fortunate. Your ability to inspire hard work and creativity is truly unparalleled, and your ability to see potential in a skinny 19-year-old and open doors for him is greatly appreciated. To Eduardo Lazarowski and Catja van Heusden, I owe you such thanks for giving me my first break in science and taking me under your wings. To Matt Redinbo and Eric Ortlund, who first took the time to teach me how to be independent and to think to the next steps, thank you for all the lessons you taught me.

I would also like to acknowledge the UNC Medical Scientist Training Program, both faculty and students. Training in the two disciplines of clinical medicine and research science is not an easy undertaking, but this Program has strived to excel, and to do so with a camaraderie that is a true rarity. I owe special thanks to Gene Orringer, Kim Rathmell, and Mohanish Deshmukh for all their support and faith in me. David Siderovski, you are the true

definition of “a gentleman and a scholar.” Your willingness to offer your time and guidance, even to someone such as I whose field is set far apart from your own, has been unmatched. Alison Regan and Carol Herion have been so incredibly fun and supportive, and I have taken such heart from your humor and your dedication to each of us in the Program. Dr. Ryan Phillips, you have been a true friend to me and a great guide as I navigate the Allbritton Lab, the Pharmacology Department, and the MSTP.

To all my friends outside of science and the lab, you’ve become my family in Chapel Hill, and without each of you I would have burned out a long time ago. You have truly kept me going all these years with your constant friendship and ever-present good humor. I have so enjoyed all our game nights, trips to the beach, and bar trivia gatherings. A great deal of my motivation to work in science and medicine comes from the desire to see that others might have the good times and the friendship that we share. If every person in the world had friends like you, no one would feel unwanted. Aaron, John, Will, Josh, Neal, Chris, Chris, Ben, and Andrew, I affirm the borrowed statement: I have never been in a fraternity, but I count you all as my brothers. Lauren, Helen, Brandy, Sarah, Sarah, Suzanne, and Ashley, you all mean the world to me. Shannon, I want you to know how much your support has meant as I navigated the past few years. Thank you so much for believing in me.

And, saving the best for last, I owe an indescribable amount of gratitude to my family: my parents Mike and Theresa, my brother Tim, my grandmother Ellen. Your love, support, encouragement, and faith in me have been constant and unwavering. Words do not and will not convey how much I value you in my life and how much I appreciate all that you have given me.

## TABLE OF CONTENTS

LIST OF TABLES .....	xv
LIST OF FIGURES .....	xvi
LIST OF ABBREVIATIONS AND SYMBOLS .....	xviii
Chapter 1: Introduction .....	1
1.1 Airway and Alveolar Disease: States of Disordered Pulmonary Fluid Homeostasis .....	1
1.1.1 Respiratory epithelia and luminal fluid films .....	1
1.1.1.1 Hierarchical organization of respiratory epithelia .....	1
1.1.1.2 Air-liquid interfaces and luminal fluid films in the pulmonary tract .....	5
1.1.2 Alveolar diseases and disordered fluid homeostasis .....	6
1.1.3 Alveolar diseases: therapeutic options and shortfalls .....	8
1.2 Physiology and Pharmacology of Pulmonary Liquid Homeostasis .....	10
1.2.1 Airway surface liquid in bronchial and bronchiolar epithelia .....	10
1.2.2 Ion and fluid transport by alveolar type 2 (AT2) epithelia .....	14
1.2.3 Ion transporters and purinergic receptors in alveolar type 1 (AT1) epithelia .....	17
1.2.4 Current methods for studying pulmonary fluid homeostasis .....	20
1.3 Microscale devices for analysis of discrete numbers of cells .....	23
1.3.1 Definition and use of microscale devices .....	23

1.3.2 Advantages of microscale devices . . . . .	25
1.3.3 Survey of previously described microscale devices relevant to alveolar cell culture . . . . .	26
1.3.3.1 Microscale devices applied to respiratory biology . . . . .	26
1.3.3.2 Microscale devices utilizing a permeable support . . . . .	28
1.3.4 Design guidelines for a microscale device applicable to AT1 cells . . . . .	31
1.4 Scope of the Dissertation . . . . .	33
1.5 Figures and Tables . . . . .	35
1.6 References . . . . .	43
Chapter 2: Characterization of freestanding photoresist films for biological and MEMS applications . . . . .	62
2.1 Introduction . . . . .	62
2.1.1 General approaches . . . . .	62
2.1.2 Lab-on-a-foil devices . . . . .	63
2.1.3 Photoresists . . . . .	64
2.1.4 Photoresists as lab-on-a-foil devices . . . . .	65
2.1.5 Overview . . . . .	66
2.2 Experimental Design . . . . .	67
2.2.1 Materials . . . . .	67
2.2.2 Fabrication and release of single-layer films . . . . .	67
2.2.3 Measurement of film properties . . . . .	68
2.2.4 Characterization of photoresist thin film release kinetics . . . . .	69
2.2.5 Patterned deposition of metal and protein . . . . .	70
2.2.6 Cell culture on a film with a single pore . . . . .	70

2.2.7 Seeding of AT2 primary cells . . . . .	71
2.3 Results and Discussion . . . . .	72
2.3.1 Fabrication of 1002F films and release from glass substrates . . . . .	72
2.3.2 Mechanical strength of freestanding 1002F films . . . . .	73
2.3.3 Fabrication of micropatterned freestanding 1002F films . . . . .	74
2.3.4 Fabrication of multilayered, micropatterned freestanding 1002F films . . . . .	75
2.3.5 1002F films as re-usable stencils for substrate patterning . . . . .	77
2.3.6 1002F films to address a single cell within a monolayer of cells . . . . .	79
2.4 Conclusions . . . . .	80
2.5 Figures and Tables . . . . .	82
2.6 References . . . . .	97
Chapter 3: Co-fabrication of 1002F and chitosan for freestanding films of permeable-bottomed microwell arrays . . . . .	102
3.1 Introduction . . . . .	102
3.1.1 General considerations . . . . .	102
3.1.2 Analysis of cellular heterogeneity . . . . .	102
3.1.3 Microfabricated platforms for analyzing cellular heterogeneity . . . . .	104
3.1.4 Chitosan . . . . .	105
3.1.5 Overview . . . . .	107
3.2 Experimental Design . . . . .	107
3.2.1 Materials . . . . .	107
3.2.2 Co-fabrication of freestanding 1002F:chitosan films . . . . .	108

3.2.3 Imaging	109
3.2.4 Multi-layer fabrication	109
3.2.5 Measurement of chitosan dry film thickness	110
3.2.6 Measurement of 1002F:chitosan film optical properties	110
3.2.7 Diffusion testing	111
3.2.8 Calculation of diffusivity constant for chitosan membranes in 1002F:chitosan hybrid films	113
3.2.9 Spatially controlled protein conjugation	118
3.2.10 Isolated clonal expansion and analysis of heterogeneity of cell proliferation in entrapped, nonadherent cells	119
3.2.11 Growth of AT1-like cells	120
3.2.12 Statistical testing	120
3.3 Results and Discussion	121
3.3.1 Co-fabrication of freestanding 1002F:chitosan films	121
3.3.2 Multi-layer 1002:chitosan:1002F sandwich films	122
3.3.3 Chitosan hydrogel thickness measurements	123
3.3.4 Optical properties	125
3.3.5 Diffusion testing of micropatterned 1002F: chitosan hybrid films	126
3.3.6 Calculation of diffusion coefficients and MW cutoffs for chitosan membranes in 1002F:chitosan hybrid films	129
3.3.7 Spatially controlled protein conjugation	131
3.3.8 Survival and proliferation of nonadherent cells entrapped in chitosan-bottomed microwells	132
3.3.9 Isolation and expansion of clonal populations in discrete medium pockets	133

3.3.10 Analysis of cell division heterogeneity in entrapped, nonadherent cells .....	134
3.3.11 Growth of primary human AT2 cells as AT1 surrogates .....	136
3.4 Conclusions .....	136
3.5 Figures and Tables .....	138
3.6 References .....	154
Chapter 4: Co-fabrication of 1002F and chitosan for freestanding films of permeable-bottomed microwell arrays .....	161
4.1 Introduction .....	161
4.1.1 Cellular polarization in epithelial tissues .....	161
4.1.2 Advantages of microfabricated devices for studies of fundamental cell processes .....	162
4.1.3 Microfabricated devices for study of polarized cells .....	162
4.1.4 Design of a protocol for micropatterning a track-etch membrane ...	164
4.1.5 Overview .....	166
4.2 Experimental Design .....	167
4.2.1 Materials .....	167
4.2.2 Photoresist-based micropatterning of track-etch membranes .....	168
4.2.3 Imaging of freestanding, micropatterned track-etch membranes ....	169
4.2.4 Assessing micropore patency by measuring solute diffusion .....	169
4.2.5 Testing epithelial cell polarization on micropatterned track-etch membranes .....	170
4.3 Results and Discussion .....	171
4.3.1 Method development for micropatterning photoresist	

atop track-etch membranes .....	171
4.3.2 Optimization of fabrication parameters .....	173
4.3.3 Testing membrane micropore patency using solute diffusion .....	175
4.3.4 Growth of polarized MDCK cells in microwells	
patterned atop track-etch membranes .....	176
4.4 Conclusions .....	178
4.5 Figures and Tables .....	179
4.6 References .....	184
Chapter 5: Conclusions and Future Directions .....	188
5.1 Overall summary and conclusions .....	188
5.1.1 Freestanding 1002F photoresist films .....	188
5.1.2 Chitosan-bottomed microwell arrays .....	189
5.1.3 Photoresist-based micropatterning of polyester	
track-etch membranes .....	189
5.2 Anticipated future directions .....	190
5.2.1 Freestanding 1002F photoresist films .....	190
5.2.2 Chitosan-bottomed microwell arrays .....	191
5.2.3 Track-etch membranes micropatterned with an	
overlying photoresist layer .....	192
5.2.4 Adaptation of technology prototypes for specific	
study of primary AT1 cells .....	193
5.3 Potential for future therapies for and insights into ARDS .....	194
5.4 References .....	196

## LIST OF TABLES

Table 1.1: Comparison of overall ion and water transport properties between AT1 and AT2 cells . . . . .	41
Table 1.2: Comparison of ion transporter density in AT1 and AT2 cells. . . . .	42
Table 2.1: Process parameters for 1002F photoresist films . . . . .	94
Table 2.2: Removal of 1002F films by immersion in water . . . . .	95
Table 2.3: Mechanical properties of 1002F films . . . . .	96
Table 3.1: Design overview of a microwell array platform for culture of single AT1 cells under an ALI . . . . .	152
Table 3.2: Comparison of diffusion constants to solute molecular weight for chitosan membranes in 1002F:chitosan hybrid films . . . . .	153
Table 4.1 Process conditions for micropatterning track-etch membranes with 1002F photoresist . . . . .	183

## LIST OF FIGURES

Figure 1.1: Hierarchical organization of heterogeneous epithelial subtypes in the respiratory tree .....	35
Figure 1.2: Alveolar pathology in ARDS .....	36
Figure 1.3: Models of lung fluid homeostasis .....	37
Figure 1.4: Real-time measurement of ASL and AvSL by confocal microscopy .....	38
Figure 1.5: Insufficiency of standard culture models to study primary AT1 cells .....	39
Figure 1.6: Design overview of a microwell array platform for culture of single AT1 cells under an ALI .....	40
Figure 2.1: Fabrication and release of photoresist thin films .....	82
Figure 2.2: Removal of 1002F films with various solvents .....	83
Figure 2.3: Removal of 1002F films from fabrication substrate .....	84
Figure 2.4: Tensile testing of freestanding, released 1002F films .....	85
Figure 2.5: Flexibility of freestanding 1002F films .....	86
Figure 2.6: Fabrication versatility of photoresist films .....	87
Figure 2.7: Formation of high-aspect ratio through-holes in 1002F photoresist films .....	88
Figure 2.8: Seeding of AT1-like cells into microstrainers .....	89
Figure 2.9: Use of 1002F film as a stencil .....	90
Figure 2.10: Application of photoresist thin films as inexpensive, re-usable stencils for metal deposition .....	91
Figure 2.11: Protein surface micropatterning using freestanding microarray 1002F films as stencils .....	92
Figure 2.12: 1002F films for loading exogenous molecules into single cells in a monolayer .....	93
Figure 3.1: Fabrication and release of hydrogel-bottomed microwell array films .....	138

Figure 3.2: Imaging of released chitosan-bottomed microwell array films . . . . .	139
Figure 3.3: Fabrication of multi-layer 1002F:chitosan:1002F films . . . . .	140
Figure 3.4: Dependency of chitosan film thickness on spin coating speed . . . . .	141
Figure 3.5: Optical properties of chitosan films . . . . .	142
Figure 3.6: Permeability of micropatterned 1002F:chitosan films to small molecules . . . .	143
Figure 3.7: Diffusion of FITC-conjugated dextrans through chitosan membranes in micropatterned 1002F:chitosan films . . . . .	144
Figure 3.8: Visualization of FITC-dextran diffusion through chitosan membranes in individual microwells . . . . .	145
Figure 3.9: Determination of diffusion constants and molecular weight cut-off for chitosan membranes in micropatterned 1002F:chitosan films . . . . .	146
Figure 3.10: Selective and covalent modification of chitosan film surfaces . . . . .	147
Figure 3.11: Entrapment of non-adherent cells in culture medium micropockets . . . . .	148
Figure 3.12: Physical isolation of clonal cell populations in microwell medium pockets . . . . .	149
Figure 3.13: Physical isolation of clonal cell populations in microwell medium pockets . . . . .	150
Figure 3.14: Growth of primary AT1-like cells in laminin-coated 1002F:chitosan microwells . . . . .	151
Figure 4.1: Fabrication and release of photoresist-micropatterned track-etch membranes . . . . .	179
Figure 4.2: Imaging of track-etch membranes micropatterned with photoresist . . . . .	180
Figure 4.3: Verification of pore patency via solute diffusion . . . . .	181
Figure 4.4: Polarization of MDCK cells grown on photoresist-patterned track-etch membranes . . . . .	182

## LIST OF ABBREVIATIONS AND SYMBOLS

$\lambda$	wavelength
$\Omega$	ohm
1002F	EPON™ resin 1002F, an epoxy negative photoresist
2D	two-dimensional
3D	three-dimensional
A549	human alveolar adenocarcinoma cell line
Ab	antibody
ADO	adenosine
ALI	air-liquid interface
APTES	3-aminopropyltriethoxysilane
Aqp	aquaporin
ARDS	Acute Respiratory Distress Syndrome
ASL	airway surface liquid
AT1	alveolar type 1
AT2	alveolar type 2
ATP	adenosine triphosphate
Au	gold
AvSL	alveolar surface liquid
Ba/F3	non-adherent human leukemia cell line
BSA	bovine serum albumin
C	concentration

Ca <sup>++</sup>	calcium cation
cAMP	cyclic AMP
CF	cystic fibrosis
CFTR	cystic fibrosis transmembrane conductance regulator
CHANL	Chapel Hill Analytical and Nanofabrication Laboratory
Cl <sup>-</sup>	chloride anion
cm	centimeter
cm <sup>2</sup>	square centimeter
cm <sup>3</sup>	cubic centimeter
CO <sub>2</sub>	carbon dioxide
°C	degrees Celcius
D	diffusion coefficient (alternatively, diffusivity)
Da	daltons
ddH <sub>2</sub> O	double-deionized water
DI	deionized
DMEM	Dulbecco's Modified Eagle Medium
DNA	deoxyribonucleic acid
EtOH	ethanol
ECM	extracellular matrix
ECMO	extracorporeal membrane oxidation
<i>e.g.</i>	for example
EM	electron microscopy
ENaC	epithelial sodium channel

FACS	fluorescence-activated cell sorting
FBS	fetal bovine serum
FITC	fluorescein isothiocyanate
g	gram
G $\alpha_q$	G-protein alpha-q subunit
G $\alpha_s$	G-protein alpha-s subunit
GBL	$\gamma$ -butyrolactone
GFP	green fluorescent protein
GPA	Granulomatosis with Polyangiitis
GPa	gigapascals
GPCR	G-protein coupled receptor
h	hours
<i>h</i>	thickness
H1299	human non-small cell lung adenocarcinoma cell line
H <sub>2</sub> O	water
HCO <sub>3</sub> <sup>-</sup>	bicarbonate anion
hr	hours
HSC	high-specificity cation
IPA	isopropyl alcohol
<i>i.e.</i>	meaning
ICU	intensive care unit
Ig	immunoglobulin
IL	interleukin

J	joule
$K_{0.5}$	half-maximal activity concentration
kDa	kilodaltons
KGF	keratinocyte growth factor
ln	natural logarithm
log	base-ten logarithm
m	meter
M	molar
% m/m	percent mass per unit mass
$m^2$	square meters
MAPK	mitogen-activated protein kinase
MDCK II	Madin-Darby Canine Kidney
MEMS	microelectromechanical system(s)
mg	milligram
min	minute
mJ	millijoule
mL	milliliter
mm	millimeter
$mm^2$	square millimeters
mM	millimolar
MPa	megapascals
mRNA	messenger ribonucleic acid
MW	molecular weight

N	number of moles
N <sub>2</sub>	nitrogen gas
Na <sup>+</sup>	sodium cation
NaCl	sodium chloride
NaOH	sodium hydroxide
NCI-H441	adherent human bronchiolar adenocarcinoma cell line
nL	nanoliters
nm	nanometers
nM	nanomolar
NSC	non-specific cation
O <sub>2</sub>	oxygen gas
P2X	purine-gated cation channel
P2Y	purine-activated GPCR
Pa	pascals
PBS	phosphate buffered saline
PCL	periciliary layer
PCR	polymerase chain reaction
PCT	polycarbonate
PCTE	polycarbonate track-etch
Pd	palladium
PDMS	polydimethylsiloxane
PEB	post-exposure bake
PET	polyethylene terephthalate

PETE	polyester track-etch
PGMEA	propylene glycol methylether acetate
PKA	protein kinase A
pL	picoliters
pS	picosiemens
PTFE	polytetrafluoroethylene
RAGE	Receptor for Advanced Glycation Endproducts
RNA	ribonucleic acid
rpm	rotations per minute
RPMI	Rosalind Park Memorial Institute
RT-PCR	reverse-transcriptase polymerase chain reaction
s	seconds
S	siemens
SEM	scanning electron microscopy
sulfo-SMCC	Sulfosuccinimidyl-4-(N-maleimidomethyl)cyclohexane-1-carboxylate
SP-A	surfactant protein A
SU-8	an epoxy negative photoresist
TC	tissue culture
TEER	transepithelial electrical resistance
T <sub>g</sub>	glass transition temperature
TNF- $\alpha$	tumor necrosis factor-alpha
$\mu$	micro
$\mu$ g	micrograms

$\mu\text{L}$	microliters
$\mu\text{m}$	micrometers or microns
$\mu\text{m}^2$	square micrometers
$\mu\text{M}$	micromolar
UTP	uridine triphosphate
UV	ultraviolet
V	volume
% v/v	percent volume per unit volume

## **Chapter 1: Introduction**

### **1.1 Airway and Alveolar Disease: States of Disordered Pulmonary Fluid Homeostasis**

#### **1.1.1 Respiratory epithelia and luminal fluid films**

##### **1.1.1.1 Hierarchical organization of respiratory epithelia**

The human lung is a highly complex organ system whose function is to facilitate exchange of CO<sub>2</sub>, a by-product of energy metabolism, for the atmospheric O<sub>2</sub> that drives oxidative chemical respiration, the reaction that nearly every human cell uses to produce energy.<sup>1</sup>

Inhaled air is conducted through the nasopharynx and down the trachea, where it enters the lungs via the left and right main pulmonary bronchi. Further movement through the respiratory tree – the secondary and tertiary bronchi, the terminal bronchioles, and the respiratory bronchioles – deposits the air in the alveoli, or air sacs, located at the most distal part of the lung and at which gas exchange actually occurs.<sup>1-3</sup>

A key feature of the pulmonary tree is a hierarchical organization of the epithelial tissues lining the open-air lumen (Figure 1.1). These epithelial tissues are composed of different epithelial cell subtypes, organized according to their location in the respiratory tree. Along the trachea, bronchi, and upper parts of the respiratory bronchioles, the epithelial layer is mainly composed of pseudostratified epithelial cells, which are ciliated at the apical

membrane (Figure 1.1A).<sup>4</sup> As will be explained below, recent research has discovered that these cells, despite their lack of participation in any gas exchange, play an important role in pulmonary fluid homeostasis and in the innate immune system of the lung.<sup>5-6</sup> The epithelial layer here also has a number of goblet cells and exocrine secretory glands, both of which serve to secrete mucus onto the luminal surface. At the more distal level of the terminal bronchioles, the epithelial tissue begins to transition to a layer of simple cuboidal epithelium that replaces ciliated pseudostratified epithelium with ciliated cuboidal cells and goblet cells with “club” cells that are morphologically and functionally diverse (involved in secretion of surfactant-like glycosaminoglycans, IgA, and lysozyme, lysosome- and cytochrome P450-mediated metabolism of inhaled exogenous substances, and regeneration of the bronchiolar lining)(Figure 1.1B).<sup>4, 7-11</sup> A transition again takes place as the respiratory tree further branches into the respiratory bronchioles, in which alveoli begin to appear in the walls. Alveoli are primarily located, however, at the most distal end of the respiratory bronchioles. Whether the alveoli lie in the walls of a respiratory bronchiole or at its distal end, a third transition of epithelial cell type occurs at the alveolar atrium, where cuboidal epithelium terminates and the epithelial layer becomes composed of two types of cells, termed alveolar type 1 (AT1) and alveolar type 2 (AT2) cells (Figure 1.1C).<sup>4</sup>

AT1 cells are squamous-type epithelia with large diameters – on the order of 100  $\mu\text{m}$  – and extremely thin cytoplasm, save for a perinuclear region containing a number of organelles.<sup>12</sup> Electron microscopy studies of alveoli reveal that AT1 cytoplasm thickness is at times as low as 50 nm.<sup>13</sup> By combining a large cell diameter (and hence surface area) and low cytoplasmic thickness, AT1 cells are especially adapted to facilitating efficient gas exchange between the alveolar lumen and the capillary beds that underlie 70% of the alveolar

basement membrane.<sup>14</sup> Together, AT1 cells are estimated to make up 40% of the alveolar cells and 97-98% of the total alveolar surface area.<sup>13</sup>

AT1 cells are thought to be terminally differentiated cells that arise from AT2 cells, cuboidal cells that make up the remaining 60% of alveolar cells but just 2-3% of the alveolar surface area.<sup>15</sup> Classic experiments by Evans *et al.* and Adamson and Bowden, as well as more recent work, showed that AT2 cells function as progenitor cells that can divide and differentiate, eventually assuming an AT1 morphology in order to preserve the alveolar epithelial surface in the event an AT1 cell undergoes apoptosis or death.<sup>16-19</sup> More advanced studies recently showed that in response to cellular injury (either AT2 cell-specific ablation or hyperoxic damage to AT1 cells), lineage-labeled AT2 cells clonally divide and self-renew in both mouse and human adult lungs, and that lipofibroblasts may help these cells form a specific pulmonary stem cell niche.<sup>20-21</sup>

AT2 cells have further importance as the source of pulmonary surfactant, a mixture of secreted proteins (surfactant proteins SP-A, -B, -C, and -D) and phospholipids (mainly dipalmitoylphosphatidylcholine).<sup>22</sup> Not only does this surfactant mixture help to opsonize any stray bacteria that reach the alveolus, it also accomplishes the imperative task of maintaining alveolar and small airway patency by reducing the surface tension of the epithelial surface.<sup>23-24</sup> In addition, AT2 cells synthesize and secrete immune effector molecules such as CXC chemokines and complement proteins.<sup>25-27</sup>

Advances in our understanding of stem cell biology through gene expression profiles have prompted studies aimed at more clearly delineating the gene expression differences between the AT1 and AT2 populations, with special focus on AT2 cells undergoing transdifferentiation towards an AT1-like morphological and molecular phenotype.<sup>28-31</sup>

Gonzalez *et al.* analyzed freshly isolated AT1 and AT2 cells and cultured AT2 cells, finding over 600 genes differentially expressed in two-way comparisons between the three populations.<sup>28</sup> Treutlein *et al.* recently used single-cell RNA sequencing to examine distal lung cells from the developing lungs of embryonic mice, and noted the presence of a “bipotential progenitor” cell that had expressed both AT1 and AT2 markers, potentially identifying a progenitor state through which transdifferentiating AT2 cells pass as they begin to downregulate typical AT2 gene expression patterns (typically surfactant proteins SP A-D) and upregulate typical AT1 patterns (such as podoplanin, aquaporin-5 (Aqp5), caveolin-1, and receptor for advanced glycation end products (RAGE)).<sup>32</sup> One possible interpretation of this data, which seem to argue against the classical model of AT2-to-AT1 transdifferentiation is that the “bipotential progenitor” represents a population of late stage, lung-specific, stem cells that give rise to a small group of differentiated, functional AT1 cells for the immediate needs of the lung and to a group of AT2 cells to replenish the AT1 population in the adult organism, once the pluripotent stem cell population has decreased. However, some have also called into question whether AT1 cells are truly terminally differentiated: a report by Gonzalez *et al.* observes that AT1 cells can divide *in vitro* and stain for the proliferation marker OCT-4, and three other reports detail the use of keratinocyte growth factor (KGF) to attenuate or even reverse the AT2-to-AT1 transdifferentiation, as measured by expression of AT1 or AT2 markers Aqp5 and SP-A and activation of mitogen-activated protein kinase (MAPK) pathways.<sup>33-36</sup>

In the normal state, the alveolus (though not its epithelial layer) is also home to a small number of immune cells, such as dendritic and plasma cells, but most notably the alveolar macrophage, a sentry immune cell whose function is to phagocytose any stray

pathogens entering the alveolus in inhaled air and any cellular debris that results from turnover of the epithelial layer.<sup>4</sup>

### **1.1.1.2 Air-liquid interfaces and luminal fluid films in the pulmonary tract**

In addition to a hierarchical organization of the cellular subtypes found in the epithelial layer, a second key feature of the respiratory tree is presence of a physiologic air-liquid interface (ALI) just above the epithelial tissue, due to the open-air lumen to which the epithelia that line the respiratory tract face. Flow of blood through capillary beds below the basement membrane on which the epithelia lie ensures delivery of nutrients and removal of metabolic by-products, as well as ensuring proper electrolyte balance across the cell membrane and availability of fluid to maintain cellular hydration.<sup>4</sup> While air in the lungs has relatively high humidity (achieved via humidification of inhaled air that takes place in the nasopharynx), respiratory epithelial tissue nonetheless greatly differs from other epithelial tissues that are bathed in large fluid volumes (large relative to the cell volume) on both sides of the basement membrane, basal and luminal.<sup>14</sup> Importantly, the presence of an ALI appears to have a role in maintaining a differentiated and polarized phenotype for the epithelial layer and thus appears to be a key and necessary component of normal *in vivo* physiology, a concept that will be discussed further in section 1.2.4.<sup>37-40</sup>

However, rather than having an apical surface that is completely dry, epithelia at all levels of the respiratory tree (from the trachea to the alveolus) are known to have a thin sol-gel layer on the luminal surface. Thus, the true location of the respiratory ALI does not lie at the epithelial layer, but rather just above it. Similar to the hierarchical heterogeneity of epithelial subtype observed along the respiratory tree, the apical fluid layer varies in thickness from an order of ~10  $\mu\text{m}$  in the trachea and bronchi, where the fluid is termed the

airway surface liquid (ASL), to an estimated 0.2  $\mu\text{m}$  in the alveoli, where it is known as the alveolar surface liquid (AvSL).<sup>41-42</sup> Thinning of the fluid layer in the more distal parts of the lung reflects the need to minimize the diffusion distance and optimize gas exchange efficiency.

The conservation of the apical fluid layer thickness within a given level of the respiratory tree suggests that the lung can homeostatically regulate the thickness (and hence the volume) of the fluid layer in both the airways and alveoli. Two opposing observations support this. First, because the water content of the humidified air in the lungs lacks the volume to match the estimated 20-30 mL that comprises the respiratory thin fluid layer over the surface area of the entire lung ( $\sim 100 \text{ m}^2$ ), let alone the estimated 700 mL of fluid thought to be lost in the proximal airways due to evaporation, the fluid layer must be generated from the respiratory tract itself (and not “raining out” from the air inhaled into it).<sup>41, 43</sup> At the same time, the demonstration of rapid clearance of pulmonary fluid at birth, when the location of gas exchange moves from the placenta to the lung, and the observation that a small fluid bolus instilled into the lungs is cleared into the interstitium suggest that fluid clearance out of the respiratory lumen is a normal physiological process.<sup>44-46</sup> However, as will be discussed below, this process of pulmonary fluid homeostasis can be disrupted by certain lung diseases.

### **1.1.2 Alveolar diseases and disordered fluid homeostasis**

A number of human diseases can affect the alveolus and disrupt its normal function. Heart failure, for example, commonly causes edema of the pulmonary interstitium and can lead to an influx of fluid into the alveolus.<sup>47</sup> Severe pneumonia can also fill alveoli with a fluid thick with necrotic debris. Alveolar hemorrhage, in which the surrounding capillaries bleed into the alveolar space, can result from a number of etiologies, including exposure to

toxic inhalants, Goodpasture's Syndrome, Granulomatosis with Polyangiitis (GPA), and connective tissue and autoimmune diseases (*e.g.* systemic lupus erythematosus).<sup>48-49</sup>

However, the most serious example of alveolar disease is Acute Respiratory Distress Syndrome (ARDS), in which an insult to the alveolar-capillary interface is enough to damage the alveolar epithelial cells, the capillary endothelial cells, and even the basement membrane separating the cell layers (Figure 1.2A).<sup>50</sup> This compromise of the normal alveolar-capillary barrier (Figure 1.2B) increases its permeability, leading to the influx of a highly proteinaceous fluid into the alveoli that results in severe and intractable alveolar flooding and a severe compromise in gas exchange. Numerous etiologies (most commonly septic pneumonia or aspiration/inhalation injury) can cause ARDS, but the clinical pattern is the same: rapid onset of dyspnea and arterial hypoxemia that is refractory to O<sub>2</sub> therapy, followed by worsening respiratory failure as the alveoli further fill with fluid and the alveolar basement membrane becomes hyalinized with thick protein deposits (Figure 1.2C).<sup>50</sup>

The clinical picture reflects the two stages of ARDS pathology progression. In the acute or exudative stage, injury to the alveolar-capillary interface results in influx of protein-rich edematous fluid and neutrophils, setting off localized inflammation and release of a variety of cytokines and chemokines, including tumor necrosis factor-alpha (TNF- $\alpha$ ) and interleukins 1 and 8 (IL-1, IL-8). Damage to epithelial and endothelial cells continues and is accompanied by increasing deposition of fibrin-rich hyaline films along the basement membrane, a pathologic picture known as diffuse alveolar damage. Between days 5 and 7, the hyaline membrane formation begins to slow, but gas exchange remains compromised even as the edema resolves due to the hyalinization of the alveolar basement membrane. At this stage, the organizing or fibroproliferative stage, necrotic debris is removed by activated

macrophages, inflammation is reduced, and a slow repopulation of the alveolar and endothelial layers by resident progenitor cells occurs as those cells proliferate and spread over fresh extracellular matrix laid down by fibroblasts activated by the inflammation.<sup>51</sup>

At its onset, ARDS is a medical emergency that usually necessitates admission to an intensive care unit (ICU), and epidemiologic data suggest that there are close to 200,000 cases of ARDS in the U.S. annually.<sup>50, 52</sup> Up to 20% of patients in intensive care units on mechanical ventilation meet ARDS criteria, and current overall mortality rates of ARDS patients lie at 37-45%, and are as high as 50-60% for some patient groups, such as the elderly and those with pre-existing cardiovascular conditions.<sup>50, 53-54</sup>

The most serious complication shared by all of the diseases described above is the persistent presence of fluid in the alveolar space. This fluid can disrupt the gas exchange function of alveoli, owing to a great increase in the diffusion distance without a corresponding increase in oxygen solubility in the fluid. Additionally, the fluid can also result in damage to the epithelial layer itself, further compromising gas exchange. The presence of intractable alveolar flooding in these disease states, but not in normal states, suggests a compromise of normal alveolar fluid homeostasis via an increased influx of fluid from the bloodstream or interstitium into the alveolus (increased rate of entry), a reduced clearance of fluid from the alveolar space (decreased exit rate), or both.<sup>55-56</sup>

### **1.1.3 Alveolar diseases: therapeutic options and shortfalls**

Certain cases of alveolar flooding due to disease can be treated and resolved without complication. Pulmonary edema, for example, can be treated via a combination of diuretics (to promote alveolar fluid resorption) and appropriate management of the underlying etiology, *e.g.* cardiac failure (to prevent continued alveolar flooding).<sup>57</sup> Alveolar hemorrhagic

diseases, namely Goodpasture's Disease, lupus, and GPA, can be managed with immunosuppression, with fluid in the alveolus being gradually resorbed over time and the erythrocytes broken down by resident alveolar macrophages.<sup>49</sup>

ARDS, however, continues to present a treatment challenge, due to both the persistence of alveolar fluid (owing to basement membrane disruption and hyalinization) and the damage to the epithelial and endothelial cells themselves. While the triggering etiology (*e.g.* sepsis) can sometimes be treated and resolved, the patient is left in a hypoxemic state with flooded, fibrotic alveoli, and hence respiratory support with a mechanical ventilator is the mainstay of ARDS treatment.<sup>56</sup> Recent clinical trials advocating a switch from traditional to low-tidal volume ventilation have led to some improvement in relevant patient outcomes, namely hospital and overall mortality and number of ventilator-free days.<sup>58-59</sup> However, low-tidal volume ventilation is nonetheless only an improvement in supportive therapy, not a direct address of ARDS pathophysiology. Similarly, the FACTT Trial indicated that while patients who received conservative fluid management in the ICU in order to reduce alveolar flooding required less time on a mechanical ventilator, overall 60-day survival was not increased.<sup>60</sup> Recently, clinical trials of both inhaled and infused  $\beta_2$ -adrenergic receptor agonists that had demonstrated *in vitro* efficacy in potentiating fluid clearance by AT2 cell monolayers failed to show improvements in patient mortality.<sup>61-62</sup> Other clinical trials have demonstrated the failure of inhaled nitric oxide, antioxidant compounds, and exogenous pulmonary surfactant in reducing morbidity or mortality.<sup>63</sup> Even in those patients who survive ARDS and can be discharged from the ICU, functional morbidities remain. Herridge *et al.* found reduced exercise tolerance and diffusion capacities in ARDS patients five years after hospital discharge.<sup>64</sup>

Considering the prevalence and variety of etiologies that can result in ARDS (notably sepsis from either community or nosocomial sources) and the epidemiologic data on ARDS mortality, ARDS presents a significant source of morbidity and mortality to the public health. Given the central role alveolar flooding occupies in ARDS pathophysiology, a strategic approach to potentiating alveolar fluid removal, especially in the early stages of ARDS before basement membrane hyalinization occurs, is an important and pressing biomedical research goal.

## **1.2 Physiology and Pharmacology of Pulmonary Liquid Homeostasis**

### **1.2.1 Airway surface liquid in bronchial and bronchiolar epithelia**

In order to most efficiently develop a strategy, pharmacologic or otherwise, to potentiate alveolar fluid clearance, a full and complete understanding of alveolar fluid homeostasis mechanisms and regulation is needed. A great deal of information exists on fluid homeostasis in the upper airways, and so provides a useful place to begin generating a model of fluid clearance in the more distal lung spaces.

Research efforts comparing bronchial epithelia from healthy subjects and patients with cystic fibrosis (CF) have given great insight into fluid balance in the upper airways. Cystic fibrosis (CF) is a genetic disorder characterized by progressive lung disease due to the buildup and infection of abnormally viscous mucus in the airways.<sup>65</sup> CF was classically thought to be due to a pathological overproduction of mucus with abnormal composition.<sup>66</sup> However, the discovery of altered transport of chloride ( $\text{Cl}^-$ ) and sodium ( $\text{Na}^+$ ) ions by CF epithelia have led to a model of CF not as a disease of abnormal mucus, but rather as a failure of mucus clearance due to dysregulated ion transport and fluid homeostasis on the airway

luminal surface.<sup>5-6, 41, 67</sup> Discoveries of reduced chloride anion ( $\text{Cl}^-$ ) secretion to, and increased sodium cation ( $\text{Na}^+$ ) resorption from, the airway surface by epithelia of CF patients compared to healthy subjects were found in the 1980s via bioelectric measurements.<sup>68-72</sup> Subsequent functional reconstitution of the gene product shown to be mutated in CF – termed the cystic fibrosis transmembrane conductance regulator (CFTR) - revealed it to be a chloride channel.<sup>73-76</sup> As further research was undertaken to better understand how CFTR loss also resulted in abnormally high  $\text{Na}^+$  resorption through the epithelial sodium channel (ENaC), two studies by Matsui *et al.* suggested that these ion transport abnormalities resulted in depletion of the layer of fluid approximately 10  $\mu\text{m}$  thick found on the luminal surface of ciliated airway epithelia.<sup>77-78</sup> In normal airways, this apical fluid hydrates a layer the approximate thickness of the respiratory cilia (hence the term ‘periciliary layer,’ PCL), and the mucus sol-gel layer above it (together known as the airway surface liquid ASL). The presence of fluid in the PCL allows efficient and coordinated beating of the cilia atop the cells, allowing the movement of mucus in the overlying sol-gel layer up the respiratory tree and out of the lung in a process termed mucociliary clearance (MCC). The dehydration observed in CF airways leads to ciliary stasis and a reduction in mucociliary clearance.

Based on data comparing healthy and CF subjects, airway fluid is thought to be maintained via a CFTR- and ENaC-dependent transport of chloride and sodium (respectively) to the airway surface, creating an osmotic pressure that draws water onto the surface, resulting in proper ciliary function and mucociliary clearance.<sup>41</sup> In CF, loss of CFTR-dependent  $\text{Cl}^-$  secretion to the apical surface and increased ENaC-mediated  $\text{Na}^+$  absorption from the apical surface, reverses the osmotic pressure, leading to airway surface and mucus dehydration and a cessation of normal mucus clearance.<sup>5-6, 67</sup>

This hypothesis also describes a regulatory mechanism for airway surface ion transport: extracellular concentrations of the nucleotide adenosine triphosphate (ATP) and its metabolites. Knowledge that activation of protein kinase A (PKA) by cAMP stimulated chloride conductance in normal airway epithelia, but not in CF cells, suggested a role for cAMP-dependent PKA signaling in CFTR activation.<sup>79-81</sup> Determination of CFTR's primary structure identified several consensus phosphorylation sites for PKA, explaining the lack of response to cAMP or PKA in CF cells.<sup>73</sup> Further research into the regulation of this ion transport system in normal airways revealed a role for constitutive release of ATP to the luminal surface, its subsequent metabolism by ecto-nucleotidases to adenosine, and activation by that adenosine of the A<sub>2b</sub> adenosine receptor, an apical membrane G<sub>α<sub>s</sub></sub>-associated GPCR.<sup>82-83</sup> This activation, resulting in adenylate cyclase stimulation and increases in intracellular concentrations of cAMP, leads to PKA activation and phosphorylation of CFTR. Subsequent increases in chloride secretion and ENaC inhibition by CFTR generates the osmotic gradient for water flow to the airway surface, which dilutes surface adenosine concentrations and reduces A<sub>2b</sub> receptor activation, thus providing negative feedback to the regulatory pathway.<sup>84</sup>

Interestingly, a second signaling pathway utilizing surface P2 purinergic receptors was coincidentally discovered that came to be a target for pharmacologically potentiating directed ion transport and correcting the disordered fluid homeostasis in CF.<sup>85</sup> Early experiments had shown that chloride conductance in both normal and CF epithelia could be increased using calcium ionophores, suggesting an alternative pathway to ion transport that might present a druggable route to increasing airway ion transport.<sup>86</sup> Further work into this alternative pathway showed that ion transport could be potentiated by supply of exogenous

ATP and uridine triphosphate (UTP) nucleotides to the extracellular surface of airway epithelia.<sup>87-92</sup> Later data demonstrated a connection between apical P2Y purinergic receptors, to which ATP and UTP are agonists, and Ca<sup>++</sup>-dependent increases in chloride conductance.<sup>93-94</sup> These P2Y purinoreceptors on the apical membranes of airway epithelia activate chloride secretion via a G $\alpha_q$ -mediated release of intracellular calcium that targets TMEM16A calcium-dependent chloride channels found in respiratory epithelia.<sup>95</sup>

In summary then, the leading model for fluid homeostasis in the airway involves active chloride and sodium ion secretion onto the airway surface, creating an osmotic pressure that draws water onto the apical membrane, where it hydrates the airway surface with a ~10  $\mu$ m-thick fluid layer that facilitates proper cilia function and mucociliary clearance (Figure 1.3A). Regulation of this CFTR- and ENaC-mediated chloride and sodium ion balance is achieved under normal conditions by the constitutive extracellular release and metabolism of ATP to adenosine, which fine-tunes airway surface hydration via A<sub>2b</sub> receptor binding and downstream cAMP-mediated activation of CFTR.<sup>6, 96</sup> As will be discussed below, much of the same mechanistic and regulatory machinery of airway fluid homeostasis is also found in alveolar cells.

Importantly, a complete understanding of the mechanisms and regulation of directed ion transport and fluid homeostasis in airway epithelia has led to the successful design of a number of pharmacologic therapies for correcting fluid homeostasis imbalance in CF. First, identification of CFTR as the defective protein behind CF, and many decades of focused drug development, has led to a new class of drugs designed to potentiate mutant forms of CFTR that are present at the membrane.<sup>97-101</sup> Clinical tests of compounds developed by Vertex Pharmaceuticals, namely VX-770 and -809, have demonstrated preclinical and some

clinical success in improving lung function. Second, an understanding of how loss of CFTR-mediated ion transport results in defective fluid homeostasis led to the demonstration that inhaled doses of hypertonic saline could provide an osmotic draw that restores proper airway surface hydration to normal functional levels. By doing so, Donaldson *et al.* reported an increase in sustained mucus clearance and lung function in CF patients.<sup>102</sup> Third, the identification of accessory purinergic signaling pathways led to the development of several drug candidates for potentiating chloride secretion, and thus airway surface hydration, through non-CFTR means. Synthetic analogues of ATP were found to potentiate *in vitro*  $\text{Ca}^{++}$ -dependent chloride secretion and were taken into clinical trials.<sup>103-104</sup>

### **1.2.2 Ion and fluid transport by alveolar type 2 (AT2) epithelia**

In 1995 Bastacky *et al.* used scanning electron microscopy to show the presence of a continuous, 0.2  $\mu\text{m}$ -thick apical fluid layer in alveoli.<sup>42</sup> While this was the first direct measurement of the basal thickness of the alveolar surface liquid (AvSL), the first evidence that fluid homeostasis occurs in the alveolus had come a decade before, when a demonstration by Matthay *et al.* of differential clearance rates of fluid and protein instilled into sheep alveoli was published at the same time that the first cultures of isolated primary AT2 cells were shown to participate in active ion transport.<sup>105-106</sup> Since that time, alveolar ion transport has been studied extensively using a variety of models, including animal and human whole perfused lungs and an innovative lung slice preparation.<sup>107-108</sup> Rat models have been widely used due to demonstrations that total lung fluid clearance rates in rats are similar to those of isolated, perfused human lungs *ex vivo*.<sup>107</sup> Despite these clinically-relevant models, however, a complete understanding of alveolar fluid homeostasis has proven elusive,

and hence there remains a crucial role for basic *in vitro* studies of purified primary alveolar cells.

A number of published studies have specifically examined ion transport in AT2 cells. Early work showed that monolayers of cultured AT2 cells took up  $^{22}\text{Na}^+$  in an apical-to-basolateral direction and produced measurable transepithelial potential differences when cultured on permeable supports.<sup>106, 109</sup> Further work by a number of groups has shown that rat AT2 cells, both *in situ* and cultured on permeable supports, contain the basolateral Na/K/ATPase and ENaC. Bioelectric studies of rat AT2 cell monolayers and patch-clamp studies of individual rat AT2 cells have firmly established the functionality of these proteins.<sup>40, 46, 110-112</sup> Studies by Fang *et al.* have demonstrated a role for CFTR in AT2 cells.<sup>113</sup> ENaC has been a subject of particular investigation in the alveolar biology community.<sup>111, 114</sup> One general set of studies has focused on the balance and relative activity between two functional variants of ENaC. One variant, termed highly-selective (HSC) has a low, amiloride-sensitive conductance (approximately 6 pS, amiloride  $K_{0.5} = 37$  nM) but a >40 fold selection of sodium over potassium cation, while the non-selective (NSC) variant is amiloride-insensitive ( $K_{0.5} = 2.2$   $\mu\text{M}$ ) and cation nonselective, albeit with a higher conductance (21 pS).<sup>114</sup> Jain *et al.* noted that cultured AT2 monolayers preferentially expressed the HSC ENaC variant when cultured under an ALI, suggesting that a shift in ENaC function in AT2 cells can accompany a transition from a basal to a flooded environment, such as that observed with alveolar disease.<sup>40</sup> A second general set of studies has focused on potential modalities by which AT2 ENaC channels are regulated. Adrenergic, purinergic, and dopaminergic signaling, as well as the influence of steroid hormones, oxygen tension, and inflammatory chemokines have all been investigated, with particular efforts

trying to reconcile failed clinical trials of  $\beta_2$ -adrenergic agonists with *in vitro* studies suggesting the efficacy of this agonist class.<sup>115-125</sup> An as-yet unresolved question concerns whether CFTR, or at least some kind of  $\text{Cl}^-$  transport, is required for ENaC activation. Jiang *et al.* showed that adrenergic stimulation of  $\text{Na}^+$  transport in AT2 cells involved the activation of apical  $\text{Cl}^-$  channels, while Mutlu *et al.* showed a similar effect but demonstrated a role for CFTR as the intermediate in ENaC activation.<sup>117, 119</sup> Interestingly, CFTR-mediated  $\text{Cl}^-$  secretion in confluent cultures of primary AT2 cells was shown to be calcium-dependent, a relationship not found in epithelia of the upper airways.<sup>126</sup>

Striking similarities in the regulation of ion transport and fluid homeostasis were also recently shown between bronchial epithelial and AT2 cells at the monolayer level. Bove *et al.* used confluent monolayers of AT2 cells to show that AT2 ion transport and fluid movement is regulated by nucleotides via purinergic signaling pathways similar to those of bronchial epithelia in the larger airways.<sup>126</sup> Addition of ATP and UTP to AT2 cell monolayers produced ion fluxes inhibited with ion transporter modulators. Similar addition of ATP and UTP to cell monolayers led to increases in apical fluid thickness, while addition of the nucleotide-scavenging enzyme apyrase produced the opposite effect. Moreover, AT2 cells grown in monolayers expressed the P2X<sub>4</sub> and P2Y<sub>2</sub> purinergic receptors.<sup>126</sup> The significance of this report was twofold. First, its study of ion transport by monolayers of human AT2 cells validated similar data showing functional ion transporters in rat AT2 monolayers. Second, analysis of the role of nucleotide signaling in these monolayers provided the first data for a conserved apical fluid thickness regulatory mechanism between human airway and alveolar epithelial cells. These demonstrated similarities in ion and fluid

transport mechanism and regulation are made more interesting by the identification of such molecular machinery in AT1 cells as well.

### **1.2.3 Ion transporters and purinergic receptors in alveolar type 1 (AT1) epithelia**

While bronchial and AT2 cells have been studied extensively, the physiology of AT1 cells, which populate >98% of the alveolar surface area, remains poorly understood. For many years, this was due to technical difficulties in the isolation and purification of AT1 cells, which are larger, more fragile, and lower yielding in primary cell harvests than AT2 cells.<sup>127</sup> One advance for the AT1 field came with the identification and use of antibodies to apical integral membrane proteins specific to AT1 cells: chiefly, RTI40 in rodents and HTI56 in humans.<sup>128-129</sup> This advance enabled positive selection strategies that allowed for the isolation of AT1 populations at purities of >85%, with cellular viabilities of >95%.<sup>130-132</sup> Typical isolation/purification protocols currently involve enzymatic digestion of the distal airspaces with elastase to liberate alveolar cells, labeling of the AT1, AT2, and macrophage cells with antibodies to cell-specific markers, and lastly either negative depletion by magnetic bead immunoselection or positive enrichment by fluorescence-activated cell sorting (FACS).<sup>133</sup>

An early experiment implicating a role for AT1 cells in fluid transport came with the localization of the aquaporin-5 (Aqp5) molecular water channel to the apical membrane of alveolar epithelia in situ.<sup>134</sup> A seminal experiment showing that the presence of Aqp5 in isolated AT1 cells in suspension conferred extremely high water permeability led to an early theory that AT1 cells played a small role in alveolar fluid homeostasis, with directed ion transport being achieved by the AT2 cells and water passively flowing through Aqp5 channels in AT1 cells.<sup>135</sup>

However, more recent advances in AT1 cell biology have called into question the idea that AT1 cells play only a passive role in alveolar fluid transport. This paradigm shift has occurred because of the identification of similar ion transport machinery in AT1 cells through radionuclide uptake, electrophysiology, and mRNA and protein-level expression studies. First to suggest a higher role were two independent studies by Borok and Johnson showing that isolated rat AT1 cells immunostain for ENaC and the Na/K/ATPase.<sup>127, 130</sup> These proteins, both active in ion transport, were also shown in parallel rat alveolar tissue sections. Johnson also showed that isolated AT1 cells in suspension could actively take up  $^{22}\text{Na}^+$  in an amiloride-inhibitable fashion.<sup>130</sup> Cell-attached patch clamp studies of individual, nonconfluent AT1 cells showed function of HSC and NSC ENaC and CFTR, as well as a number of other channels such as potassium and cyclic-nucleotide gated (CNG) cation channels and the  $\text{Cl}^-/\text{HCO}_3^-$  anion exchanger.<sup>131-132</sup> Apart from showing electrophysiologic function of the ion channels previously identified by immunofluorescence, this work was significant in that measurements of channel density and area suggest that AT1 cells contain a significantly greater number of ion channels than AT2 cells. By applying the calculated channel density found in AT1 versus AT2 cells to the surface area of each cell type, AT1 cells were found to have a seven-fold greater osmotic permeability, a forty-fold higher number of  $\text{Na}^+$  channels, and six times as many CFTR channels.<sup>136</sup> While a caveat central to these studies is that the measured cells were grown in suspension or unpolarized on glass, the identification of ion channels studied *in vitro* with positive *in situ* immunostaining of alveolar tissue sections for those same channels supports these data.

Based on the presence of ion- and water-transporting molecules in AT1 cells, the large amount of lung surface area known to be covered by AT1 cells, and the expression of

higher numbers of functional ion channels in AT1 versus AT2 cells, an alternative model theorizes that AT1 cells achieve the bulk of both ion and water transport (compared to the smaller AT2 cells) in the alveolus (Figure 1.3B). In this model, similar to that of the airway,  $\text{Cl}^-$  and  $\text{Na}^+$  are moved across the apical membrane of both AT1 and AT2 cells by specific ion channels (presumably CFTR and ENaC, respectively), and water follows down its osmotic gradient through Aqp5.<sup>136-137</sup> Curiously, patients with CF who thus lack functional CFTR do not exhibit signs of alveolar disease, suggesting the possibility of either an alternative primary anion transporter as the driver of alveolar fluid homeostasis, or the upregulation of an alternative, secondary mechanistic pathway in CF patients that could present a pharmacological target in all patients with alveolar disease.<sup>126</sup>

In addition to the expression of similar ion transporters in AT1 cells as in AT2 and bronchial cells, evidence exists to suggest that adenosinergic and purinergic signaling pathways may serve to regulate AT1 ion transport in similar fashions to pathways observed in AT2 and bronchial cells. The same study that demonstrated purinergic regulation of AT2 monolayer fluid homeostasis showed that AT2 cells in the process of transdifferentiating to an AT1-like state continued to express P2X<sub>4</sub>, P2Y<sub>2</sub>, -Y<sub>4</sub>, and Y<sub>6</sub> receptors. Expression of the A<sub>2A</sub> and A<sub>2B</sub> variants of the adenosine receptor was also observed, suggesting that AT1 cells express these receptors as well.<sup>126</sup> Any one of three additional sets of data would strengthen this claim: whole-cell patch-clamp electrophysiologic studies (such as those performed by Johnson *et al.* on AT1 cells grown on glass) employing adenosinergic or purinergic ligands; RT-PCR or immunofluorescent staining of freshly isolated AT1 cells for adenosinergic or purinergic receptors; and/or immunostaining of *in situ* alveolar tissue sections for those

receptors. In the latter case, however, the lack of reliable P2Y or P2X receptor antibodies makes this difficult to achieve.

In summary, then, the expression of similar ion transport molecular machinery in bronchial, AT2, and AT1 cells, as well as apparent similarities in the pathways regulating ion transport in bronchial and AT2 cells, suggest conserved mechanisms and regulation of ion transport and fluid homeostasis in both the airway and the alveolus. Taken together, these similarities also provide compelling evidence that, if a detailed understanding of the physiology is available, successful pharmacological targets for potentiating alveolar fluid clearance can be identified for use in alveolar diseases.

Given the success of *in vitro* cultures of bronchial and AT2 cells in replicating the *in vivo* physiology, the logical direction for subsequent research, then, would be to determine whether *in vitro* cultures of purified AT1 cells directly participate in directed ion and fluid transport and to elucidate the mechanisms and regulatory elements of that process. However, testing this theory of ion and fluid transport by AT1 cells has proven difficult due to technical difficulties in AT1 culture, beyond the difficulties encountered in AT1 isolation: the formation of intercellular gaps between AT1 cells in culture that render useless the gold standard methods for measuring ion and fluid transport in cultured cells.

#### **1.2.4 Current methods for studying pulmonary fluid homeostasis**

A great deal of the data used in formulating the current model of fluid homeostasis by bronchial epithelia, as well as a number of studies with AT2 cells, used monolayers of primary cells cultured under ALI conditions. The current gold standard for ALI culture involves seeding primary cells on permeable supports that allow cells to polarize and establish high-resistance transepithelial electrical seals.<sup>138-140</sup> The supports, now

commercially available and typically composed of either track-etched polyester or microwoven fluoropolymer (for more details, see Chapter 4), feature pores that permit the exchange of fluid, ions, and other solutes across the support. By seeding cells onto the support, supplying growth media to the compartment below the support, and evacuating fluid from the apical surface, the primary cells can be cultured across an ALI that ensures cells can obtain nutrients and expel metabolites from the culture medium below, while still replicating the ALI that characterizes their natural *in vivo* microenvironment.

The necessity for permeable supports is twofold: the maintenance of proper *in vivo* cellular physiology, and the use of bioelectric and microscopic assessment of ion and fluid transport. In the first case, a wealth of evidence exists showing that some kind of permeable support is necessary to achieve proper polarization of the cell membrane into apical and basolateral faces, a key feature of the respiratory epithelium.<sup>37-38, 141-146</sup> Initial studies by Whitcutt *et al.* revealed a greater degree of ciliated columnar morphology and mucus production *in vitro* of tracheal cells cultured under an ALI on a permeable gelatin support.<sup>37</sup> Later work by Johnson *et al.* showed enhanced sodium transport and the effect of amiloride blockade in bronchial epithelia cultured under an ALI compared to standard immersion culture.<sup>142</sup> In fact, the need for a culture support that closely mimics the *in vivo* basement membrane is so strict for primary bronchial epithelial cells that when the support becomes less or even more porous than the native basement membrane (the latter case seen in attempts to grow primary bronchial cells on supports with pores 3.0  $\mu\text{m}$  in diameter), the epithelial layer fails to properly form, instead assuming a true single-cell-deep monolayer and not the multi-layer architecture seen of a true pseudostratified epithelium *in vivo*.<sup>138</sup> While AT1 and AT2 cells exist as a pure single-cell monolayer and not a pseudostratified epithelium, at least

two studies have nonetheless shown that ALI conditions influence bioelectric properties in AT2 monolayers as well.<sup>39-40</sup>

In addition to promoting a recapitulation of both the *in vivo* epithelial layer architecture and the molecular physiology of the epithelial cells themselves, use of permeable supports also allows testing of tissue-scale epithelial function using bioelectric and confocal microscopic methods to study ion and fluid transport, respectively. In the first case, a setup known as an Ussing chamber is utilized to allow for real-time monitoring of voltage potential differences across an epithelial layer, with the capability to rapidly introduce interrogatory compounds such as ion transporter modulators to either the apical or basolateral faces of the cell.<sup>138</sup> Supply of an inhibitor to a specific ion transporter present in the membranes of cells in the monolayer, for example, begets a reproducible and dose-dependent change in the transepithelial potential difference measured by the chamber apparatus. In this way, studies of ion channel expression can be used to guide the design of specific bioelectric experiments. In the second case, confocal microscopy is used to directly observe fluid movement across an epithelial layer. A typical protocol, pioneered by the Boucher Labs, involves labeling the apical surface fluid with a fluorophore-conjugated, high-molecular weight dextran and using a laser-scanning confocal microscope to scan through the apical fluid and epithelial cell layers. By measuring the thickness of the fluorescent layer above the cells, the thickness and volume of the surface liquid can be determined. Time course serial imaging of the fluid layer allows quantitation of water flux in response to perturbations of the mechanistic or regulatory molecular machinery (Figure 1.4).<sup>147</sup>

Both the bioelectric and confocal microscopy methods depend on the presence of high-resistance transepithelial electrical seals in the epithelial layer, which act to prevent

leakage of ions and fluid. Primary bronchial and AT2 cells readily form epithelial layers in culture that have transepithelial seals with resistances on the order of  $500 \Omega \cdot \text{cm}^2$  at the minimum (Figure 1.5A).<sup>126, 138, 148</sup> However, primary AT1 cells in culture spontaneously form intercellular gaps.<sup>132, 149</sup> Comparison of these gaps, which reach sizes of up to  $50 \mu\text{m}$  (Figure 1.5B), with *in vivo* alveolar ultrastructure led to the proposal that these gaps are the attempts of AT1 cells in culture to form pores of Kohn, an interalveolar gap involved in collateral ventilation of adjacent alveoli that prevent alveolar collapse. Regardless of their purpose, these gaps act to short-circuit bioelectric measurements and allow fluid leakage in microscopy studies, and so constitute a technical barrier that must be overcome for useful study of AT1 cells.<sup>132, 149</sup>

Given the imperative to directly assess ion and fluid transport by AT1 cells, and the problem posed by the intercellular gaps they form, I hypothesized that a novel cell culture platform fabricated with microscale features would enable the culture of small numbers of or even single primary AT1 cells while circumventing the problem posed by the AT1 intercellular gaps. Construction of such a platform lies in the field of microfabrication.

### **1.3 Microscale devices for analysis of discrete numbers of cells**

#### **1.3.1 Definition and use of microscale devices**

The term ‘microfabricated’ or ‘microscale’ device refers to any of a huge number of devices described in the chemical and biomedical research literature, each of which possesses micron-scale patterned features. In a general sense, these features can be physical, chemical, or both.<sup>150-151</sup> For example, physical features might include pedestals, channels, or wells. Chemical patterns could be islands of extracellular matrix protein, patterns of growth factors,

or gradients of substrate stiffness. Combinations of these patterning schema open applications such as directed or ordered cellular co-cultures, tailoring substrate stiffness for experiments on cellular mechanotransduction, or spatially-defined gradients of chemotactic factors.<sup>152-155</sup>

The most common methods in use in the microfabrication field include soft lithography, photolithography, and injection molding, with a number of others also available.<sup>156-159</sup> Soft lithography most commonly uses the optically clear silicone polymer polydimethylsiloxane (PDMS) to create structures from a master mold. By casting uncured PDMS onto the mold, heat curing, and later removing the polymerized PDMS, a final structure of negative relief from the master mold is formed.<sup>158</sup> Photolithography typically uses photoactive polymers known as photoresists to create its structures. By exposing the photoresist to UV light through a mask patterned with microscale 2D features, the photoresist can be selectively polymerized according to the mask pattern. Injection molding, typically done with cyclic olefin co-polymer, a thermoset, or a thermoplastic, involves the instillation of a polymer in its liquid form around a mold, after which the polymer is allowed to cool and set, forming a negative relief of the mold.

In addition to general classifications of device composition and construction, the majority of devices used in biomedical research endeavors and fabricated using these materials typically fall into one of several general design categories: valved or laminar flow microfluidics, droplet microfluidics, microwell arrays, micropedestal arrays, and micropatterned surfaces.<sup>160-161</sup> Laminar flow microfluidic devices feature liquid flow through ordered microchannels, typically bordered by PDMS, at user-defined flow rates. By contrast, droplet microfluidics usually feature an interfaced flow of two immiscible liquids to create

droplets composed of one phase that are driven through the device microchannels by flow of the other phase. Microwell arrays feature an ordered pattern of pits into which a cells or some other analyte of interest is deposited. Micropedestal arrays, the opposite relief pattern of microwell arrays, disperse the analyte, typically cells, onto the sides or top of small physical posts patterned onto a surface. While microwell and micropedestal arrays are both patternings of physical features, micropatterned surfaces generally entail chemical patternings of some kind. Though a comprehensive review of the microfabrication field, apart from the focused survey described in sections below, is beyond the scope for this dissertation, there are several excellent reviews of this field, which is rapidly growing and becoming highly relevant for biomedical research.<sup>162-167</sup> These surveys summarize recent advances not only in the materials and techniques of microfabricated devices, but also in the novel and innovative applications for which these devices are being used.

### **1.3.2 Advantages of microscale devices**

A wealth of literature exists that describe in detail the advantages microscale devices bring to biomedical research. Chief among these advantages is the relative ease of adapting these devices for use with automated instrumentation and high throughput methods, which take advantage of the patterned nature of the devices via algorithms that not only enable rapid and precise analysis, but an orderly reference of assay results. Additionally, because of the small size of the features in these devices, a reduced consumption of reagents can be achieved. One unique advantage some, though not all, microscale devices have over traditional platforms is the ability to select for, isolate, and physically recover cells of interest in post-analytical stages.<sup>160, 164, 168-169</sup> Review articles, such as those cited above, provide greater detail regarding these advantages.

Most relevant to this dissertation is the compelling case that microscale devices make as tools for analyses of single or discretely small numbers of cells. Because the design of these devices allows for precise engineering of the shape, size, and surface chemistry of the area used for cell growth, these devices allow unparalleled control of the physical and chemical microenvironment to which a cell or group of cells is exposed as it grows.<sup>150, 164, 170-171</sup> By achieving such control, researchers gain the ability to create novel bio-inspired platforms that can precisely interrogate the mechanisms and regulation of fundamental cellular processes and to gather highly sensitive, cell-specific data platforms.<sup>165, 172-175</sup> Be it due to the inherently small size of their features, or the frequent need for gathered data to meaningfully discern between groups of or even single cells, microscale devices are also uniquely suited to performing the highly sensitive measurements necessary for high throughput, single cell analysis.<sup>160-161, 176</sup>

Thus, given their advantages and utility as single-cell analytical platforms, a research goal of designing and building a microscale device for the study of primary AT1 cells was formed.

### **1.3.3 Survey of previously described microscale devices relevant to alveolar cell culture**

#### **1.3.3.1 Microscale devices applied to respiratory biology**

Several microfabricated platforms have been developed and applied to respiratory biology inquiries. Reports of these platforms were consulted for their potential for use with primary AT1 cells. Because they can be patterned so easily and with such a high degree of control over their dimensions, a number of platforms utilize cell-lined microchannels to examine the role of shear stresses on cell attachment and vitality. Propagation of liquid plugs down the microchannels simulated the opening of occluded airways, providing data relevant

to studies of pulmonary surfactant dysfunction or depletion.<sup>177-179</sup> Building on these past works, a study by Douville *et al.* created a microfluidic model of the alveolus in which sheets of primary murine alveolar cells or cells from the human immortalized alveolar epithelial A549 cell line were grown on a flexible membrane of PDMS subjected to a migrating ALI.<sup>180</sup> This study demonstrated the role of migrating ALIs in worsening the cellular damage caused by cyclic stretch/compression as compared to cells that were entirely submerged or air-exposed when stretched, results relevant to research on ventilator-induced lung injury.

Additionally, a seminal study by the Ingber Group engineered a “lung-on-a-chip” device that featured a microporous membrane separating two microchannels.<sup>181</sup> On one side of the membrane, a sheet of immortalized endothelial cells were exposed to a fluid filled microchannel. The opposite side of the membrane was covered with sheets of cells from either small airway NCI H-441 or alveolar A549 cell lines, creating an ALI across the membrane. A noteworthy feature of this device was the pair of microchannels that laterally bordered the membrane: reducing or normalizing air pressure to these side channels created stretch or relaxation forces that simulated the expansion of the pulmonary tissues that occurs during inspiration.

Several of the studies cited above are surveyed in a review of efforts to study respiratory physiology on chip-based platforms.<sup>182</sup> This review reiterates the need for an ALI in culture of pulmonary cells as a way to recapitulate true *in vivo* architecture. Several attempts to create a co-culture model of the alveolar-capillary barrier, typically via culture of alveolar and endothelial cell lines on opposite sides of a porous membrane, were discussed. Of note, this review includes coverage of chip-based research efforts at extracorporeal

membrane oxidation (ECMO), a direct therapeutic end goal not falling within the physiology- and pharmacology-oriented research goals of this dissertation.

While useful advances, none of these devices are suited for research with primary AT1 cells, for at least one of a variety of reasons: incompatibility with primary cell use, designs that do not feature permeable supports, or designs that do not appropriately replicate the physicochemical features of the alveolar architecture. For example, while the “lung-on-a-chip” represents an impressive engineering advance, its use of sheets of cells grown atop a membrane with large, 10  $\mu\text{m}$ -diameter pores does not sufficiently replicate the alveolar microenvironment, which features smaller physical concavities approximately 250  $\mu\text{m}$  in diameter whose basement membrane has submicron-scale porosity.<sup>1, 183</sup> The microfluidic alveolar model developed by Douville *et al.* has similar shortfalls: sheets of cells 6 mm in diameter, grown on an impermeable membrane 100  $\mu\text{m}$  thick, do not replicate the alveolar microenvironment seen by an AT1 cell. Given the shortcomings of these otherwise laudable devices as they relate to AT1 culture, other examples of microtechnology that utilize permeable membranes were explored.

### **1.3.3.2 Microscale devices utilizing a permeable support**

To date there has been some success in combining microscale technologies with porous or otherwise permeable materials, even if they have not been used in respiratory biology studies. Porous membranes are used most commonly in microfluidic setups fabricated with PDMS, and a number of studies focused on methods in which to incorporate the membranes into the fabricated devices. A common design for these systems involves the fabrication of devices using stacked PDMS layers with a microporous membrane sandwiched in the middle, creating separate PDMS flow channels separated by the membrane. The

membranes and the PDMS layers are most commonly bonded either indirectly using a thin PDMS mortar layer or directly via the organosilane 3-aminopropyltriethoxysilane (APTES).<sup>184-186</sup> However, most of the studies cited above bond only the membrane edges, at the macroscopic scale, to the borders of PDMS layers. A literature review did not locate any studies that involve bonding membranes to PDMS films with a microscale pattern, likely due in one part to the relative difficulty in making through-hole arrays in such films in the first place and due in another part to difficulty in establishing uniform seals around each microwell that eliminate communicating gaps between them. Indeed, the smallest area of membrane exposed was still 4 mm<sup>2</sup>.<sup>187</sup> Use of “microfluidic stickers” presents an alternative method that is chemically distinct from the sandwich methods described above, but nearly identical in general concept.<sup>188</sup>

Studies employing the PDMS-membrane sandwich method have used the membrane in a microfluidic setup in such varied applications as establishing standing chemical gradients to which cells can be exposed without the harsh shearing forces of high flow rates.<sup>188-190</sup> In a general sense, seeding cells onto one side of the membrane allows for single-stream perfusion at relatively slow rates – or even static culture – that do not introduce shearing stresses to the cell. On the other side of the membrane, flows from two entering fluid streams, one of which carries a solute of interest, meet in the middle. This interface allows a standing chemical gradient of the solute to be set up along an axis orthogonal to the flow direction in the middle of the channel, with the extent of the gradient controlled by the flow rates. Because the cells are separated from these higher flow rates by the membrane, shearing forces are spared. A second category of applications for this kind of microfluidic setup is that of a plasma filter. Both Aran *et al.* and Son *et al.* describe use of the membrane for isotonic

and hemolysis-free filtration of plasma from whole blood.<sup>191-192</sup> By using membranes with pores too small for red blood cells, whole blood infused into the system could be efficiently separated into two compartments, with one compartment retaining erythrocytes and leukocytes and the other containing only plasma, with low shear stress and minimal erythrocyte hemolysis.

Other reports utilize the membrane to recapitulate the polarization seen *in vivo* of certain types of non-respiratory epithelial cells. For example, Jang and Suh created a microfluidic “kidney-on-a-chip” using PDMS bonded to a porous membrane on which sheets of primary rat inner medullary collecting duct (IMCD) cells were cultured.<sup>193-194</sup> The McGuigan Group successfully patterned MDCK and retinal epithelial cells into microcolonies atop commercially-available porous substrates.<sup>195</sup> A device fabricated as an extension of “lung-on-a-chip” technology, described in the previous section, was used to grow cells from an immortalized colon adenocarcinoma-derived cell line, hence the term “gut-on-a-chip.”<sup>196</sup> Alternatively, insertion of cylindrical electrodes on each side of the membrane allows measurement of the transepithelial electrical resistance (TEER) of a monolayer of cells cultured on the membrane.<sup>187</sup> This concept was later extended in a microfluidic model of the blood-brain barrier that incorporated electrodes to measure TEER into the device.<sup>197</sup>

A few devices do attempt to introduce micropatterns onto porous membranes. The Takayama Group developed a method to microstamp PDMS that could pattern microwells 5  $\mu\text{m}$  in height and as small as 50  $\mu\text{m}$  in diameter atop a porous polyester membrane.<sup>198</sup> Two reports – one of which used a combination of electrospun polyblend fibers and soft lithography, the other using a mesh-supported submicron membrane of parylene C –

combined microscale patterning with a unique permeable surface, but fabrication of these devices requires both large manpower and highly specialized equipment.<sup>199-200</sup> A similar requirement for specialized equipment is one drawback to a recent report describing the ability to thermoform polyester or polycarbonate into films with 3D topographies.<sup>201</sup> The fabricator must have ready access to not only a specialty thermoforming apparatus, but also to a heavy ion accelerator in order to track-etch pores into the final product.

Despite the many examples presented, these platforms have inherent limitations that prevent their immediate use or adaptation for AT1 cells. Chief among these limitations is an inability to pattern the membranes themselves, either directly or via the enclosures of a microfluidic device to the specifications needed by a device for primary AT1 culture. Indeed, the McGuigan Group's cell colony micropatterns and the Takayama Group's orthogonally-oriented microchannel array represent the works most relevant to culture of primary AT1 cells, but each of these two methods has detractors: the McGuigan Group's micropatterns appear to be limited to features larger than approximately 250  $\mu\text{m}$  (comparative AT1 diameter is 50-100  $\mu\text{m}$ ), and the Takayama Group's PDMS microstamps were so thin (5  $\mu\text{m}$  in height) that cells readily migrated out of the microwells and spread over the entire surface.<sup>195, 198</sup>

#### **1.3.4 Design guidelines for a microscale device applicable to AT1 cells**

As discussed above, a simple adaptation of previously developed technology platforms is unlikely to be of use in studying primary AT1 cells. Thus, there exists a need for a new microscale platform, designed and validated for the purpose of culturing single or

small or discrete numbers of primary AT1 cells in a microenvironment mimicking that of the native alveolus (Figure 1.6A).

Such a platform should satisfy several design guidelines. First, its construction and assembly should be compatible with standard microfabrication techniques so as to minimize the need for designing entirely new fabrication methods. Second, the platform and its prototypes should be relatively rapid and inexpensive to construct, so as to ensure an efficient use of manpower and materials. Third, the fabrication method should allow micron-level precision in patterning the platform. Figure 1.6B illustrates a number of the parameters that should be amenable to control, including the diameter of the microwell elements, the height of the microwell walls, and the interwell spacing. One special consideration will have to be the well diameter, as it would be desirable to pattern microwells the approximate diameter of AT1 cells as they exist *in vivo*. A second consideration will have to be given to the well depth. While it would be ideal that wells would be deep enough to prevent the migration or spreading of the AT1 cells out of the wells, wells must also be shallow enough that polarized, differentiated AT1 cells will have the transport capacity (energetically and kinetically) to be able to transport fluid in the well down to a volume that reflects the thin AvSL seen *in vivo*. While optimization of well depth and diameter will be an expected step in translating a finished microdevice to use with primary AT1 cells, identifying early on a fabrication technique that allows control over these parameters to a level sufficient for use with AT1 cells would be ideal. Fourth, the platform must incorporate some kind of microporous or otherwise permeable support on which the primary cells can be grown, as bioelectric and confocal microscopy studies will be central to the application of the platform and a wealth of literature has shown the effects of ALI growth on the differentiation and polarization of

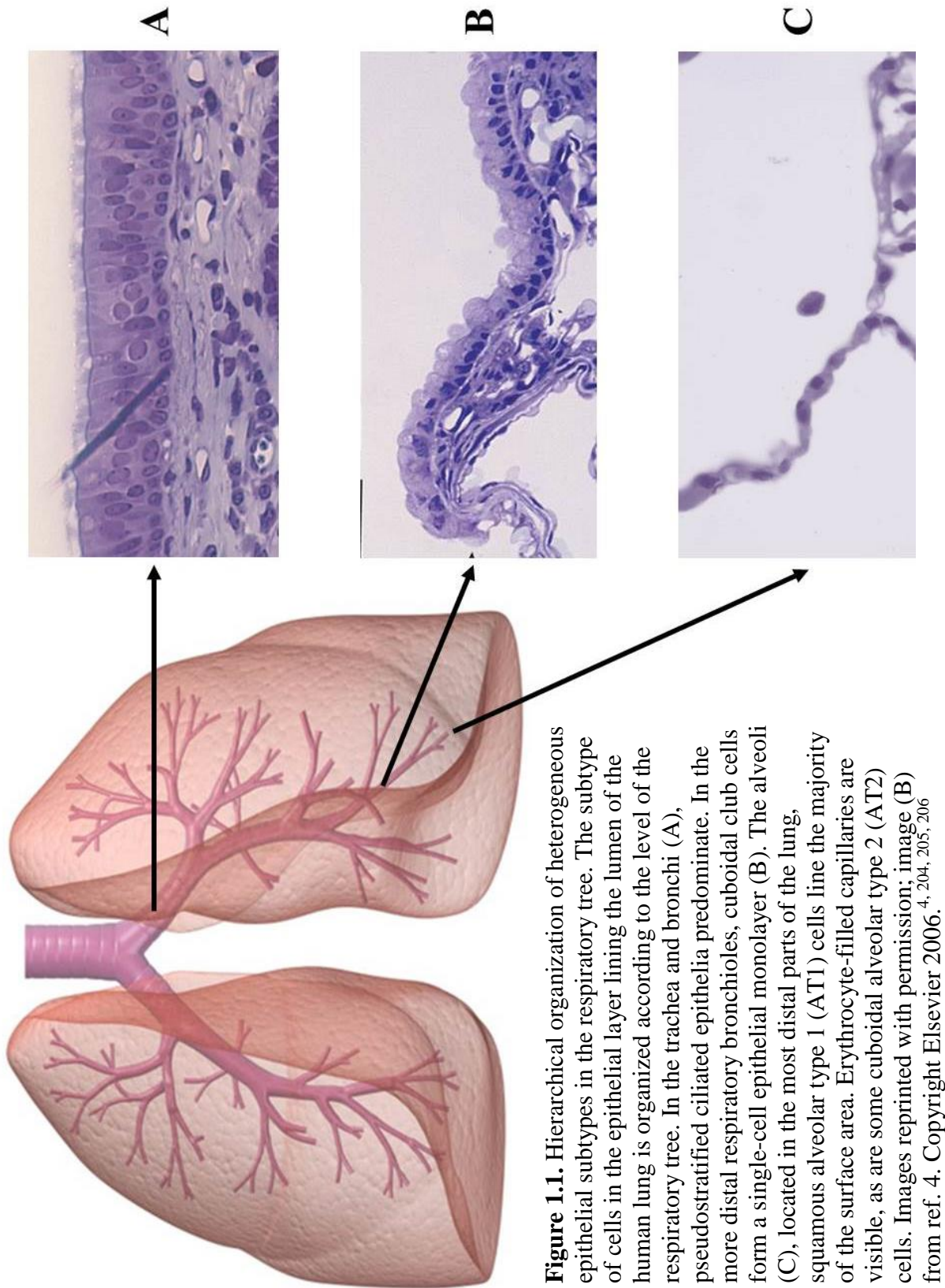
respiratory epithelial cells. However, as has been described in Section 1.2.4, the mere presence of arbitrary pores in the device may not be enough, as even bronchial and primary AT2 cells fail to differentiate when pores are either too large or too small.<sup>138</sup> Ideally, control over some aspects of the support, such as its thickness, can be achieved (as shown in Figure 1.6B). Lastly, an ability to tailor the microwell, such as through surface chemistry modifications or ECM deposition, so as to customize the microenvironment seen by cells to one that closely mimics the basement membrane and other aspects of the *in vivo* microenvironment, would be optimal. Empirical evidence already exists that AT1 and AT2 cells have different ECM preferences, and that ECM choice can guide respiratory alveolar differentiation.<sup>133, 202</sup>

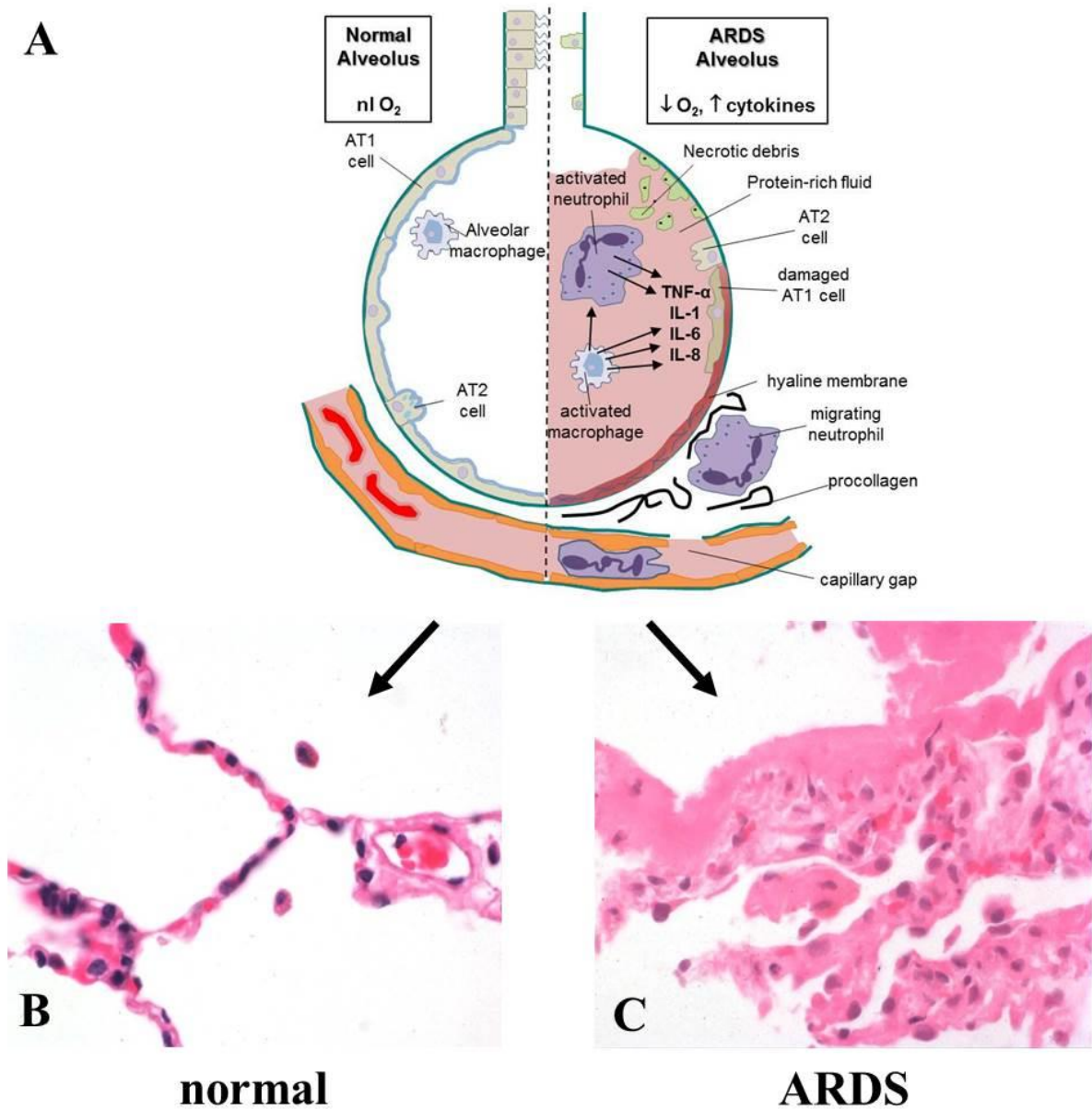
## **1.4 Scope of the Dissertation**

This dissertation describes the development and characterization of a microfabricated device, featuring an array of microwells patterned atop a porous or otherwise permeable support. The overall focus for the dissertation is on generating a complete characterization of the device in an acellular state, a necessary task before the device can be used for cellular studies, as knowledge of the physicochemical properties of the platform is needed to accurately interpret observed cellular responses. Full understanding and command of these properties and the device's limitations ensures maximum utility of the device for later cellular studies. However, certain cell-based applications, for which only minimal optimization was necessary, are also presented. Chapter 2 presents a method for fabricating a microwell array and explores the fabrication parameters and limits. Special attention is paid to the novelty of the method: release of the completed microwell array intact from the

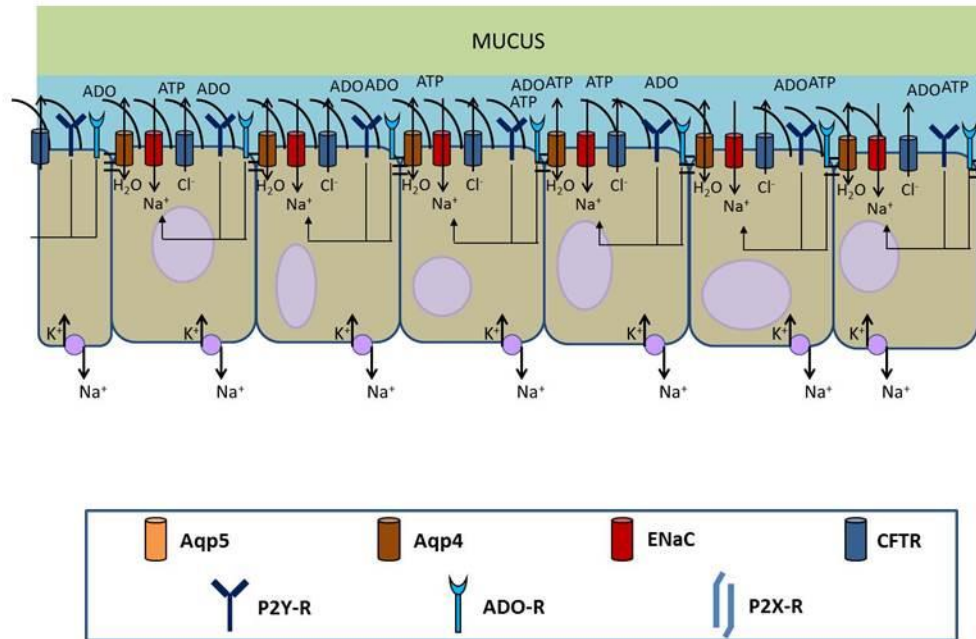
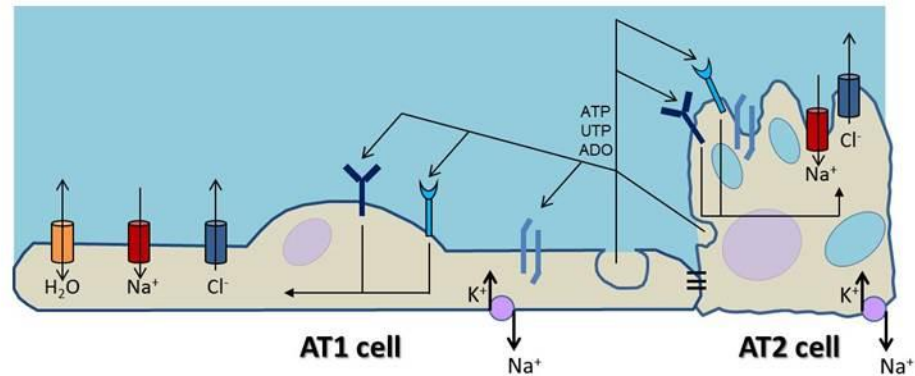
fabrication substrate. These results have been published in the *Journal of Micromechanics and Microengineering*.<sup>203</sup> Chapter 3 introduces a permeable support, composed of the hydrogel chitosan, to the array described in Chapter 2, with special attention to elucidating the support layer's ability and limitations in allowing the diffusion of solutes across it. Review of the microfabrication literature suggests that this is the first reported co-fabrication of hydrogel and photoresist, and the first release of a freestanding film of permeable-bottom microwell arrays. These results are currently being prepared as a manuscript for submission to the journal *Biomaterials*. Chapter 4 describes the application of the microwell array fabrication method described in Chapter 2 to commercially available permeable supports, which feature track-etched submicron-scale cylindrical pores. Preservation of the pore patency after the fabrication is completed is presented, as are data showing the ability to pattern features as small as 25  $\mu\text{m}$  atop the support layer, the smallest feature size reported to date for patterned commercial membranes. A manuscript describing these findings is in preparation for submission to the journal *Lab on a Chip*. Chapter 5 describes potential future directions for these devices, including suggested protocols for immediate translation into experiments with primary AT1 cells, as well as novel potential applications of these technologies for a range of research endeavors, pulmonary and otherwise.

## 1.5 Figures and Tables

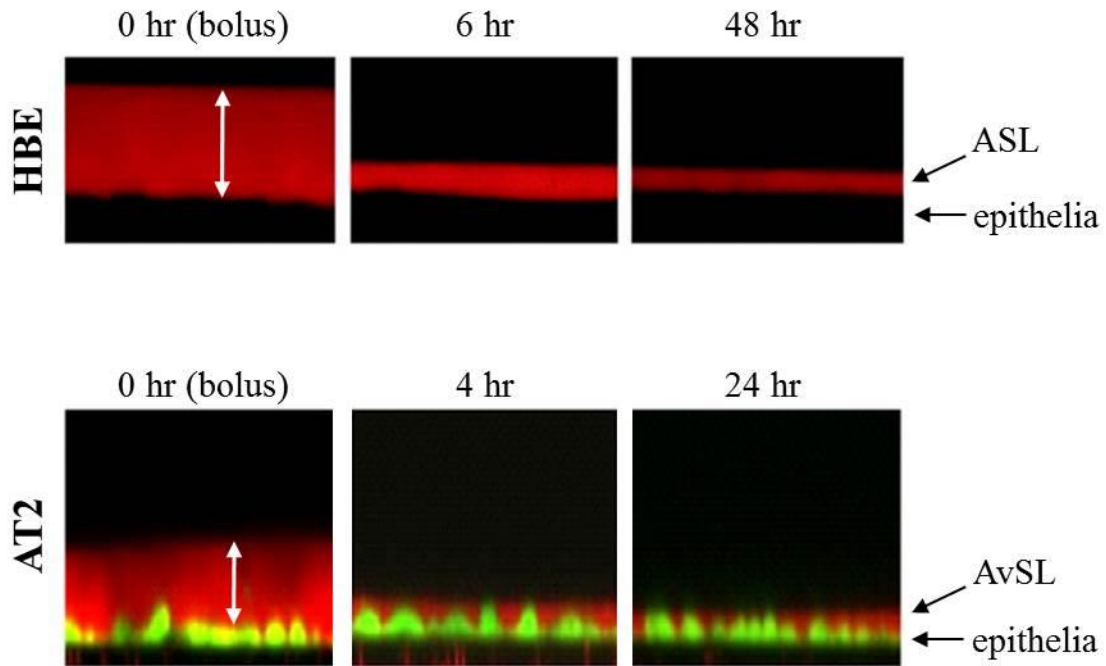




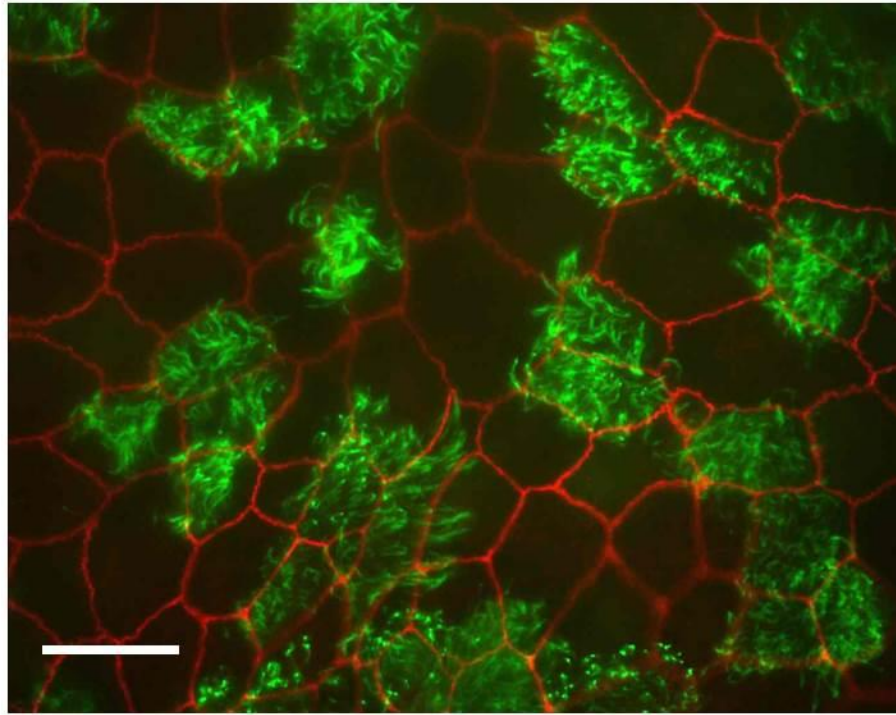
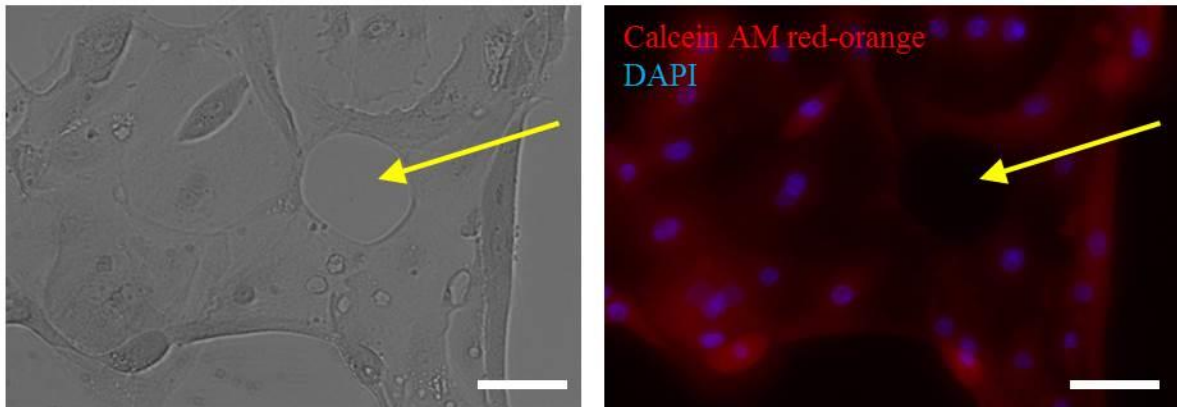
**Figure 1.2.** Alveolar pathology in ARDS. (A) Representation of normal alveoli and pathologic alveoli due to ARDS, indicating the fluid-flooded and pro-inflammatory state characteristic of ARDS, as well as epithelial cell death and hyaline membrane formation. Adapted from Ware and Matthay.<sup>56</sup> (B-C) Histological H&E preparations of normal (B) and ARDS (C) alveolar tissue. Images reprinted with permission.<sup>206, 207</sup>

**A****B**

**Figure 1.3.** Models of lung fluid homeostasis. (A) Fluid homeostasis in the proximal airways by ciliated pseudostratified epithelia is achieved by directed ion transport using ENaC and CFTR to create an osmotic gradient that drives water flux through aquaporin molecular water channels to the airway surface, a process normally regulated by signaling of extracellular adenosine, a metabolite of ATP. Proper hydration of the periciliary layer (blue) allows efficient transport of an overlying mucus layer (green). Adapted from Boucher.<sup>5</sup> (B) Proposed fluid homeostasis model in the alveoli, in which directed ion transport is thought to create similar osmotic gradients that drive water flux. Signaling of both extracellular adenosine, metabolized from ATP, through adenosine receptors and ATP and UTP directly through P2Y and P2X receptors is thought to regulate this process. Adapted from Dobbs *et al.*<sup>136</sup>



**Figure 1.4.** Real-time measurement of ASL and AvSL by confocal microscopy. Epithelial layers of primary human (A) bronchial epithelia (HBE) and (B) AT2 cells were cultured under ALI conditions. Apical surface liquid was stained by addition of a bolus of fluid containing 70-kDa Texas Red-conjugate dextran. AT2 (but not HBE) cell cytoplasm was also stained with calcein AM green. Measurement of the red fluorescent layer above the epithelial layer, as indicated by the double-headed arrows, allows quantification of the ASL or AvSL over time. Scale bars: (A) 7  $\mu\text{m}$ ; (B) 5  $\mu\text{m}$ . Images reprinted with permission from the American Society for Biochemistry and Molecular Biology.<sup>96, 126</sup>

**A****B**

**Figure 1.5.** Insufficiency of standard culture models to study primary AT1 cells. (A) Immunofluorescence micrograph of a monolayer of normal human bronchial epithelia cultured atop permeable supports and under an ALI. The tight junction protein ZO-1 is stained in red, while  $\beta$ -tubulin, a component of cilia, is stained in green. The presence of tight junctions indicates an intact monolayer with high TEER. Image reprinted with permission from Elsevier.<sup>208</sup> (B) Brightfield (left) and immunofluorescent (right) micrographs of transdifferentiating AT2 cells grown in culture atop polystyrene. Nuclei are stained in blue with DAPI, while cytoplasm is stained in red with calcein AM red-orange. Yellow arrows indicate intercellular gaps that reduce monolayer TEER values. Scale bars: (A) 10  $\mu$ m; (B) 75  $\mu$ m.

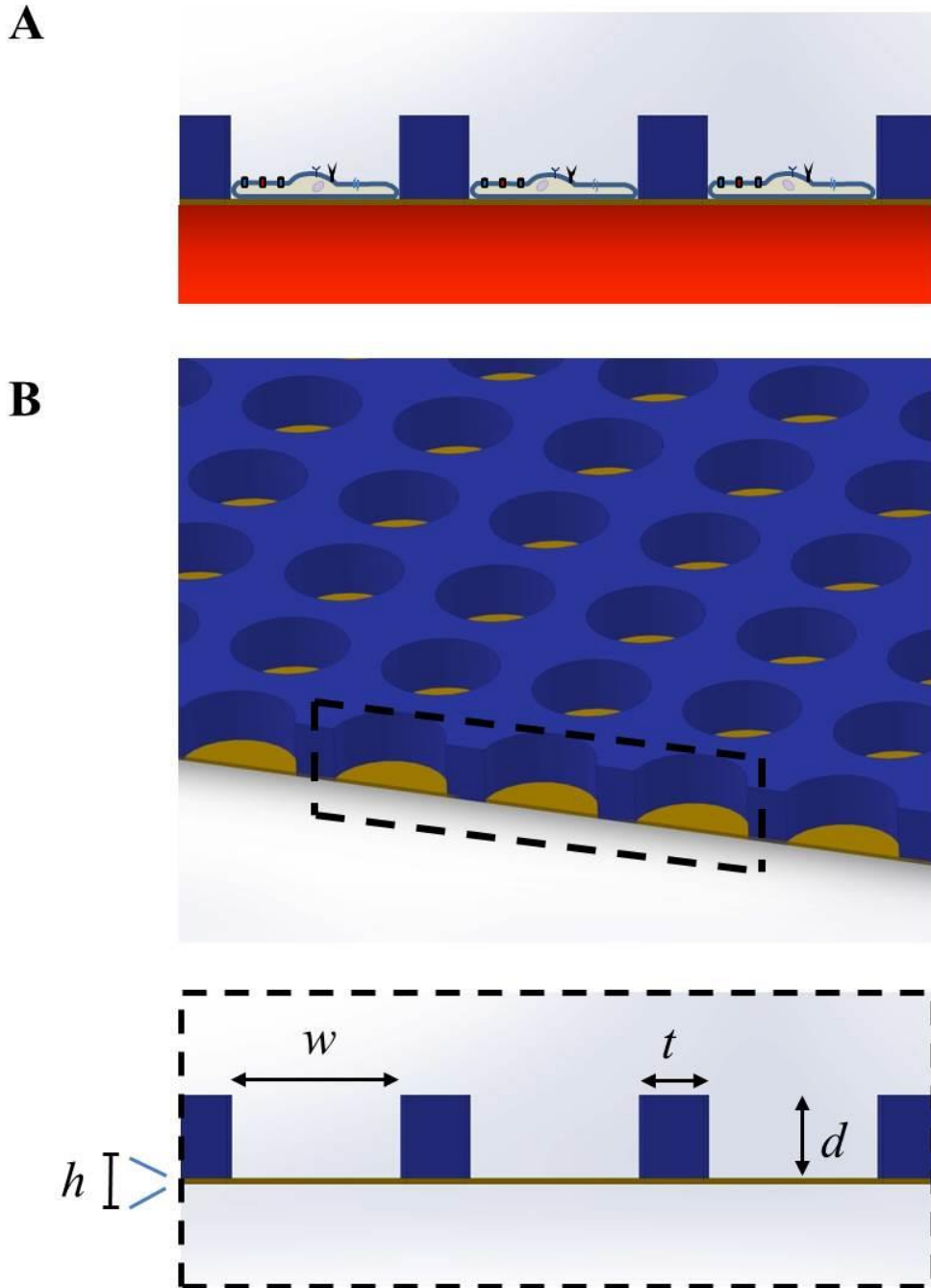


**Figure 1.6.** Design overview of a microwell array platform for culture of single AT1 cells under an ALI. (A) Concept illustration of several AT1 cells grown individually in microwells with permeable bottoms under an ALI. ALI conditions allow for cellular polarization and expression of relevant ion transporters and regulatory receptors, while the single cell format avoids the formation of intercellular gaps. (B) Design schematic for an array of permeable-bottomed microwells. An ideal fabrication method will allow control over a number of parameters for the microwell array, namely the well diameter  $w$ , the interwell spacing  $t$ , the depth of the well  $d$ , and the thickness  $h$  of the permeable layer.

**Table 1.1.** Comparison of overall ion and water transport properties between AT1 and AT2 cells. Data taken from permeability and patch clamp studies of primary rat alveolar cells. Reprinted with permission from Karger Publishers.<sup>136</sup>

<b>Property</b>	<b>AT1:AT2 whole-cell ratio</b>	<b>Reference</b>
Cell surface area	43	13
Osmotic water permeability	7	135
Apical Na <sup>+</sup> channels / cell	~ 40	131
CFTR channels / cell	6	131

**Table 1.2.** Comparison of ion transporter density in AT1 and AT2 cells. Data obtained from patch clamp studies in primary rat alveolar cells. Reprinted with permission from ref 131. Copyright 2006, National Academy of Sciences, U.S.A.<sup>131</sup>

Ion channel	Density in AT1 cells (per $\mu\text{m}^2$ )	Density in AT2 cells (per $\mu\text{m}^2$ )
ENaC (HSC variant)	1.49	1.63
ENaC (NSC variant)	0.104	0.167
$\text{K}^+$ ( $\text{Ba}^{2+}$ -sensitive)	0.433	0
CNG (+/- $\text{Ca}^{2+}$ in bath)	0.194 / 0.468	0
CFTR (after cAMP)	0.082	0.982

## 1.6 REFERENCES

1. E. R. Weibel. *The pathway for oxygen : structure and function in the mammalian respiratory system*. Harvard University Press: Cambridge, Mass. 1984. 425 p.
2. P. Gehr, M. Bachofen, and E. R. Weibel. "The normal human lung: ultrastructure and morphometric estimation of diffusion capacity." *Respir Physiol*. **1978**, *32*, 121-40.
3. F. N. Low. "Electron microscopy of the rat lung." *Anat Rec*. **1952**, *113*, 437-49.
4. B. Young. *Wheater's Functional Histology : a text and colour atlas*. 5th ed. Churchill Livingstone / Elsevier: Edinburgh. 2006. 437 p.
5. R. C. Boucher. "Evidence for airway surface dehydration as the initiating event in CF airway disease." *J Intern Med*. **2007**, *261*, 5-16.
6. R. C. Boucher. "Cystic fibrosis: a disease of vulnerability to airway surface dehydration." *Trends Mol Med*. **2007**, *13*, 231-40.
7. G. D. Massaro, G. Singh, R. Mason, C. G. Plopper, A. M. Malkinson, and D. B. Gail. "Biology of the Clara cell." *Am J Physiol*. **1994**, *266*, L101-6.
8. C. G. Plopper, A. T. Mariassy, and L. H. Hill. "Ultrastructure of the nonciliated bronchiolar epithelial (Clara) cell of mammalian lung: I. A comparison of rabbit, guinea pig, rat, hamster, and mouse." *Exp Lung Res*. **1980**, *1*, 139-54.
9. S. F. Stinson, and C. G. Loosli. "Ultrastructural evidence concerning the mode of secretion of electron-dense granules by Clara cells." *J Anat*. **1978**, *127*, 291-8.
10. C. J. Serabjit-Singh, C. R. Wolf, R. M. Philpot, and C. G. Plopper. "Cytochrome p-450: localization in rabbit lung." *Science*. **1980**, *207*, 1469-70.
11. A. Giangreco, S. D. Reynolds, and B. R. Stripp. "Terminal bronchioles harbor a unique airway stem cell population that localizes to the bronchoalveolar duct junction." *Am J Pathol*. **2002**, *161*, 173-82.
12. J. D. Crapo, S. L. Young, E. K. Fram, K. E. Pinkerton, B. E. Barry, and R. O. Crapo. "Morphometric characteristics of cells in the alveolar region of mammalian lungs." *Am Rev Respir Dis*. **1983**, *128*, S42-6.
13. K. C. Stone, R. R. Mercer, P. Gehr, B. Stockstill, and J. D. Crapo. "Allometric relationships of cell numbers and size in the mammalian lung." *Am J Respir Cell Mol Biol*. **1992**, *6*, 235-43.

14. R. Rhoades, and D. R. Bell. *Medical physiology : principles for clinical medicine*. 4th ed. Wolters Kluwer Health/Lippincott Williams & Wilkins: Philadelphia. 2013. 819 p.
15. K. C. Stone, R. R. Mercer, B. A. Freeman, L. Y. Chang, and J. D. Crapo. "Distribution of lung cell numbers and volumes between alveolar and nonalveolar tissue." *Am Rev Respir Dis*. **1992**, *146*, 454-6.
16. M. J. Evans, L. J. Cabral, R. J. Stephens, and G. Freeman. "Renewal of alveolar epithelium in the rat following exposure to NO<sub>2</sub>." *Am J Pathol*. **1973**, *70*, 175-98.
17. M. J. Evans, L. C. Cabral, R. J. Stephens, and G. Freeman. "Acute Kinetic Response and Renewal of the Alveolar Epithelium following Injury by Nitrogen Dioxide." *Chest*. **1974**, *65*, 62S-65S.
18. M. J. Evans, L. J. Cabral, R. J. Stephens, and G. Freeman. "Transformation of alveolar type 2 cells to type 1 cells following exposure to NO<sub>2</sub>." *Exp Mol Pathol*. **1975**, *22*, 142-50.
19. I. Y. Adamson, and D. H. Bowden. "The type 2 cell as progenitor of alveolar epithelial regeneration. A cytodynamic study in mice after exposure to oxygen." *Lab Invest*. **1974**, *30*, 35-42.
20. T. J. Desai, D. G. Brownfield, and M. A. Krasnow. "Alveolar progenitor and stem cells in lung development, renewal and cancer." *Nature*. **2014**, *507*, 190-4.
21. C. E. Barkauskas, M. J. Crouse, C. R. Rackley, E. J. Bowie, D. R. Keene, B. R. Stripp, S. H. Randell, P. W. Noble, and B. L. Hogan. "Type 2 alveolar cells are stem cells in adult lung." *J Clin Invest*. **2013**, *123*, 3025-36.
22. J. R. Wright, and S. Hawgood. "Pulmonary surfactant metabolism." *Clin Chest Med*. **1989**, *10*, 83-93.
23. A. J. Tenner, S. L. Robinson, J. Borchelt, and J. R. Wright. "Human pulmonary surfactant protein (SP-A), a protein structurally homologous to C1q, can enhance FcR- and CR1-mediated phagocytosis." *J Biol Chem*. **1989**, *264*, 13923-8.
24. C. B. Daniels, and S. Orgeig. "Pulmonary surfactant: the key to the evolution of air breathing." *News Physiol Sci*. **2003**, *18*, 151-7.
25. R. J. Mason. "Biology of alveolar type II cells." *Respirology*. **2006**, *11 Suppl*, S12-5.
26. J. N. Vanderbilt, E. M. Mager, L. Allen, T. Sawa, J. Wiener-Kronish, R. Gonzalez, and L. G. Dobbs. "CXC chemokines and their receptors are expressed in type II cells and upregulated following lung injury." *Am J Respir Cell Mol Biol*. **2003**, *29*, 661-8.

27. R. C. Strunk, D. M. Eidlen, and R. J. Mason. "Pulmonary alveolar type II epithelial cells synthesize and secrete proteins of the classical and alternative complement pathways." *J Clin Invest.* **1988**, *81*, 1419-26.
28. R. Gonzalez, Y. H. Yang, C. Griffin, L. Allen, Z. Tigue, and L. Dobbs. "Freshly isolated rat alveolar type I cells, type II cells, and cultured type II cells have distinct molecular phenotypes." *Am J Physiol Lung Cell Mol Physiol.* **2005**, *288*, L179-89.
29. Z. Borok, A. Hami, S. I. Danto, S. M. Zabski, and E. D. Crandall. "Rat serum inhibits progression of alveolar epithelial cells toward the type I cell phenotype in vitro." *Am J Respir Cell Mol Biol.* **1995**, *12*, 50-5.
30. K. Dahlin. "Identification of Genes Differentially Expressed in Rat Alveolar Type I Cells." *Am J Respir Cell Mol Biol.* **2004**, *31*, 309-316.
31. D. Gou, T. Narasaraju, N. R. Chintagari, N. Jin, P. Wang, and L. Liu. "Gene silencing in alveolar type II cells using cell-specific promoter in vitro and in vivo." *Nucl Acid Res.* **2004**, *32*, e134.
32. B. Treutlein, D. G. Brownfield, A. R. Wu, N. F. Neff, G. L. Mantalas, F. H. Espinoza, T. J. Desai, M. A. Krasnow, and S. R. Quake. "Reconstructing lineage hierarchies of the distal lung epithelium using single-cell RNA-seq." *Nature.* **2014**, *509*, 371-5.
33. R. F. Gonzalez, L. Allen, and L. G. Dobbs. "Rat alveolar type I cells proliferate, express OCT-4, and exhibit phenotypic plasticity in vitro." *Am J Physiol Lung Cell Mol Physiol.* **2009**, *297*, L1045-55.
34. Z. Borok, R. L. Lubman, S. I. Danto, X.-L. Zhang, S. M. Zabski, L. S. King, D. M. Lee, P. Agre, and E. D. Crandall. "Keratinocyte Growth Factor Modulates Alveolar Epithelial Cell Phenotype In Vitro: Expression of Aquaporin 5 " *Am J Respir Cell Mol Biol.* **1998**, *18*, 554-561.
35. J. Wang, K. Edeen, R. Manzer, Y. Chang, S. Wang, X. Chen, C. J. Funk, G. P. Cosgrove, X. Fang, and R. J. Mason. "Differentiated Human Alveolar Epithelial Cells and Reversibility of their Phenotype In Vitro." *Am J Respir Cell Mol Biol.* **2007**, *36*, 661-668.
36. R. Qiao, W. Yan, C. Clavijo, R. Mehrian-Shai, Q. Zhong, K. J. Kim, D. Ann, E. D. Crandall, and Z. Borok. "Effects of KGF on Alveolar Epithelial Cell Transdifferentiation Are Mediated by JNK Signaling." *Am J Respir Cell Mol Biol.* **2007**, *38*, 239-246.
37. M. J. Whitcutt, K. B. Adler, and R. Wu. "A biphasic chamber system for maintaining polarity of differentiation of cultured respiratory tract epithelial cells." *In Vitro Cell Dev Biol.* **1988**, *24*, 420-8.

38. T. E. Gray, K. Guzman, C. W. Davis, L. H. Abdullah, and P. Nettesheim. "Mucociliary differentiation of serially passaged normal human tracheobronchial epithelial cells." *Am J Respir Cell Mol Biol.* **1996**, *14*, 104-12.
39. L. G. Dobbs, M. S. Pian, M. Maglio, S. Dumars, and L. Allen. "Maintenance of the differentiated type II cell phenotype by culture with an apical air surface." *American Journal of Physiology - Lung Cellular and Molecular Physiology.* **1997**, *273*, L347-L354.
40. L. Jain, X.-J. Chen, S. Ramosevac, L. A. Brown, and D. C. Eaton. "Expression of highly selective sodium channels in alveolar type II cells is determined by culture conditions." *American Journal of Physiology - Lung Cellular and Molecular Physiology.* **2001**, *280*, L646-L658.
41. R. C. Boucher. "Molecular insights into the physiology of the 'thin film' of airway surface liquid." *J Physiol.* **1999**, *516 ( Pt 3)*, 631-8.
42. J. Bastacky, C. Y. Lee, J. Goerke, H. Koushafar, D. Yager, L. Kenaga, T. P. Speed, Y. Chen, and J. A. Clements. "Alveolar lining layer is thin and continuous: low-temperature scanning electron microscopy of rat lung." *J Appl Physiol.* **1995**, *79*, 1615-28.
43. P. H. Burri. "Structural aspects of prenatal and postnatal growth and development of the lung." In *Lung Growth and Development*, McDonald, J. A., Ed. Marcel Dekker: New York. 1997. Vol. 100, 1-35.
44. L. Jain, and D. C. Eaton. "Physiology of fetal lung fluid clearance and the effect of labor." *Semin Perinatol.* **2006**, *30*, 34-43.
45. M. A. Matthay, H. G. Folkesson, and A. S. Verkman. "Salt and water transport across alveolar and distal airway epithelia in the adult lung." *American Journal of Physiology - Lung Cellular and Molecular Physiology.* **1996**, *270*, L487-L503.
46. M. A. Matthay, H. G. Folkesson, and C. Clerici. "Lung Epithelial Fluid Transport and the Resolution of Pulmonary Edema." *Physiol Rev.* **2002**, *82*, 569-600.
47. D. Pinto, and R. Kociol. Pathophysiology of cardiogenic pulmonary edema *UpToDate* [Online], 2012. [http://www.uptodate.com/contents/pathophysiology-of-cardiogenic-pulmonary-edema?source=search\\_result&search=Pathophysiology+of+cardiogenic+pulmonary+edema&selectedTitle=1%7E58](http://www.uptodate.com/contents/pathophysiology-of-cardiogenic-pulmonary-edema?source=search_result&search=Pathophysiology+of+cardiogenic+pulmonary+edema&selectedTitle=1%7E58) (accessed March 17, 2013).
48. S. Weinberger. *Principles of Pulmonary Medicine*. 4th ed. Saunders, an imprint of Elsevier: 2004.

49. M. I. Schwartz. The diffuse alveolar hemorrhage syndromes *UpToDate* [Online], 2013. <http://www.uptodate.com/contents/the-diffuse-alveolar-hemorrhage-syndromes?source=machineLearning&search=alveolar+hemorrhage&selectedTitle=1~93&sectionRank=2&anchor=H2#H2> (accessed 06/01/2014).
50. M. D. Siegel. Acute respiratory distress syndrome: Epidemiology, pathophysiology, pathology, and etiology in adults *UpToDate* [Online], 2014. [http://www.uptodate.com/contents/acute-respiratory-distress-syndrome-epidemiology-pathophysiology-pathology-and-etiology-in-adults?source=related\\_link](http://www.uptodate.com/contents/acute-respiratory-distress-syndrome-epidemiology-pathophysiology-pathology-and-etiology-in-adults?source=related_link) (accessed May 31, 2014).
51. J. F. Tomashefski, Jr. "Pulmonary pathology of the adult respiratory distress syndrome." *Clin Chest Med.* **1990**, *11*, 593-619.
52. G. D. Rubenfeld, E. Caldwell, E. Peabody, J. Weaver, D. P. Martin, M. Neff, E. J. Stern, and L. D. Hudson. "Incidence and outcomes of acute lung injury." *N Engl J Med.* **2005**, *353*, 1685-93.
53. F. Frutos-Vivar, N. Nin, and A. Esteban. "Epidemiology of acute lung injury and acute respiratory distress syndrome." *Curr Opin Crit Care.* **2004**, *10*, 1-6.
54. C. Y. Wang, C. S. Calfee, D. W. Paul, D. R. Janz, A. K. May, H. Zhuo, G. R. Bernard, M. A. Matthay, L. B. Ware, and K. N. Kangelaris. "One-year mortality and predictors of death among hospital survivors of acute respiratory distress syndrome." *Intensive Care Med.* **2014**, *40*, 388-96.
55. M. A. Matthay. "Alveolar Epithelium: Role in Lung Fluid Balance and Acute Lung Injury." *Proceedings of the American Thoracic Society.* **2005**, *2*, 206-213.
56. L. B. Ware, and M. A. Matthay. "The acute respiratory distress syndrome." *New England Journal of Medicine.* **2000**, *342*, 1334-49.
57. W. S. Colucci. Treatment of acute decompensated heart failure: Components of therapy *UpToDate* [Online], 2014. [http://www.uptodate.com/contents/treatment-of-acute-decompensated-heart-failure-components-of-therapy?source=search\\_result&search=cardiogenic+pulmonary+edema&selectedTitle=2~63](http://www.uptodate.com/contents/treatment-of-acute-decompensated-heart-failure-components-of-therapy?source=search_result&search=cardiogenic+pulmonary+edema&selectedTitle=2~63) (accessed May 31, 2014).
58. "Ventilation with lower tidal volumes as compared with traditional tidal volumes for acute lung injury and the acute respiratory distress syndrome. The Acute Respiratory Distress Syndrome Network." *New England Journal of Medicine.* **2000**, *342*, 1301-8.
59. C. Putensen, N. Theuerkauf, J. Zinserling, H. Wrigge, and P. Pelosi. "Meta-analysis: ventilation strategies and outcomes of the acute respiratory distress syndrome and acute lung injury." *Ann Intern Med.* **2009**, *151*, 566-76.

60. H. P. Wiedemann, A. P. Wheeler, G. R. Bernard, B. T. Thompson, D. Hayden, B. deBoisblanc, A. F. Connors, Jr., R. D. Hite, and A. L. Harabin. "Comparison of two fluid-management strategies in acute lung injury." *New England Journal of Medicine*. **2006**, 354, 2564-75.
61. M. A. Matthay, R. G. Brower, S. Carson, I. S. Douglas, M. Eisner, D. Hite, S. Holets, R. H. Kallet, K. D. Liu, N. MacIntyre, M. Moss, D. Schoenfeld, J. Steingrub, and B. T. Thompson. "Randomized, placebo-controlled clinical trial of an aerosolized beta(2)-agonist for treatment of acute lung injury." *Am J Respir Crit Care Med*. **2011**, 184, 561-8.
62. F. Gao Smith, G. D. Perkins, S. Gates, D. Young, D. F. McAuley, W. Tunnicliffe, Z. Khan, and S. E. Lamb. "Effect of intravenous beta-2 agonist treatment on clinical outcomes in acute respiratory distress syndrome (BALTI-2): a multicentre, randomised controlled trial." *Lancet*. **2012**, 379, 229-35.
63. M. D. Siegel. Acute respiratory distress syndrome: Novel therapies in adults *UpToDate* [Online], 2014. [http://www.uptodate.com/contents/acute-respiratory-distress-syndrome-novel-therapies-in-adults?source=related\\_link](http://www.uptodate.com/contents/acute-respiratory-distress-syndrome-novel-therapies-in-adults?source=related_link) (accessed May 31, 2014).
64. M. S. Herridge, C. M. Tansey, A. Matte, G. Tomlinson, N. Diaz-Granados, A. Cooper, C. B. Guest, C. D. Mazer, S. Mehta, T. E. Stewart, P. Kudlow, D. Cook, A. S. Slutsky, and A. M. Cheung. "Functional disability 5 years after acute respiratory distress syndrome." *New England Journal of Medicine*. **2011**, 364, 1293-304.
65. S. D. Strausbaugh, and P. B. Davis. "Cystic fibrosis: a review of epidemiology and pathobiology." *Clin Chest Med*. **2007**, 28, 279-88.
66. R. E. Wood, T. F. Boat, and C. F. Doershuk. "Cystic fibrosis." *Am Rev Respir Dis*. **1976**, 113, 833-78.
67. R. C. Boucher. "Airway surface dehydration in cystic fibrosis: pathogenesis and therapy." *Annu Rev Med*. **2007**, 58, 157-70.
68. M. R. Knowles, M. J. Stutts, A. Spock, N. Fischer, J. T. Gatzky, and R. C. Boucher. "Abnormal ion permeation through cystic fibrosis respiratory epithelium." *Science*. **1983**, 221, 1067-70.
69. J. R. Yankaskas, M. R. Knowles, J. T. Gatzky, and R. C. Boucher. "Persistence of abnormal chloride ion permeability in cystic fibrosis nasal epithelial cells in heterologous culture." *Lancet*. **1985**, 1, 954-6.
70. R. C. Boucher, M. J. Stutts, M. R. Knowles, L. Cantley, and J. T. Gatzky. "Na<sup>+</sup> transport in cystic fibrosis respiratory epithelia. Abnormal basal rate and response to adenylate cyclase activation." *J Clin Invest*. **1986**, 78, 1245-52.

71. C. U. Cotton, M. J. Stutts, M. R. Knowles, J. T. Gatzky, and R. C. Boucher. "Abnormal apical cell membrane in cystic fibrosis respiratory epithelium. An in vitro electrophysiologic analysis." *J Clin Invest.* **1987**, *79*, 80-5.
72. R. C. Boucher, C. U. Cotton, J. T. Gatzky, M. R. Knowles, and J. R. Yankaskas. "Evidence for reduced Cl<sup>-</sup> and increased Na<sup>+</sup> permeability in cystic fibrosis human primary cell cultures." *J Physiol.* **1988**, *405*, 77-103.
73. J. R. Riordan, J. M. Rommens, B. Kerem, N. Alon, R. Rozmahel, Z. Grzelczak, J. Zielenski, S. Lok, N. Plavsic, J. L. Chou, and et al. "Identification of the cystic fibrosis gene: cloning and characterization of complementary DNA." *Science.* **1989**, *245*, 1066-73.
74. B. Kerem, J. M. Rommens, J. A. Buchanan, D. Markiewicz, T. K. Cox, A. Chakravarti, M. Buchwald, and L. C. Tsui. "Identification of the cystic fibrosis gene: genetic analysis." *Science.* **1989**, *245*, 1073-80.
75. M. P. Anderson, D. P. Rich, R. J. Gregory, A. E. Smith, and M. J. Welsh. "Generation of cAMP-activated chloride currents by expression of CFTR." *Science.* **1991**, *251*, 679-82.
76. C. E. Bear, C. H. Li, N. Kartner, R. J. Bridges, T. J. Jensen, M. Ramjeesingh, and J. R. Riordan. "Purification and functional reconstitution of the cystic fibrosis transmembrane conductance regulator (CFTR)." *Cell.* **1992**, *68*, 809-18.
77. H. Matsui, S. H. Randell, S. W. Peretti, C. W. Davis, and R. C. Boucher. "Coordinated clearance of periciliary liquid and mucus from airway surfaces." *J Clin Invest.* **1998**, *102*, 1125-31.
78. H. Matsui, B. R. Grubb, R. Tarran, S. H. Randell, J. T. Gatzky, C. W. Davis, and R. C. Boucher. "Evidence for periciliary liquid layer depletion, not abnormal ion composition, in the pathogenesis of cystic fibrosis airways disease." *Cell.* **1998**, *95*, 1005-15.
79. M. Li, J. D. McCann, C. M. Liedtke, A. C. Nairn, P. Greengard, and M. J. Welsh. "Cyclic AMP-dependent protein kinase opens chloride channels in normal but not cystic fibrosis airway epithelium." *Nature.* **1988**, *331*, 358-60.
80. R. A. Schoumacher, R. L. Shoemaker, D. R. Halm, E. A. Tallant, R. W. Wallace, and R. A. Frizzell. "Phosphorylation fails to activate chloride channels from cystic fibrosis airway cells." *Nature.* **1987**, *330*, 752-4.
81. R. C. Boucher, E. H. Cheng, A. M. Paradiso, M. J. Stutts, M. R. Knowles, and H. S. Earp. "Chloride secretory response of cystic fibrosis human airway epithelia.

- Preservation of calcium but not protein kinase C- and A-dependent mechanisms." *J Clin Invest.* **1989**, *84*, 1424-31.
82. E. R. Lazarowski, R. C. Boucher, and T. K. Harden. "Constitutive release of ATP and evidence for major contribution of ecto-nucleotide pyrophosphatase and nucleoside diphosphokinase to extracellular nucleotide concentrations." *Journal of Biological Chemistry.* **2000**, *275*, 31061-8.
83. E. R. Lazarowski, S. J. Mason, L. Clarke, T. K. Harden, and R. C. Boucher. "Adenosine receptors on human airway epithelia and their relationship to chloride secretion." *Br J Pharmacol.* **1992**, *106*, 774-82.
84. E. R. Lazarowski, R. Tarran, B. R. Grubb, C. A. van Heusden, S. Okada, and R. C. Boucher. "Nucleotide release provides a mechanism for airway surface liquid homeostasis." *J Biol Chem.* **2004**, *279*, 36855-64.
85. E. R. Lazarowski, and R. C. Boucher. "Purinergic receptors in airway epithelia." *Curr Opin Pharmacol.* **2009**, *9*, 262-7.
86. N. J. Willumsen, and R. C. Boucher. "Activation of an apical Cl<sup>-</sup> conductance by Ca<sup>2+</sup> ionophores in cystic fibrosis airway epithelia." *Am J Physiol.* **1989**, *256*, C226-33.
87. S. J. Mason, A. M. Paradiso, and R. C. Boucher. "Regulation of transepithelial ion transport and intracellular calcium by extracellular ATP in human normal and cystic fibrosis airway epithelium." *Br J Pharmacol.* **1991**, *103*, 1649-56.
88. M. R. Knowles, L. L. Clarke, and R. C. Boucher. "Activation by extracellular nucleotides of chloride secretion in the airway epithelia of patients with cystic fibrosis." *New England Journal of Medicine.* **1991**, *325*, 533-8.
89. H. A. Brown, E. R. Lazarowski, R. C. Boucher, and T. K. Harden. "Evidence that UTP and ATP regulate phospholipase C through a common extracellular 5'-nucleotide receptor in human airway epithelial cells." *Mol Pharmacol.* **1991**, *40*, 648-55.
90. M. J. Stutts, T. C. Chinet, S. J. Mason, J. M. Fullton, L. L. Clarke, and R. C. Boucher. "Regulation of Cl<sup>-</sup> channels in normal and cystic fibrosis airway epithelial cells by extracellular ATP." *Proc Natl Acad Sci USA.* **1992**, *89*, 1621-5.
91. M. R. Knowles, L. L. Clarke, and R. C. Boucher. "Extracellular ATP and UTP induce chloride secretion in nasal epithelia of cystic fibrosis patients and normal subjects in vivo." *Chest.* **1992**, *101*, 60S-63S.
92. L. L. Clarke, and R. C. Boucher. "Chloride secretory response to extracellular ATP in human normal and cystic fibrosis nasal epithelia." *Am J Physiol.* **1992**, *263*, C348-56.

93. M. Flezar, and S. Heisler. "P2-purinergic receptors in human breast tumor cells: coupling of intracellular calcium signaling to anion secretion." *J Pharmacol Exp Ther.* **1993**, *265*, 1499-510.
94. A. M. Paradiso, S. J. Mason, E. R. Lazarowski, and R. C. Boucher. "Membrane-restricted regulation of Ca<sup>2+</sup> release and influx in polarized epithelia." *Nature.* **1995**, *377*, 643-6.
95. J. R. Rock, W. K. O'Neal, S. E. Gabriel, S. H. Randell, B. D. Harfe, R. C. Boucher, and B. R. Grubb. "Transmembrane protein 16A (TMEM16A) is a Ca<sup>2+</sup>-regulated Cl<sup>-</sup> secretory channel in mouse airways." *Journal of Biological Chemistry.* **2009**, *284*, 14875-80.
96. R. Tarran, B. Button, M. Picher, A. M. Paradiso, C. M. Ribeiro, E. R. Lazarowski, L. Zhang, P. L. Collins, R. J. Pickles, J. J. Fredberg, and R. C. Boucher. "Normal and Cystic Fibrosis Airway Surface Liquid Homeostasis." *Journal of Biological Chemistry.* **2005**, *280*, 35751-35759.
97. F. Van Goor, S. Hadida, P. D. Grootenhuys, B. Burton, D. Cao, T. Neuberger, A. Turnbull, A. Singh, J. Joubbran, A. Hazlewood, J. Zhou, J. McCartney, V. Arumugam, C. Decker, J. Yang, C. Young, E. R. Olson, J. J. Wine, R. A. Frizzell, M. Ashlock, and P. Negulescu. "Rescue of CF airway epithelial cell function in vitro by a CFTR potentiator, VX-770." *Proc Natl Acad Sci USA.* **2009**, *106*, 18825-30.
98. F. J. Accurso, S. M. Rowe, J. P. Clancy, M. P. Boyle, J. M. Dunitz, P. R. Durie, S. D. Sagel, D. B. Hornick, M. W. Konstan, S. H. Donaldson, R. B. Moss, J. M. Pilewski, R. C. Rubenstein, A. Z. Uluer, M. L. Aitken, S. D. Freedman, L. M. Rose, N. Mayer-Hamblett, Q. Dong, J. Zha, A. J. Stone, E. R. Olson, C. L. Ordonez, P. W. Campbell, M. A. Ashlock, and B. W. Ramsey. "Effect of VX-770 in persons with cystic fibrosis and the G551D-CFTR mutation." *New England Journal of Medicine.* **2010**, *363*, 1991-2003.
99. B. W. Ramsey, J. Davies, N. G. McElvaney, E. Tullis, S. C. Bell, P. Drevinek, M. Griese, E. F. McKone, C. E. Wainwright, M. W. Konstan, R. Moss, F. Ratjen, I. Sermet-Gaudelus, S. M. Rowe, Q. Dong, S. Rodriguez, K. Yen, C. Ordonez, and J. S. Elborn. "A CFTR potentiator in patients with cystic fibrosis and the G551D mutation." *New England Journal of Medicine.* **2011**, *365*, 1663-72.
100. F. Van Goor, S. Hadida, P. D. Grootenhuys, B. Burton, J. H. Stack, K. S. Straley, C. J. Decker, M. Miller, J. McCartney, E. R. Olson, J. J. Wine, R. A. Frizzell, M. Ashlock, and P. A. Negulescu. "Correction of the F508del-CFTR protein processing defect in vitro by the investigational drug VX-809." *Proc Natl Acad Sci USA.* **2011**, *108*, 18843-8.

101. H. Y. Ren, D. E. Grove, O. De La Rosa, S. A. Houck, P. Sopha, F. Van Goor, B. J. Hoffman, and D. M. Cyr. "VX-809 corrects folding defects in cystic fibrosis transmembrane conductance regulator protein through action on membrane-spanning domain 1." *Mol Biol Cell*. **2013**, *24*, 3016-24.
102. S. H. Donaldson, W. D. Bennett, K. L. Zeman, M. R. Knowles, R. Tarran, and R. C. Boucher. "Mucus clearance and lung function in cystic fibrosis with hypertonic saline." *N Engl J Med*. **2006**, *354*, 241-50.
103. B. R. Yerxa, J. R. Sabater, C. W. Davis, M. J. Stutts, M. Lang-Furr, M. Picher, A. C. Jones, M. Cowlen, R. Dougherty, J. Boyer, W. M. Abraham, and R. C. Boucher. "Pharmacology of INS37217 [P1-(Uridine 5')-P4- (2'-deoxycytidine 5')tetraphosphate, Tetrasodium Salt], a Next-Generation P2Y2 Receptor Agonist for the Treatment of Cystic Fibrosis." *Journal of Pharmacology and Experimental Therapeutics*. **2002**, *302*, 871-880.
104. K. Kunzelmann, and M. Mall. "Pharmacotherapy of the ion transport defect in cystic fibrosis: role of purinergic receptor agonists and other potential therapeutics." *Am J Respir Med*. **2003**, *2*, 299-309.
105. M. A. Matthay, C. C. Landolt, and N. C. Staub. "Differential liquid and protein clearance from the alveoli of anesthetized sheep." *J Appl Physiol Respir Environ Exerc Physiol*. **1982**, *53*, 96-104.
106. R. J. Mason, M. C. Williams, J. H. Widdicombe, M. J. Sanders, D. S. Misfeldt, and L. C. Berry, Jr. "Transepithelial transport by pulmonary alveolar type II cells in primary culture." *Proc Natl Acad Sci U S A*. **1982**, *79*, 6033-7.
107. H. G. Folkesson, and M. A. Matthay. "Alveolar epithelial ion and fluid transport: recent progress." *Am J Respir Cell Mol Biol*. **2006**, *35*, 10-9.
108. S. Bourke, H. S. Mason, Z. Borok, K. J. Kim, E. D. Crandall, and P. J. Kemp. "Development of a lung slice preparation for recording ion channel activity in alveolar epithelial type I cells." *Respir Res*. **2005**, *6*, 40.
109. G. S. Jones, P. R. Miles, R. C. Lantz, D. E. Hinton, and V. Castranova. "Ionic content and regulation of cellular volume in rat alveolar type II cells." *J Appl Physiol Respir Environ Exerc Physiol*. **1982**, *53*, 258-66.
110. G. Yue, W. J. Russell, D. J. Benos, R. M. Jackson, M. A. Olman, and S. Matalon. "Increased expression and activity of sodium channels in alveolar type II cells of hyperoxic rats." *Proc Natl Acad Sci USA*. **1995**, *92*, 8418-22.
111. D. C. Eaton, M. N. Helms, M. Koval, H. F. Bao, and L. Jain. "The Contribution of Epithelial Sodium Channels to Alveolar Function in Health and Disease." *Annual Review of Physiology*. **2009**, *71*, 403-423.

112. S. Matalon, A. Lazrak, L. Jain, and D. C. Eaton. "Invited review: biophysical properties of sodium channels in lung alveolar epithelial cells." *J Appl Physiol.* **2002**, *93*, 1852-9.
113. X. Fang. "Contribution of CFTR to apical-basolateral fluid transport in cultured human alveolar epithelial type II cells." *AJP: Lung Cellular and Molecular Physiology.* **2005**, *290*, L242-L249.
114. D. C. Eaton. "Regulation of Na<sup>+</sup> Channels in Lung Alveolar Type II Epithelial Cells." *Proceedings of the American Thoracic Society.* **2004**, *1*, 10-16.
115. V. Dumasius, J. I. Sznajder, Z. S. Azzam, J. Boja, G. M. Mutlu, M. B. Maron, and P. Factor. "2-Adrenergic Receptor Overexpression Increases Alveolar Fluid Clearance and Responsiveness to Endogenous Catecholamines in Rats." *Circulation Research.* **2001**, *89*, 907-914.
116. P. Factor. "Effects of  $\beta_2$ -adrenergic receptor overexpression on alveolar epithelial active transport\*1." *Journal of Allergy and Clinical Immunology.* **2002**, *110*, S242-S246.
117. X. Jiang, D. H. Ingbar, and S. M. O'Grady. "Adrenergic stimulation of Na<sup>+</sup>transport across alveolar epithelial cells involves activation of apical Cl<sup>-</sup>channels." *American Journal of Physiology - Cell Physiology.* **1998**, *275*, C1610-C1620.
118. G. M. Mutlu. "Upregulation of Alveolar Epithelial Active Na<sup>+</sup> Transport Is Dependent on 2-Adrenergic Receptor Signaling." *Circulation Research.* **2004**, *94*, 1091-1100.
119. G. M. Mutlu. "Interdependency of  $\beta_2$ -Adrenergic Receptors and CFTR in Regulation of Alveolar Active Na<sup>+</sup> Transport." *Circulation Research.* **2005**, *96*, 999-1005.
120. M. L. Barnard, W. G. Olivera, D. M. Rutschman, A. M. Bertorello, A. I. Katz, and J. I. Sznajder. "Dopamine stimulates sodium transport and liquid clearance in rat lung epithelium." *Am J Respir Crit Care Med.* **1997**, *156*, 709-14.
121. M. L. Barnard, K. M. Ridge, F. Saldias, E. Friedman, M. Gare, C. Guerrero, E. Lecuona, A. M. Bertorello, A. I. Katz, and J. I. Sznajder. "Stimulation of the dopamine 1 receptor increases lung edema clearance." *Am J Respir Crit Care Med.* **1999**, *160*, 982-6.
122. A. Norlin, D. L. Baines, and H. G. Folkesson. "Role of endogenous cortisol in basal liquid clearance from distal air spaces in adult guinea-pigs." *J Physiol.* **1999**, *519 Pt 1*, 261-72.

123. H. G. Folkesson, A. Norlin, Y. Wang, P. Abedinpour, and M. A. Matthay. "Dexamethasone and thyroid hormone pretreatment upregulate alveolar epithelial fluid clearance in adult rats." *J Appl Physiol.* **2000**, 88, 416-24.
124. C. Clerici, and M. A. Matthay. "Hypoxia regulates gene expression of alveolar epithelial transport proteins." *J Appl Physiol.* **2000**, 88, 1890-1896.
125. M. L. Vivona, M. Matthay, M. B. Chabaud, G. Friedlander, and C. Clerici. "Hypoxia Reduces Alveolar Epithelial Sodium and Fluid Transport in Rats . Reversal by beta - Adrenergic Agonist Treatment." *Am J Respir Cell Mol Biol.* **2001**, 25, 554-561.
126. P. F. Bove, B. R. Grubb, S. F. Okada, C. M. P. Ribeiro, T. D. Rogers, S. H. Randell, W. K. O'Neal, and R. C. Boucher. "Human Alveolar Type II Cells Secrete and Absorb Liquid in Response to Local Nucleotide Signaling." *Journal of Biological Chemistry.* **2010**, 285, 34939-34949.
127. Z. Borok, J. M. Liebler, R. L. Lubman, M. J. Foster, B. Zhou, X. Li, S. M. Zabski, K.-J. Kim, and E. D. Crandall. "Na transport proteins are expressed by rat alveolar epithelial type I cells." *American Journal of Physiology - Lung Cellular and Molecular Physiology.* **2002**, 282, L599-L608.
128. L. G. Dobbs, M. C. Williams, and R. Gonzalez. "Monoclonal antibodies specific to apical surfaces of rat alveolar type I cells bind to surfaces of cultured, but not freshly isolated, type II cells." *Biochim Biophys Acta.* **1988**, 970, 146-56.
129. L. G. Dobbs, R. F. Gonzalez, L. Allen, and D. K. Froh. "HTI56, an integral membrane protein specific to human alveolar type I cells." *J Histochem Cytochem.* **1999**, 47, 129-37.
130. M. D. Johnson. "Alveolar epithelial type I cells contain transport proteins and transport sodium, supporting an active role for type I cells in regulation of lung liquid homeostasis." *Proc Natl Acad Sci USA.* **2002**, 99, 1966-1971.
131. M. D. Johnson. "Functional ion channels in pulmonary alveolar type I cells support a role for type I cells in lung ion transport." *Proc Natl Acad Sci USA.* **2006**, 103, 4964-4969.
132. M. Johnson, L. Allen, and L. Dobbs. "Characteristics of Cl<sup>-</sup> uptake in rat alveolar type I cells." *American Journal of Physiology - Lung Cellular and Molecular Physiology.* **2009**, 297, L816-L827.
133. R. F. Gonzalez, and L. G. Dobbs. "Isolation and culture of alveolar epithelial Type I and Type II cells from rat lungs." *Methods in Molecular Biology.* **2013**, 945, 145-59.

134. S. Nielsen, L. S. King, B. M. Christensen, and P. Agre. "Aquaporins in complex tissues. II. Subcellular distribution in respiratory and glandular tissues of rat." *Am J Physiol.* **1997**, 273, C1549-61.
135. L. G. Dobbs, R. Gonzalez, M. A. Matthay, E. P. Carter, L. Allen, and A. S. Verkman. "Highly water-permeable type I alveolar epithelial cells confer high water permeability between the airspace and vasculature in rat lung." *Proc Natl Acad Sci USA.* **1998**, 95, 2991-2996.
136. L. G. Dobbs, M. D. Johnson, J. Vanderbilt, L. Allen, and R. Gonzalez. "The Great Big Alveolar TI Cell: Evolving Concepts and Paradigms." *Cellular Physiology and Biochemistry.* **2010**, 25, 55-62.
137. L. G. Dobbs, and M. D. Johnson. "Alveolar epithelial transport in the adult lung." *Respir Physiol Neurobiol.* **2007**, 159, 283-300.
138. M. L. Fulcher, S. Gabriel, K. A. Burns, J. R. Yankaskas, and S. H. Randell. "Well-differentiated human airway epithelial cell cultures." *Methods Mol Med.* **2005**, 107, 183-206.
139. S. H. Randell, M. L. Fulcher, W. O'Neal, and J. C. Olsen. "Primary epithelial cell models for cystic fibrosis research." *Methods in Molecular Biology.* **2011**, 742, 285-310.
140. M. L. Fulcher, and S. H. Randell. "Human nasal and tracheo-bronchial respiratory epithelial cell culture." *Methods in Molecular Biology.* **2013**, 945, 109-21.
141. M. Yamaya, W. E. Finkbeiner, S. Y. Chun, and J. H. Widdicombe. "Differentiated structure and function of cultures from human tracheal epithelium." *Am J Physiol.* **1992**, 262, L713-24.
142. L. G. Johnson, K. G. Dickman, K. L. Moore, L. J. Mandel, and R. C. Boucher. "Enhanced Na<sup>+</sup> transport in an air-liquid interface culture system." *Am J Physiol.* **1993**, 264, L560-5.
143. P. M. de Jong, M. A. van Sterkenburg, S. C. Hesselting, J. A. Kempenaar, A. A. Mulder, A. M. Mommaas, J. H. Dijkman, and M. Ponc. "Ciliogenesis in human bronchial epithelial cells cultured at the air-liquid interface." *Am J Respir Cell Mol Biol.* **1994**, 10, 271-7.
144. S. H. Bernacki, A. L. Nelson, L. Abdullah, J. K. Sheehan, A. Harris, C. W. Davis, and S. H. Randell. "Mucin gene expression during differentiation of human airway epithelia in vitro. Muc4 and muc5b are strongly induced." *Am J Respir Cell Mol Biol.* **1999**, 20, 595-604.

145. Y. J. Zhang, W. K. O'Neal, S. H. Randell, K. Blackburn, M. B. Moyer, R. C. Boucher, and L. E. Ostrowski. "Identification of dynein heavy chain 7 as an inner arm component of human cilia that is synthesized but not assembled in a case of primary ciliary dyskinesia." *Journal of Biological Chemistry*. **2002**, 277, 17906-15.
146. P. H. Karp, T. O. Moninger, S. P. Weber, T. S. Nesselhauf, J. L. Launspach, J. Zabner, and M. J. Welsh. "An in vitro model of differentiated human airway epithelia. Methods for establishing primary cultures." *Methods in Molecular Biology*. **2002**, 188, 115-37.
147. E. N. Worthington, and R. Tarran. "Methods for ASL measurements and mucus transport rates in cell cultures." *Methods in Molecular Biology*. **2011**, 742, 77-92.
148. L. Wiszniewski, L. Jornot, T. Dudez, A. Pagano, T. Rochat, J. S. Lacroix, S. Suter, and M. Chanson. "Long-term cultures of polarized airway epithelial cells from patients with cystic fibrosis." *Am J Respir Cell Mol Biol*. **2006**, 34, 39-48.
149. M. D. Johnson. "Ion transport in alveolar type I cells." *Molecular BioSystems*. **2007**, 3, 178.
150. M. Nikkhah, F. Edalat, S. Manoucheri, and A. Khademhosseini. "Engineering microscale topographies to control the cell-substrate interface." *Biomaterials*. **2012**, 33, 5230-46.
151. A. Folch, and M. Toner. "Microengineering of cellular interactions." *Annu Rev Biomed Eng*. **2000**, 2, 227-56.
152. S. N. Bhatia, U. J. Balis, M. L. Yarmush, and M. Toner. "Effect of cell-cell interactions in preservation of cellular phenotype: cocultivation of hepatocytes and nonparenchymal cells." *Faseb J*. **1999**, 13, 1883-900.
153. J. Fu, Y. K. Wang, M. T. Yang, R. A. Desai, X. Yu, Z. Liu, and C. S. Chen. "Mechanical regulation of cell function with geometrically modulated elastomeric substrates." *Nat Methods*. **2010**, 7, 733-6.
154. J. L. Tan, J. Tien, D. M. Pirone, D. S. Gray, K. Bhadriraju, and C. S. Chen. "Cells lying on a bed of microneedles: an approach to isolate mechanical force." *Proc Natl Acad Sci USA*. **2003**, 100, 1484-9.
155. N. P. Westcott, and M. N. Yousaf. "Chemoselective ligand patterning of electroactive surfaces using microfluidics." *Electrophoresis*. **2009**, 30, 3381-5.
156. B. D. Ratner, and S. J. Bryant. "Biomaterials: where we have been and where we are going." *Annual review of biomedical engineering*. **2004**, 6, 41-75.

157. P. Zorlutuna, N. Annabi, G. Camci-Unal, M. Nikkhah, J. M. Cha, J. W. Nichol, A. Manbachi, H. Bae, S. Chen, and A. Khademhosseini. "Microfabricated biomaterials for engineering 3D tissues." *Adv Mater.* **2012**, *24*, 1782-804.
158. G. M. Whitesides, E. Ostuni, S. Takayama, X. Jiang, and D. E. Ingber. "Soft lithography in biology and biochemistry." *Annual review of biomedical engineering.* **2001**, *3*, 335-73.
159. B. D. Gates, Q. Xu, M. Stewart, D. Ryan, C. G. Willson, and G. M. Whitesides. "New approaches to nanofabrication: molding, printing, and other techniques." *Chem Rev.* **2005**, *105*, 1171-96.
160. K. R. Love, S. Bagh, J. Choi, and J. C. Love. "Microtools for single-cell analysis in biopharmaceutical development and manufacturing." *Trends in Biotechnology.* **2013**, *31*, 280-6.
161. W. M. Weaver, P. Tseng, A. Kunze, M. Masaeli, A. J. Chung, J. S. Dudani, H. Kittur, R. P. Kulkarni, and D. Di Carlo. "Advances in high-throughput single-cell microtechnologies." *Curr Opin Biotechnol.* **2014**, *25*, 114-23.
162. G. B. Salieb-Beugelaar, G. Simone, A. Arora, A. Philippi, and A. Manz. "Latest Developments in Microfluidic Cell Biology and Analysis Systems." *Anal Chem.* **2010**, *82*, 4848-4864.
163. P. Neuzi, S. Giselsbrecht, K. Lange, T. J. Huang, and A. Manz. "Revisiting lab-on-a-chip technology for drug discovery." *Nature Reviews Drug discovery.* **2012**, *11*, 620-32.
164. M. L. Kovarik, P. C. Gach, D. M. Ornoff, Y. Wang, J. Balowski, L. Farrag, and N. L. Allbritton. "Micro total analysis systems for cell biology and biochemical assays." *Anal Chem.* **2012**, *84*, 516-40.
165. M. L. Kovarik, D. M. Ornoff, A. T. Melvin, N. C. Dobes, Y. Wang, A. J. Dickinson, P. C. Gach, P. K. Shah, and N. L. Allbritton. "Micro total analysis systems: fundamental advances and applications in the laboratory, clinic, and field." *Anal Chem.* **2013**, *85*, 451-72.
166. C. E. Sims, and N. L. Allbritton. "Analysis of single mammalian cells on-chip." *Lab Chip.* **2007**, *7*, 423-40.
167. L. C. Kam, K. Shen, and M. L. Dustin. "Micro- and nanoscale engineering of cell signaling." *Annual review of biomedical engineering.* **2013**, *15*, 305-26.
168. M. Mehling, and S. Tay. "Microfluidic cell culture." *Curr Opin Biotechnol.* **2014**, *25*, 95-102.

169. C. E. Sims, M. Bachman, G. P. Li, and N. L. Allbritton. "Choosing one from the many: selection and sorting strategies for single adherent cells." *Analytical and Bioanalytical Chemistry*. **2007**, 387, 5-8.
170. J. Y. Park, S. Takayama, and S. H. Lee. "Regulating microenvironmental stimuli for stem cells and cancer cells using microsystems." *Integr Biol (Camb)*. **2010**, 2, 229-40.
171. I. Y. Wong, S. N. Bhatia, and M. Toner. "Nanotechnology: emerging tools for biology and medicine." *Genes Dev*. **2013**, 27, 2397-408.
172. J. Voldman, M. L. Gray, and M. A. Schmidt. "Microfabrication in biology and medicine." *Annual review of biomedical engineering*. **1999**, 1, 401-25.
173. N. Li, A. Tourovskaia, and A. Folch. "Biology on a chip: microfabrication for studying the behavior of cultured cells." *Crit Rev Biomed Eng*. **2003**, 31, 423-88.
174. J. Shim, T. F. Bersano-Begey, X. Zhu, A. H. Tkaczyk, J. J. Linderman, and S. Takayama. "Micro- and nanotechnologies for studying cellular function." *Current topics in medicinal chemistry*. **2003**, 3, 687-703.
175. M. L. Yarmush, and K. R. King. "Living-cell microarrays." *Annual review of biomedical engineering*. **2009**, 11, 235-57.
176. M. T. Guo, A. Rotem, J. A. Heyman, and D. A. Weitz. "Droplet microfluidics for high-throughput biological assays." *Lab Chip*. **2012**, 12, 2146-55.
177. Y. Zheng, H. Fujioka, S. Bian, Y. Torisawa, D. Huh, S. Takayama, and J. B. Grotberg. "Liquid plug propagation in flexible microchannels: A small airway model." *Phys Fluids (1994)*. **2009**, 21, 71903.
178. H. Tavana, C.-H. Kuo, Q. Y. Lee, B. Mosadegh, D. Huh, P. J. Christensen, J. B. Grotberg, and S. Takayama. "Dynamics of Liquid Plugs of Buffer and Surfactant Solutions in a Micro-Engineered Pulmonary Airway Model." *Langmuir*. **2009**, 26, 3744-3752.
179. H. Tavana, P. Zamankhan, P. Christensen, J. Grotberg, and S. Takayama. "Epithelium damage and protection during reopening of occluded airways in a physiologic microfluidic pulmonary airway model." *Biomed Microdevices*. **2011**, 13, 731-742.
180. N. J. Douville, P. Zamankhan, Y. C. Tung, R. Li, B. L. Vaughan, C. F. Tai, J. White, P. J. Christensen, J. B. Grotberg, and S. Takayama. "Combination of fluid and solid mechanical stresses contribute to cell death and detachment in a microfluidic alveolar model." *Lab Chip*. **2011**, 11, 609-19.

181. D. Huh, B. Matthews, A. Mammoto, M. Montoya-Zavala, H. Hsin, and D. Ingber. "Reconstituting Organ-Level Lung Functions on a Chip." *Science*. **2010**, 328, 1662-1668.
182. S. Kumar Mahto, J. Tenenbaum-Katan, and J. Sznitman. "Respiratory physiology on a chip." *Scientifica (Cairo)*. **2012**, 2012, 364054.
183. M. Ochs, J. R. Nyengaard, A. Jung, L. Knudsen, M. Voigt, T. Wahlers, J. Richter, and H. J. Gundersen. "The number of alveoli in the human lung." *Am J Respir Crit Care Med*. **2004**, 169, 120-4.
184. B. H. Chueh, D. Huh, C. R. Kyrtos, T. Houssin, N. Futai, and S. Takayama. "Leakage-free bonding of porous membranes into layered microfluidic array systems." *Anal Chem*. **2007**, 79, 3504-8.
185. K. Aran, L. A. Sasso, N. Kamdar, and J. D. Zahn. "Irreversible, direct bonding of nanoporous polymer membranes to PDMS or glass microdevices." *Lab Chip*. **2010**, 10, 548-52.
186. V. Sunkara, D. K. Park, H. Hwang, R. Chantiwas, S. A. Soper, and Y. K. Cho. "Simple room temperature bonding of thermoplastics and poly(dimethylsiloxane)." *Lab Chip*. **2011**, 11, 962-5.
187. N. J. Douville, Y. C. Tung, R. Li, J. D. Wang, M. E. El-Sayed, and S. Takayama. "Fabrication of two-layered channel system with embedded electrodes to measure resistance across epithelial and endothelial barriers." *Anal Chem*. **2010**, 82, 2505-11.
188. M. Morel, J. C. Galas, M. Dahan, and V. Studer. "Concentration landscape generators for shear free dynamic chemical stimulation." *Lab Chip*. **2012**, 12, 1340-6.
189. T. Kim, M. Pinelis, and M. M. Maharbiz. "Generating steep, shear-free gradients of small molecules for cell culture." *Biomed Microdevices*. **2009**, 11, 65-73.
190. D. M. Cate, C. G. Sip, and A. Folch. "A microfluidic platform for generation of sharp gradients in open-access culture." *Biomicrofluidics*. **2010**, 4, 44105.
191. K. Aran, A. Fok, L. A. Sasso, N. Kamdar, Y. Guan, Q. Sun, A. Undar, and J. D. Zahn. "Microfiltration platform for continuous blood plasma protein extraction from whole blood during cardiac surgery." *Lab Chip*. **2011**, 11, 2858-68.
192. J. H. Son, S. H. Lee, S. Hong, S. M. Park, J. Lee, A. M. Dickey, and L. P. Lee. "Hemolysis-free blood plasma separation." *Lab Chip*. **2014**, 14, 2287-2292.
193. K. J. Jang, and K. Y. Suh. "A multi-layer microfluidic device for efficient culture and analysis of renal tubular cells." *Lab Chip*. **2010**, 10, 36-42.

194. K. J. Jang, A. P. Mehr, G. A. Hamilton, L. A. McPartlin, S. Chung, K. Y. Suh, and D. E. Ingber. "Human kidney proximal tubule-on-a-chip for drug transport and nephrotoxicity assessment." *Integrative Biology*. **2013**, *5*, 1119-29.
195. A. C. Paz, S. Javaherian, and A. P. McGuigan. "Tools for micropatterning epithelial cells into microcolonies on transwell filter substrates." *Lab Chip*. **2011**, *11*, 3440-8.
196. H. J. Kim, D. Huh, G. Hamilton, and D. E. Ingber. "Human gut-on-a-chip inhabited by microbial flora that experiences intestinal peristalsis-like motions and flow." *Lab Chip*. **2012**, *12*, 2165-74.
197. R. Booth, and H. Kim. "Characterization of a microfluidic in vitro model of the blood-brain barrier (muBBB)." *Lab Chip*. **2012**, *12*, 1784-92.
198. Y. S. Torisawa, B. Mosadegh, S. P. Cavnar, M. Ho, and S. Takayama. "Transwells with Microstamped Membranes Produce Micropatterned Two-Dimensional and Three-Dimensional Co-Cultures." *Tissue Eng Part C Methods*. **2010**.
199. D. Gallego-Perez, N. Higuera-Castro, R. K. Reen, M. Palacio-Ochoa, S. Sharma, L. J. Lee, J. J. Lannutti, D. J. Hansford, and K. J. Gooch. "Micro/nanoscale technologies for the development of hormone-expressing islet-like cell clusters." *Biomed Microdevices*. **2012**, *14*, 779-89.
200. B. Lu, D. Zhu, D. Hinton, M. Humayun, and Y.-C. Tai. "Mesh-supported submicron parylene-C membranes for culturing retinal pigment epithelial cells." *Biomed Microdevices*. **2012**, *14*, 659-667.
201. R. Truckenmuller, S. Giselbrecht, C. van Blitterswijk, N. Dambrowsky, E. Gottwald, T. Mappes, A. Rolletschek, V. Saile, C. Trautmann, K. F. Weibezahn, and A. Welle. "Flexible fluidic microchips based on thermoformed and locally modified thin polymer films." *Lab Chip*. **2008**, *8*, 1570-9.
202. B. E. Isakson, R. L. Lubman, G. J. Seedorf, and S. Boitano. "Modulation of pulmonary alveolar type II cell phenotype and communication by extracellular matrix and KGF." *Am J Physiol Cell Physiol*. **2001**, *281*, C1291-9.
203. D. M. Ornoff, Y. Wang, and N. L. Allbritton. "Characterization of freestanding photoresist films for biological and MEMS applications." *J Micromech Microeng*. **2013**, *23*, 025009.
204. iStock "Human Lung, Image #6388736." <http://www.istockphoto.com/photo/human-lung-6388736?st=4cea017> (accessed June 1, 2014).
205. U. o. N. C. S. o. Medicine, "Human bronchi." In *Virtual Histology Library*, Univ. of North Carolina School of Medicine: Chapel Hill, 2009.

206. W. Funkhouser, "Normal human alveoli.". Univ. of North Carolina School of Medicine: Chapel Hill, 2009.
207. W. Funkhouser, "Human alveoli, Acute Respiratory Distress Syndrome.". Univ. of North Carolina School of Medicine: Chapel Hill, 2009.
208. C. Pohl, M. I. Hermanns, C. Uboldi, M. Bock, S. Fuchs, J. Dei-Anang, E. Mayer, K. Kehe, W. Kummer, and C. J. Kirkpatrick. "Barrier functions and paracellular integrity in human cell culture models of the proximal respiratory unit." *Eur J Pharm Biopharm.* **2009**, 72, 339-49.

## **Chapter 2: Characterization of freestanding photoresist films for biological and MEMS applications**

### **2.1 Introduction**

#### **2.1.1 General approaches**

When considering a microfabricated system for culturing primary AT1 cells, several general design approaches were first considered. Typical strategies for plating single cells include limiting dilution, micropallet arrays, and arrays of microwells. Limiting dilution was recognized as offering no advantage for primary AT1 cell growth, as single AT1 cells seeded onto traditional permeable supports would not be able to spread out over a macroscopic area. Arrays of micropallets, pedestal-shaped structures formed atop glass substrates, have not been fabricated in a fashion that would allow culture under an ALI.<sup>1</sup> Microcup and microtable variants of the micropallet format have been fabricated, and it may be possible to fabricate the cup or table surfaces to make them permeable, but this approach would require significant labor and be technically complex.<sup>2-3</sup> This approach was also viewed as impractical due to the need to release and subsequently collect the microcup or microtable arrays for subsequent bioelectric analyses. Traditional microwell arrays made out of PDMS or other materials typically used in microfabrication do not offer a permeable support, and thus do not currently allow culture under an ALI. However, modification of a microwell-array format that allows both segregation of cells and an array of through-holes to make the microwells permeable presented a promising start.

Observation that, in long-term culture of cells atop arrays of micropallets formed from negative photoresist, some of the micropallets would spontaneously detach from the glass fabrication substrate led to the hypothesis that entire films of photoresist could be fabricated and released intact from the glass fabrication substrate. By patterning microscale wells into a layer of 1002F (in the opposite relief from traditional micropallet fabrication strategies) and releasing the film, an array of through-holes could be achieved that would permit exchange of water and solutes across the photoresist film, a useful start to an AT1 culture platform.

### **2.1.2 Lab-on-a-foil devices**

A film released in this fashion could function as a lab-on-a-foil, a device type that is an area of emerging importance. These devices use flexible substrates less than 500  $\mu\text{m}$  in thickness and are well-suited for a number of chemical and biological applications due to their rapid thermal transfer, low reagent use, laminar flow regimes, and flexibility - many of the same reasons that microfluidic-based lab-on-chip devices have become so attractive to the chemical and biological fields.<sup>4</sup> Freestanding, micropatterned films have been made using polydimethylsiloxane (PDMS) and parylene C. PDMS is frequently used in microelectromechanical systems (MEMS) and is inexpensive, optically transparent, and easily delaminated from the fabrication surface.<sup>5</sup> However, the fabrication of through-hole structures in PDMS is technically difficult, and thin PDMS films are mechanically fragile, limiting the range of useful thicknesses. Though a photopatternable PDMS-like silicone exists, it cannot be released from its fabrication substrate.<sup>6</sup> Thick PDMS films (100  $\mu\text{m}$ ) have been patterned by filling a microfluidic mold or by using an open photoresist mold followed by pressure application, but these processes require pre-existing molds and an overlying

adhesive layer to prevent the PDMS from rising above the level of the mold surface.<sup>7</sup> Parylene C, a transparent poly(p-xylene) formulation, has also been shown to be amenable for forming micropatterned films and to be biocompatible, but its fabrication process is complex and requires multiple time-consuming steps including chemical vapor deposition, thermal evaporation, and reactive ion etching.<sup>8</sup> Thus, an inexpensive, biocompatible material that can be reliably patterned and quickly released to form a freestanding film, using a minimum of equipment and effort, would be a significant advance for the biomaterials and microfabrication fields.

### **2.1.3 Photoresists**

Photoresists are light-sensitive resins used in a variety of industrial, chemical, and biotechnological applications. Positive photoresists are polymers typically spun to a low thickness over a substrate. Exposure to light induces localized disruption of the polymer backbone, such that areas exposed to light become soluble in a developing solution.<sup>9</sup> Negative photoresists, by contrast, are high-viscosity solutions typically composed of a monomeric resin and a photoinitiator in an organic solvent.<sup>9-11</sup> Upon exposure to light, the resin is converted into a high-molecular weight, insoluble form by the polymerization of resin monomer. This polymerization results from a change in the local chemical environment brought about by the light-induced generation of free radicals or strong acids from the photoinitiator. First used as protective layers in semiconductor patterning processes, photoresists have also found widespread use in recent years in a variety of applications outside the microelectronics industry.<sup>9-10</sup> For example, patterned photoresists placed on a rigid substrate are often used as molds for soft lithography of PDMS and other polymers.<sup>5, 12-16</sup> They also have application as protective layers during the etching of metals and silicon, as

sacrificial layers to pattern silanes, polymers, and biomolecules, and as structural roles in microfabricated devices.<sup>1, 17-36</sup> Pyrolysis of patterned photoresist films generates clear, microscale carbon electrodes.<sup>37-40</sup> Despite the many applications illustrated above, photoresists generally have been relegated to use as a sacrificial layer or as a rigid structural component remaining on its fabrication substrate (usually glass or silicon).

#### **2.1.4 Photoresists as lab-on-a-foil devices**

Though freestanding photoresist films have potential as lab-on-a-foil devices, little about such films has been reported in the literature. One reason may be that most commercially-available photoresists are not ideal for use in applications requiring a freestanding film, since these resists are brittle and inflexible.<sup>41-43</sup> Abgrall *et al.* detailed the fabrication use of freestanding films of the popular photoresist SU-8 for use in a lab-on-a-foil concept, but the film was laminated to a polyester support layer.<sup>44</sup> Other groups have fabricated and released membranes made of SiN, thin single-crystal Si, or a trilayer of metal, photoresist, and anti-reflective coating for various stenciling applications.<sup>45-47</sup> Wang and colleagues detailed the use of films of a negative photoresist to capture intact human colon crypts.<sup>48</sup> These photoresist films were detached from their glass fabrication substrates after completion of the lithography. McPherson and Walker recently showed that 1002F photoresist films could be released and used as mechanical sieves.<sup>49</sup> However, those reports did not characterize the release conditions for the films or the limits of film patterning. Thus, the ultimate patterning resolution and aspect ratio for such films, as well as the material properties, are not known.

To have wide utility, freestanding photoresist films should have several characteristics. First, the resist should be easily patterned by conventional methods. Second,

the material must be amenable to facile release from the fabrication substrate without harsh solvents. Third, a material that is transparent in the visible wavelengths and possessing little autofluorescence would insure compatibility with light and fluorescence microscopy techniques. Fourth, the material used should be structurally resilient and flexible in a range of thicknesses.

The photoresist 1002F meets the above criteria, possessing low autofluorescence and high biocompatibility.<sup>50</sup> 1002F is a negative photoresist whose monomer form contains epoxy groups, similar to the widely-used negative photoresist SU-8, that are induced to polymerize in a linear fashion in the presence of an acid catalyst. Mixing of 1002F monomer resin with triarylsulfonium hexafluoroantimonate salts, which act as a photoinitiator by generating acid moieties in response to activation with UV light, are mixed in the solvent  $\gamma$ -butyrolactone to form a viscous photoresist that can be spin coated onto glass substrates to give films of uniform and predictable thickness. Compared to SU-8, 1002F offers comparable biocompatibility and much reduced autofluorescence.<sup>50</sup>

### **2.1.5 Overview**

This chapter characterizes the fabrication, micropatterning, and release of 1002F films. The ability of various solvents to release the films from the underlying fabrication substrate is considered, as are the release kinetics. Fabrication parameters for a variety of film thicknesses, patterned with through-holes of a variety of shapes and sizes and in multiple layers, were measured. Properties of the films such as the patterning aspect ratio and resolution as well as the Young's modulus were assessed. Lastly, two applications of the films, the use as stencils for achieving patterned deposition of metal onto a substrate and the study of single cells atop a micropore, were demonstrated. This is the first quantitative

description of the fabrication of freestanding films using a photoresist. These results established the utility of flexible, freestanding 1002F photoresist films for use as an industrial, chemical, or biological tool.

## **2.2 Experimental Design**

### **2.2.1 Materials**

EPON resin 1002F photoresist (phenol, 4,4'-(1-methylethylidene)bis-, polymer with 2,2'-[(1-methylethylidene) bis(4,1-phenyleneoxymethylene)]bis-[oxirane]) was obtained from Miller-Stephenson (Sylmar, CA). UVI-6976 photoinitiator (triarylsulfonium hexafluoroantimonate salts in propylene carbonate) was purchased from Dow Chemical (Torrance, CA). SU-8 photoresist was obtained from MicroChem Corp. (Newton, MA).  $\gamma$ -butyrolactone (GBL) and developer (propylene glycol methylether acetate, PGMEA) were obtained from Sigma-Aldrich (St. Louis, MO). PDMS (Sylgard 184 silicone elastomer kit) was purchased from Dow Corning (Midland, MI). Chrome photolithography masks were designed in-house using TurboCAD software and printed by FineLine Imaging (Boulder, CO). Dulbecco's modified Eagle's medium (DMEM), fetal bovine serum (FBS), and penicillin/streptomycin were obtained from Invitrogen (Carlsbad, CA). H1299 cells were obtained from American Type Culture Collection (ATCC, Manassas, VA).

### **2.2.2 Fabrication and release of single-layer films**

1002F-10, 1002F-50, and 1002F-100 negative photoresists were prepared by dissolving EPON 1002F resin and triarylsulfonium hexafluoroantimonate salts in GBL (described previously).<sup>50</sup> Films of 1002F photoresist of various thicknesses (4.5-225  $\mu\text{m}$ ) were obtained by spin-coating 1002F-10, -50, or -100 on precleaned glass slides.<sup>50</sup> The

coated slides were then soft-baked at 95°C in an oven to remove organic solvent. After cooling to room temperature, the slides were exposed to UV light from an Oriel collimated UV light source (1.68 mW/cm<sup>2</sup>, Newport Stratford, Inc., Stratford, CT) through a patterned chrome photomask. A two-step post-exposure bake, first at 95 °C and then at 120 °C, followed UV exposure. After cooling to room temperature, unpolymerized monomer was removed by developing the slide in propylene glycol methylether acetate (PGMEA), rinsing with 2-propanol, and drying under a nitrogen stream. Films were hard-baked at 120 °C for 2 h. Unless stated otherwise, films were released from the glass substrate by incubated in water for 12 h on a laboratory shaker (60 rpm, Bellco Biotechnology, Bellco Glass, NJ) at 23°C. Films were detached from the glass slide by sliding a razor beneath the film at its corner and using tweezers to gently peel the film away from the glass slide. Detached films were dried under room air.

### **2.2.3 Measurement of film properties**

Photoresist thin films were imaged with a Nikon Eclipse TE2000-U inverted fluorescence microscope under brightfield conditions and the image recorded with a cooled CCD camera (Photometrix Cool Snap *fx*, Roper Scientific, Tucson, AZ) controlled by NIS Elements software (Nikon, Melville, NY). Films were also imaged using an FEI Quanta 200 FEG scanning electron microscope (SEM) with a Shottky field emission gun, operated under low-vacuum conditions (0.38 torr) (Chapel Hill Analytical and Nanofabrication Laboratory (CHANL)). Film thickness was determined using SEM and profilometry (KLA-Tencor P-15 Profilometer, KLA-Tencor, San Jose, CA). Aspect ratios were measured by cutting films and measuring the film thickness and dimensions of through-holes using SEM. 1002F films were subjected to tensile strength testing using dogbone-shaped films 50 µm in thickness and 0.3

cm wide and 2.4 cm long using an EnduraTEC Smart Test Series tension loader. Films were subjected to axial stress using a 5-lb load cell and pulled at a rate of 0.01 mm/s until failure. The Young's Modulus was determined to be the slope of the best-fit line in a plot of the axial stress versus strain, as measured photographically over the course of the tensile strength test, and the ultimate tensile stress determined as the axial stress in the film just prior to mechanical failure.

#### **2.2.4 Characterization of photoresist thin film release kinetics**

The release of photoresist thin films from glass substrates was assessed using different solvents over a 24-h time course. Twenty square-shaped photoresist thin films 50- $\mu\text{m}$  thick with dimensions of 25 x 25 mm were fabricated and immersed in either acetone, 75% (v/v) ethanol, deionized laboratory water, or a 1% (w/v) detergent solution (Contrex Labware Detergent, Decon Labs, PA) (5 films per solvent dish). Films were shaken for 24 h in covered dishes. The dishes were observed after 1, 8, 12 and 24 h for spontaneous detachment of films. After 24 h, slides were removed from solvent dishes and assessed for the attached films assessed for their ability to be removed. Three independent trials were conducted, each on a separate day.

The time needed for release of a film incubated in deionized laboratory water was also measured. Twenty films with dimensions identical to those described in the above paragraph were fabricated and immersed in water in covered laboratory dishes on a shaker for 1, 2, 4, 8, and 12 h. At each time point, the films in each dish (5 films per time point) were observed for spontaneous detachment. The ability of undetached films to be released from the glass substrate using a razor blade was also assessed. Three independent trials were conducted, each on a separate day.

### **2.2.5 Patterned deposition of metal and protein**

Patterned deposition of metal through photoresist film stencils was accomplished using a Cressington 108 Sputter Coater (Cressington, United Kingdom), which was monitored using an MTM-10 thickness monitor. Between 10 and 20 nm of Au:Pd was deposited on substrates under an argon gas plasma. Sputtering was performed on glass substrates using un-released and released films as stencils and on PDMS substrates using released films as stencils. Released films used as stencils were attached to the surface of new glass substrates using clamps or placed on PDMS using manual pressure. All substrates were imaged before and after deposition and after removal of the photoresist stencil by brightfield microscopy.

Additionally, patterned deposition of protein through photoresist film stencils was accomplished by applying a 50 µg/mL solution of rhodamine B-conjugated bovine serum albumin (BSA) to microarrays atop solid surfaces. Patterning was performed first on glass substrates using un-released films. After release, films were placed on PDMS substrates by applying manual pressure, or were thermobonded to glass or polystyrene substrates by applying pressure to the film and heating at 95°C. Thermobonded films could later be released via incubation in deionized water. All substrates were imaged before and after protein deposition via epifluorescence microscopy.

### **2.2.6 Cell culture on a film with a single pore**

H1299 lung adenocarcinoma cells were cultured in Dulbecco's modified Eagle's medium (DMEM) supplemented with penicillin/streptomycin and 5% fetal bovine serum. 1002F photoresist films with a single through-hole 10 µm in diameter were fabricated, released, and attached to a support column so that the film separated an upper and lower fluid

chamber. After microscopic evaluation to ensure that films contained only one pore and were free of defects, films were plasma treated and the surface of the upper chamber was coated with 100  $\mu\text{g}/\text{mL}$  collagen (type I from rat tail) for 1 h. H1299 cells were cultured in the upper chamber on the film until the cells were confluent on the film surface (24 h). Media in the basal (lower) compartment was replaced with DMEM containing calcein AM dye (10  $\mu\text{M}$ ). The film was imaged at the site of the pore after 5 min using a Nikon TE300 inverted epifluorescence microscope.

### **2.2.7 Seeding of AT2 primary cells**

Primary human AT2 cells were obtained as a gift from Dr. Peter Bove of the Cystic Fibrosis Research and Treatment Center at the Univ. of North Carolina School of Medicine. Briefly, cells were harvested from human explant lungs obtained with patient consent under a protocol approved by the Univ. of North Carolina School of Medicine Institutional Review Board via elastase digestion of the distal airspaces as a modification of previously published protocols.<sup>51</sup> After negative immunoselection using magnetic beads to remove contaminating erythrocytes and macrophages, AT2 cells were seeded into microstrainers with microwells 75  $\mu\text{m}$  in diameter and patterned with 5.0  $\mu\text{m}$  pores in the lower layer. Cells were monitored via brightfield microscopy for their ability to spread out and assume an AT1-like morphology.

## 2.3 Results and Discussion

### 2.3.1 Fabrication of 1002F films and release from glass substrates

Films of 1002F photoresist (25 mm x 25 mm x 50  $\mu\text{m}$ ,  $\ell$  x  $w$  x  $h$ ) were fabricated on a glass substrate with a 100 x 100 array of 75- $\mu\text{m}$  diameter through-holes spaced 20  $\mu\text{m}$  apart (Figure 2.1). Process conditions for this fabrication and several others with slight variances are given in Table 2.1. After fabrication, the films were incubated in four different solvents: acetone, 75% (v/v) ethanol in water, water, and 1% (w/v) detergent in water. The ability of the films to be released from the substrate was then assessed over time and all released films were visually inspected for defects. All films incubated in acetone spontaneously detached from the glass substrate by 1 h, but were distorted and rigid. At 24 h, films in ethanol, water, and detergent remained adhered to the glass substrate but could be detached by inserting a razor blade between the film and substrate. Films incubated in 75% ethanol curled upon release and could not be flattened. By contrast, all films placed in either water or detergent appeared undistorted and remained flat upon release (Figures 2.1 and 2.2). Representative images of films removed in each of the four solvents are shown in Figure 2.2. Since the highest quality films were released after incubation in water, this solvent was selected for all subsequent characterizations of film release.

The time required for the release of photoresist films from fabrication substrates was assessed by immersing the films in water for varying times. Film releasability was then assessed. All films were visually inspected and characterized as “releasable without damage,” “released but damaged,” or “not releasable” (Table 2.2). Released films with any defect observed either visually or via brightfield microscopy were considered damaged. The most common defects observed were tearing and/or irreversible bending of the films. By 2 h

of water immersion, all films were releasable but 60% were damaged during the release process (Table 2.2, Figure 2.3). By 4 h, 87% of the films were released without damage and by 12 h, all of the films were released undamaged (Table 2.2). Thus the 1002F photoresist films were easily released without damage by 12 h using simple solvent systems and without the need for an underlying sacrificial or water-soluble layer.

### **2.3.2 Mechanical strength of freestanding 1002F films**

To study the mechanical strength of freestanding 1002F films, the Young's modulus and ultimate tensile stress were measured. Dogbone-shaped films of 1002F were fabricated, released, and subjected to tension testing (Figure 2.4). The Young's modulus for 1002F films was determined to be  $1.43 \pm 0.21$  GPa, and the ultimate tensile stress determined to be  $54.5 \pm 3.1$  MPa (final elongation  $105.1 \pm 0.5$  %)(Table 2.3). By comparison, the Young's modulus of SU-8 has been reported as  $2.2 \pm 0.1$  GPa, and the Young's moduli for parylene and PDMS were reported to be 3.2 GPa and 0.75-4 MPa, respectively, suggesting that 1002F photoresist is mechanically similar to parylene and SU-8 but more resilient than PDMS.<sup>52-56</sup> In addition, 1002F films were shown to be flexible (Figure 2.5) and amenable to mechanical manipulation without damage to the films, in contrast to films fabricated with the more brittle SU-8. It is hypothesized that this flexibility is due to the presence of only two epoxy residues in the molecular structure of the 1002F monomer unit, necessitating that 1002F photopolymerization occur in a linear fashion. SU-8, by contrast, has eight epoxy moieties per monomer and thus polymerizes largely via cross-linking reactions, which may contribute to its brittle nature.

### 2.3.3 Fabrication of micropatterned freestanding 1002F films

The potential to fabricate freestanding photoresist films of a variety of thicknesses with features that faithfully replicated a master was assessed. 1002F photoresist films of varying thickness (4.5 - 225  $\mu\text{m}$ ) were first formed on a glass substrate and incubated in water for 24 h. All films, regardless of thickness, were released without damage.

Representative electron micrographs of films with thicknesses of 4.5  $\mu\text{m}$  and 225  $\mu\text{m}$  are shown in Figure 2.6A. To determine whether a mask pattern through which the photoresist was exposed with UV light could be faithfully reproduced in the free-standing films, features in a variety of shapes and sizes were photopatterned into the 1002F. The 1951 USAF Resolution Target was used as a standardized feature target. Figure 2.6B shows replication of level 3-3 of the 1951 USAF Resolution Target. Rectangles 247.5  $\mu\text{m}$  long and 49.5  $\mu\text{m}$  wide were recreated as rectangular through-holes  $248.9 \pm 2.9 \mu\text{m}$  in length and  $51.0 \pm 3.1 \mu\text{m}$  in width on the film. Areas of this standard mask that were visible to the unaided eye could also be fabricated, such as the features 2.5-mm in length (Figure 2.7A), without loss of film integrity.

In addition to using the 1951 USAF Resolution Target, other masks, custom-designed in the lab, were tested. Faithful replication of the mask pattern was observed for a variety of designs ranging in dimensions from 645 to 25  $\mu\text{m}$  in 50- $\mu\text{m}$  thick films exposed to a UV dose of 350  $\text{mJ} / \text{cm}^2$ . For example, mask circles (75  $\mu\text{m}$  diameter) yielded circular through-holes on the film of diameter  $74.3 \pm 2.5 \mu\text{m}$  (mean  $\pm$  standard deviation) (Figure 2.1B). Mask spirals with a 645  $\mu\text{m}$  in height and a 42  $\mu\text{m}$  line width were reproduced in the film as spirals  $644.8 \pm 3.0 \mu\text{m}$  in height and  $42.6 \pm 1.7 \mu\text{m}$  wide (Figure 2.6B). Mask squares of either 25 or 250  $\mu\text{m}$  to a side yielded square film holes of dimensions  $24.4 \pm 1.4 \mu\text{m}$  and  $250.1 \pm 3.2 \mu\text{m}$

on a side, respectively (Figure 2.6C). The smallest through-hole that could be reliably fabricated into films 50  $\mu\text{m}$  thick was  $10.1 \pm 0.6 \mu\text{m}$  in diameter, using a mask with circles 10- $\mu\text{m}$  in diameter (Figure 2.7C). The smallest through-hole that could be reliably fabricated overall was  $5.1 \pm 0.5 \mu\text{m}$  in diameter, fabricated in a film 4.5  $\mu\text{m}$ -thick film using a mask with 5- $\mu\text{m}$  circles (Figure 2.6C, Table 1.1).

The maximum ratio for the film thickness-to-hole width (aspect ratio) that could be fabricated in a freestanding film was also measured. The 1951 USAF Resolution Target was again used as a standard mask. Features with an aspect ratio of 6:1 were easily formed when fabricating rectangular holes into the film (Figure 2.6D). Using custom masks, the maximal aspect ratio for both circular and square features was shown to be 4.5:1 (Figure 2.7C-D). By comparison, we have previously fabricated freestanding 1002F micropillars at an aspect ratio of 4:1. A higher resolution mask and alignment system may further enhance the aspect ratio and resolution.

#### **2.3.4 Fabrication of multilayered, micropatterned freestanding 1002F films**

The potential to generate photoresist films with multiple layers, each carrying a different pattern of features, was explored. An initial layer of 1002F photoresist was photopatterned onto a glass slide. After hard-baking and plasma treatment, a second layer of 1002F was then spin-coated over the initial layer, exposed through a different mask and then processed as for the first layer of resist. As an example, a two-layer film was fabricated in which the first layer (5- $\mu\text{m}$  thick) possessed circular pores 5  $\mu\text{m}$  in diameter with a 10  $\mu\text{m}$  spacing (edge-to-edge). The second layer (50- $\mu\text{m}$  thick) possessed circular wells 75  $\mu\text{m}$  in diameter with a 25- $\mu\text{m}$  spacing (Figure 2.6E). All of these multilayered films ( $n = 8$ ) were released from the substrate without damage after a 24-h incubation in water. The resulting

array of wells with porous bottoms is termed a microstrainer. Figure 2.6E shows scanning electron micrographs of released microstrainers as imaged from below (left panel) and above (right panel) the microwell layer, showing the pore layer and the overlying microwell pattern. Because of how the microwell walls attach to the underlying pore layer, this type of fabrication may have potential in stabilizing films containing pores with small ( $< 10 \mu\text{m}$ ) diameters. Since pores this small require lower doses of UV light in order to avoid overexposure from diffraction effects, films with smaller pores can sometimes detach from the fabrication substrate during development, likely due to dissolution of thin monomer layers lying just above the substrate that were not adequately exposed. By creating overlying “wells” with relatively large diameters (on the order of  $200\text{-}500 \mu\text{m}$ ), large areas of pores with small diameters can be created, using the overlying well walls to enhance their stability and prevent detachment of the entire film from the substrate. Aside from this fabrication potential, microstrainer arrays have the potential for such uses as directed chemotaxis assays of individual cells, and in isolating and arraying single cells using gravity-driven flow through the porous well base for the subsequent analysis and tracking of cell behavior.

The latter application was utilized in a proof-of-principle test of AT1 culture. Primary rat AT2 cells, which are known to spread and assume an AT1-like morphology after several days in culture, were seeded onto microstrainers with wells  $75 \mu\text{m}$  in diameter featuring pores  $5.0 \mu\text{m}$  in diameter. Cells were seeded at low density increase the probability of seeding only a single cell per well. After 5 d in culture, minimal spreading was observed by these cells, suggesting an aversion to the relatively large pore size (Figure 2.8).

The practical difficulty in fabricating through-holes in 1002F smaller than  $5.0 \mu\text{m}$  presents an issue for the further development of 1002F microstrainers for use in growing

primary AT1 or other respiratory epithelia under ALI conditions. Anecdotal evidence suggests that primary cells fail to properly differentiate when grown on commercially-available supports with pores 3.0  $\mu\text{m}$  in diameter; cells grown on supports with pores 0.4  $\mu\text{m}$  in diameter were consistently observed to achieve a higher degree of differentiation and polarization.<sup>57</sup> Therefore, given the difficulty of fabricating pores on the order of 5.0  $\mu\text{m}$ , and the apparent need for primary respiratory epithelia to be grown on supports with pores 400nm or smaller, other approaches will likely have to be pursued for generating a permeable layer. Microstrainers will, however, continue to present potential for growing other cell types.

### **2.3.5 1002F films as re-usable stencils for substrate patterning**

Stencils for metal sputtering are traditionally made of stainless steel, PDMS, or parylene. However these materials generally possess one or more of the following weaknesses: high cost, complex fabrication, or mechanical instability.<sup>7, 55, 58</sup> To determine whether micropatterned 1002F films might be employed as low-cost, re-usable stencils for materials deposition onto a variety of surfaces, 1002F films were fabricated with an array of 75- $\mu\text{m}$  holes. The films were released and then placed onto the substrate (glass or PDMS) to be coated with a metal pattern (Figure 2.9). A 20 nm-thick layer of Au:Pd mixture was then sputtered onto the photoresist-substrate assembly. The diameter of the metal dots patterned onto the substrate was  $75.2 \pm 3.3 \mu\text{m}$  for the glass substrate and  $74.1 \pm 4.2 \mu\text{m}$  for the PDMS substrate. Thus the 1002F stencil pattern was faithfully replicated onto the substrates. Furthermore the 1002F stencil was easily separated from the substrates after each use and could be re-used (Figure 2.10). The stencil pattern was reused up to 8 times (the greatest number tested) yielding a patterned spot diameter of  $76.3 \pm 1.9 \mu\text{m}$ . In these experiments, no

mechanical disruption or tearing of films was observed. Compliant membranes composed of SiN, thin single-crystal Si, or a trilayer of metal, photoresist, and anti-reflective coating have previously been used for stenciling applications.<sup>45-47</sup> While resolutions as low as 1  $\mu\text{m}$  could be achieved with these films, freestanding photoresist films are easier to fabricate and release.

Additionally, released films were used as stencils for patterned deposition of protein onto solid supports. Application of a 50  $\mu\text{g/mL}$  solution of rhodamine B-conjugated BSA to micropatterned 1002F films atop solid surfaces yielded spatially-specific adsorption of protein. This scheme was used to achieve directed protein adsorption in patterns that faithfully replicated the mask pattern on the glass substrate on which the 1002F film was fabricated (Figure 2.11A). Once released, the film could be again used for protein patterning by manually bonding onto PDMS substrates or thermobonding at 95°C onto other glass or polystyrene substrates. Excellent replication of the mask pattern was observed for protein deposition onto PDMS surfaces (Figure 2.11B), likely due to the good conformal adhesion PDMS offers to overlying substrates. The mask pattern was reproduced less faithfully on subsequent glass and polystyrene substrates (Figure 2.11C-D), likely due to inconsistencies in the thermobonding process needed to ensure that protein solution did not undercut the through-hole array in the stencil. However, further optimization of the thermobonding process would likely improve this application. Of note, this protein patterning method requires no modifications to substrate surface chemistry or use of exogenous crosslinker molecules.

### **2.3.6 1002F films to address a single cell within a monolayer of cells**

Films (25 mm x 25 mm x 20  $\mu\text{m}$ ,  $\ell$  x w x h) with a single through-hole, 10  $\mu\text{m}$  in diameter, were fabricated and released. A fluid reservoir was attached on either side of the film and H1299 cells were cultured to confluency on one side of the film. Media containing calcein AM dye was supplied to the compartment lacking the cells. Only the cell spanning the single pore should have access to the calcein AM-containing compartment. The nonfluorescent, membrane-permeant calcein AM is rapidly metabolized within cells to the fluorescent, membrane-impermeant dye calcein. Thus, living cells exposed to calcein AM become brightly fluorescent as the dye is metabolized and trapped within their cytosol. Fluorescence images of the cell-covered film demonstrated a single H1299 cell that was fluorescent (Figure 2.12). This cell was also observed to span the 10- $\mu\text{m}$  pore. All surrounding cells remained nonfluorescent and so did not have access to the fluid in the opposite compartment. The ability to easily micropattern photoresist films with discrete through-holes small enough for a single cell to span is an important advantage of 1002F films relative to PDMS and parylene films, and to commercially-available microporous membranes for cell culture. By growing cells atop a freestanding film with a single through-hole, we are able to show the delivery of an exogenous agent (here, the cytoplasmic dye calcein AM) to a single cell within a contiguous monolayer.

Contemporary methods of achieving this would rely on either micropipette injection of the single cell or on a single-cell microelectroporator. Both of these methods suffer from the drawbacks of having to mechanically or electrophoretically puncture a cell membrane in order to load it with the compound of choice, actions that might alter the cell physiology or even destroy the cell. Single-pore 1002F films, by contrast, avoid the need for such harsh

methods and do so without the need for any additional equipment. The main drawback to single-pore 1002F films in relation to microinjection or electroporation, however, is an inability to choose a particular single cell to be loaded: the cell that will be loaded is by definition the cell spanning the pore, and no other.

Nonetheless, 1002F films fabricated in this manner offer potential for such applications as enabling customizable study of the permeability of a single cell – even when a cell is part of a contiguous monolayer – to exogenous molecules (drugs, hormones, etc.) or for observing the permeation of a supplied agent through a monolayer through gap junctions in adjacent cells.

## **2.4 Conclusions**

The photoresist 1002F can be micropatterned with good replication of a master using photolithography and released without damage from the fabrication substrate in a matter of hours, all without the need for an underlying sacrificial layer. Freestanding films have previously been made using PDMS and parylene. PDMS films are mechanically fragile and the fabrication of through-holes is technically difficult. Parylene films have high autofluorescence and require complex, multi-step fabrication schemes. By contrast, 1002F photoresist films are mechanically resilient, have low autofluorescence, require only basic UV photolithography to micropattern, and can be made with through-holes with dimensions much smaller than those of PDMS (~35  $\mu\text{m}$  limit).<sup>7</sup> Freestanding photoresist films can be used as stencils for material deposition, as patterned supports for cell culture, and as platforms to interrogate single cells within a monolayer. Thus, freestanding photoresist films have potential in future chemical and biological applications and particularly as lab-on-a-foil

devices. For the particular use of culturing primary AT1 cells, 1002F microstrainers are impractical. However, released films of micropatterned 1002F hold outstanding potential in forming the overall structure of freestanding microwell arrays in which to grow primary AT1 cells, provided they can be co-fabricated and released with another material that can act as a permeable layer.

## 2.5 Figures and Tables

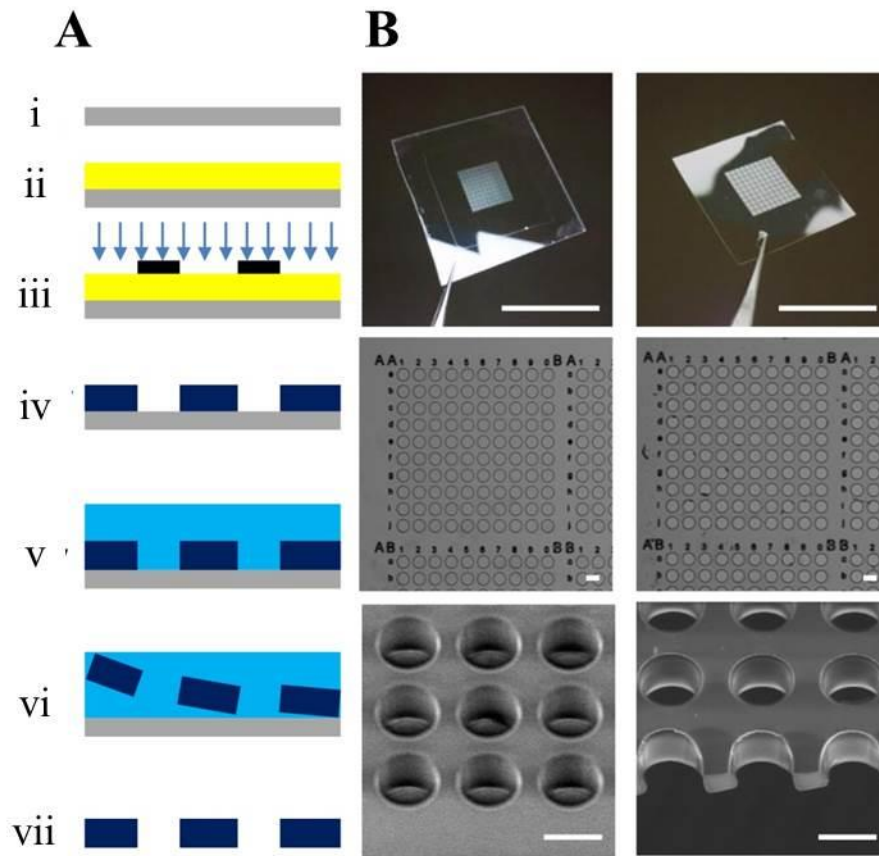


**Figure 2.1.** Fabrication and release of photoresist thin films. (A) Schematic illustration of fabrication and release protocol: atop a clean glass substrate (i) a layer of negative photoresist monomer is spin-coated (ii). After exposure to UV light through a chrome mask (iii), the film is developed to remove unpolymersed monomer (iv). The patterned film is immersed in an aqueous solution (v) to reduce film adhesion to the glass substrate (vi). The intact film can be removed from the substrate and dried (vii). (B) Macroscopic (top row), brightfield optical (middle row) and SEM (bottom row) images of a 50  $\mu\text{m}$ -thick film of 1002F photoresist (dimensions 25 mm x 25 mm) with an array of  $10^4$  circular wells (75  $\mu\text{m}$  diameter) before (left column) and after (right column) release in deionized water. Scale bars: 25 mm (top row), 75  $\mu\text{m}$  (middle and bottom rows).

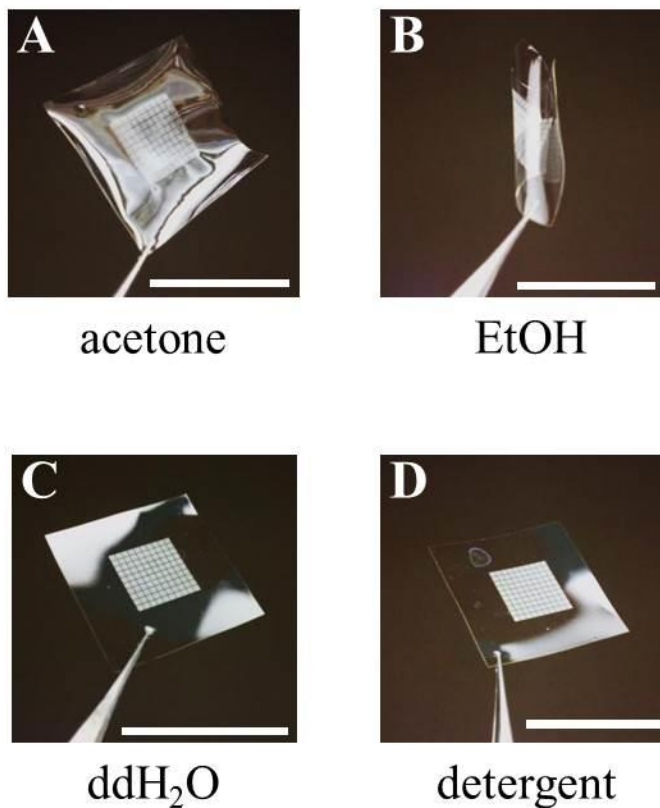


**Figure 2.2.** Removal of 1002F films with various solvents. Images of 25 mm x 25 mm films of 1002F photoresist (50  $\mu\text{m}$  thick) with an array of  $10^4$  circular wells 75  $\mu\text{m}$  in diameter after removal from glass using (A) acetone, (B) 75% (v/v) ethanol, (C) deionized water, and (D) a 1% (w/v) detergent solution. Note the distortion in the films removed by acetone or ethanol, compared to the intact, even films removed with aqueous solutions. Scale bars: 25 mm.

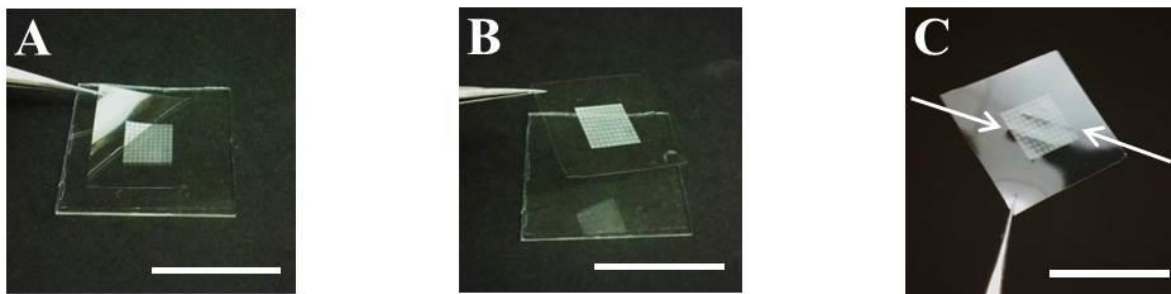


**Figure 2.3.** Removal of 1002F films from fabrication substrate. (A) After soaking in deionized water for a sufficient length of time, films of micropatterned 1002F can be removed by applying a razor blade at the film corner and then gently lifting with laboratory forceps. (B) The resulting film is flat and undamaged. (C) If the soaking time is insufficient, films can still be removed from the substrate, but may be damaged in the removal process, leading to the introduction of “shear” lines (noted by the white arrows) in the films. These “shear” lines are permanent bends in the film and prevent the film from lying flat. Scale bars: 25 mm.

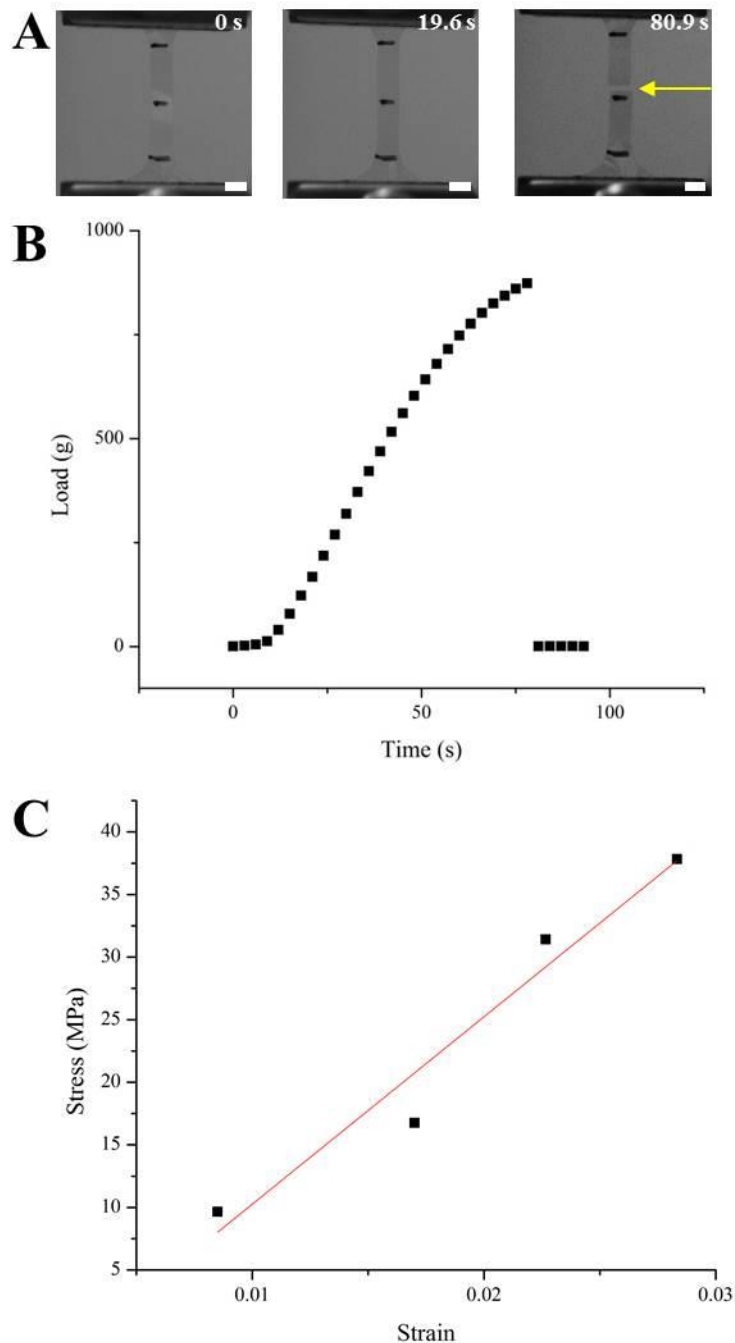


**Figure 2.4.** Tensile testing of freestanding, released 1002F films. Dogbone-shaped, freestanding 1002F films were subjected to tensile testing. (A) Image time series of a dogbone film undergoing testing at indicated times. Yellow arrow indicates linear break in the film just after mechanical failure at 80.9 s. Scale bars: 3 mm. (B) Time course load applied to film in (A) for calculation of its ultimate tensile strength. (C) Elastic region stress-strain plot for film tested in (A) for determination of the film's Young's Modulus. Multiple (n=4) films were tested in this fashion to obtain mean values for the Young's Modulus and ultimate tensile stress.

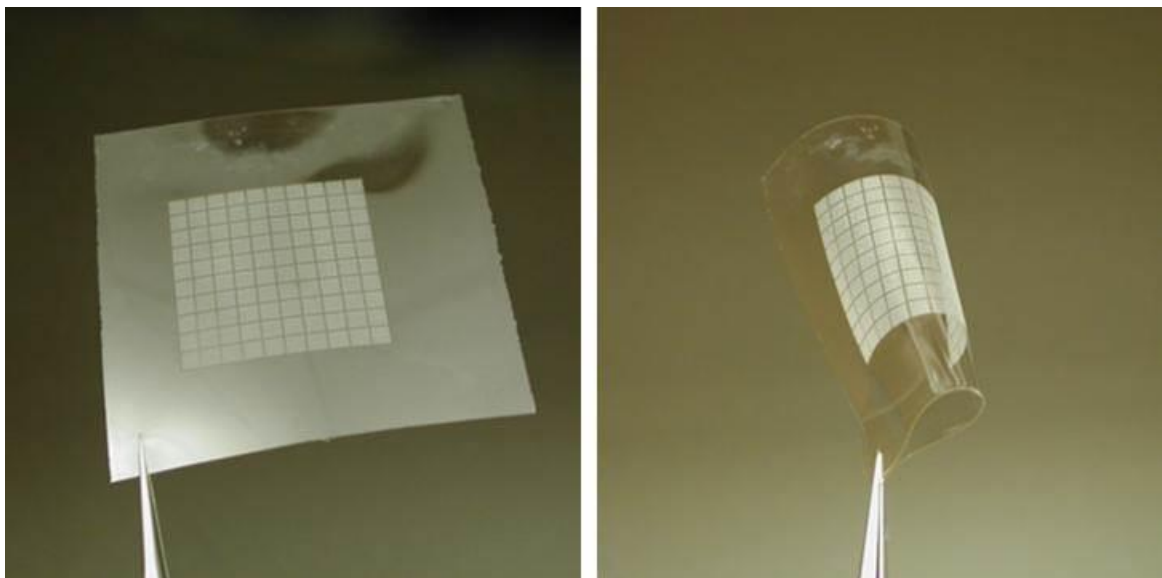


**Figure 2.5.** Flexibility of freestanding 1002F films. Freestanding 1002F photoresist films demonstrated flexibility and mechanical resilience. Images above show 25 mm x 25 mm 1002F films 50  $\mu\text{m}$  thick, patterned with an array of  $10^4$  circular wells 75  $\mu\text{m}$  in diameter, released from the fabrication substrate. Films would readily lie flat (A) but could be manipulated (B) without damage to the film. The films returned to their original flat orientation after manipulation.

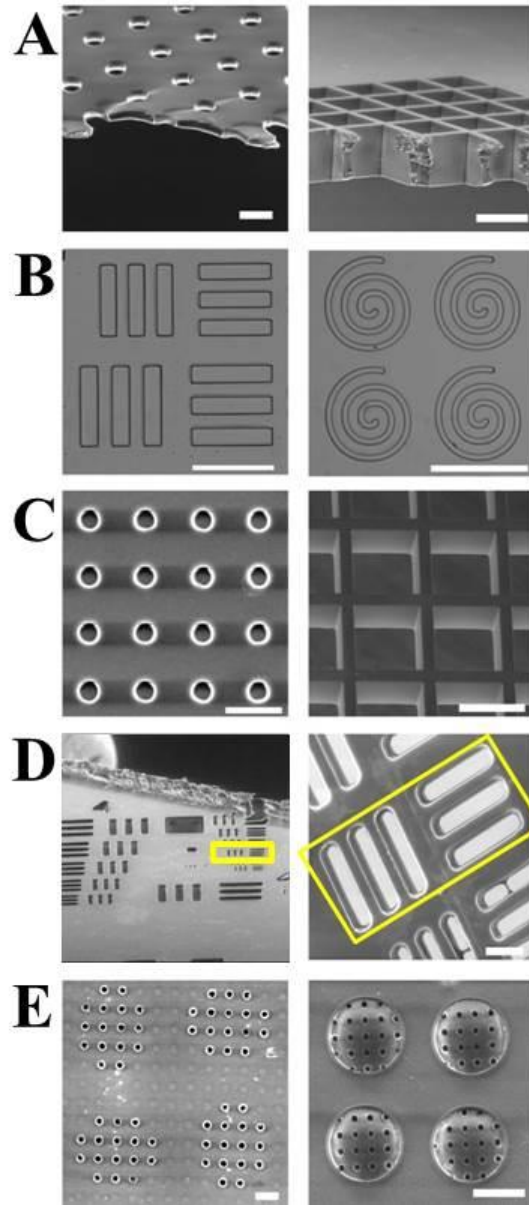


**Figure 2.6.** Fabrication versatility of photoresist films. 1002F films can be fabricated with a variety of thicknesses (A), through-hole shapes (B), and through-holes sizes (C). The film in (D) demonstrates an aspect ratio of 6:1. (E) Films with multiple layers each carrying a different pattern could be fabricated. Scale bars (left to right, top to bottom): 20, 200, 275, 625, 15, 250, 250, 25, 20, 50  $\mu\text{m}$ .

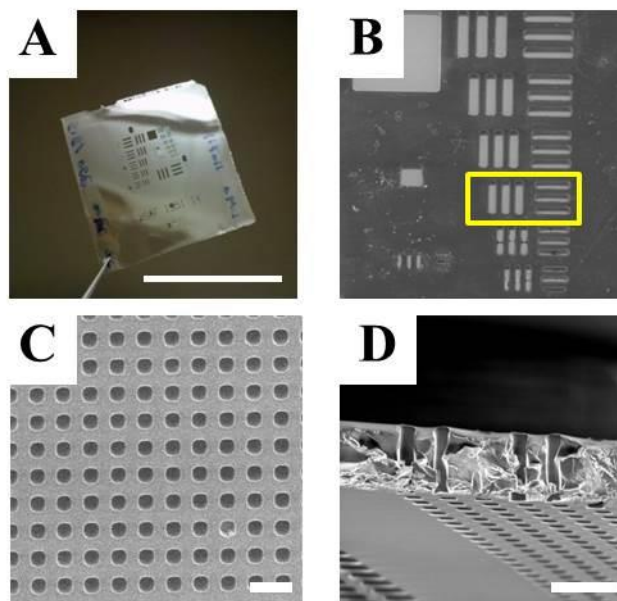


**Figure 2.7.** Formation of high-aspect ratio through-holes in 1002F photoresist films. 1002F photoresist films could be fabricated with through-holes with aspect ratios as high as 6:1 for rectangular through-holes and 4.5:1 for square through-holes. (A) A 70  $\mu\text{m}$ -thick film of 1002F patterned with the 1951 USAF Resolution Target. The film is structurally stable even in areas with holes of millimeter size. (B) Scanning electron micrograph of the film shown in (A) illustrating the smallest size trench that was resolved (level 5-4, 11.0  $\mu\text{m}$  in width), an aspect ratio of 6.36 : 1. (C) A 45  $\mu\text{m}$ -thick film of 1002F is shown with through-holes 10  $\mu\text{m}$  in diameter. (D) A 100  $\mu\text{m}$ -thick film of 1002F is shown with through-holes 25  $\mu\text{m}$  to a side, illustrating an aspect ratio of 4:1. Scale bars: 25mm, 100  $\mu\text{m}$ , 30  $\mu\text{m}$ , 100  $\mu\text{m}$ .

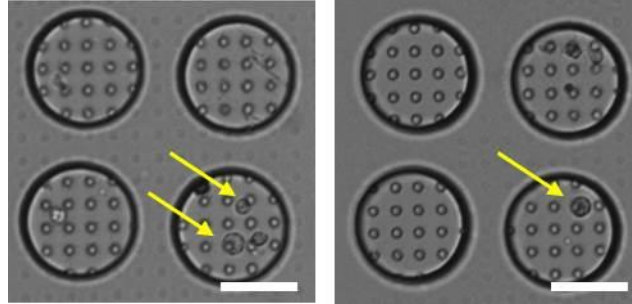


**Figure 2.8.** Seeding of AT1-like cells into microstrainers. Primary AT2 cells were seeded onto microstrainers with wells 75  $\mu\text{m}$  in diameter featuring pores 5.0  $\mu\text{m}$  in diameter. Cells were seeded at low density increase the probability of seeding only a single cell per well. Wells from two regions of the film are shown. Scale bars: 50  $\mu\text{m}$ .

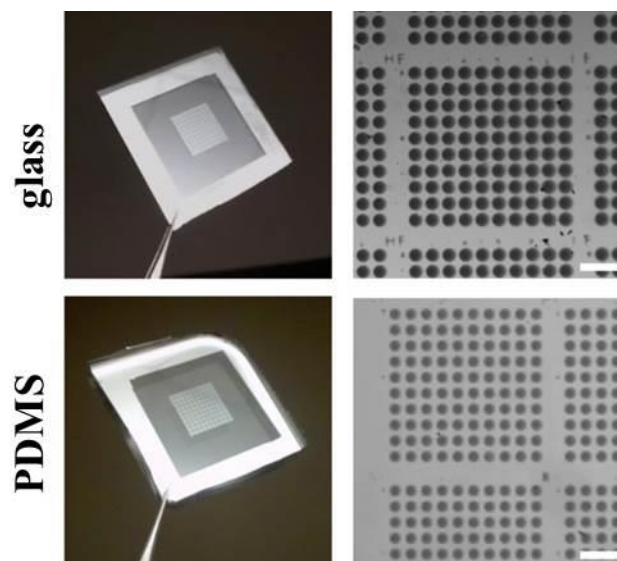


**Figure 2.9.** Use of 1002F film as a stencil. Glass (top panels) and PDMS (bottom panels) were patterned with Au:Pd (20-nm thick layer) through a 1002F stencil. Macroscopic images of the sputtered substrates are shown in the left column (scale bars, 200  $\mu\text{m}$ ), while brightfield microscopic images are displayed in the right column. The macroscopic film is 25 x 25 mm.

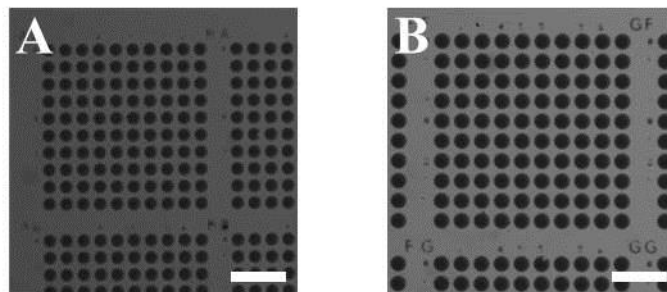


**Figure 2.10.** Application of photoresist thin films as inexpensive, re-usable stencils for metal deposition. (A) A glass substrate (25 mm x 25 mm, 50- $\mu$ m thick) was sputtered with an array of Au:Pd circles (20 nm thick, 75  $\mu$ m diameter) using a 1002F stencil. (B) Re-use of the same 1002F stencil to create a second Au:Pd-patterned glass slide. Scale bars: 250  $\mu$ m.

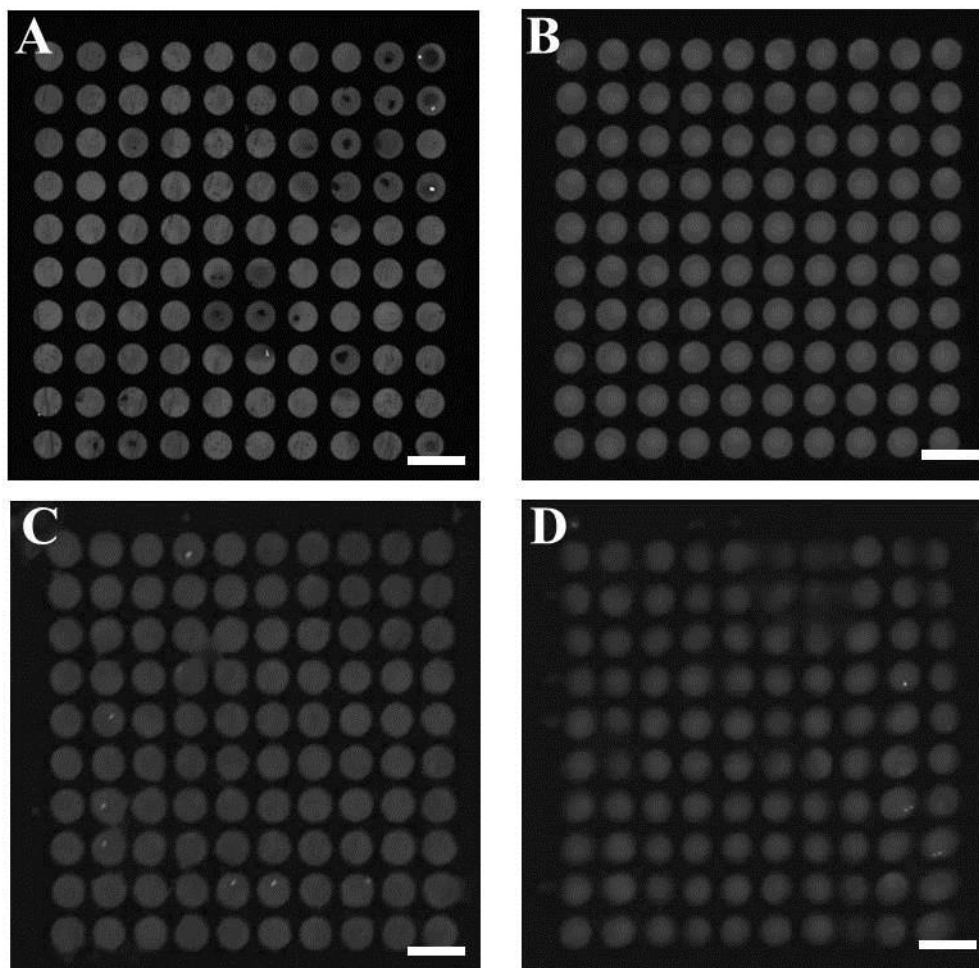


**Figure 2.11.** Protein surface micropatterning using freestanding microarray 1002F films as stencils. 1002F arrays with 75  $\mu\text{m}$ -diameter microwells and a solution of rhodamine B-conjugated BSA (50  $\mu\text{g}/\text{mL}$ ) were used to micropattern BSA onto solid supports. An unreleased array was first used to micropattern BSA onto the glass fabrication substrate (A), after which the film was released. The film was subsequently bonded to PDMS (B) or other glass (C) or polystyrene (D) supports and for protein micropatterning on these surfaces. Scale bars: 150  $\mu\text{m}$ .

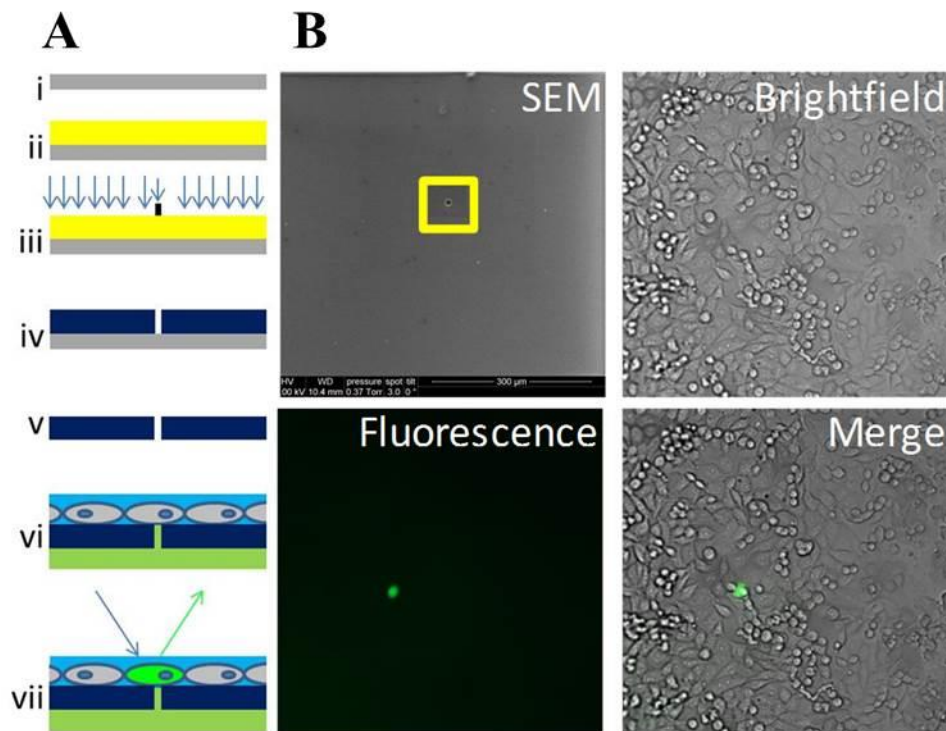


**Figure 2.12.** 1002F films for loading exogenous molecules into single cells in a monolayer. (A) Schematic illustration of fabrication, cell seeding, and cell staining: a film of 1002F photoresist with a single through-hole, 10  $\mu\text{m}$  in diameter, is fabricated and released (i-v). H1299 cells were seeded onto the film and allowed to grow to confluency, at which time media containing 10  $\mu\text{M}$  calcein AM dye was supplied to the lower compartment in order to load only the cell spanning the through-hole (vi). The film was then imaged at the site of the pore under brightfield and epifluorescence conditions(vii). (B) Images of the 1002F film with a single through-hole. SEM micrograph shows the location of the single through-hole; brightfield micrograph shows a confluent layer of H1299 cells; fluorescence micrograph shows a single cell spanning the through-hole that has been loaded with the calcein dye; brightfield and fluorescence images have been merged to illustrate the single fluorescent cell in the monolayer.

**Table 2.1.** Process parameters for 1002F photoresist films

Resist formulation	1002F-10			1002F-50			1002F-100		
	5	10	50	75	125	95	135	225	
Desired film thickness ( $\mu\text{m}$ )	5	10	50	75	125	95	135	225	
Spin-coating step 1 (rpm/sec) <sup>a</sup>	500/10	500/10	500/10	500/10	500/10	500/10	500/10	500/10	
Spin-coating step 2 (rpm/sec)	3100/30	2000/30	2100/30	1500/30	1000/30	2000/30	1500/30	1000/30	
Soft-bake 95°C (min)	5	10	50	75	90	100	100	100	
UV exposure ( $\text{mJ}/\text{cm}^2$ )	215	240	300	350	475	500	525	550	
Post-exposure bake step 1- 95°C (min)	3	4	5	5	5	5	5	5	
Post-exposure bake step 2- 120°C (min)	3	4	5	5	5	5	5	5	
Develop (min)	0.25 <sup>b</sup>	0.33 <sup>b</sup>	5	6	7	7	7	11	
Resolution ( $\mu\text{m}$ ) <sup>c</sup>	5	5	10	25	75	25	50	150	

<sup>a</sup> Laurell Technologies Corp., Model WS-400B-6NPP/Lite spin coater

<sup>b</sup> Denotes development by gentle rinsing

<sup>c</sup> Films made with 1002F-10 were patterned using chrome masks with square or circular features from 5 to 15  $\mu\text{m}$  (diameter or side length, respectively). Films made with 1002F-50 or 1002F-100 were patterned with a single chrome mask with square features in a range of sizes (10, 25, 50, 75, 100, 150, 175, 200, 250  $\mu\text{m}$ ).

**Table 2.2.** Removal of 1002F films by immersion in water

<b>Time (h)</b>	<b>Undamaged (%)<sup>a</sup></b>	<b>Damaged (%)<sup>a</sup></b>	<b>Non-removable (%)<sup>a</sup></b>
1	7 ± 12*	20 ± 34	73 ± 31
2	40 ± 17	60 ± 17	0 ± 0
4	87 ± 12	13 ± 12	0 ± 0
8	93 ± 12	6 ± 12	0 ± 0
12	100 ± 0	0 ± 0	0 ± 0

<sup>a</sup>Average ± standard deviation (n = 3 independent trials with 20 films/trial)

**Table 2.3.** Mechanical properties of 1002F films

Replicate	Young's Modulus (GPa)	Ultimate Tensile Stress (MPa)	% elongation
1	1.53	56.8	4.36
2	1.12	51.1	5.45
3	1.50	57.5	5.10
4	1.56	52.7	5.31
Mean	1.43	54.5	5.05
Std. Dev.	0.21	0.31	0.48

## 2.6 REFERENCES

1. Y. Wang, C. E. Sims, P. Marc, M. Bachman, G. P. Li, and N. L. Allbritton. "Micropatterning of Living Cells on a Heterogeneously Wetted Surface." *Langmuir*. **2006**, 22, 8257-8262.
2. W. Xu, C. E. Sims, and N. L. Allbritton. "Microcup arrays for the efficient isolation and cloning of cells." *Anal Chem*. **2010**, 82, 3161-7.
3. J. H. Pai, W. Xu, C. E. Sims, and N. L. Allbritton. "Microtable arrays for culture and isolation of cell colonies." *Anal Bioanal Chem*. **2010**, 398, 2595-604.
4. A. Webster, J. Greenman, and S. J. Haswell. "Development of microfluidic devices for biomedical and clinical application." *J Chem Technol Biot*. **2011**, 86, 10-17.
5. H. Becker, and L. E. Locascio. "Polymer microfluidic devices." *Talanta*. **2002**, 56, 267-87.
6. S. P. Desai, B. M. Taff, and J. Voldman. "A photopatternable silicone for biological applications." *Langmuir*. **2008**, 24, 575-81.
7. A. Folch, B. H. Jo, O. Hurtado, D. J. Beebe, and M. Toner. "Microfabricated elastomeric stencils for micropatterning cell cultures." *J Biomed Mater Res*. **2000**, 52, 346-53.
8. T. Y. Chang, V. G. Yadav, S. De Leo, A. Mohedas, B. Rajalingam, C. L. Chen, S. Selvarasah, M. R. Dokmeci, and A. Khademhosseini. "Cell and protein compatibility of parylene-C surfaces." *Langmuir*. **2007**, 23, 11718-11725.
9. M. J. Madou. *Fundamentals of Microfabrication: The Science of Miniaturization*. 2nd ed. CRC Press: Boca Raton. 2002.
10. J. M. Shaw, J. D. Gelorme, N. C. LaBianca, W. E. Conley, and S. J. Holmes. "Negative photoresists for optical lithography." *IBM J Res Dev*. **1997**, 41, 81-94.
11. C. Grant Willson, and B. C. Trinquet. "The Evolution of Materials for the Photolithographic Process." *Journal of Photopolymer Science and Technology*. **2003**, 16, 621-627.
12. T. Deng, H. Wu, S. T. Brittain, and G. M. Whitesides. "Prototyping of masks, masters, and stamps/molds for soft lithography using an office printer and photographic reduction." *Anal Chem*. **2000**, 72, 3176-80.
13. Y. Wang, C. Phillips, W. Xu, J. H. Pai, R. Dhopeswarkar, C. E. Sims, and N. Allbritton. "Micromolded arrays for separation of adherent cells." *Lab Chip*. **2010**, 10, 2917-24.

14. D. Huh, B. Matthews, A. Mammoto, M. Montoya-Zavala, H. Hsin, and D. Ingber. "Reconstituting Organ-Level Lung Functions on a Chip." *Science*. **2010**, 328, 1662-1668.
15. B. A. Peeni, D. B. Conkey, J. P. Barber, R. T. Kelly, M. L. Lee, A. T. Woolley, and A. R. Hawkins. "Planar thin film device for capillary electrophoresis." *Lab Chip*. **2005**, 5, 501-5.
16. G. J. Wang, Y. C. Lin, and S. H. Hsu. "The fabrication of PLGA microvessel scaffolds with nano-patterned inner walls." *Biomed Microdevices*. **2010**, 12, 841-8.
17. M. Geissler, J. M. McLellan, and Y. Xia. "Edge-spreading lithography: use of patterned photoresist structures to direct the spreading of alkanethiols on gold." *Nano Lett*. **2005**, 5, 31-6.
18. P. Lommens, D. Van Thourhout, P. F. Smet, D. Poelman, and Z. Hens. "Electrophoretic deposition of ZnO nanoparticles, from micropatterns to substrate coverage." *Nanotechnology*. **2008**, 19, 245301.
19. N. E. Hebert, B. Snyder, R. L. McCreery, W. G. Kuhr, and S. A. Brazill. "Performance of pyrolyzed photoresist carbon films in a microchip capillary electrophoresis device with sinusoidal voltammetric detection." *Anal Chem*. **2003**, 75, 4265-71.
20. H. Ogihara, M. Fukasawa, and T. Saji. "Method for Patterning Various Nanomaterials: Electrochemical Deposition of Patterned Ni Thin Films and Their Utilization as a Strippable Mask." *ACS Appl Mat Int*. **2011**, 3, 2108-2111.
21. J. Cho, H. Jang, B. Yeom, H. Kim, R. Kim, S. Kim, K. Char, and F. Caruso. "Modulating the pattern quality of micropatterned multilayer films prepared by layer-by-layer self-assembly." *Langmuir*. **2006**, 22, 1356-64.
22. S. L. Tao, K. C. Papat, J. J. Norman, and T. A. Desai. "Surface modification of SU-8 for enhanced biofunctionality and nonfouling properties." *Langmuir*. **2008**, 24, 2631-6.
23. L. A. Chrisey, C. E. O'Ferrall, B. J. Spargo, C. S. Dulcey, and J. M. Calvert. "Fabrication of patterned DNA surfaces." *Nucl Acid Res*. **1996**, 24, 3040-7.
24. Y. Erkan, I. Czolkos, A. Jesorka, L. M. Wilhelmsson, and O. Orwar. "Direct immobilization of cholesteryl-TEG-modified oligonucleotides onto hydrophobic SU-8 surfaces." *Langmuir*. **2007**, 23, 5259-63.
25. H. Sorribas, C. Padeste, and L. Tiefenauer. "Photolithographic generation of protein micropatterns for neuron culture applications." *Biomaterials*. **2002**, 23, 893-900.

26. C. S. Lee, S. H. Lee, S. S. Park, Y. K. Kim, and B. G. Kim. "Protein patterning on silicon-based surface using background hydrophobic thin film." *Biosens Bioelectron.* **2003**, *18*, 437-44.
27. J. Doh, and D. J. Irvine. "Photogenerated polyelectrolyte bilayers from an aqueous-processible photoresist for multicomponent protein patterning." *J Am Chem Soc.* **2004**, *126*, 9170-1.
28. P. S. Petrou, M. Chatzichristidi, A. M. Douvas, P. Argitis, K. Misiakos, and S. E. Kakabakos. "A biomolecule friendly photolithographic process for fabrication of protein microarrays on polymeric films coated on silicon chips." *Biosens Bioelectron.* **2007**, *22*, 1994-2002.
29. B. S. Flavel, A. J. Gross, D. J. Garrett, V. Nock, and A. J. Downard. "A simple approach to patterned protein immobilization on silicon via electrografting from diazonium salt solutions." *ACS Appl Mat Int.* **2010**, *2*, 1184-90.
30. S. D. Psoma, P. D. van der Wal, O. Frey, N. F. de Rooij, and A. P. Turner. "A novel enzyme entrapment in SU-8 microfabricated films for glucose micro-biosensors." *Biosens Bioelectron.* **2010**, *26*, 1582-7.
31. M. Agirregabiria, F. J. Blanco, J. Berganzo, M. T. Arroyo, A. Fullaondo, K. Mayora, and J. M. Ruano-Lopez. "Fabrication of SU-8 multilayer microstructures based on successive CMOS compatible adhesive bonding and releasing steps." *Lab Chip.* **2005**, *5*, 545-52.
32. Y. Sun, P. T. Vernier, M. Behrend, L. Marcu, and M. A. Gundersen. "Electrode microchamber for noninvasive perturbation of mammalian cells with nanosecond pulsed electric fields." *IEEE Trans Nanobioscience.* **2005**, *4*, 277-83.
33. M. Agirregabiria, F. J. Blanco, J. Berganzo, A. Fullaondo, A. M. Zubiaga, K. Mayora, and J. M. Ruano-Lopez. "SDS-CGE of proteins in microchannels made of SU-8 films." *Electrophoresis.* **2006**, *27*, 3627-34.
34. G. T. Salazar, Y. Wang, G. Young, M. Bachman, C. E. Sims, G. P. Li, and N. L. Allbritton. "Micropallet arrays for the separation of single, adherent cells." *Anal Chem.* **2007**, *79*, 682-7.
35. Y. Wang, G. Young, M. Bachman, C. E. Sims, Li, and N. L. Allbritton. "Collection and Expansion of Single Cells and Colonies Released from a Micropallet Array." *Anal Chem.* **2007**, *79*, 2359-2366.
36. K. D. Barbee, A. P. Hsiao, M. J. Heller, and X. Huang. "Electric field directed assembly of high-density microbead arrays." *Lab Chip.* **2009**, *9*, 3268-74.

37. L. Alan M. "Photodefinable carbon films: Electrical properties." *J Non-Cryst Solids*. **1985**, *70*, 99-109.
38. J. Kim, X. Song, K. Kinoshita, M. Madou, and R. White. "Electrochemical Studies of Carbon Films from Pyrolyzed Photoresist." *J Electrochem Soc*. **1998**, *145*, 2314-2319.
39. S. Ranganathan, R. McCreery, S. M. Majji, and M. Madou. "Photoresist-Derived Carbon for Microelectromechanical Systems and Electrochemical Applications." *J Electrochem Soc*. **2000**, *147*, 277-282.
40. S. Ranganathan, and R. L. McCreery. "Electroanalytical performance of carbon films with near-atomic flatness." *Anal Chem*. **2001**, *73*, 893-900.
41. H. Lorenz, M. Despont, N. Fahrni, N. LaBianca, P. Renaud, and P. Vettiger. "SU-8: a low-cost negative resist for MEMS." *J Micromech Microeng*. **1997**, *7*, 121-124.
42. R. Feng, and R. J. Farris. "Influence of processing conditions on the thermal and mechanical properties of SU8 negative photoresist coatings." *J Micromech Microeng*. **2003**, *13*, 80-88.
43. H. S. Khoo, K. K. Liu, and F. G. Tseng. "Mechanical strength and interfacial failure analysis of cantilevered SU-8 microposts." *J Micromech Microeng*. **2003**, *13*, 822-831.
44. P. Abgrall, C. Lattes, V. Conederal, X. Dollat, S. Colin, and A. M. Gue. "A novel fabrication method of flexible and monolithic 3D microfluidic structures using lamination of SU-8 films." *J Micromech Microeng*. **2006**, *16*, 113-121.
45. K. Sidler, L. G. Villanueva, O. Vazquez-Mena, V. Savu, and J. Brugger. "Compliant membranes improve resolution in full-wafer micro/nanostencil lithography." *Nanoscale*. **2012**, *4*, 773-778.
46. S. Ghadarghadr, C. P. Fucetola, L. Lee Cheong, E. E. Moon, and H. I. Smith. "3D nanostructures by stacking pre-patterned fluid-supported single-crystal Si membranes." *Journal of Vacuum Science & Technology B: Microelectronics and Nanometer Structures*. **2011**, *29*, 06F401-06F401-3.
47. K. Du, Y. Liu, I. Wathuthanthri, and C.-H. Choi. "Dual applications of free-standing holographic nanopatterns for lift-off and stencil lithography." *Journal of Vacuum Science & Technology B: Microelectronics and Nanometer Structures*. **2012**, *30*, 06FF04.
48. Y. Wang, R. Dhopeswarkar, R. Najdi, M. L. Waterman, C. E. Sims, and N. Allbritton. "Microdevice to capture colon crypts for in vitro studies." *Lab Chip*. **2010**, *10*, 1596.

49. A. L. McPherson, and G. M. Walker. "A photo-defined membrane for precisely patterned cellular and microparticle arrays." *AIP Adv.* **2012**, 2, 012153.
50. J.-H. Pai, Y. Wang, G. T. A. Salazar, C. E. Sims, M. Bachman, G. P. Li, and N. L. Allbritton. "Photoresist with Low Fluorescence for Bioanalytical Applications." *Anal Chem.* **2007**, 79, 8774-8780.
51. R. F. Gonzalez, and L. G. Dobbs. "Isolation and culture of alveolar epithelial Type I and Type II cells from rat lungs." *Methods in Molecular Biology.* **2013**, 945, 145-59.
52. J. Gao, L. Guan, and J. Chu. "Determining the Young's modulus of SU-8 negative photoresist through tensile testing for MEMS applications." *Proc SPIE 7544, Sixth International Symposium on Precision Engineering Measurements and Instrumentation.* **2010**, 754464-754464.
53. H. S. Noh, K. S. Moon, A. Cannon, P. J. Hesketh, and C. P. Wong. "Wafer bonding using microwave heating of parylene intermediate layers." *J Micromech Microeng.* **2004**, 14, 625-631.
54. J. C. Lotters, W. Olthuis, P. H. Veltink, and P. Bergveld. "The mechanical properties of the rubber elastic polymer polydimethylsiloxane for sensor applications." *J Micromech Microeng.* **1997**, 7, 145-147.
55. D. Wright, B. Rajalingam, J. M. Karp, S. Selvarasah, Y. Ling, J. Yeh, R. Langer, M. R. Dokmeci, and A. Khademosseini. "Reusable, reversibly sealable parylene membranes for cell and protein patterning." *J Biomed Mater Res.* **2008**, 85A, 530-538.
56. D. Fuard, T. Tzvetkova-Chevolleau, S. Decossas, P. Tracqui, and P. Schiavone. "Optimization of poly-di-methyl-siloxane (PDMS) substrates for studying cellular adhesion and motility." *Microelectron Eng.* **2008**, 85, 1289-1293.
57. M. L. Fulcher, S. Gabriel, K. A. Burns, J. R. Yankaskas, and S. H. Randell. "Well-differentiated human airway epithelial cell cultures." *Methods Mol Med.* **2005**, 107, 183-206.
58. S. M. Yi, S. H. Jin, J. D. Lee, and C. N. Chu. "Fabrication of a high-aspect-ratio stainless steel shadow mask and its application to pentacene thin-film transistors." *J Micromech Microeng.* **2005**, 15, 263-269.

## **Chapter 3: Co-fabrication of 1002F and chitosan for freestanding films of permeable-bottomed microwell arrays**

### **3.1 Introduction**

#### **3.1.1 General considerations**

As demonstrated in Chapter 2, films of micropatterned 1002F can be reliably micropatterned and released from the fabrication substrate to give a freestanding film. However, when seeded into microstrainers patterned with 5.0  $\mu\text{m}$  pores, AT2 cells failed to transdifferentiate and assume an AT1-like morphology, a trait they exhibit on certain other surfaces when seeded at low-density. Therefore, a different approach is needed for creating a permeable bottom to the microwell onto which primary AT1 cells are to be seeded and grown under ALI conditions. This chapter presents a method to co-fabricate a micropatterned and freestanding 1002F photoresist film with a film of the hydrogel chitosan to create a freestanding array of permeable, hydrogel-bottomed microwells. In addition to its potential for growing cells under an ALI, a microwell platform that incorporates a permeable support presents an additional utility: the analysis of cellular heterogeneity.

#### **3.1.2 Analysis of cellular heterogeneity**

Heterogeneity among the various cells in a biological system is emerging as an important subject area of biomedical research, with applications in cancer biology, immunology, stem cell biology and regenerative medicine.<sup>1-8</sup> The end goal of such

studies is to translate data describing biochemical or genetic differences between cells, even cells with similar physiologic roles and lineages, into models that explain how those differences affect the overall cellular phenotype and function. In order to detect differences between cells in a representative population, the analytical method must easily identify and differentiate between physically similar but nonetheless biochemically different cells within a population. If the analytical method lacks sufficient power to achieve this, however, then the cells must be separated to a degree that differences can be detected while preserving as much of the *in vivo* physiology as possible.

While a number of methods are currently available for analyzing cellular heterogeneity, limitations in each method exist.<sup>9-11</sup> Limiting dilution, such as on 384-well plates, is a well-established method for the isolation, clonal expansion, and analysis of different cells from a population. While this method can be used to isolate even single cells, there is significant labor and cost involved in this, resulting in low overall throughput. Flow cytometry, another widely used approach, can generate a large amount of data, but is limited to a single interrogation step, unless the cells are sorted via the accompanying fluorescence-activated cell sorting (FACS) technology. Even so, this approach demands that cells be dislodged, a preparatory step that can alter the physiology of the cells and possibly induce cellular apoptosis, creating the need for large numbers of cells to achieve a sufficient recovery of cells.<sup>12-15</sup> FACS can also lead to cell physiology changes due to the charged nature of the sorting apparatus. Furthermore, this approach cannot differentiate between individual cells once they have been sorted. While certain high-throughput technologies, namely microtiter plates that reduce the number of cells studied per well, have led to improved understanding of cellular heterogeneity, very often these platforms simply increase

the number of compartments analyzed per unit area and do not offer advances in the ability to discriminate between different cells – only different responses from different wells.

### **3.1.3 Microfabricated platforms for analyzing cellular heterogeneity**

Microfabricated platforms allow the study of biological systems with unparalleled control of the physical and chemical microenvironment to which a cell or group of cells is exposed. Such technology permits precise customization of the shape, size, and surface chemistry of the area used for cell growth.<sup>16-19</sup> By achieving such control, researchers gain the ability to interrogate the mechanisms and regulation of fundamental cellular processes and to create novel bio-inspired platforms.<sup>20-24</sup>

In addition to the approaches described above, some types of microfabricated devices have been used to study cellular heterogeneity. Microwell arrays, typically constructed from polydimethylsiloxane (PDMS), can be used to array cells at low density into physically separate wells. However, biochemical crosstalk (in the form of secreted paracrine signaling molecules distributed by the culture media solution over the entire area of cell growth) and cell migration from one well to another can lead to confounded data, as readouts from different groups of cells are not guaranteed to constitute independent measurements.<sup>11, 25</sup>

While certain methods, such as overlaying a physical barrier onto microwells seeded with cells, can reduce such confounding, cell survival and viability can be compromised over the long term as cells consume the small quantities of culture media with which they are seeded.<sup>26</sup> Micropallet or micraft arrays, consisting of a large number of individual pedestal elements onto which cells can be seeded, can sometimes prevent physical migration of cells, but nonetheless do not eliminate biochemical crosstalk from distributed paracrine signals. Additionally, such platforms are ill-suited for nonadherent cells.<sup>11, 27-28</sup> Droplet microfluidics,

another approach for high-throughput cellular analysis, can rapidly assay large numbers of isolated cells, but long-term culture of cells in droplets is difficult due to reduced delivery of oxygen and nutrients.<sup>11, 29</sup> In addition, analytical reagents must be pre-loaded into the droplet with the cells and subsequent analyses based on data obtained in the initial screening are technically difficult to set up.<sup>30</sup>

Therefore, a platform that allows for user-customized interrogation of discrete numbers of cells, grown in a microenvironment tailored to mimic *in vivo* conditions, and yet isolated so as to improve the independence of measured responses, and yet still arrayed in a fashion that permits high-throughput analysis, would be a useful tool for analysis of cellular heterogeneity. It was recognized that the most common methods and materials in use in the microfabrication field – including soft lithography using polydimethylsiloxane (PDMS), photolithography using photoresists, injection molding using cyclic olefin co-polymer, among others – grow cells atop impermeable supports.<sup>31-34</sup> This led to the hypothesis that by incorporating a permeable layer into a microwell array, cells could be seeded and then physically confined in a permanent or semi-permanent fashion to the wells. The permeable layer would not only allow the cells to be maintained in culture long term, but would also allow analyses to be performed at times chosen by the user.

### **3.1.4 Chitosan**

Chitosan is a cationic polysaccharide composed of D-glucosamine and N-acetyl D-glucosamine derived from the chemical de-acetylation of chitin that has begun to see increased use in a number of biological applications.<sup>35-38</sup> Many of the chemical and physical properties of chitosan – including the tensile strength, moisture absorption, and degradability – have been well characterized.<sup>39-49</sup> Of note, the molecular structure of chitosan features a

free amine group in those saccharide units that have been deacetylated. This free amine group not only is responsible for chitosan's pH-dependent solubility, but also allows the conjugation of exogenous molecules to the polysaccharide chain.<sup>37, 50-51</sup> Chitosan has been shown to be biocompatible to a number of cell types, including endothelial, hepatic, and peripheral nerve cells and orthopedic tissues.<sup>52-56</sup> Chitosan can be manipulated to form hydrogels, porous scaffolds, and dry films.<sup>38, 47, 57</sup> Of particular interest were studies showing that drugs could freely diffuse across chitosan layers, suggesting that chitosan capsules and films are permeable at the nanoscale and therefore giving chitosan a potential role in drug and gene delivery systems.<sup>58-62</sup> A key feature of chitosan employed by some of these studies is the amine group, which protonates in a pH-dependent manner and induces swelling of the chitosan matrix, increasing its network pore size and permitting diffusion of drugs entrapped within. Recently, a microfluidic setup was utilized for the *in situ* generation of a semi-permeable chitosan microscaffold for the formation of bacterial biofilms.<sup>63-64</sup> Flowing liquid streams of chitosan (dissolved in pH 5 solution) and buffer (pH 10) were merged in a microfluidic channel, leading to precipitation of chitosan and the interface that created a hydrogel window at the convergence of the two fluid streams. Analysis of the film showed that it was semi-permeable, and subsequent modification with alginate allowed the deposition and culture of bacterial biofilms.

Due to its biocompatibility and pH-dependent solubility and swelling, chitosan presented potential for incorporation into a hybrid freestanding film with 1002F. Notably, pH-dependent protonation of the chitosan amine group allows tailoring of chitosan solution densities to viscosities that permit spin coating. Thus, the ability to co-fabricate chitosan and UV-micropatterned photoresist films to form a hybrid platform was investigated.

### 3.1.5 Overview

This chapter presents a method to co-fabricate a micropatterned and freestanding 1002F photoresist film with a film of the hydrogel chitosan to create a freestanding array of hydrogel-bottomed microwells. These films are shown to have optical properties ideal for microscopy applications, and the chitosan layers are shown to be semi-permeable with a molecular exclusion of  $16.2 \pm 6.3$  kDa. By seeding cells into the microwells, overlaying a layer of inert mineral oil, and supplying media on the bottom surface, cells could be physically isolated from one another but maintained in culture for at least 5 days. Use of this method, which reduces confounding biochemical crosstalk between cells and eliminates mixing of different clonal populations, will enable high-throughput studies of cellular heterogeneity with increased ability to customize dynamic interrogations compared to currently available technologies.

## 3.2 Experimental design

### 3.2.1 Materials

Chitosan (medium molecular weight),  $\gamma$ -Butyrolactone (GBL), photoresist developer (propylene glycol methyl ether acetate, PGMEA), toluidine blue, FITC-dextran (average molecular weights 4, 10, 20, 40, and 70 kDa), and mineral oil were purchased from Sigma-Aldrich (St. Louis, MO). EPON resin 1002F photoresist was obtained from Miller-Stephenson (Sylmar, CA). UVI-6976 photoinitiator (triarylsulfonium hexafluoroantimonate salts in propylene carbonate) was purchased from Dow Chemical (Torrance, CA). Polydimethylsiloxane (PDMS, Sylgard 184 elastomer kit) was obtained from Dow Corning (Midland, MI). Sulfosuccinimidyl 4-[N-maleimidomethyl]cyclohexane-1-carboxylate (sulfo-

SMCC) was obtained from Thermo Scientific (Rockford, IL). Chrome photolithography masks were designed in-house using TurboCAD software and printed by FineLine Imaging (Boulder, CO). RPMI 1640 medium, fetal bovine serum (FBS), penicillin/streptomycin, tetramethylrhodamine-conjugated BSA, and calcein AM red-orange were obtained from Life Technologies (Grand Island, NY). Wild type Ba/F3 cells were obtained from American Type Culture Collection (Manassas, VA). Transwell™ polystyrene cassettes, 12- and 24-mm in diameter and hereafter referred to as “cassettes,” were kind gifts from Dr. Brian Button at the Univ. of North Carolina School of Medicine.

### **3.2.2 Co-fabrication of freestanding 1002F:chitosan films**

Medium molecular weight chitosan was dissolved in 0.5% (w/w) acetic acid to a concentration of 2% (w/w). Dry films of chitosan were obtained by spin coating dissolved chitosan onto pre-cleaned, air plasma oxidized glass slides and baked at 95°C for 1 h. Following a 2-min air plasma treatment, micropatterned films of 1002F negative photoresist were fabricated atop the dry chitosan films as described previously.<sup>65</sup> Briefly, EPON resin 1002F negative photoresist, dissolved in GBL and mixed with UVI-6076 photoinitiator, was spin-coated atop the dry chitosan films to a desired thickness of 50 μm and soft-baked at 95°C to remove organic solvent. After exposure to UV light through a patterned chrome photomask, the hybrid film was given a post-exposure bake, first at 95°C and then at 120°C, and then developed in PGMEA to remove unpolymerized photoresist monomer. The resulting micropatterned hybrid film was hard-baked, first at 95°C and then at 120°C, to solidify the photoresist layer. After affixing a polystyrene cassette using a thin PDMS mortar layer, the chitosan layer was neutralized and the hybrid film released via incubation in a 0.1% (w/w) aqueous solution of sodium hydroxide. Precise process conditions for hybrid

films with a photoresist layer 50  $\mu\text{m}$  thick are identical to those previously reported, with the exception that the hybrid films were incubated in 0.1% (w/w) NaOH for 48 h before release.<sup>65</sup> Immediately after release, the hybrid films were gently washed with deionized water and the chitosan hydrogel layer was rehydrated by immersion in phosphate buffered saline (PBS) pH 7.4 for at least 12 hours before use.

### **3.2.3 Imaging**

Hybrid films were imaged using an FEI Quanta 200 FEG scanning electron microscope (SEM) with a shottky field emission gun, operated under low-vacuum conditions (0.38 torr) (Chapel Hill Analytical and Nanofabrication Laboratory (CHANL)). High-resolution images of the chitosan layer at the bottom of microwells in critical point-dried hybrid films were also obtained using a Hitachi S-4700 Cold Cathode Field Emission scanning electron microscope (CHANL). A Nikon Eclipse TE2000-U inverted fluorescence microscope was used to image films during diffusion and protein conjugation experiments and for all cellular analyses. Brightfield and fluorescence micrographs recorded with a cooled CCD camera (Photometrix Cool Snap fx, Roper Scientific, Tucson, AZ) controlled by NIS Elements software (Nikon, Melville, NY). Fluorescence micrographs were analyzed using Image J (NIH, Bethesda, MD).

### **3.2.4 Multi-layer fabrication**

Multi-layer 1002F:chitosan:1002F sandwich films were fabricated using a layer-by-layer approach. First, 1002F photoresist was spin-coated to a thickness of 25  $\mu\text{m}$  onto a clean glass slide. After UV exposure and post-exposure bake (see above section 3.2.1), the film was spin coated with chitosan hydrogel without developing away unpolymerized 1002F monomer. After a brief bake to remove chitosan aqueous solvent, the film was again spin

coated with 1002F to a thickness of 50  $\mu\text{m}$ , soft-baked, and UV exposed through a hexagonal photomask 0.38 cm to a side. After a post-exposure bake, the 3-layer sandwich film was incubated overnight in 0.1% (w/w) NaOH, and then gently released using laboratory forceps. The film was then subjected to a two-sided development to remove unpolymerized photoresist monomer. The sandwich films were then baked to remove lingering solvent and imaged by scanning electron microscopy.

### **3.2.5 Measurement of chitosan dry film thickness**

The thicknesses of dry chitosan films were determined via profilometry. After spin-coating chitosan solution onto clean glass slides and baking at 95°C for 1 h, dry films were scored with a razor to produce trenches in the dry films. Film thickness was determined by using a profilometer (KLA-Tencor P-15 Profilometer, KLA-Tencor, San Jose, CA) to measure the height difference between the dry film surface and the glass surface in the trenches.

### **3.2.6 Measurement of 1002F:chitosan film optical properties**

Glass coverslips were deposited into the wells of a 6-well polystyrene plate, and background absorbance spectra from 300-800 nm were obtained using a SpectraMax M5 microplate reader (Molecular Devices, Sunnyvale, CA). Dry films of chitosan were prepared above the same coverslips by spin-coating chitosan solution at 500 rpm and baking for 1 h at 95°C. Coverslips were then neutralized in 0.1% (w/w) NaOH for 30 min and rehydrated in 1X PBS at pH 7.4 for 1 h. Absorbance spectra from 300-800 nm for the dry films were obtained by measuring absorbance for the spin-coated coverslips and subtracting out the absorbance values obtained before spin coating. Six replicates were tested and replicates were averaged to give an average absorbance spectrum.

Measurement of fluorescence values for chitosan co-fabricated with 1002F was achieved using films fabricated as described above using chitosan spin coated at 500 rpm. After the baking step, either 1002F or the negative photoresist SU-8 was then spin-coated to a thickness of 50  $\mu\text{m}$ , and UV-micropatterned with 100  $\mu\text{m}$ -diameter wells as described above. After the fabrication process was complete, films were imaged using an inverted epifluorescence microscope equipped with UV (ex 340-380 nm / em 435-485 nm), GFP (ex 465-495 nm / em 515-555 nm), Texas Red (ex 522-592 nm / em 584-664 nm), and Cy5 (ex 588-668 nm / em 652-732 nm) Nikon filter sets. Quantitative fluorescence of the chitosan and photoresist layers in each wavelength set was measured using ImageJ to calculate the mean pixel intensity in the microwell spaces (for chitosan) and in the wall spaces (for the photoresists). Two films were measured for each of the two photoresists, and chitosan layers in all four hybrid films were measured. Two regions per film were analyzed in each wavelength set.

### **3.2.7 Diffusion testing**

1002F:chitosan hybrid films micropatterned with 900 100- $\mu\text{m}$  diameter wells were fabricated, affixed to 12-mm diameter polystyrene cassettes, oxidized for 2 min with an air plasma, and released as described above. The films were then placed into the macro-scale wells of a 12-well plate, suspended by the cassette approximately 1 mm from the well bottom. PBS was supplied into the cassette (upper) and the dish (lower) compartments at volumes (0.5 and 1.5 mL, respectively) recommended by the plate manufacturer to give an equal height between the two compartments. Either toluidine blue dye (MW 270 Da) or one of several FITC-dextran (average molecular weights 4, 10, 20, and 40 kDa) was supplied into the upper fluid compartment as bolus solutions in PBS to a final concentration of either

0.01% (w/w)(toluidine blue) or 200  $\mu\text{g}/\text{mL}$  (FITC-dextran). Rhodamine B-conjugate dextran (70 kDa) at a concentration of 200  $\mu\text{g}/\text{mL}$  was supplied as a high-MW, slow-transit negative control across the several experiments. Plates were covered to prevent evaporation, and incubated at room temperature. At regular time points, 60 and 15  $\mu\text{L}$  samples were taken from both the bottom and top (respectively) fluid compartments for analysis using a SpectraMax M5 microplate reader (Molecular Devices, Sunnyvale, CA). Seven different devices, representing four different fabrication batches of films, were tested in this manner. Commercially-available track-etch membranes with pores 400 nm in diameter (Corning Life Sciences, Tewksbury MA) was also tested as positive controls for dye diffusion. Toluidine blue concentrations were measured via absorbance at 633 nm, while FITC-dextran concentrations were measured via fluorescence (excitation 490 nm / emission 520 nm). Rhodamine B-dextran fluorescence was measured as well (excitation 545 nm / emission 580 nm).

Additional 1002F:chitosan hybrid films were micropatterned, affixed to polystyrene cassettes, and released as described above. The cassette (upper) compartment was then supplied with a solution containing 200  $\mu\text{g}/\text{mL}$  of both rhodamine B-dextran (a 70 kDa, negative diffusion control) and of one of several FITC-dextran (molecular weights 10, 20, or 40 kDa). After incubating for 1 min, the dextran mixture was carefully aspirated off so as to leave droplets of the dextran solution remaining in the hydrogel-bottomed microwells. After depositing 500  $\mu\text{L}$  of mineral oil into the cassette compartment to cover the microwell array and prevent evaporation, the cassette was placed into a well in a 12-well plate containing 1.5 mL of 1X PBS. At regular time intervals, fluorescence images of the microwell array were obtained with an inverted fluorescence microscope. Fluorescence micrographs were analyzed

using Image J to generate quantitative fluorescence values for each microwell. Hybrid films that had not been released and whose microwells were thus blind-ended were used as negative diffusion controls to correct for any photobleaching. Fluorescence values, averaged for each microwell, were used to construct a time course of dextran diffusion across the chitosan membrane and out of the well. Fluorescence of the negative control solute rhodamine B-conjugated dextran 70 kDa was measured independently of FITC-dextran fluorescence; microwells exhibiting diffusion of this negative control solute were counted as artifacts. Six microwell arrays were used for each molecular weight of FITC-dextran tested.

### **3.2.8 Calculation of diffusivity constant for chitosan membranes in 1002F:chitosan hybrid films**

Calculation of the diffusion constant (also known as the diffusivity) was achieved by modeling the plate wells in which the 1002F:chitosan hybrid films were incubated during each diffusion experiment as a closed, two-compartment system, separated by a membrane of fixed thickness  $h$  and permeable area  $A$ . similar to a model described by Lee *et al.*<sup>66</sup> The upper compartment, assigned the arbitrary designation “1” in this model, has a fixed volume  $V_1$  of 0.5 mL and serves as the “source” of the diffusing solute. The lower compartment (designated “2”), whose volume  $V_2$  is fixed at 1.5 mL of fluid, serves as the “sink” compartment into which the solute diffuses via movement through and across the chitosan membrane of fixed thickness  $h$  and area  $A$  in the hybrid film. Volumes of each compartment are based on the volumes of fluid supplied to them at the initiation of the diffusion experiment. The source compartment is supplied with diffusing solute to an initial concentration of  $C_1^0$ , while the sink compartment starting concentration,  $C_2^0$ , is assumed to be zero. The thickness of the membrane in the model, termed  $h$ , is the thickness of the

chitosan layer only, as diffusion is assumed to only occur through the chitosan layer, and not the 1002F layer, an assumption supported by early experiments (data not shown).

This diffusion model has two characteristics: first, compartments have finite and fixed volumes; and second, there is a finite amount of solute that is supplied to the source compartment. Hence, the amount of solute in the total system is fixed.

Furthermore, a number of assumptions are made regarding this system. The first assumption is that diffusion of solute through and across the membrane takes more time than diffusion of the solute within the liquid in each compartment (*i.e.* that the diffusion coefficient for the solute in the liquid is far greater than that of the coefficient for the same solute through the membrane). Hence, solutions in the compartments are assumed to be well-mixed and thus no concentration gradient exists within either compartment. Second, it is assumed that within the membrane itself, any gradient of solute concentration exists only in the  $z$ -direction (perpendicular to the membrane). Third, quasi-steady state is assumed for the membrane, postulating that the time for the solute concentration to stabilize to a linear profile in the  $z$ -direction is much shorter than the diffusion time through the membrane. Fourth, it is assumed that the diffusion coefficient for the solute in the membrane is not a function of its concentration. The fifth and final assumption is that there is no accumulation of solute at either membrane interface; hence the number of moles that enter the membrane from the source interface during any particular time period equals the number of moles that leave the membrane at the sink interface.

Assuming a linear profile for the gradient within the membrane under the quasi-steady state assumption, the concentration of solute within the membrane in the  $z$ -direction varies with  $z$  and can be written as:

Equation 3.1:

$$C_m = C_1 + (C_2 - C_1) * \frac{z}{h}$$

By applying Fick's First Law and the equation above to the membrane layer, the flux J can be written as:

Equation 3.2:

$$J = -D * \frac{dC}{dz} = -D * \left( \frac{C_2 - C_1}{h} \right)$$

Because the system is closed, the total number of moles of solute, N is fixed and is:

Equation 3.3:

$$N = C_1 V_1 + C_2 V_2 + A * \int_0^h C_m dz$$

By combining Equation 3.3 with Equation 3.1, the total number of moles can be re-written as:

Equation 3.4

$$N = C_1 \left( V_1 + \frac{Ah}{2} \right) + C_2 \left( V_2 + \frac{Ah}{2} \right)$$

By differentiating both sides with respect to time, the molar velocity is obtained:

Equation 3.5:

$$\frac{dN}{dt} = 0 = \frac{dC_1}{dt} \left( V_1 + \frac{Ah}{2} \right) + \frac{dC_2}{dt} \left( V_2 + \frac{Ah}{2} \right)$$

By expressing the molar velocity as a product of the molar flux and the area A, and applying the assumption about no accumulation of solute at either membrane interface, the molar velocity can be described as:

Equation 3.6:

$$JA = \frac{dC_2}{dt} \left( V_2 + \frac{Ah}{2} \right) = \frac{-dC_1}{dt} \left( V_1 + \frac{Ah}{2} \right)$$

Note that *Equation 3.3* can be re-arranged to give either of the following two equations:

*Equation 3.7:*

$$C_1 = \frac{N - C_2 \left( V_2 + \frac{Ah}{2} \right)}{\left( V_1 + \frac{Ah}{2} \right)}$$

or

*Equation 3.8:*

$$C_2 = \frac{N - C_1 \left( V_1 + \frac{Ah}{2} \right)}{\left( V_2 + \frac{Ah}{2} \right)}$$

By combining *Equation 3.4* above with *Equations 3.6* (molar velocity) and *3.2* (Fick's Law), a differential equation for  $C_2$  can be obtained:

*Equation 3.9:*

$$\frac{dC_2}{dt} = \frac{DAV}{h \left( V_1 + \frac{Ah}{2} \right) \left( V_2 + \frac{Ah}{2} \right)} * \left[ \frac{N}{V} - C_2 \right]$$

This derivation introduces a new term,  $V$ , where

*Equation 3.10:*

$$V = V_1 + V_2 + Ah$$

Similarly, *Equations 3.2, 3.4, and 3.6* can be combined to give a differential equation for  $C_1$ :

*Equation 3.11*

$$\frac{dC_1}{dt} = \frac{DAV}{h \left( V_1 + \frac{Ah}{2} \right) \left( V_2 + \frac{Ah}{2} \right)} * \left[ \frac{N}{V} - C_1 \right]$$

The similarities between the final differential equations for  $C_1$  and  $C_2$  make sense in light of Fick's First Law, which relates the flux to the first derivative of the concentration. Viewed from the sink compartment, the concentration of solute diffusing into the compartment begins low and rises rapidly before tapering off; thus, the first derivative of the concentration is initially strongly positive and levels off to become weakly positive at later time. Similarly, when viewed from the perspective of the source compartment, the concentration of solute diffusing out of the compartment begins high and rapidly decreases before tapering off as equilibrium is approached; thus, the first derivative of the concentration is initially strongly negative and levels off to become weakly negative at later time. This transition of the first derivative from a high magnitude (either positive or negative in sign) to a lower magnitude (again, either positive or negative in sign) is identical in both the source and sink compartments, and thus the differential equations describing the flux will appear similar. The only difference between them will therefore be the sign (positive or negative), and this is supplied by the direction in which the concentration ( $C_1$  or  $C_2$ ) changes.

Solving the differential equations for  $C_1$  or  $C_2$  by integration over time gives an expression for  $C_1$  or  $C_2$  that has only one unknown variable,  $D$ . Integrating the expression for  $C_2$  and applying initial conditions gives:

*Equation 3.12:*

$$C_2 = \frac{N}{V} - \left[ \frac{N}{V} - C_2^o \right] * e^{-\frac{D}{h*\tau}(t-t^o)}$$

where the term  $\tau$  (Greek tau, not to be confused with  $t$ , for time) is:

*Equation 3.13:*

$$\tau = \frac{\left( V_1 + \frac{Ah}{2} \right) \left( V_2 + \frac{Ah}{2} \right)}{AV}$$

Using natural logarithms on *Equation 3.12* linearizes it in terms of the time parameter  $t$ :

*Equation 3.14:*

$$-\frac{D}{h * \tau} (t - t^o) = \ln \left[ \frac{\left(\frac{N}{V} - C_2\right)}{\left(\frac{N}{V} - C_2^o\right)} \right]$$

*Equation 3.14* allows determination of the diffusion coefficient  $D$ , since values for all other variables are known:  $\tau$  and  $h$  depend on the membrane parameters,  $C_2^o$  and  $N$  are given by the experimental setup, and  $C_2$  is measured for a certain timepoint  $t$ . By plotting the natural logarithm value depicted at the right in *Equation 3.14* against time adjusted for the tau term (e.g.  $t/\tau$ ), the slope of the now-linearized data curve can be used to calculate the diffusion coefficient  $D$ :

*Equation 3.15:*

$$slope = \frac{D}{h}$$

Application of the above operations to the  $C_1$  equations gives an expression similar to

*Equation 3.14:*

*Equation 3.16:*

$$-\frac{D}{h * \tau} (t - t^o) = \ln \left[ \frac{\left(\frac{N}{V} - C_1\right)}{\left(\frac{N}{V} - C_1^o\right)} \right]$$

and a similar plot of the natural logarithm term on the right side of *Equation 3.16* against  $t/\tau$  will give *Equation 3.15*.

### 3.2.9 Spatially controlled protein conjugation

1002F:chitosan hybrid films micropatterned with 100- $\mu\text{m}$  diameter wells were fabricated, affixed to polystyrene cassettes as described above, and treated with an air plasma

for 2 min. Films were patterned with protein via a covalent coupling strategy using the reagent sulfo-SMCC. A sulfo-SMCC solution was prepared by dissolving 2 mg of sulfo-SMCC in 1.5 mL of 50 mM sodium phosphate, pH 7.4. The cassette compartment of the film was then supplied with 500  $\mu$ L of the sulfo-SMCC solution and incubated at room temperature for 40 minutes. After removing sulfo-SMCC solution and washing three times with PBS, activated films were imaged to measure fluorescence background and then incubated with 250  $\mu$ L of BSA-tetramethylrhodamine (0.1 mg/mL) for 40 minutes at room temperature in the dark. After aspirating away the protein solution and washing three times with PBS, films were imaged via fluorescence microscopy and the fluorescence within the microwell spaces was quantified. Unactivated 1002F:chitosan films were used as controls, and three films were used for each experimental group.

### **3.2.10 Isolated clonal expansion and analysis of heterogeneity of cell proliferation in entrapped, nonadherent cells**

Wild-type Ba/F3 cells were cultured in RPMI 1640 medium supplemented with penicillin/streptomycin and 10% fetal bovine serum. 1002F:chitosan hybrid films micropatterned with 100- $\mu$ m diameter wells were fabricated, affixed to 12 mm-diameter polystyrene cassettes, and released as described above. After ethanol sterilization, films were placed into 12-well plates filled in the bottom compartments with RPMI 1640 medium either containing or lacking 10% FBS. Ba/F3 cells were deposited into the cassette compartment at a density of  $1.5 \times 10^4$  cells /  $\text{cm}^2$ . After 20 minutes, microarrays were inspected via brightfield microscopy to confirm that cells had settled into the chitosan-bottomed microwells, at which point the media in the cassette (upper) compartment was carefully aspirated away and 200  $\mu$ L of filter-sterilized mineral oil was overlaid in order to trap the cells in medium droplets in the microwells. Cells were also seeded at the same density into

two additional sets of chitosan-bottomed microwell arrays fabricated with a design identical to that described above but not released (so as to yield blind-ended microwells). After cell seeding, one array set was left to incubate without removing the cell seeding media, while a second array set had its media removed and was overlaid with 200  $\mu$ L of sterile mineral oil. All arrays were imaged daily with brightfield microscopy to assess cell survival and/or proliferation. The number of cells present in each well was manually counted and recorded at daily time points.

### **3.2.11 Growth of AT1-like cells**

Primary human AT2 cells were obtained as a gift from Dr. Peter Bove of the Cystic Fibrosis Research and Treatment Center at the Univ. of North Carolina School of Medicine. Briefly, cells were harvested from human explant lungs obtained with patient consent under a protocol approved by the Univ. of North Carolina School of Medicine Institutional Review Board via elastase digestion of the distal airspaces as a modification of previously published protocols.<sup>67</sup> After negative immunoselection using magnetic beads to remove contaminating erythrocytes and macrophages, AT2 cells were seeded into arrays of chitosan-bottomed microwells 75  $\mu$ m in diameter at a density of  $1 \times 10^4$  cells per  $\text{cm}^2$ . Cells were monitored via brightfield microscopy for their ability to spread out and assume an AT1-like morphology. At day 9 of culture, cells were stained for 2 h with Hoescht 33342 (1  $\mu$ g/mL) and calcein AM red-orange (10  $\mu$ M) and imaged by brightfield and fluorescence microscopy.

### **3.2.12 Statistical testing**

Unless otherwise stated, all statistical analyses performed utilized the student t-test. Statistical significance was defined as  $p < 0.05$ .

## 3.3 Results and Discussion

### 3.3.1 Co-fabrication of freestanding 1002F:chitosan films

Freestanding 1002F:chitosan hybrid films were fabricated and micropatterned using the strategy depicted in Figure 3.1A. Briefly, the viscous chitosan solution was spin-coated onto plasma oxidized glass slides and baked to give dry chitosan films. After a second air plasma treatment, 1002F negative photoresist was spin-coated atop the dry chitosan films and soft-baked to remove organic solvent. After exposure to UV light through a patterned chrome photomask and chemical development to remove unpolymerized photoresist monomer, the hybrid films were hard-baked to solidify the photoresist layer. The resulting hybrid films, featuring an array of microwells patterned into the 1002F film and bottomed by a layer of chitosan, were released from the glass substrate by immersion in dilute aqueous NaOH. By affixing a polystyrene cassette and placing into a 6- or 12-well plate the films adopted a setup similar to commercially available Transwell™ permeable supports, in which a membrane (here, the chitosan layer) separates two compartments: an “upper” compartment that interfaced with the photoresist film and the microwells patterned into it, and the “lower” compartment that lay beneath the chitosan layer. Figure 3.1B depicts how the addition of the cassette established these compartments.

Scanning electron micrographs of the resulting released hybrid film, shown in Figure 3.2, illustrated how the thin chitosan layer forms a bottom to the microwells that are patterned from the photoresist layer. High-resolution scanning electron micrographs of the chitosan layer, shown in Figure 3.2C, revealed a uniform film approximately 400 nm thick composed of entangled chitosan polysaccharide chains with tortuous pores of irregular shape and diameters on the order of tens of nanometers. Figure 3.2D reveals the chitosan layer to

have a pebbled, irregular surface, again showing pores of irregular shape and diameters on the orders of tens of nanometers.

### **3.3.2 Multi-layer 1002F:chitosan:1002F sandwich films**

Early experiments with fabricating 1002F:chitosan hybrid films revealed that, when 1002F wells >500  $\mu\text{m}$  in diameter were fabricated atop chitosan films, the chitosan had a tendency to tear away from the well walls during release and remain on the glass fabrication substrate. Predicting that an underlying layer of micropatterned 1002F would enhance the structural stability of the chitosan layer when a larger well was patterned above, the ability to generate 1002F:chitosan:1002F sandwich films by delaying development of the patterned 1002F until after the film had been released was assessed. Figure 3.3A illustrates the fabrication scheme, in which a layer of 1002F spin coated atop a glass slide was UV-exposed and post-exposure baked but a development step to remove unpolymerized monomer was withheld. Chitosan hydrogel solution was then spin coated atop this layer.

Withholding the development step in the fabrication of the lower 1002F layer was based on the reasoning that subsequent baking steps would cause evaporation of the chitosan aqueous solvent and led to deposition of a thin, 400 nm-thick film of chitosan that would coat the microwell walls but neither fill the microwell space nor span it. This prediction was confirmed in trials in which a development step was included in the fabrication of the first 1002F layer.

After spin coating the chitosan layer and baking to remove its solvent, a second layer of 1002F was spin coated atop the dry chitosan film. UV exposure of this film through a mask with features of larger or equal, but not smaller, size than the first 1002F layer was followed by a post-exposure bake. Again development was withheld. Instead, the 2-layer

sandwich film was released after an overnight soaking in dilute NaOH, and unpolymerized 1002F monomer was removed from both sides of the sandwich film simultaneously by immersing in developer. Figure 3.3B shows scanning electron micrographs of the resulting sandwich film: the upper panel of micrographs shows the edge of a large hexagonal well 0.38 cm to a side, inside of which a chitosan layer of submicron thickness was visible. The underlying microwell pattern was faintly visible, similar to results shown in Figure 3.2B (chitosan-bottomed microwell arrays imaged from the lower compartment revealed the microwell pattern). When imaged from the opposite face, the microwell pattern of the first 1002F layer was clearly visible (Figure 3.2B, lower panel). In future endeavors, it might be expected that, due to the multiple baking steps involved after processing of the first 1002F layer, the sizes of the features in the lower layer of 1002F are likely to be reduced in comparison to the sizes of features in the mask, due to local diffusion of photoacid generator in the first 1002F layer. However, careful control of processing conditions can likely minimize these effects, which are expected to be less when features of the lower layer are larger in size. This application has the potential for generating sandwich films for patterned co-culture of two different cell types, one on each side of the chitosan membrane and able to be grown in two different patterns. An extension of this concept will be to create sandwich films that have the same pattern on both sides of the chitosan membrane using only a single mask and UV exposure step.

### **3.3.3 Chitosan hydrogel thickness measurements**

Several properties of the chitosan films prepared in this fabrication protocol were evaluated. First, the thicknesses of dry films spin-coated at various speeds were measured using profilometry. Figure 3.4 shows the thickness of dry films resulting from spin coating

chitosan at various speeds, suggesting that varied thicknesses of the chitosan layer (for such considerations as mechanical strength) can be achieved simply by varying the spin coating speed. Table 3.1 gives the thickness measurements of dry films generated from several spin coat speeds. Additional formulations of the chitosan solution with higher or lower concentrations of chitosan would be expected to give thicker or thinner films, respectively, based on identical spin coat speeds.

These results show that the thickness of a dry chitosan film fabricated by spin coating at the speed typically used in the co-fabrication protocol (2000 rpm) was  $349 \pm 24$  nm. Comparison of this thickness to the measured thickness of the chitosan layer in hybrid films that had been imaged after being released and rehydrated (see Figure 3.2C) reveals that released and rehydrated films are 12.5% thicker than dry films. This increase in thickness is likely due to slight osmotic swelling of the chitosan hydrogel layer that occurs in a pH-dependent manner<sup>68</sup>. Because the pH of the rehydrating solution is 7.4 (the pH requirement of cultured cells, for which these films will be used) and the amine groups on the chitosan become neutralized at higher pH (pKa 6.3), hydrogel theory predicts only slight equilibrium swelling at this pH, consistent with the results shown here.

It is worth pointing out that, given the submicron thickness of the alveolar basement membrane *in vivo*, thin hydrogel surfaces such as that of the chitosan layers used in this study may offer a more realistic replication of the alveolar basement membrane than commercially-available microporous supports used for cell culture, which are typically at least 10  $\mu$ m thick.<sup>69</sup> This feature of chitosan films may be useful for future studies of AT1 cells.

### 3.3.4 Optical properties

Because brightfield and especially fluorescence microscopy is anticipated to be a chief means of analyzing cells cultured on the 1002F: chitosan hybrid films, the absorption and autofluorescence of chitosan films were measured. Absorbance spectra of glass coverslips spin coated with chitosan at 500 rpm to a thickness of  $\sim 800 \mu\text{m}$ , shown in Figure 3.5A, revealed absorbance below 0.02 ( $\geq 95.5\%$  transmittance) for hydrated chitosan films at wavelengths above 400 nm. Because these films were thicker by a factor of  $\sim 2$  than chitosan layers in typically fabricated 1002F:chitosan hybrid films, absorbance of chitosan layers fabricated with the typical protocol is likely to be even less.

Fluorescence measurements of chitosan films  $\sim 800 \mu\text{m}$  in thickness similarly revealed that chitosan films had very low autofluorescence, compared to 1002F and especially SU-8 photoresists. The green wavelengths had the highest autofluorescence values: mean pixel intensity for chitosan films was  $63.8 \pm 2.6$ , whereas the 1002F layer ( $45 \mu\text{m}$  thick) had pixel intensities of  $840.5 \pm 126.6$  and the SU-8 layer ( $45 \mu\text{m}$  thick) had pixel intensities of  $4046.3 \pm 292.4$ . Figure 3.5B shows fluorescence values in four different filter sets commonly used in fluorescence microscopy for chitosan, 1002F, and SU-8. While there are significant differences in thickness between the chitosan and photoresist layers tested, the thickness of each layer reflects a typical thickness used in the hybrid photoresist:chitosan film, and so provides a useful comparison. Overall, the low absorption and autofluorescence of chitosan across the visible wavelengths suggest that microscopy-based methods for cellular analysis will be quite compatible with 1002F:chitosan hybrid films.

### 3.3.5 Diffusion testing of micropatterned 1002F: chitosan hybrid films

In order to determine whether solutes could diffuse across the chitosan layer at the bottom of the microwells in the 1002F:chitosan films, the permeability of the chitosan layer to small-molecule solute diffusion was first measured. A general diffusion scheme is depicted in Figure 3.6A. Freestanding chitosan:1002F hybrid films affixed to polystyrene cassettes were placed in a 12-well plate and PBS was supplied to the upper and lower compartments. Commercially-available Transwell™ track-etch membranes were used as positive controls. Addition of a bolus of concentrated dye to the upper compartment created a gradient to drive solute diffusion from the “source” compartment, across the chitosan membrane, and into the lower “sink” compartment.

Toluidine blue dye (MW 270 Da) seeded into the upper compartment was visually observed to enter and disperse throughout the lower compartment (Figure 3.6B). Quantitation of toluidine blue concentration in the lower compartment over time revealed that after 8 h, toluidine blue concentration was  $41.5 \pm 1.5$  % of its later maximal value in wells with 1002F:chitosan films and  $16.3 \pm 0.6$ % of the concentration in the top compartment, whereas the concentration in the positive control wells was  $51.4 \pm 0.1$ % of its maximal value and  $23.8 \pm 0.0$ % of the concentration in the top compartment. By 48 hr, toluidine blue concentration in wells with 1002F:chitosan membranes had reached  $90.8 \pm 3.2$ % maximal value and  $88.9 \pm 1.3$ % of the top compartment concentration, compared with  $90.9 \pm 0.9$ % and  $98.2 \pm 13.4$ % (respectively) for the positive control. Figure 3.6C illustrates the time course of absolute toluidine blue concentration in the lower compartment for 1002F:chitosan membranes and the Transwell™ positive control membranes. These data suggest that chitosan membranes have comparable permeability to small molecules as membranes with cylindrical track-etch

micropores, indicating that the chitosan hydrogel layer remained permeable to small molecules after the fabrication process was completed. Employing this same method with a high-MW FITC-conjugated dextran (MW 70 kDa) instead of toluidine blue dye, however, revealed that after 48 hours of incubation, the concentration of solute in the bottom compartment was only  $0.2 \pm 0.1\%$  of that in the top compartment, compared to a value of  $31.6 \pm 2.2\%$  for a positive control.

Given the possibility that the chitosan layer had a molecular exclusion limit, wherein solutes with molecular weights above the limit were unable to diffuse through the chitosan film, diffusion of solutes in a range of molecular weights was investigated. Fluorophore-conjugated dextrans are commercially available in several molecular weights and have been used in permeability studies of other membranes.<sup>66, 70</sup> Using the method described above, diffusion of FITC-conjugated dextrans of molecular weights 4, 10, 20, and 40 kDa were investigated. Figure 3.7 shows the concentration of each dextran, relative to its theoretical equilibrium concentration  $C_{eq}$ , over the course of time. Transwell™ membranes were used as positive controls in all experiments. Dextrans with molecular weights 4 and 10 kDa were shown to diffuse through chitosan membranes, reaching half-theoretical maximum values by 48 and 120 hr, respectively (Figure 3.7). Compared to those dextrans, diffusion of dextran with MW 20 kDa was greatly reduced, reaching  $C / C_{eq}$  value of only 0.2 after 5 days of incubation, and dextran with MW 40 kDa did not exhibit appreciable diffusion at all, consistent with earlier data that FITC-dextran with a higher MW of 70 kDa exhibited virtually no diffusion across the membrane. In all experiments except the positive controls, diffusion of 70 kDa rhodamine B-conjugated dextran was not observed, consistent with earlier results.

In order to further validate the above data, a method to track and measure molecular diffusion in individual wells in an ensemble fashion was devised. Depositing a solution containing FITC-conjugated dextran of a given molecular weight into the top compartment and then aspirating the solution away was found to cause the film surface to discontinuously de-wet, leading to the entrapment of droplets containing fluorescent dextran in the chitosan-bottomed microwells. Overlay of a layer of mineral oil to prevent water evaporation and immediately supplying an aqueous solution to the bottom compartment allowed the entire chitosan hydrogel layer and the microwells they bordered to remain hydrated. Via serial imaging of the well array, quantitative fluorescence values and hence dye concentration in each microwell were obtained, and time courses of dextran diffusion across the chitosan membrane and out of the well were generated. Because fluorophore-conjugated dextran with a molecular weight of 70 kDa was found to exhibit very slow transit across the chitosan layer (see above), rhodamine B-conjugated dextran (MW 70 kDa) was employed to identify microwells whose chitosan bottoms happened to contain a fabrication defect that would leakage of dye through the defect. Any microwell that exhibited movement of the 70 kDa rhodamine B-conjugated dextran across the chitosan layer and out of the microwell would be classified as an artifact and ignored.

Data generated in this fashion, shown in Figure 3.8, revealed that the chitosan films had defects at a rate of less than 0.1% of microwells observed, and were permeable to fluorescein and FITC-dextrans of molecular weights 4, 10, and 20 kDa. While fluorescein and FITC-dextran 4 kDa were qualitatively observed to traverse the membrane, quantitative data on their diffusion across the chitosan membrane could not be obtained, as these solutes diffused through the chitosan layer extremely rapidly, exiting the well within 60 seconds of

being loaded. Dextrans of average molecular weights 10 and 20 kDa reached half of their equilibrium values by 2 and 5 hours, respectively (Figure 3.8, first and second rows). By contrast, FITC-dextran 40 kDa exhibited no decline in fluorescence values (Figure 3.8, third row), consistent with data in Figure 3.7 showing no appreciable diffusion of FITC-dextran 40 kDa.

### **3.3.6 Calculation of diffusion coefficients and MW cutoffs for chitosan membranes in 1002F:chitosan hybrid films**

A mathematical model based on Fick's First Law and reported by Lee *et al.*<sup>66</sup> was used to calculate the diffusion coefficient,  $D$ , for dextrans of various molecular weights that exhibited diffusion through the chitosan membrane. Mathematical details are described in Section 3.2.8 above. Figure 3.9A illustrates the closed, two-compartment model used in these calculations, which resembles the overall layout of the Transwell™-type experimental setup employed here to test diffusion. Figure 3.9B shows a plot of diffusion coefficients determined using this model versus  $\log(\text{MW})$ . These values, which range in order of magnitude from  $10^{-9}$  to  $10^{-12}$   $\text{cm}^2 / \text{s}$  and are reported in Table 3.2, fall within the range of previously reported values for slow solute diffusion within a solid.<sup>71</sup> Lower molecular weight dextrans predictably had higher diffusion coefficients, and 40 kDa dextran was found to have a diffusivity a full order of magnitude less than that of 20kDa dextran. Fitting a line to the linear region of diffusion coefficients in this plot allows extrapolation to find the molecular weight that would give a zero-value diffusion coefficient, which is the theoretical molecular exclusion limit. Using this method, a theoretical molecular exclusion limit of  $16.2 \pm 6.3$  kDa was determined for the chitosan membrane in the 1002F:chitosan hybrid films. This value and range, at its minimum, agrees with the diffusion of 10 kDa-MW FITC-dextran observed here, and at its maximum, also agrees with observed diffusion of 20 kDa-MW FITC-dextran.

Additionally, the value appears to be in agreement with the failure to observe diffusion of 40- and 70 kDa MW dextrans through the membrane.

Two points are worth noting. First, the calculated molecular exclusion limit is a theoretical value based on a linear extrapolation, and so solutes with molecular weights higher than the theoretical cutoff can still exhibit measurable diffusion, a case also found in the data of Lee *et al.*<sup>66</sup> Second, it should be remembered that commercially-available FITC-dextrans, while nonetheless useful, include a range of molecular weights classified by their average. Therefore, it is entirely possible to observe diffusion of samples with an average molecular weight higher than the theoretical exclusion limit, as the observed diffusion may be due to solute molecules with weights on the lower end of the range (below the average).

However, this theoretical molecular exclusion limit, and the failure to observe diffusion of dextrans > 40 kDa, might seem at odds with previous reports describing the size of pores in chitosan microparticles or capsules as being 10  $\mu\text{m}$  or higher.<sup>38, 56</sup> Additionally, the Bentley Group reported that antibodies with a molecular weight greater than 150 kDa could permeate through chitosan membranes fabricated *in situ* on a microfluidic device.<sup>63</sup> However, the processing conditions under which chitosan membrane was formed in these other reports differ greatly from those reported here, in which chitosan membranes were required to be prepared as dry films in order to facilitate photoresist spin coating and UV photolithography. It is hypothesized that the processing steps employed in the fabrication process described here, especially the baking steps necessary for proper polymerization of the photoresist, lead to a high degree of entanglement and possibly even chemical crosslinking that reduce the network pore size and therefore lower the molecular exclusion size limit. While no reports of permeability through chitosan films that had been baked at

high temperatures could be found, two early reports describing permeability through chitosan films that had been dried reported the exclusion of solutes with molecular weights above 13 kDa, while permitting passage of solutes 2.9 kDa and lighter.<sup>72-73</sup> These early reports support the findings described here. It has not escaped notice that these results suggest two further applications for this platform. First, numerous possibilities exist to chemically modify the chitosan films in ways that may permit adjustment of the permeability. Second, the molecular exclusion limit presents opportunities for the selective entrapment of molecules with high molecular weights, such as growth factors, secreted reporters, or antibodies in the wells. Exploration of these questions is the subject of future research in this area.

### **3.3.7 Spatially controlled protein conjugation**

The free amine group in the molecular structure of chitosan has been used in numerous applications for conjugating exogenous molecules to chitosan surfaces<sup>37, 50-51</sup>. Hence, the potential to utilize the amine group to achieve spatially controlled molecular patterning was explored. Chitosan:1002F hybrid films micropatterned with 100- $\mu\text{m}$  diameter wells were patterned with protein via a covalent coupling strategy using the heterobifunctional crosslinker sulfo-SMCC, which allows conjugation of molecules with free amine moieties to molecules with free sulfhydryl moieties. Sulfo-SMCC supplied to the top compartment of released films was used to activate the chitosan surface lining the bottoms of the microwells, after which tetramethylrhodamine-conjugated BSA was supplied to the top compartment. Compared with unactivated films, sulfo-SMCC treated films exhibited a fold increase of 2.2 in average fluorescence within the microwells, suggesting that activation of the chitosan surface resulted in higher deposition of protein onto the microwell bottoms as compared to protein adsorption onto the same surface. It is noteworthy that this covalent

conjugation scheme, which uses the amine-to-sulfhydryl linker reagent sulfo-SMCC, can likely be adapted to utilize other crosslinkers, heterobifunctional or otherwise, or amine-reactive silanes in order to allow user-defined and spatially-controlled surface functionalizations that are selective for the chitosan layer at the bottom of the microwells. Additionally, because the conjugation scheme described here can be carried out either before or after film release, the potential exists to generate a heterofunctionalized chitosan membrane – with one set of exogenous molecules conjugated to the chitosan facing the upper compartment and another set of exogenous molecules conjugated to the chitosan facing the bottom compartment. Additionally, given the molecular weight cutoff for the chitosan films (see section above), it is possible that crosslinker reagents and conjugation molecules will diffuse throughout the film thickness, resulting in a film impregnated with covalently-bound exogenous molecules.

### **3.3.8 Survival and proliferation of nonadherent cells entrapped in chitosan-bottomed microwells**

Inspired by the success of the well-by-well diffusion monitoring tactic described above (see Figure 3.8), it was hypothesized that a similar setup, depicted in Figure 3.11A, would enable physical isolation of clonal cell populations without a loss of cell viability. By applying cells onto a microwell array at low density, microwells would be seeded with discrete numbers of cells. Subsequent aspiration of seeding medium would discontinuously de-wet the film surface, leaving discrete medium pockets containing cells in each microwell. Application of a mineral oil layer atop the array would physically entrap those cells within the well spaces. By also supplying culture medium to the compartment below the chitosan membrane, nutrients could be exchanged across the permeable chitosan film and cells could be maintained and clonally expanded within each microwell.

To first evaluate the ability of cells to survive when isolated into discrete medium pockets found within microwells, wild-type Ba/F3 cells, an immortalized non-adherent murine pro-B cell line derived from the marrow of C3H mice, were seeded onto patterned 1002F:chitosan hybrid films. After removal of seeding media and mineral oil overlay, media either containing or lacking FBS was supplied to the bottom compartment, and the arrays were imaged daily for the next three days. At 72 h in culture, cells entrapped within microwell arrays supplied with serum-positive media to the lower compartment remained viable and had begun to proliferate (Figure 3.11B). By contrast, cells entrapped within microwell arrays supplied with serum-free media to the lower compartment failed to proliferate and adopted a shrunken morphologic appearance consistent with apoptosis. These data are consistent with previous reports that the Ba/F3 cell line is dependent on serum growth factors or the cytokine IL-3 cytokine for survival, undergoing apoptosis upon serum or cytokine removal.<sup>74-75</sup> Therefore, the observed proliferation of cells in the presence of serum-positive media on the opposite side of the chitosan film and the failure of cells to proliferate when media was serum-free suggest that the chitosan membranes were functionally permeable to serum growth factors necessary for proliferation of the cells.

### **3.3.9 Isolation and expansion of clonal populations in discrete medium pockets**

To further demonstrate utility of this platform in isolating clonal populations of cells, wild type Ba/F3 cells were seeded onto the hybrid platform and isolated via oil overlay as described above. Clonal expansion of cells was monitored in comparison to cells seeded onto two control platforms. Each control platform was a 1002F:chitosan hybrid film that had not been released from the substrate and whose microwells were therefore blind-ended. In one control, cells were seeded and overlaid with mineral oil as on the test platform; in the second

control, cells were seeded and grown in media without any oil overlay. The first (oil-overlay) control exhibited no clonal expansion of cells (presumably due to either rapid depletion of nutrients from the ~400-pL microwell volume or poor delivery of oxygen)(Figure 3.12A). This was in sharp contrast to the second control, in which clonal expansion was observed. However, on this control, 0% (n = 62) of wells empty after the initial cell seeding remained empty by 48 hours (Figure 3.12B), suggesting that mixing of clonal populations was occurring. By comparison, cells grown on the released 1002F:chitosan hybrid platform and supplied with media also exhibited heterogeneous clonal expansion (Figure 3.12C). At the same time, however, there was no observed migration of cells into microwells that were empty after the initial cell seeding, unlike that observed in Figure 3.12B. These results confirm the hypothesis that this platform could be used to clonally expand cells but keep different clonal populations separate, all the while permitting each of those populations to be interrogated en masse.

### **3.3.10 Analysis of cell division heterogeneity in entrapped, nonadherent cells**

In order to demonstrate a proof-of-principle application for analyzing cellular heterogeneity, the proliferation of discrete numbers of Ba/F3 cells into clonal populations was quantified in 47 separate microwells containing cells. As shown in Figure 3.13A, cells heterogeneously proliferated and expanded while on the microwell array. Figure 3.13B shows that the average number of cells per well increased to  $1.6 \pm 0.6$  at 24 hours,  $2.3 \pm 1.1$  at 48 hours, and finally to  $5.2 \pm 4.2$  at 72 hours for wells initially seeded with a single cell. Cells in wells with 2 cells initially expanded to  $3.2 \pm 0.9$ ,  $4.9 \pm 2.3$ , and  $11.1 \pm 6.5$  cells by 24, 48, and 72 hours respectively. The high variability in the number of cells per well, especially by day 3 in culture, suggests that some cells were proliferating faster than others,

generating greater numbers of daughter clone cells. Average cell doubling times were determined to be  $31.4 \pm 3.9$  and  $29.8 \pm 3.4$  hours for wells with 1 and 2 cells per well initial seeding, respectively. However, suspecting that there was a large range of doubling times, a histogram of cell doubling time was constructed by calculating the doubling times of cells in 47 microwells. Figure 3.13C shows that cell doubling time ranged from <20 to slightly over 80 hr. While 45% of cells had doubling times between 22 and 34 hr (*i.e.* there were not two wholly separate populations of “fast” and “slow” dividers that drove the average to a middle value), the presence of *some* apparent fast and slow dividers (doubling times < 20 and >60 hr) was appreciated.

These results compare favorably with the growing realization that small sets within a population of cells act to maintain the entire population, either through rapid proliferation to offset the effects of other cells dying off, or through the secretion of paracrine factors that induce nearby cells to divide. One recent report examined proliferation of hematopoietic stem cells grown in a novel microfluidic device featuring nanoliter-scale growth chambers.<sup>76</sup> By continuously perfusing media to the chamber apertures, clonal cell populations within the chambers could be maintained for up to 72 hr. While that device and the platform described here offer better and longer culture of cells than other currently available technologies (including many microscale approaches), the 1002F:chitosan hybrid films described here have the additional advantage of requiring no other specialty equipment, namely continuous perfusion devices, for growing cells after the devices are fabricated.

### **3.3.11 Growth of primary human AT2 cells as AT1 surrogates**

Finally, in order to begin direct evaluation of the 1002F:chitosan films were use in growing primary AT1 cells under an ALI, primary human AT2 cells seeded into chitosan-bottomed microwell arrays 100  $\mu\text{m}$  in diameter that had been coated with the ECM protein laminin, a known component of the alveolar basement membrane.<sup>77</sup> Cells were seeded at a low density ( $1 \times 10^4$  cells/cm<sup>2</sup>) to as to increase the probability of obtaining a single cell per well (Poisson probabilities for  $n = 0, 1, 2, 3$  cells per well are 0.456, 0.358, 0.141, and 0.037 respectively). After 9 days in culture, cells were stained with Hoescht 33342 and calcein AM red-orange to label cell nuclei and cytoplasm, respectively. A small number of cells (~1%) were observed to have spread out over the microwell bottom area and adopted an AT1-like squamous morphology (Figure 3.14). These finding suggest that, with further optimization, this platform holds potential for use in direct study of primary AT1 cell ion and fluid transport. Further work will focus on tailoring ECM and microwell dimensions to promote reproducible cell spreading over the entire microwell bottom area.

## **3.4 Conclusions**

Here, the development of a microfabricated cellular analysis platform that will enable high-throughput study of cellular heterogeneity in response to user-defined and dynamically controlled stimulations is described. This platform features an array of microscale wells, formed via the first reported co-fabrication of a photoresist film with chitosan to form a freestanding array of microwells bound by a semi-permeable hydrogel layer. Deposition of a layer of inert mineral oil above the well layer allows cells lying in the wells to be physically isolated from other wells, preventing cellular migration and reducing

biochemical crosstalk that might confound results. The chitosan layer at the bottom of the microwells maintains chemical access to the cells for exchange of nutrients and small molecules supplied by the user for cellular interrogation. Use of this platform will enable future high-throughput studies of the diversity in cellular biochemistry and genetics. In addition, the observation of a limited number of primary AT2 cells spreading out over the microwell surface and adopting an AT1-like molecular phenotype were observed, suggesting potential of this platform, after optimizations are conducted, for growth of primary AT1 cells.

### 3.5 Figures and Tables

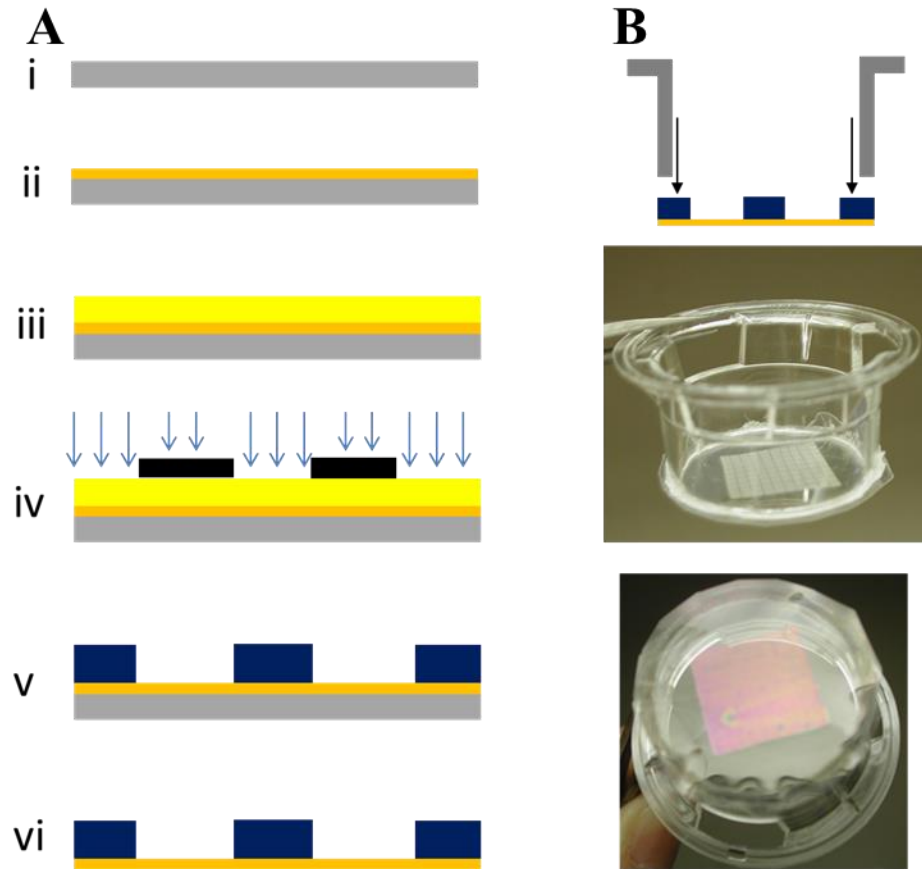


**Figure 3.1.** Fabrication and release of hydrogel-bottomed microwell array films. (A) Fabrication and release protocol. Atop a clean glass slide (i), the chitosan hydrogel layer is deposited via spin-coating (ii). 1002F negative photoresist is then spin-coated atop chitosan hydrogel layer (iii). UV exposure through a patterned photomask (iv) and subsequent development yields a microwell array with chitosan hydrogel bottoms (v). Soaking in dilute NaOH allows release from the glass substrate, yielding a freestanding chitosan:1002F hybrid film (vi). (B) Attachment of a polystyrene cassette to the film creates a two-compartment cell culture system. The apical and basolateral compartments are separated by the chitosan hydrogel layer (note the purple sheen of the submicron chitosan layer).

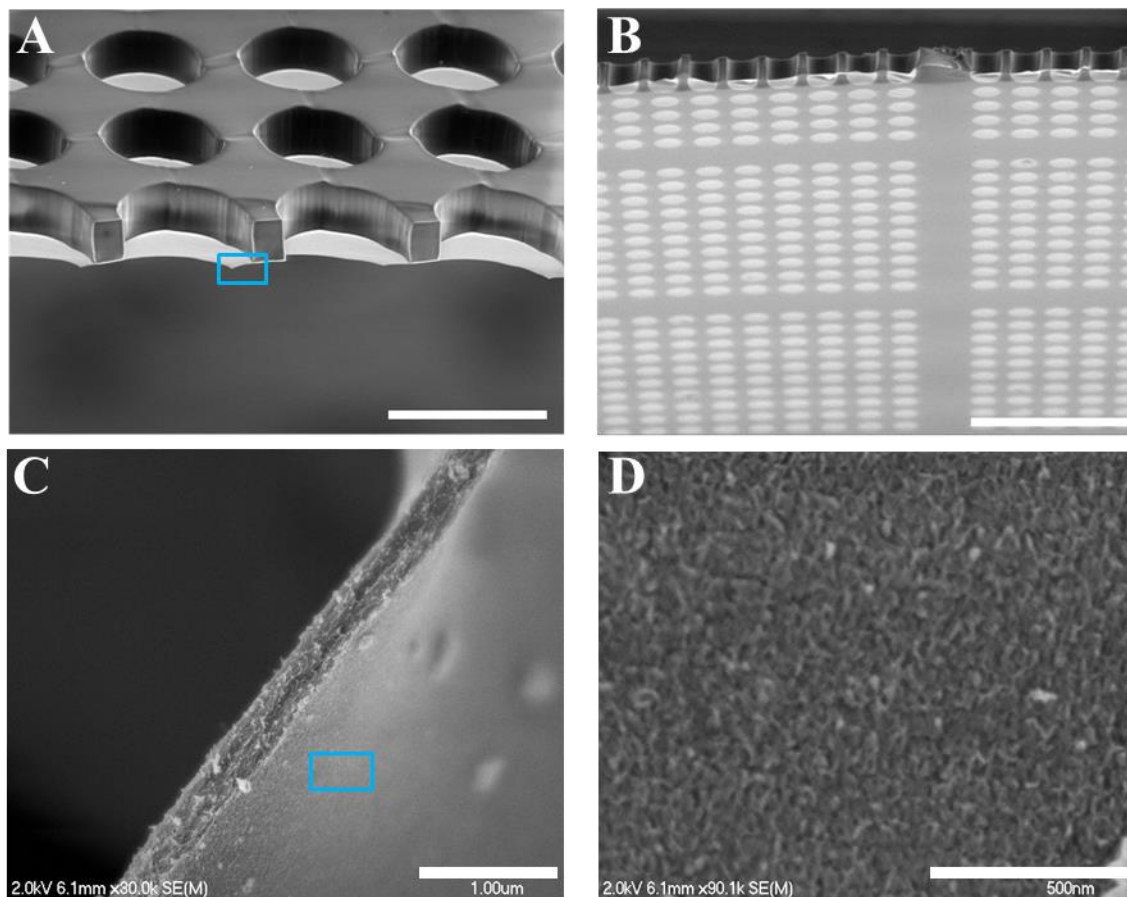


**Figure 3.2.** Imaging of released chitosan-bottomed microwell array films. (A-B) Scanning electron micrographs of released, freestanding 1002F:chitosan films imaged from above (A) and below (B) the 1002F layer. Each film features an array of  $10^4$  75  $\mu\text{m}$ -diameter circular wells 50  $\mu\text{m}$  deep. (C-D) Scanning electron micrograph of chitosan hydrogel layer cross-section (C) and surface (D). (C) shows the area marked by the blue box in (A), while (D) shows the area marked by the blue box in (C). Scale bars: (A) 100  $\mu\text{m}$ ; (B) 400  $\mu\text{m}$ ; (C) 1  $\mu\text{m}$ ; (D) 500 nm.

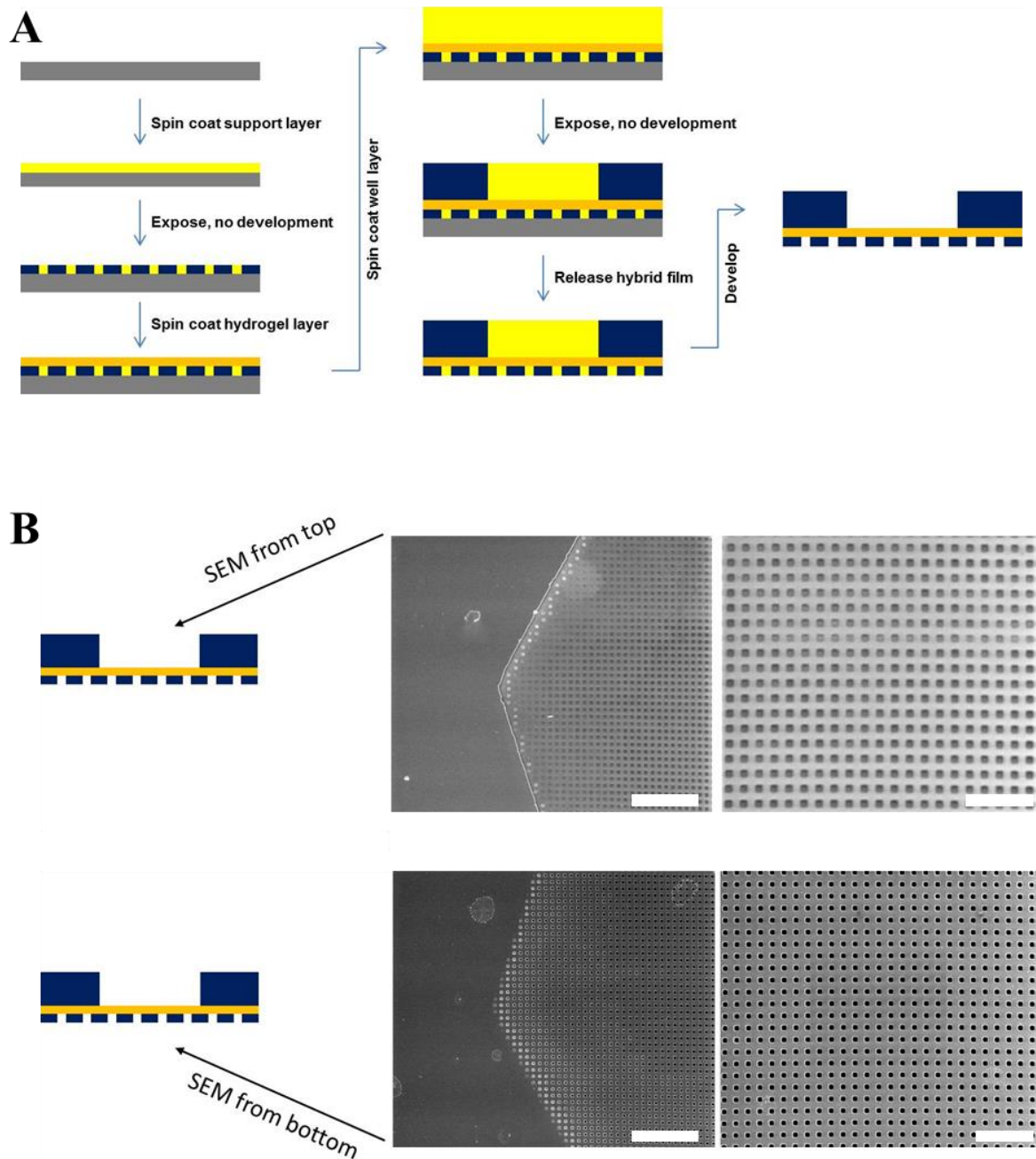


**Figure 3.3.** Fabrication of multi-layer 1002F:chitosan:1002F films. (A) Strategy for fabricating 1002F:chitosan:1002F sandwich films. By delaying the removal of unpolymerized 1002F monomer until after the release of the hybrid film, a single development step allows for creation of a three-layer film with chitosan hydrogel in the middle. (B) Scanning electron micrographs of a 1002F:chitosan:1002F sandwich film. The top layer contains a single large, hexagonal well, while the bottom layer contains an array of 25- $\mu\text{m}$  square microwells. Scale bars: 500  $\mu\text{m}$  (left column), 250  $\mu\text{m}$  (right column).

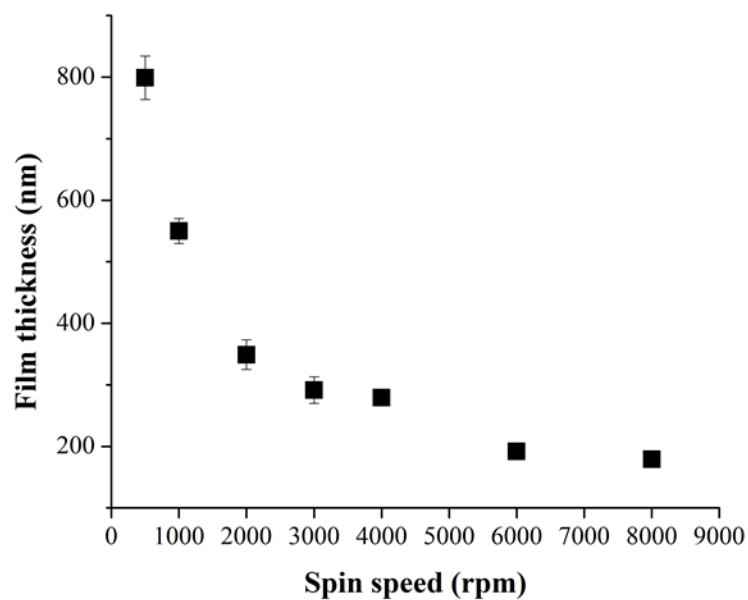


**Figure 3.4.** Dependency of chitosan film thickness on spin coating speed. Chitosan hydrogel was spin coated at the indicated speeds atop glass slides. Films were dried by baking, after which film thicknesses were measured by profilometry. Data are from  $n > 3$  replicates per spin coating speed. Data shown are mean  $\pm$  SD.

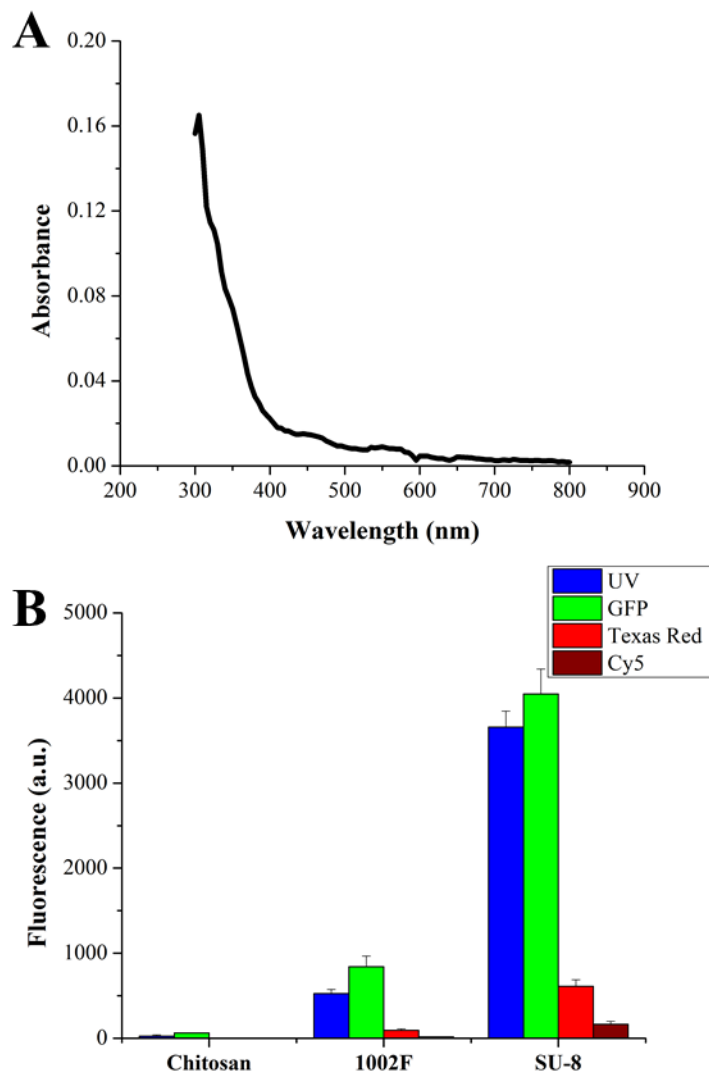


**Figure 3.5.** Optical properties of chitosan films. (A) Absorbance spectrum of hydrated chitosan films 800  $\mu\text{m}$  in thickness. Spectrum is based on mean absorbance from  $n = 6$  films. (B) Autofluorescence of chitosan, 1002F, and SU-8 layers in chitosan films co-fabricated and micropatterned with either 1002F or SU-8. Data presented are as mean  $\pm$  SD,  $n \geq 2$  films each.

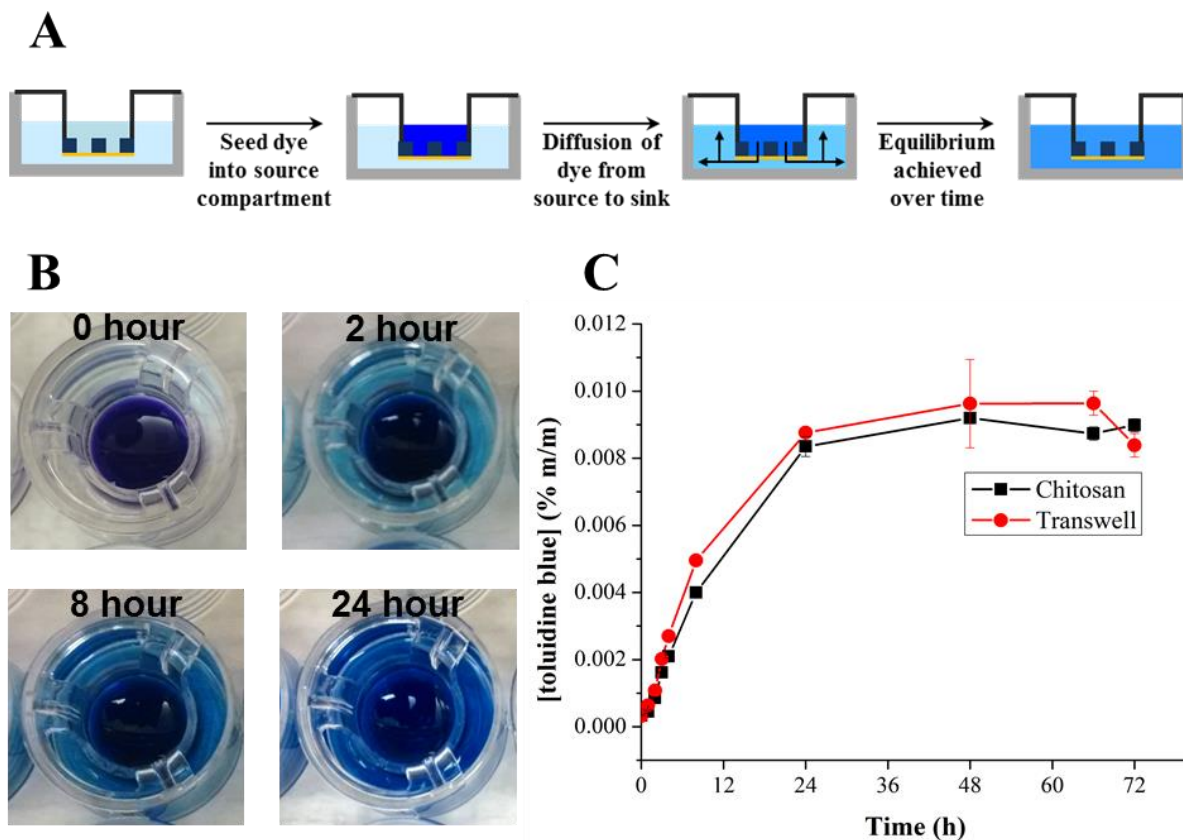


**Figure 3.6.** Permeability of micropatterned 1002F:chitosan films. (A) Workflow diagram for testing solute diffusion through chitosan-bottomed microwell arrays. After seeding concentrated dye into the upper compartment, dye solute will diffuse across the film and into the bottom compartment. Samples are taken at regular intervals from each compartment to determine solute concentration in the compartments. (B) Photographs illustrating diffusion of toluidine blue dye across a chitosan-bottomed 1002F microwell array into the bottom compartment over a 24 hour period. (C) Quantitation of toluidine blue concentration in the bottom compartment. A polyester Transwell™ membrane with pores 0.4  $\mu\text{m}$  in diameter was used as a positive control. Data are presented as mean  $\pm$  SD for  $n = 7$  films.

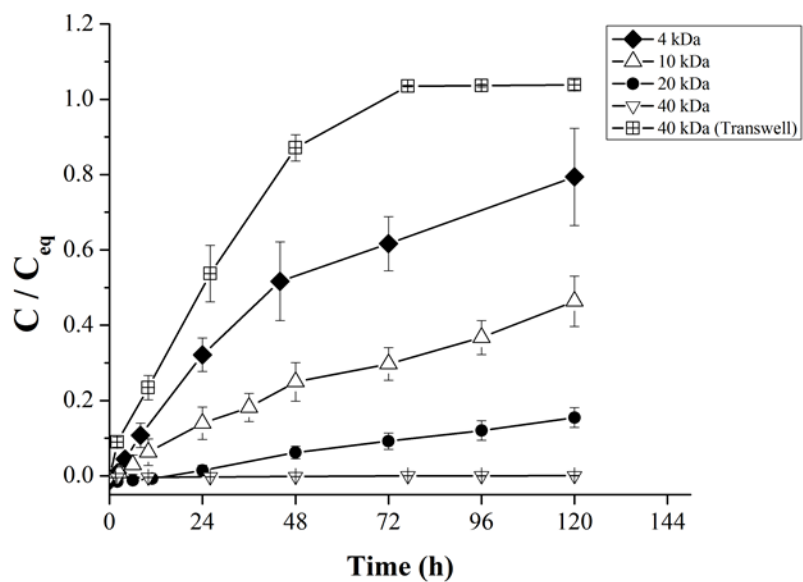


**Figure 3.7.** Diffusion of FITC-conjugated dextrans through chitosan membranes in micropatterned 1002F:chitosan films. Quantitation of ratio of FITC-dextran concentration  $C$  to its theoretical equilibrium value  $C_{eq}$  for four different molecular weights of dextran diffusing across a chitosan-bottomed 1002F microwell array. A polyester Transwell™ membrane with pores 0.4  $\mu\text{m}$  in diameter was used as a positive control. Data are presented as mean  $\pm$  SD for each time point,  $n = 7$  films.

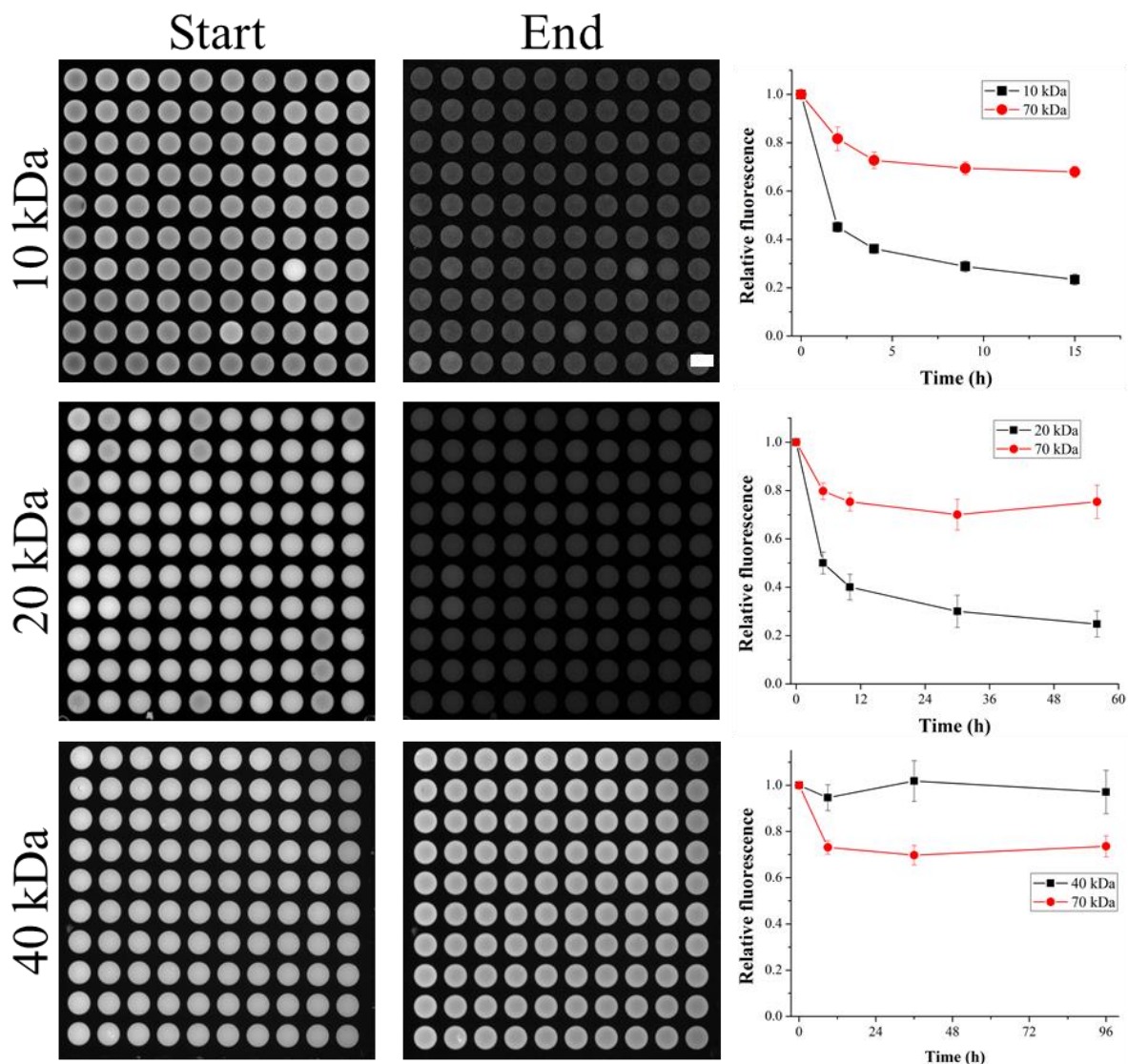


**Figure 3.8.** Visualization of FITC-dextran diffusion through chitosan membranes in individual microwells. Chitosan-bottomed microwell arrays are supplied with FITC-dextran with average molecular weights of 10, 20, or 40 kDa and a 70 kDa rhodamine B-dextran negative control. Dye is confined to the microwells by a discontinuous de-wetting process and a layer of mineral oil is overlaid to prevent evaporation. Serial imaging of the arrays, as well as a blind-ended array to control for photobleaching, allows quantitation of [FITC-dextran] over time. Left and middle columns show arrays just after dye seeding and at termination of experiment, respectively. Plots in right column show quantitation of relative fluorescence over time for both FITC-dextran and the rhodamine B-dextran control. Data are presented as mean  $\pm$  SD for  $n = 6$  films per weight of FITC-dextran tested. All fluorescence micrographs show wells 100  $\mu\text{m}$  in diameter. Scale bar (upper right): 100  $\mu\text{m}$ .

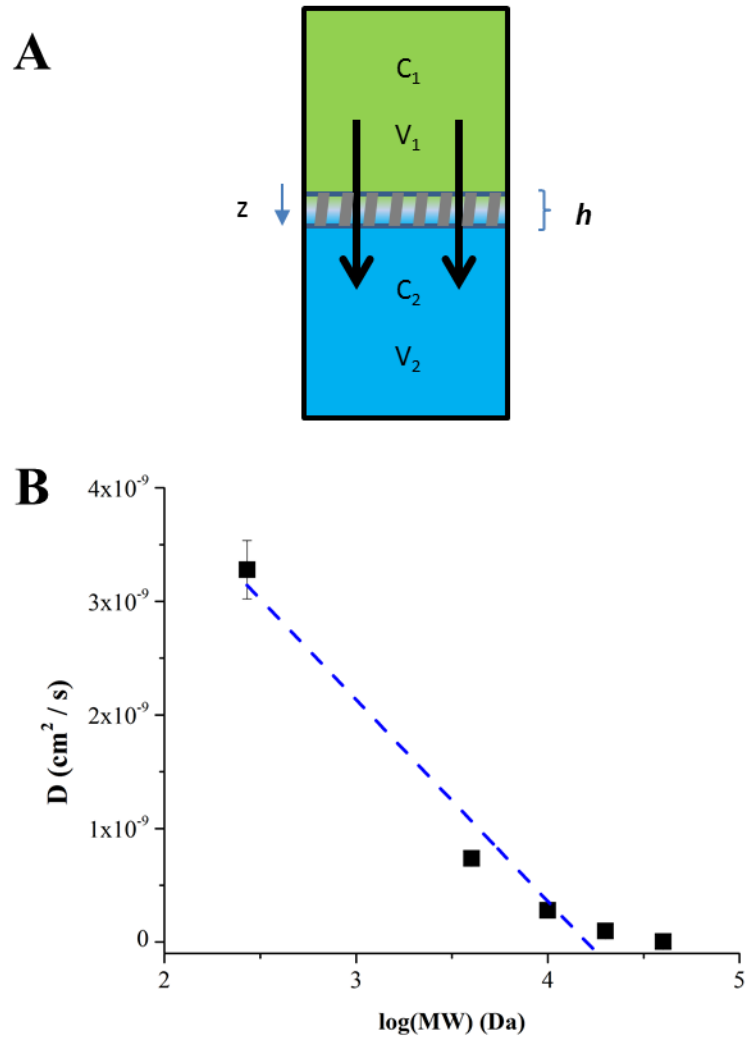


**Figure 3.9.** Determination of diffusion constants and molecular weight cut-off for chitosan membranes in micropatterned 1002F:chitosan films. (A) Diffusion model employed in this study, based on Lee *et al.* Supply of dye to the upper source compartment creates a gradient that drives diffusion of the dye across the membrane and into the sink compartment below. Each compartment has a volume  $V$ , throughout which dye exists at some concentration  $C$ . (B) Determination of the theoretical molecular exclusion limit of chitosan films in the 1002F:chitosan hybrid devices via extrapolation in a plot of diffusivity vs  $\log(\text{MW})$ . Data are presented as mean  $\pm$  SD for the diffusion coefficient calculated for each MW shown. The theoretical molecular weight exclusion limit is the extrapolated x-intercept of a line fitted to the linear region of the  $D$  vs  $\log(\text{MW})$  plot.

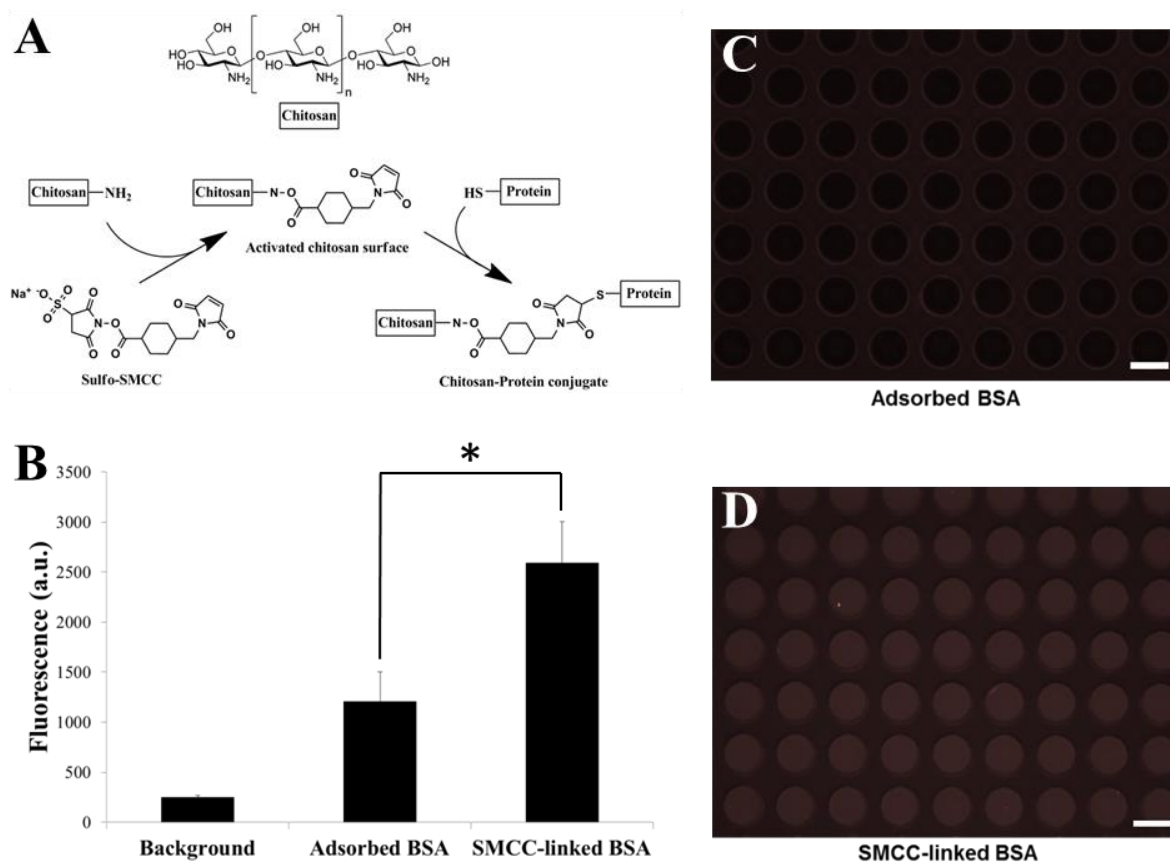


**Figure 3.10.** Selective and covalent modification of chitosan film surfaces. (A) Covalent conjugation scheme. Use of the heterobifunctional linker sulfo-SMCC allows functionalization of the chitosan surface via its amine moiety to covalently attach macromolecules with sulfhydryl groups to the surface. (B) Fluorescence of chitosan-bottomed microwell arrays comparing adsorption versus covalent attachment of BSA-tetramethylrhodamine. \*  $p < 0.05$ . (C-D) Fluorescence micrographs of chitosan-bottomed microwell arrays comparing adsorption (C) versus covalent attachment (D) of BSA-tetramethylrhodamine. Scale bars: 75  $\mu\text{m}$ .

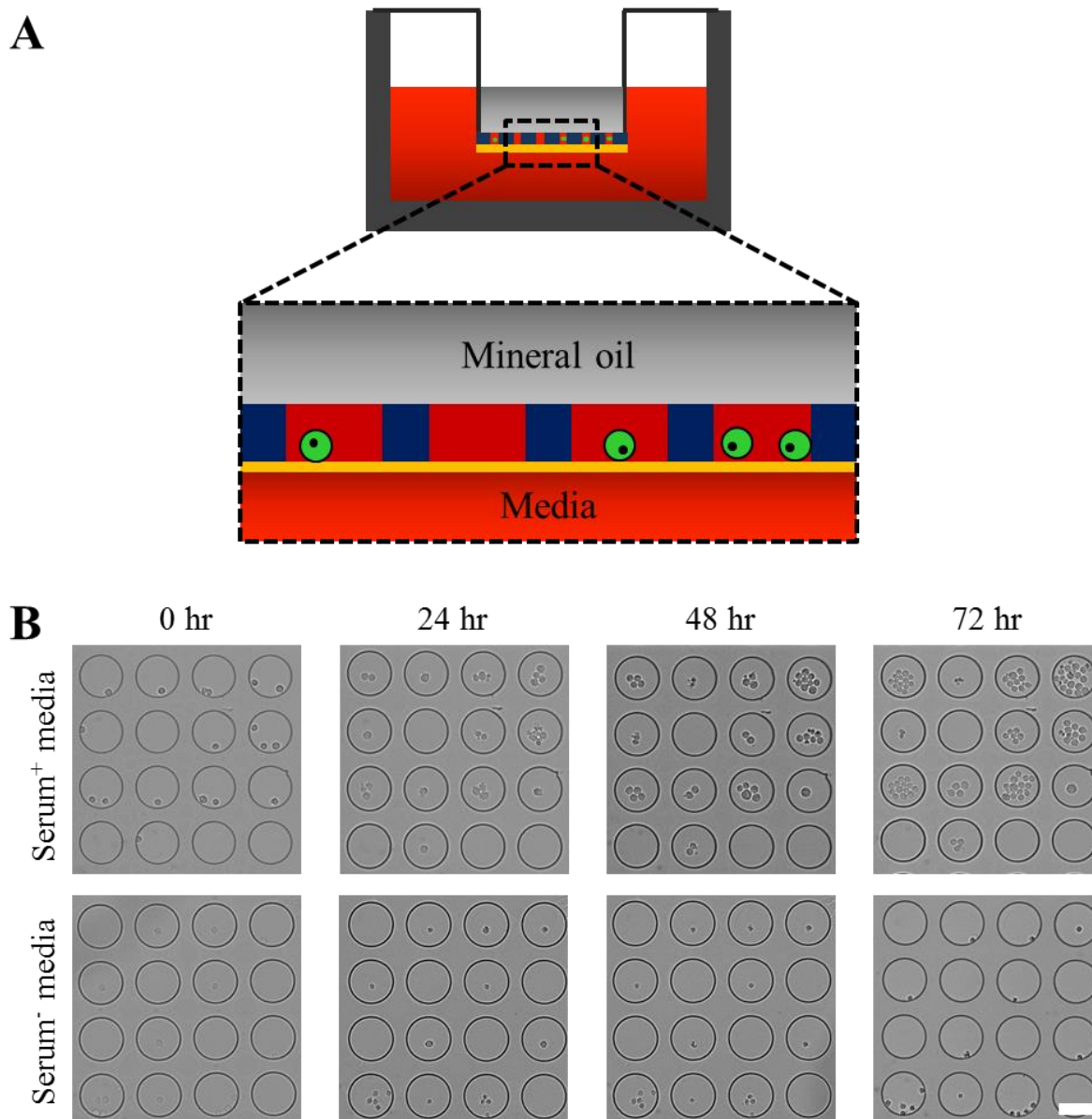


**Figure 3.11.** Entrapment of non-adherent cells in culture medium micropockets. (A) Design schematic for entrapping and maintaining nonadherent cells within micropockets of culture medium. Seeding cells into chitosan-bottomed microwells and aspirating excess media off discontinuously de-wets the upper compartment. Overlay of mineral oil entraps cells in the microwells. (B) Functional permeability of chitosan membranes to serum growth factors. Wild-type Ba/F3 cells were seeded into medium micropockets and media either containing or lacking serum was supplied to the lower compartment. Cells were monitored daily over the next three days to monitor for cell survival and/or proliferation. Scale bar (lower right): 100  $\mu\text{m}$ .

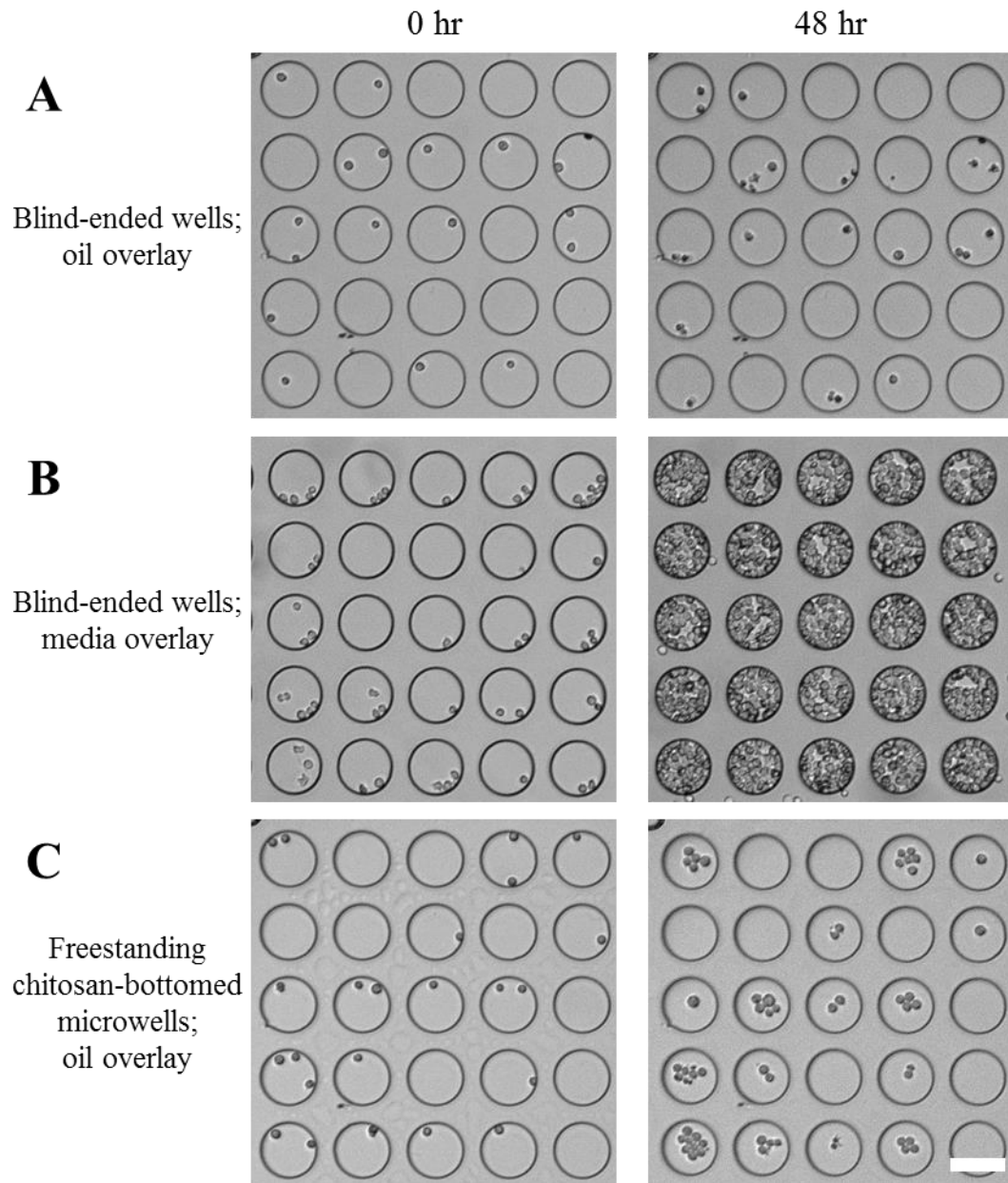


**Figure 3.12.** Physical isolation of clonal cell populations in microwell medium pockets. Wild-type Ba/F3 cells were seeded into unreleased (blind-end) (A-B) or released (C) 1002F:chitosan microwell arrays and imaged daily over 48 hours. Blind-end microwell arrays were either overlaid with mineral oil (A) or culture medium (B). Freestanding microwell arrays were overlaid with mineral oil in the upper compartment, while culture medium was supplied to the bottom compartment. Scale bar (lower right): 100  $\mu\text{m}$ .

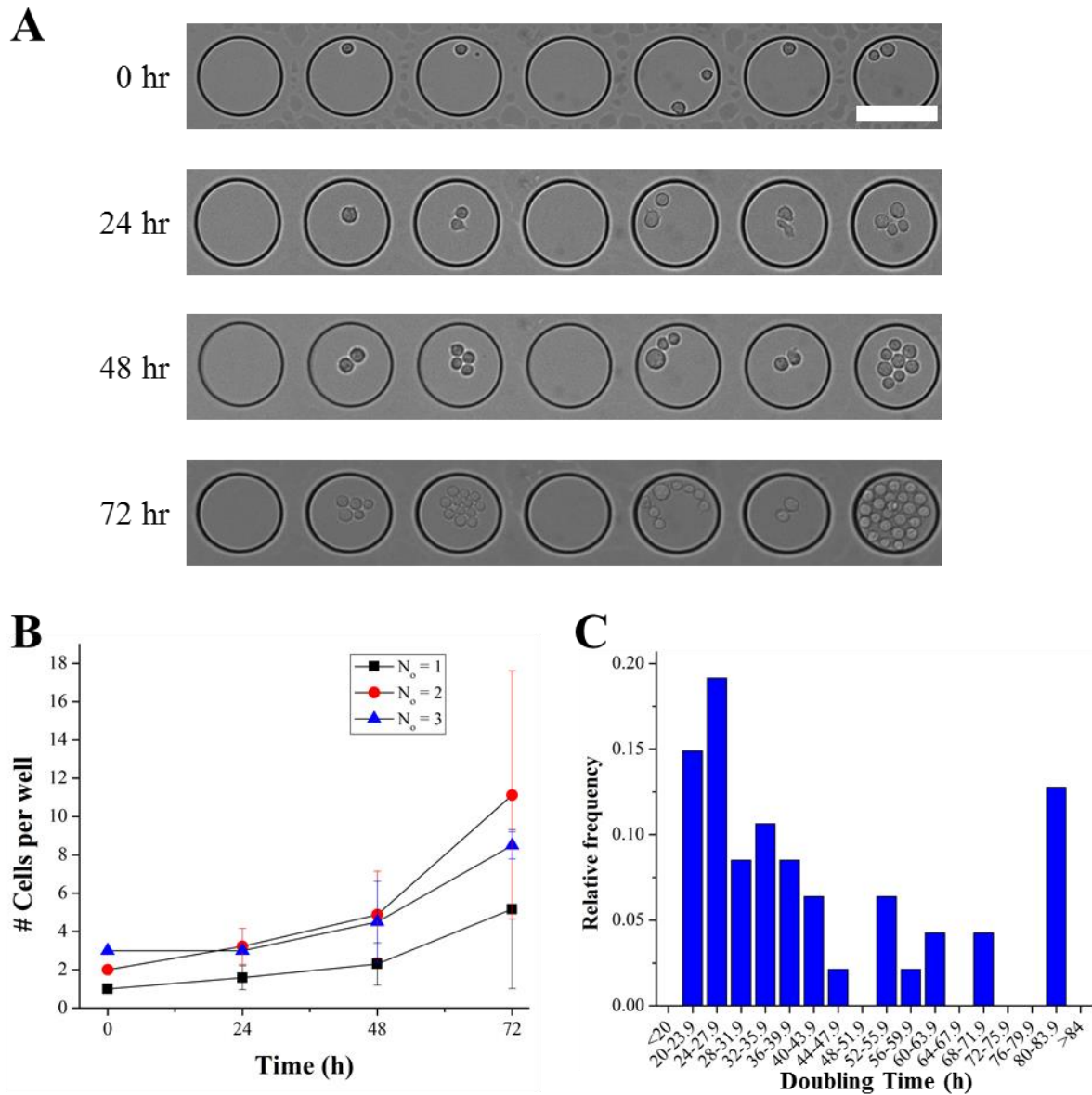


**Figure 3.13.** Quantitation of cell proliferation in microwell medium pockets. (A) Several adjacent wells illustrate the heterogeneity of cell proliferation within a population of wild-type Ba/F3 cells. (B) Measurement of number of cells per microwell, segregated by the initial number of cells in each microwell. Data are shown as mean  $\pm$  SD for 47 microwells. (C) Cell doubling time, calculated and aggregated based on all cells present within a given microwell, was determined for 47 separate microwells. The histogram shows relative frequencies of cell doubling times.

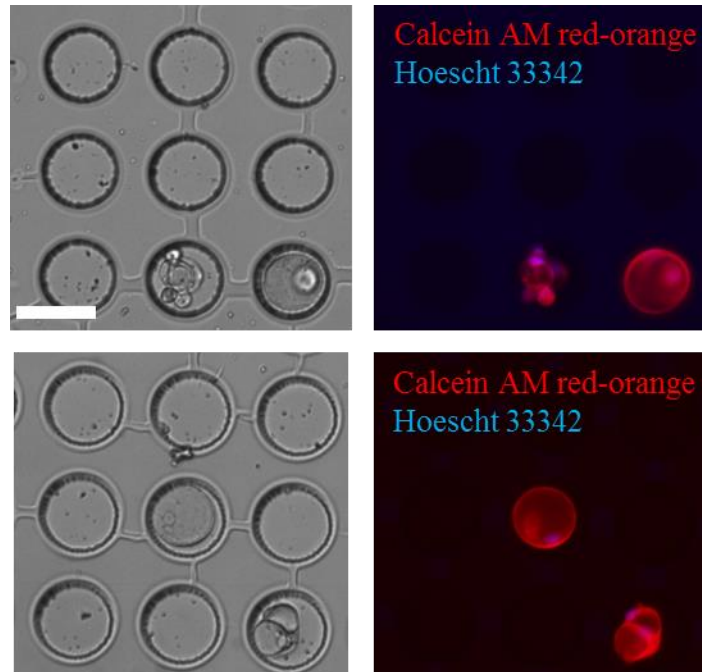


**Figure 3.14.** Growth of primary AT1-like cells in laminin-coated 1002F:chitosan microwells. Two examples of primary AT2 cells, seeded at low density into chitosan-bottomed microwell arrays coated with laminin, are shown. Brightfield and fluorescence micrographs were taken of cells grown for three days in culture and then stained with Hoescht 33342 and calcein AM red-orange to label nuclei and cytoplasm, respectively. Cytoplasmic labeling was performed to identify cells that had spread out over the coated chitosan in the bottoms of the microwells and adopted an AT1-like morphology. Scale bar (upper left): 75  $\mu\text{m}$ .

**Table 3.1** Spin coat speed determination of chitosan film thickness. Chitosan hydrogel was spin coated atop glass slides at the spin coat speeds indicated below. The thickness of the resulting dry film was determined by profilometry.

<b>Speed (rpm)</b>	<b>Thickness (nm)</b>
500	798.8 ± 35.3
1000	549.8 ± 20.3
2000	348.9 ± 24.2
3000	291.4 ± 21.5
4000	279.1 ± 0.4
6000	191.8 ± 4.0
8000	179.2 ± 1.9

**Table 3.2** Comparison of diffusion constants to solute molecular weight for chitosan membranes in 1002F:chitosan hybrid films. Diffusion coefficients were determined from the slopes of plots generated based on Equation 3.14, as described in text.

MW (Da)	log MW	D (cm <sup>2</sup> / s)	Error in D
270	2.431364	3.28 x 10 <sup>-9</sup>	2.58 x 10 <sup>-10</sup>
4000	3.60206	7.36 x 10 <sup>-10</sup>	3.54 x 10 <sup>-11</sup>
10000	4	2.81 x 10 <sup>-10</sup>	1.02 x 10 <sup>-11</sup>
20000	4.30103	9.68 x 10 <sup>-11</sup>	2.27 x 10 <sup>-12</sup>
40000	4.60206	3.42 x 10 <sup>-12</sup>	1.36 x 10 <sup>-13</sup>

### 3.6 REFERENCES

1. M. A. Walling, and J. R. Shepard. "Cellular heterogeneity and live cell arrays." *Chem Soc Rev.* **2011**, *40*, 4049-76.
2. C. E. Meacham, and S. J. Morrison. "Tumour heterogeneity and cancer cell plasticity." *Nature.* **2013**, *501*, 328-37.
3. V. Almendro, A. Marusyk, and K. Polyak. "Cellular heterogeneity and molecular evolution in cancer." *Annu Rev Pathol.* **2013**, *8*, 277-302.
4. C. H. Chung, P. S. Bernard, and C. M. Perou. "Molecular portraits and the family tree of cancer." *Nat Genet.* **2002**, *32 Suppl*, 533-40.
5. K. Ghoreschi, A. Laurence, X. P. Yang, K. Hirahara, and J. J. O'Shea. "T helper 17 cell heterogeneity and pathogenicity in autoimmune disease." *Trends Immunol.* **2011**, *32*, 395-401.
6. J. J. Taylor, M. K. Jenkins, and K. A. Pape. "Heterogeneity in the differentiation and function of memory B cells." *Trends Immunol.* **2012**, *33*, 590-7.
7. K. H. Narsinh, N. Sun, V. Sanchez-Freire, A. S. Lee, P. Almeida, S. Hu, T. Jan, K. D. Wilson, D. Leong, J. Rosenberg, M. Yao, R. C. Robbins, and J. C. Wu. "Single cell transcriptional profiling reveals heterogeneity of human induced pluripotent stem cells." *J Clin Invest.* **2011**, *121*, 1217-21.
8. P. Cahan, and G. Q. Daley. "Origins and implications of pluripotent stem cell variability and heterogeneity." *Nat Rev Mol Cell Biol.* **2013**, *14*, 357-68.
9. C. Smith. "Cancer biology: Cancer shows strength through diversity." *Nature.* **2013**, *499*, 505-508.
10. N. S. Barteneva, K. Ketman, E. Fasler-Kan, D. Potashnikova, and I. A. Vorobjev. "Cell sorting in cancer research--diminishing degree of cell heterogeneity." *Biochim Biophys Acta.* **2013**, *1836*, 105-22.
11. K. R. Love, S. Bagh, J. Choi, and J. C. Love. "Microtools for single-cell analysis in biopharmaceutical development and manufacturing." *Trends in Biotechnology.* **2013**, *31*, 280-6.
12. K. T. Piercy, R. L. Donnell, S. S. Kirkpatrick, B. L. Mundy, S. L. Stevens, M. B. Freeman, and M. H. Goldman. "Effect of harvesting and sorting on beta-1 integrin in canine microvascular cells." *J Surg Res.* **2001**, *100*, 211-6.

13. J. Seidl, R. Knuechel, and L. A. Kunz-Schughart. "Evaluation of membrane physiology following fluorescence activated or magnetic cell separation." *Cytometry*. **1999**, *36*, 102-11.
14. J. Grossmann. "Molecular mechanisms of "detachment-induced apoptosis--Anoikis"." *Apoptosis*. **2002**, *7*, 247-60.
15. P. J. Reddig, and R. L. Juliano. "Clinging to life: cell to matrix adhesion and cell survival." *Cancer Metastasis Rev*. **2005**, *24*, 425-39.
16. M. L. Kovarik, P. C. Gach, D. M. Ornoff, Y. Wang, J. Balowski, L. Farrag, and N. L. Allbritton. "Micro total analysis systems for cell biology and biochemical assays." *Anal Chem*. **2012**, *84*, 516-40.
17. J. Y. Park, S. Takayama, and S. H. Lee. "Regulating microenvironmental stimuli for stem cells and cancer cells using microsystems." *Integr Biol (Camb)*. **2010**, *2*, 229-40.
18. M. Nikkhah, F. Edalat, S. Manoucheri, and A. Khademhosseini. "Engineering microscale topographies to control the cell-substrate interface." *Biomaterials*. **2012**, *33*, 5230-46.
19. I. Y. Wong, S. N. Bhatia, and M. Toner. "Nanotechnology: emerging tools for biology and medicine." *Genes Dev*. **2013**, *27*, 2397-408.
20. M. L. Kovarik, D. M. Ornoff, A. T. Melvin, N. C. Dobes, Y. Wang, A. J. Dickinson, P. C. Gach, P. K. Shah, and N. L. Allbritton. "Micro total analysis systems: fundamental advances and applications in the laboratory, clinic, and field." *Anal Chem*. **2013**, *85*, 451-72.
21. J. Voldman, M. L. Gray, and M. A. Schmidt. "Microfabrication in biology and medicine." *Annual review of biomedical engineering*. **1999**, *1*, 401-25.
22. N. Li, A. Tourovskaia, and A. Folch. "Biology on a chip: microfabrication for studying the behavior of cultured cells." *Crit Rev Biomed Eng*. **2003**, *31*, 423-88.
23. J. Shim, T. F. Bersano-Begey, X. Zhu, A. H. Tkaczyk, J. J. Linderman, and S. Takayama. "Micro- and nanotechnologies for studying cellular function." *Current topics in medicinal chemistry*. **2003**, *3*, 687-703.
24. M. L. Yarmush, and K. R. King. "Living-cell microarrays." *Annual review of biomedical engineering*. **2009**, *11*, 235-57.
25. J. C. Love, J. L. Ronan, G. M. Grotenbreg, A. G. van der Veen, and H. L. Ploegh. "A microengraving method for rapid selection of single cells producing antigen-specific antibodies." *Nat Biotechnol*. **2006**, *24*, 703-7.

26. S. Lindstrom, and H. Andersson-Svahn. "Single-cell culture in microwells." *Methods in Molecular Biology*. **2012**, 853, 41-52.
27. Y. Wang, C. E. Sims, P. Marc, M. Bachman, G. P. Li, and N. L. Allbritton. "Micropatterning of Living Cells on a Heterogeneously Wetted Surface." *Langmuir*. **2006**, 22, 8257-8262.
28. Y. Wang, C. Phillips, W. Xu, J. H. Pai, R. Dhopeswarkar, C. E. Sims, and N. Allbritton. "Micromolded arrays for separation of adherent cells." *Lab Chip*. **2010**, 10, 2917-24.
29. H. N. Joensson, and H. Andersson Svahn. "Droplet microfluidics--a tool for single-cell analysis." *Angew Chem Int Ed Engl*. **2012**, 51, 12176-92.
30. M. T. Guo, A. Rotem, J. A. Heyman, and D. A. Weitz. "Droplet microfluidics for high-throughput biological assays." *Lab Chip*. **2012**, 12, 2146-55.
31. B. D. Ratner, and S. J. Bryant. "Biomaterials: where we have been and where we are going." *Annual review of biomedical engineering*. **2004**, 6, 41-75.
32. P. Zorlutuna, N. Annabi, G. Camci-Unal, M. Nikkhah, J. M. Cha, J. W. Nichol, A. Manbachi, H. Bae, S. Chen, and A. Khademhosseini. "Microfabricated biomaterials for engineering 3D tissues." *Adv Mater*. **2012**, 24, 1782-804.
33. G. M. Whitesides, E. Ostuni, S. Takayama, X. Jiang, and D. E. Ingber. "Soft lithography in biology and biochemistry." *Annual review of biomedical engineering*. **2001**, 3, 335-73.
34. B. D. Gates, Q. Xu, M. Stewart, D. Ryan, C. G. Willson, and G. M. Whitesides. "New approaches to nanofabrication: molding, printing, and other techniques." *Chem Rev*. **2005**, 105, 1171-96.
35. R. A. A. Muzzarelli, and C. Muzzarelli. "Chitosan chemistry: Relevance to the biomedical sciences." *Adv Polym Sci*. **2005**, 186, 151-209.
36. M. N. V. R. Kumar, R. A. A. Muzzarelli, C. Muzzarelli, H. Sashiwa, and A. J. Domb. "Chitosan chemistry and pharmaceutical perspectives." *Chem Rev*. **2004**, 104, 6017-6084.
37. S. T. Koev, P. H. Dykstra, X. Luo, G. W. Rubloff, W. E. Bentley, G. F. Payne, and R. Ghodssi. "Chitosan: an integrative biomaterial for lab-on-a-chip devices." *Lab Chip*. **2010**, 10, 3026-3042.
38. S. V. Madihally, and H. W. T. Matthew. "Porous chitosan scaffolds for tissue engineering." *Biomaterials*. **1999**, 20, 1133-1142.

39. J. Nunthanid, S. Puttipipatkachorn, K. Yamamoto, and G. E. Peck. "Physical properties and molecular behavior of chitosan films." *Drug Dev Ind Pharm.* **2001**, *27*, 143-157.
40. N. Niamsa, and Y. Baimark. "Preparation and characterization of highly flexible chitosan films for use as food packaging." *American Journal of Food Technology.* **2009**, *4*, 162-169.
41. G. Y. Lu, L. J. Kong, B. Y. Sheng, G. Wang, Y. D. Gong, and X. F. Zhang. "Degradation of covalently cross-linked carboxymethyl chitosan and its potential application for peripheral nerve regeneration." *Eur Polym J.* **2007**, *43*, 3807-3818.
42. Q. He, Q. Ao, Y. D. Gong, and X. F. Zhang. "Preparation of chitosan films using different neutralizing solutions to improve endothelial cell compatibility." *J Mater Sci-Mater M.* **2011**, *22*, 2791-2802.
43. P. C. Srinivasa, M. N. Ramesh, and R. N. Tharanathan. "Effect of plasticizers and fatty acids on mechanical and permeability characteristics of chitosan films." *Food Hydrocolloid.* **2007**, *21*, 1113-1122.
44. K. Tomihata, and Y. Ikada. "In vitro and in vivo degradation of films of chitin and its deacetylated derivatives." *Biomaterials.* **1997**, *18*, 567-575.
45. F. L. Mi, Y. C. Tan, H. F. Liang, and H. W. Sung. "In vivo biocompatibility and degradability of a novel injectable-chitosan-based implant." *Biomaterials.* **2002**, *23*, 181-191.
46. F. Berthod, G. Saintigny, F. Chretien, D. Hayek, C. Collombel, and O. Damour. "Optimization of Thickness, Pore-Size and Mechanical-Properties of a Biomaterial Designed for Deep Burn Coverage." *Clin Mater.* **1994**, *15*, 259-265.
47. C. Chatelet, O. Damour, and A. Domard. "Influence of the degree of acetylation on some biological properties of chitosan films." *Biomaterials.* **2001**, *22*, 261-268.
48. H. Zheng, Y. M. Du, J. H. Yu, and L. Xiao. "The properties and preparation of crosslinked chitosan films." *Chem J Chinese U.* **2000**, *21*, 809-812.
49. W. L. Cao, M. Y. Cheng, Q. Ao, Y. D. Gong, N. M. Zhao, and X. F. Zhang. "Physical, mechanical and degradation properties, and Schwann cell affinity of cross-linked chitosan films." *J Biomat Sci-Polym E.* **2005**, *16*, 791-807.
50. H. Yi, L. Q. Wu, W. E. Bentley, R. Ghodssi, G. W. Rubloff, J. N. Culver, and G. F. Payne. "Biofabrication with chitosan." *Biomacromolecules.* **2005**, *6*, 2881-94.

51. Y. Cheng, X. Luo, G. F. Payne, and G. W. Rubloff. "Biofabrication: programmable assembly of polysaccharide hydrogels in microfluidics as biocompatible scaffolds." *Journal of Materials Chemistry*. **2012**, *22*, 7659-7666.
52. T. W. Chung, Y. F. Lu, S. S. Wang, Y. S. Lin, and S. H. Chu. "Growth of human endothelial cells on photochemically grafted Gly-Arg-Gly-Asp (GRGD) chitosans." *Biomaterials*. **2002**, *23*, 4803-9.
53. I. F. Amaral, R. E. Unger, S. Fuchs, A. M. Mendonca, S. R. Sousa, M. A. Barbosa, A. P. Pego, and C. J. Kirkpatrick. "Fibronectin-mediated endothelialisation of chitosan porous matrices." *Biomaterials*. **2009**, *30*, 5465-75.
54. X. H. Chu, X. L. Shi, Z. Q. Feng, Z. Z. Gu, and Y. T. Ding. "Chitosan nanofiber scaffold enhances hepatocyte adhesion and function." *Biotechnol Lett*. **2009**, *31*, 347-52.
55. Q. Ao, A. Wang, W. Cao, L. Zhang, L. Kong, Q. He, Y. Gong, and X. Zhang. "Manufacture of multimicrotubule chitosan nerve conduits with novel molds and characterization in vitro." *J Biomed Mater Res A*. **2006**, *77*, 11-8.
56. A. Di Martino, M. Sittinger, and M. V. Risbud. "Chitosan: a versatile biopolymer for orthopaedic tissue-engineering." *Biomaterials*. **2005**, *26*, 5983-90.
57. K. Obara, M. Ishihara, T. Ishizuka, M. Fujita, Y. Ozeki, T. Maehara, Y. Saito, H. Yura, T. Matsui, H. Hattori, M. Kikuchi, and A. Kurita. "Photocrosslinkable chitosan hydrogel containing fibroblast growth factor-2 stimulates wound healing in healing-impaired db/db mice." *Biomaterials*. **2003**, *24*, 3437-44.
58. X. Z. Shu, K. J. Zhu, and W. H. Song. "Novel pH-sensitive citrate cross-linked chitosan film for drug controlled release." *Int J Pharm*. **2001**, *212*, 19-28.
59. J. Karlsen, and O. Skaugrud. "Excipient Properties of Chitosan." *Manuf Chemist*. **1991**, *62*, 18-19.
60. Y. Sawayanagi, N. Nambu, and T. Nagai. "Permeation of Drugs through Chitosan Membranes." *Chem Pharm Bull (Tokyo)*. **1982**, *30*, 3297-3301.
61. M. Kanke, H. Katayama, S. Tsuzuki, and H. Kuramoto. "Appilcation of Chitin and Chitosan to Pharmaceutical Preparations. I. : Film Preparation and in Vitro Evaluation." *Chem Pharm Bull (Tokyo)*. **1989**, *37*, 523-525.
62. M. M. Bonvin, and M. M. Bertorello. "In vitro sodium salicylate release from chitosan films." *Polymer Bulletin*. **1993**, *31*, 375-379.

63. X. Luo, D. L. Berlin, J. Betz, G. F. Payne, W. E. Bentley, and G. W. Rubloff. "In situ generation of pH gradients in microfluidic devices for biofabrication of freestanding, semi-permeable chitosan membranes." *Lab Chip*. **2010**, *10*, 59-65.
64. X. Luo, H. C. Wu, C. Y. Tsao, Y. Cheng, J. Betz, G. F. Payne, G. W. Rubloff, and W. E. Bentley. "Biofabrication of stratified biofilm mimics for observation and control of bacterial signaling." *Biomaterials*. **2012**, *33*, 5136-43.
65. D. M. Ornoff, Y. Wang, and N. L. Allbritton. "Characterization of freestanding photoresist films for biological and MEMS applications." *J Micromech Microeng*. **2013**, *23*, 025009.
66. C. J. Lee, J. A. Vroom, H. A. Fishman, and S. F. Bent. "Determination of human lens capsule permeability and its feasibility as a replacement for Bruch's membrane." *Biomaterials*. **2006**, *27*, 1670-1678.
67. R. F. Gonzalez, and L. G. Dobbs. "Isolation and culture of alveolar epithelial Type I and Type II cells from rat lungs." *Methods in Molecular Biology*. **2013**, *945*, 145-59.
68. A. Lowman, and N. Peppas. "Hydrogels." In *Encyclopedia of Controlled Drug Delivery*. Mathiowitz, E., Ed. Wiley-Interscience: 1999.
69. L. G. Dobbs, and M. D. Johnson. "Alveolar epithelial transport in the adult lung." *Respir Physiol Neurobiol*. **2007**, *159*, 283-300.
70. B. Lu, D. Zhu, D. Hinton, M. Humayun, and Y.-C. Tai. "Mesh-supported submicron parylene-C membranes for culturing retinal pigment epithelial cells." *Biomed Microdevices*. **2012**, *14*, 659-667.
71. W. M. Deen. *Analysis of transport phenomena*. Oxford University Press: New York. 1998. xix, 597 p.
72. S. Hirano, K. Tobetto, M. Hasegawa, and N. Matsuda. "Permeability properties of gels and membranes derived from chitosan." *J Biomed Mater Res*. **1980**, *14*, 477-85.
73. S. Hirano, K. Tobetto, and Y. Noishiki. "SEM ultrastructure studies of N-acyl- and N-benzylidene-chitosan and chitosan membranes." *J Biomed Mater Res*. **1981**, *15*, 903-11.
74. R. Palacios, and M. Steinmetz. "II-3-dependent mouse clones that express B-220 surface antigen, contain Ig genes in germ-line configuration, and generate B lymphocytes in vivo." *Cell*. **1985**, *41*, 727-34.
75. H. Dinerstein, F. Lago, L. Goujon, F. Ferrag, N. Esposito, J. Finidori, P. A. Kelly, and M. C. Postel-Vinay. "The proline-rich region of the GH receptor is essential for JAK2

- phosphorylation, activation of cell proliferation, and gene transcription." *Mol Endocrinol.* **1995**, *9*, 1701-7.
76. V. Lecault, M. Vaninsberghe, S. Sekulovic, D. J. Knapp, S. Wohrer, W. Bowden, F. Viel, T. McLaughlin, A. Jarandehi, M. Miller, D. Falconnet, A. K. White, D. G. Kent, M. R. Copley, F. Taghipour, C. J. Eaves, R. K. Humphries, J. M. Piret, and C. L. Hansen. "High-throughput analysis of single hematopoietic stem cell proliferation in microfluidic cell culture arrays." *Nat Methods.* **2011**, *8*, 581-6.
77. C. A. Vaccaro, and J. S. Brody. "Structural features of alveolar wall basement membrane in the adult rat lung." *J Cell Biol.* **1981**, *91*, 427-37.

## **Chapter 4: Micropatterning of 1002F photoresist atop track-etch membranes**

### **4.1 Introduction**

#### **4.1.1 Cellular polarization in epithelial tissues**

*In vivo*, a number of epithelial cell lineages, such as bronchial, renal, or gastrointestinal cells, have a polarized orientation relative to the basement membrane on which they sit and across which they exchange nutrients, oxygen, and metabolites.<sup>1</sup> The polarization process involves the cell establishing and segregating membrane faces with distinct molecular organizations: an apical membrane that faces some kind of lumen, and the basolateral membrane, which interfaces with ECM on the basement membrane and with adjacent cells.<sup>2-3</sup> The proper organization of these membrane faces is often essential to epithelial cell function. For example, airway cells establish cilia on the apical surface that play a key role in mucociliary clearance. Similarly, gastrointestinal cells must traffic proteins designed to metabolize and absorb nutrients to the apical membrane. Renal cells that line the nephron must organize an apical membrane face with a variety of ion transporters for regulating the body's electrolyte balance.

In order to promote polarization and allow cells to fully recapitulate the *in vivo* physiology, the most meaningful studies of polarizing cells grow those cells on microporous substrates that provide an *in vitro* mimic to the microenvironment seen *in vivo*.<sup>4-5</sup> Many

studies in the field of respiratory biology have informed our understanding of the role of permeable supports on the ability of cells to properly replicate the *in vivo* architecture. Cells grown on permeable supports have been shown to polarize and differentiate to a higher degree than similar cells grown on impermeable supports.<sup>6-10</sup>

#### **4.1.2 Advantages of microfabricated devices for studies of fundamental cell processes**

The application of microfabricated platforms to the study of biological systems has enabled unparalleled control of the physical and chemical microenvironment to which a cell or group of cells is exposed. Microfabrication technology allows for precise customization of the shape, size, and surface chemistry of the area used for cell growth.<sup>11-14</sup> By achieving such control, researchers gain the ability to interrogate the mechanisms and regulation of fundamental cellular processes and to create novel bio-inspired platforms.<sup>15-19</sup> As mentioned in Chapter 1, the most common methods and materials in use in the microfabrication field include soft lithography using polydimethylsiloxane (PDMS), photolithography using photoresists, and injection molding using cyclic olefin co-polymer, with a number of others also available.<sup>20-23</sup> Despite the availability of so many methods and materials, however, the vast majority of microfabricated platforms grow cells on impermeable surfaces.

#### **4.1.3 Microfabricated devices for study of polarized cells**

Given the advantages of microfabrication technologies as described above, a method to fabricate micropatterned platforms that feature porous or otherwise permeable areas for cell growth would be a useful advance for the study of polarized cell types. To date there has been some success in combining microscale technologies with porous or otherwise permeable materials. Porous membranes are used most commonly in microfluidic setups fabricated with PDMS. A common design for these systems involves the fabrication of

devices using stacked PDMS layers with a microporous membrane sandwiched in the middle, creating separate PDMS flow channels separated by the membrane. A number of studies employing this setup are discussed in Chapter 1. Some of these studies describe novel strategies to bond microporous membranes with the PDMS layers. Others describe the use of these setups for establishing standing chemical gradients without exposing cells to excessive shear forces or for blood plasma filtering applications. Reader is referred back to Chapter 1 for discussion of these devices.

However, some reports do utilize the membrane to recapitulate the polarization seen *in vivo* of certain types of non-respiratory epithelial cells. For example, a seminal study by the Ingber Group engineered a “lung-on-a-chip” device that featured a microporous membrane separating two microchannels.<sup>24</sup> On one side of the membrane, a sheet of immortalized endothelial cells were exposed to a fluid filled microchannel. The opposite side of the membrane was covered with sheets of cells from either small airway NCI H-441 or alveolar A549 cell lines, creating an ALI across the membrane. This device concept was later extended to grow cells from an immortalized colon adenocarcinoma-derived cell line, hence the term “gut-on-a-chip.”<sup>25</sup> A noteworthy feature of these devices was the pair of microchannels that laterally bordered the membrane: reducing or normalizing air pressure to these side channels created stretch or relaxation forces that simulated the expansion of the pulmonary tissues that occurs during inspiration and peristaltic movements in the gut. Jang and Suh created a microfluidic “kidney-on-a-chip” using PDMS bonded to a porous membrane on which sheets of primary rat inner medullary collecting duct (IMCD) cells were cultured.<sup>26-27</sup> While impressive engineering feats, a drawback shared by all of these studies is

the continued reliance on bulk populations of cells: little is done to decrease the scale of study towards smaller groups of cells.

A few devices do attempt to introduce micropatterns onto porous membranes. The McGuigan Group successfully patterned epithelial cells into microcolonies atop commercially-available porous substrates, but this approach did not allow control over the thickness of the patterned material and the size range of its features appeared limited by the ability to establish a good seal between the PDMS stamp and the membrane.<sup>28</sup> Similarly, Torisawa *et al.* reported a strategy to microstamp commercially-available track-etch membranes with a PDMS layer 5  $\mu\text{m}$  thick that could generate features on the order of 50  $\mu\text{m}$  to a side.<sup>29</sup> However, this approach offers no ability to control the height of the PDMS layer; cells seeded onto this device quickly overgrew the well spaces and formed a monolayer over the entire device area. Two reports – one of which used a combination of electrospun polyblend fibers and soft lithography, the other using a mesh-supported submicron membrane of parylene C – combined microscale patterning with a unique permeable surface, but fabrication of these devices requires both considerable manpower and highly specialized equipment.<sup>30-31</sup> A similar requirement for specialized equipment is one drawback to a recent report describing the ability to thermoform polyester or polycarbonate into films with 3D topographies.<sup>32</sup> The fabricator must have ready access to not only a specialty thermoforming apparatus, but also to a heavy ion accelerator in order to track-etch pores into the final product.

#### **4.1.4 Design of a protocol for micropatterning a track-etch membrane**

Thus, devising a strategy for generating precise micropatterns atop commercially-available membranes would be a useful advance for enabling ensemble studies of

biochemistry and physiology in populations of cells that adopt a polarized phenotype. A successful system that achieves this goal will have several key characteristics. First, the system should feature a micro- or nano-porous material that is biocompatible and easily manipulated. Second, the fabrication method should permit micron-level precision in the patterning of cell growth areas with customizable shapes and sizes, while simultaneously being both time-efficient and reproducible. Lastly, the ideal system will enable the seeding and study of single or small groups of cells so that heterogeneity of cellular responses and function can be analyzed in a high-throughput fashion.

Most of the membranes available commercially for the culture of polarized cells are composed of polyester (most commonly polyethylene terephthalate, PET), polycarbonate (PCT), or polytetrafluoroethylene (PTFE). PET and PCT are made porous by a process known as track-etching, in which sheets of each polymer are irradiated with high energy ions that ‘track’ through the sheet and cause local disruption of the polymer backbone. Subsequent soaking of these sheets in strong bases leads to etching of cylindrical pores through those regions that saw exposure to the heavy ion particles.<sup>33-34</sup> PTFE membranes, by contrast, consist of a distribution of microfibers randomly entangled at the microscale; pores with a distribution of sizes result from incomplete entanglement. Among these three materials, PTFE offers the best solvent chemical resistance due to the presence of its unreactive fluorine residues, while PCT has the greatest temperature stability. PET offers generally good resistance to both temperature and chemical solvents. Mixed cellulose ester supports, though less commonly used, are also available.

Of the materials in common or demonstrated use in the microfabrication field, photoresists present the most logical choice for combination with commercially-available

microporous membranes. PDMS is the most common overall material for microfabrication, but the fabrication of full-thickness through-holes in PDMS is technically difficult. While a report by Folch *et al.* details two methods for forming PDMS films with through-holes on a glass substrate, the ability to translate these approaches to a track-etch membrane is questionable.<sup>35</sup> Agarose has been used to micropattern PET membranes, but the maximal feature resolution with this method was suboptimal, and use of it and other hydrogels may affect the ability to measure transepithelial electrical resistance (TEER) values in cells seeded onto devices fabricated with hydrogels as the structured material.<sup>28</sup>

Photoresists present a more enticing material with which to work. A method to fabricate freestanding photoresist films was recently developed and characterized.<sup>36</sup> These films, in which full-thickness microscale through-hole wells could be patterned with a high degree of precision via UV photolithography, could be released from their fabrication substrate to give a flexible and mechanically stable product. Given the advantages of such films and the ease with which they could be fabricated and micropatterned, a strategy to combine this approach with commercially-available microporous membranes in a fashion that would yield an array of microwells patterned directly atop a microporous membrane was investigated.

#### **4.1.5 Overview**

This Chapter presents a reliable strategy to spin coat even layers of 1002F photoresist onto commercially-available track-etch microporous polyester membranes. These photoresist layers can be patterned with microwells that expose the pores in the underlying membrane. Features as small as 25  $\mu\text{m}$  could be micropatterned, with the potential to achieve an even higher resolution. This fabrication process does not appear to destabilize the membrane

micropores, meaning that macromolecules can easily traverse the membrane and enter or exit the microwells. Preservation of the micropores allows MDCK cells to grow and polarize in the wells. These results are the first known report of photopatterning microwells directly atop track-etch membranes for cell culture, and hold promise in growth of microcolonies of polarized cells for drug screening applications and studies of fundamental cell processes.

## **4.2 Experimental design**

### **4.2.1 Materials**

$\gamma$ -butyrolactone (GBL), photoresist developer (propylene glycol methyl ether acetate, PGMEA), FITC-dextran (average molecular weights 70 kDa), and mineral oil were purchased from Sigma-Aldrich (St. Louis, MO). EPON resin 1002F photoresist was obtained from Miller-Stephenson (Sylmar, CA). UVI-6976 photoinitiator (triarylsulfonium hexafluoroantimonate salts in propylene carbonate) was purchased from Dow Chemical (Torrance, CA). Polydimethylsiloxane (PDMS, Sylgard 184 elastomer kit) was obtained from Dow Corning (Midland, MI). Chrome photolithography masks were designed in-house using TurboCAD software and printed by FineLine Imaging (Boulder, CO). Transwell™ permeable cell culture supports, 24-mm in diameter and track-etched with pores 0.4  $\mu$ m in diameter, were obtained from Corning (Tewksbury, MA) via Thermo Fisher Scientific (Waltham, MA). DMEM/F-12 (1:1) medium, fetal bovine serum (FBS), penicillin/streptomycin, Alexa Fluor-488 goat anti-mouse IgG, and SlowFade anti-fade kit were obtained from Life Technologies (Grand Island, NY). Madin-Darby Canine Kidney (MDCK) type II cells transfected with a pLXSN retroviral expression vector containing HA-tagged human P2Y<sub>2</sub> purinergic receptor were a kind gift of Dr. Robert Nicholas at the Univ.

of North Carolina School of Medicine. Transwell™ polystyrene cassettes 12-mm in diameter and hereafter referred to as “cassettes,” were kind gifts from Dr. Brian Button at the Univ. of North Carolina School of Medicine. Mouse anti-HA monoclonal antibody (monoclonal antibody HA.11 from clone 16B12, catalog MMS-101R) was obtained from Covance, (Princeton, NJ).

#### **4.2.2 Photoresist-based micropatterning of track-etch membranes**

Transwell™ permeable culture supports 24 mm in diameter and in an inverted orientation were attached to square glass slides 3.5 cm to a side via a PDMS mortar, which was cured by baking at 65°C for 25 min. Following a 2-min air plasma treatment, micropatterned films of 1002F negative photoresist were fabricated atop the outward facing side of the track-etch membrane using a protocol similar to previously published methods, save for the soft- and post-exposure baking times and temperatures.<sup>36</sup> Briefly, EPON resin 1002F negative photoresist, dissolved in GBL and mixed with UVI-6076 photoinitiator, was spin-coated onto the outward-facing, upright side of the track-etch membrane to a desired thickness of 25-50 μm and soft-baked at 65°C for a number of hours to remove organic solvent. After exposure to UV light through a patterned chrome photomask and a post-exposure bake at 65°C for several hours, unpolymerized photoresist monomer was removed via development in PGMEA. A variety of masks were tested on films with varying thicknesses. The resulting micropatterned hybrid film was hard-baked at 65°C for several hours to solidify the photoresist layer. Afterwards, a 12 mm-diameter polystyrene Transwell™ cassette was mated to the area of the film containing the patterned array and attached with a thin PDMS mortar layer. After curing the mortar, the hybrid film was cut away from its original 24 mm-diameter cassette and excess unpatterned membrane outside of

the 12 mm-diameter cassette was trimmed away. In this orientation, the photoresist pattern directly faces the inner compartment of the cassette.

#### **4.2.3 Imaging of freestanding, micropatterned track-etch membranes**

Track-etch membranes micropatterned with photoresist films were imaged using an FEI Quanta 200 FEG scanning electron microscope (SEM) with a shottky field emission gun, operated under low-vacuum conditions (0.38 torr) (Chapel Hill Analytical and Nanofabrication Laboratory (CHANL)). A Nikon Eclipse TE2000-U inverted fluorescence microscope was additionally used to image films during diffusion experiments. Brightfield and fluorescence micrographs recorded with a cooled CCD camera (Photometrix Cool Snap fx, Roper Scientific, Tucson, AZ) controlled by NIS Elements software (Nikon, Melville, NY). Fluorescence micrographs were analyzed using Image J (NIH, Bethesda, MD). MDCK cells seeded onto micropatterned track-etch membranes were later immunostained and analyzed with a Zeiss CLSM 710 spectral laser scanning confocal microscope equipped with 40X/1.3 Oil Plan Neo and 63X/1.4 Oil Plan Apo objective lenses and 405 and 488 nm excitation lines (UNC School of Medicine Microscopy Services Laboratory). Confocal images were analyzed using the Imaris software package.

#### **4.2.4 Assessing micropore patency by measuring solute diffusion**

Track-etch membranes were spin coated with 1002F photoresist, which was patterned as described above with 900 100  $\mu\text{m}$ -diameter wells. After attachment of a polystyrene cassette and release as described above and a 2 min air plasma treatment, the films were placed into the macro-scale wells of a 12-well plate, suspended by the cassette approximately 1 mm from the well bottom. PBS was supplied into the cassette (upper) and the dish (lower) compartments at volumes (0.5 and 1.5 mL, respectively) recommended by the plate

manufacturer to give an equal height between the two compartments. The cassette (upper) compartment was then supplied with a solution containing 200 µg/mL of FITC-dextran (average molecular weight 70 kDa). After incubating for 1 min, the dextran mixture was carefully aspirated off so as to leave droplets of the dextran solution remaining in the microwells. Mineral oil (500 µL) was then deposited into the cassette compartment to cover the microwell array and prevent evaporation, and the cassette was incubated in the dark. At regular time intervals, fluorescence images of the microwell array were obtained with an inverted fluorescence microscope. Fluorescence micrographs were analyzed using Image J to generate quantitative fluorescence values for each microwell. Films of 1002F fabricated with the same micropattern as listed above that had not been released and whose microwells were thus blind-ended were used as negative diffusion controls to correct for any photobleaching. Fluorescence values, averaged for each microwell, were used to construct a time course of dextran diffusion across the chitosan membrane and out of the well.

#### **4.2.5 Testing epithelial cell polarization on micropatterned track-etch membranes**

MDCK cells were maintained in polystyrene tissue culture flasks in DMEM/F-12 (1:1) medium supplemented with penicillin-streptomycin, 5% v/v FBS, and G418 (500 µg/mL for selection pressure). Track-etch membranes patterned with 1002F microwells 100 µm in diameter were fabricated and released as described above. Devices were sterilized with ethanol and placed in 12-well plates. MDCK cells were dislodged via trypsinization and seeded into the microwells at a density of  $6.5 \times 10^5$  cells/cm<sup>2</sup>. Unpatterned membranes were used as controls. MDCK cells were grown on devices for 7 days with daily medium changes. On day 7, cells were washed with ice-cold PBS supplemented with 2 mM CaCl<sub>2</sub> and MgCl<sub>2</sub>, fixed with 4% (w/w) paraformaldehyde at 4°C for 30 min, and permeabilized using 100%

methanol (stored at  $-20^{\circ}\text{C}$ ) for 60 s. Cells were washed with blocking buffer (1X PBS containing 1% non-fat dry milk) for 5 min three times at room temperature. Cells were then incubated overnight at  $4^{\circ}\text{C}$  in a primary antibody solution composed of blocking buffer containing mouse monoclonal anti-HA Ab at 1:1000 dilution of stock Ab solution. The following day, the primary antibody solution was removed and cells were washed with blocking buffer for 15 min and then labeled for HA-tagged hP2Y<sub>2</sub> receptors with secondary anti-mouse Alexa Fluor 488 Ab for 1 h at room temperature. Hoescht 33342 (1  $\mu\text{g}/\text{mL}$ ) was included to label nuclei. Secondary Ab solution was removed and cells washed five times with PBS. The films were then excised from the cassettes and mounted on glass microscope slides with SlowFade anti-fade mounting medium. Confocal microscopy was performed on the films to visualize hP2Y<sub>2</sub> receptor location as an indicator of cell polarization.

Representative *xz* confocal images were obtained.

## **4.3 Results and Discussion**

### **4.3.1 Method development for micropatterning photoresist atop track-etch membranes**

Freestanding, commercially-available track-etch membranes composed of polyester (specifically, polyethylene terephthalate, PET) and polycarbonate, as well as membranes of interwoven PTFE fibers were initially investigated and tested for basic compatibility with microfabrication procedures. Polycarbonate membranes lost integrity and became distorted when exposed to solvents involved in microfabrication (namely PGMEA) and were not investigated further. Polyester and PTFE membranes displayed resilience in the presence of solvent and did not experience loss of integrity and were therefore investigated further.

A number of approaches were tested for their ability to generate flat, even films of 1002F atop PET and PTFE membranes for subsequent UV photolithography. Placement of membranes on glass slides and spin coating 1002F frequently resulted in the presence of bubbles in the space between the membrane and the overlying 1002F layer. Attempting to remedy this problem by placing the membranes first on slides coated with a layer of PDMS (instead of bare glass) increased membrane evenness and reduced bubbling. However, the adhesion to the PDMS made films difficult to release in later steps, and often resulted in shearing apart the membrane and the overlying 1002F layer.

To circumvent these issues, attempts were made to spin coat 1002F directly onto commercially-available Transwell™ cell culture membranes, which are shipped by the manufacturer pre-attached to a polystyrene cassette. This route was taken because membranes attached to cassettes in this form are taut and resistant to stretching, folding, and bending and so do not need to be flattened on another surface and later removed. In order to yield films with the desired general thickness (on the order of 10-100  $\mu\text{m}$ ), the Transwell™ films had to be inverted and the 1002F spin coated onto the membrane face opposite the one on which cells are traditionally seeded (Figure 4.1A). This is because the viscosity of 1002F prevents a given small volume from being evenly spin coated into a thin film, and spin coating the necessary volume within the cassette compartment would result in back-flow of 1002F that would thicken the resulting layer. Inverted Transwell™ supports were thus attached to square glass slides using a PDMS mortar layer to keep the support steady during the spin coating process.

Using this approach, even, uniform films of 1002F could be reproducibly spin coated atop PET and PTFE Transwell™ membranes. Taking these films through the 1002F UV

photolithography process resulted in the successful patterning of full-thickness 1002F microwells atop PET, but not PTFE, membranes. The micropatterns atop PTFE membranes did not faithfully replicate the mask features, presumably due to scattering of incident UV light by air pockets trapped in the membrane spaces. Further work in remedying this issue was left to future directions, and the remainder of the efforts described here focused on work with PET films only. During the development process, the outside of the polystyrene cassette was observed to be damaged by the developer solvent. However, given the disposable nature of the Transwell supports (in their usual use), and the lack of any precipitate observed in the microwells, this was of no concern. In order to maintain the flatness of the final product but still re-orient the hybrid film back to an orientation useful for cell culture (i.e. microwells facing the cassette compartment), a 12 mm-diameter Transwell™ cassette was mated in the opposite orientation to the hybrid film (still facing out from the original 24 mm-diameter cassette). After bonding the smaller cassette to the film using a thin PDMS mortar layer, the hybrid film was cut away from the larger cassette and excess hybrid film lying outside the smaller cassette space was trimmed away.

#### **4.3.2 Optimization of fabrication parameters**

Subsequent analysis of the track-etch membrane at the bottom of the microwells using scanning electron microscopy revealed that many of the micropores, grossly visible by brightfield light microscopy, had a distorted or shrunken appearance and were smaller in diameter than those pores examined on control membranes that had not been spin coated with 1002F.

It was hypothesized that the temperatures employed in the soft-, post-exposure, and hard-bake steps of the fabrication process were the cause of the micropore distortions.

Indeed, the glass transition temperature ( $T_g$ ) for PET is reported to be 67-80°C, evidence that the 95°C and 120°C baking temperatures, combined with the presence of organic solvents, may be inducing structural changes that cause the micropores to collapse.<sup>37-38</sup> Based on previous in-lab work showing that SU-8, a negative photoresist similar to 1002F, can be cured by baking at 65°C for longer periods of time compared to the times required for curing at 95°C or 120°C, a revised fabrication protocol that featured soft-, post exposure, and hard-bake steps being completed at 65°C for longer times was devised. A temperature of 65°C was chosen in one part based on the required cure temperature for SU-8 photoresist, and in another part based on a report of the 1002F melting temperature of 56.8°C.<sup>39</sup> By baking above the melting temperature of 1002F but below the  $T_g$  of the PET membrane, efficient solvent removal and crosslinking could be achieved for 1002F, while preserving the pore structure in the PET membrane. Subsequent SEM analysis of hybrid films with 1002F spin coated at 2500 rpm to a thickness of 45  $\mu\text{m}$  and patterned with microwells 100  $\mu\text{m}$  in diameter using 6 h-long 65°C soft- and post exposure bakes revealed that pore integrity was greatly improved. Figure 4.1 illustrates the final optimized fabrication strategy, and Table 4.1 lists the optimized fabrication protocols for three different thicknesses of 1002F. Figures 4.2A and 4.2B show the open pores at the completion of the fabrication process, suggesting that the lower temperature baking steps result in improved retention of pore structure and integrity.

Having successfully devised a spin coating and micropatterning strategy, the ability to generate films with a variety of thicknesses and to pattern microwells with even smaller sizes and higher aspect ratios was explored. 1002F films spin coated at various speeds were found to give film thicknesses atop track-etch membranes identical to previously-reported

thicknesses of films spin coated onto glass.<sup>36</sup> Additionally, 1002F layers atop track-etch membranes could be patterned with microwells as small as 25  $\mu\text{m}$  to a side. Maximal aspect ratios for these small features of at least 1.8:1 could be obtained (Figure 4.2D). These results suggest that this fabrication protocol offers a greater degree of parameter control relative to other micropatterning strategies described previously, which offered either no control over film thickness or a higher reported minimum feature size.<sup>28-29</sup>

#### **4.3.3 Testing membrane micropore patency using solute diffusion**

Mindful that results of early experiments showed that pores viewed under brightfield microscopy were actually distorted (when viewed with higher resolution SEM), the need to assess pore patency of the full thickness of the track-etch membrane was recognized. To show that membrane micropores remained functionally patent from one side to the other, the ability of a macromolecule – FITC-dextran 70 kDa – to diffuse from the microwell spaces and through the membrane was assessed. A method to track and measure molecular diffusion in individual microwells in an ensemble fashion was employed (Figure 4.3A). Depositing a solution containing FITC-dextran into the upper cassette compartment, and then aspirating the solution, caused discontinuous de-wetting of the film surface, leading to the entrapment of droplets containing fluorescent dextran in the membrane-bottomed microwells. Overlay of a layer of mineral oil to prevent water evaporation and immediately supplying an aqueous solution to the bottom compartment allowed the entire track-etch membrane and the microwells to remain hydrated. Via serial imaging of the microwell array, quantitative fluorescence values and hence dye concentration in each microwell were obtained, and time courses of dextran diffusion across the PET membrane and out of the well were generated.

Data generated in this fashion, shown in Figure 4.3B and Figure 4.3C, revealed that micropores at the bottoms of the majority of microwells were functionally patent and permeable to FITC-dextran. Fluorescence in the microwells was observed to decrease to near-baseline over ~ 24 h (Figure 4.3B). Quantitation of fluorescence in each microwell suggested that, on average, half-maximal reduction in microwell fluorescence (relative to a standard) was reached between 1 and 2 h of incubation (Figure 4.3C). However, variability in dextran diffusion out of the microwells was quantitatively observed. Interquartile ranges for the relative well fluorescence values were as high as 21.2% (at 2 h), though by 26 h it had fallen to 7.7%. Future work will attempt to ascertain the reason for this variation. While it is true that microwells with a different number of patent micropores would be expected to have different absolute rates of diffusive flux due to differences in porous surface area, the reported micropore density of the PET membranes used here is sufficiently high that microwells 100  $\mu\text{m}$  in diameter would be expected to have on average ~300 pores; Poisson statistics suggest that a well with a micropore number low enough to cause such a large reduction in diffusion would be highly improbable. However, one potential and more likely explanation is that some of the micropores are clogged with unpolymerized photoresist monomer that was not removed by developer. Application of developer to the inside compartment during development may help reduce this.

#### **4.3.4 Growth of polarized MDCK cells in microwells patterned atop track-etch membranes**

To evaluate the ability of a model cell line to form polarized monolayers, MDCK cells expressing an HA-tagged variant of the hP2Y<sub>2</sub> purinergic receptor were seeded into 100  $\mu\text{m}$ -diameter microwells patterned atop PET track-etch membranes. After 7 days of culture, cells were stained using Hoescht 33342 to label nuclei and immunostained with an anti-HA

Ab to mark the location of hP2Y<sub>2</sub> receptors. In cells that have undergone polarization and established segregated apical and basolateral membranes, the hP2Y<sub>2</sub> has previously been shown to be preferentially trafficked to the apical membrane of polarized cells, at which 97 ± 2% of expressed molecules are found, whereas in unpolarized cells the receptor is homogeneously distributed over the entire membrane.<sup>4</sup> MDCK cells seeded into microwells atop the PET membranes had qualitative localization of hP2Y<sub>2</sub> fluorescence at the apical membrane (Figure 4.4A), suggesting that cells grown in these microwells were able to achieve polarization. Control cells seeded onto an unpatterned PET membrane had a similar staining pattern. Data from these imaging studies suggests that receptor localization observed in cells grown on microdevices was not due to a culture artifact, but rather to the ability of MDCK cells, when grown on microdevices, to properly polarize.

Interestingly, MDCK cells were not observed to remain confined to the microwells, but rather formed a 3D monolayer along the entire profile of the surface, growing along the microwell bottoms, up the side walls, and across the wall tops and into the adjacent microwell. In a recent report, Paz *et al.* reported that aspiration of media from the upper compartment effected a removal of cells that had not landed in a microwell, and that cells grown in microwells did not migrate out. That procedure will be repeated in the future work with the microplatform developed here; other approaches to confine cells only to the microwells will be to seed at a lower overall cell density or to graft a PEG or cell-repellent organosilane to the 1002F surface. Where possible in these future experiments, quantitative measurements of TEER will be employed. Due to technical issues regarding the PDMS mortar layer used to seal the films with the cassette, TEER values were not able to be obtained, but efforts are underway to achieve this.

What was surprising about the 3D monolayer observed was the observation that all cells appeared to have polarized (as evidence by hP2Y<sub>2</sub> receptor segregation to the apical membrane), even those cells whose basal surface was not in direct contact with the permeable PET membrane. This observation is but one example of how this microplatform will enable future study of the fundamental process of cell polarization. For example, it is possible that polarization of cells on the microwell wall is brought about by cell-cell signaling mechanisms originating from the polarized cells sitting on the PET membrane that induce cells on the well wall to polarize as well. By varying the micropattern design of the overall film, this and other questions about cell polarization can be investigated.

#### **4.4 Conclusions**

Here, a reliable strategy to spin coat even layers of 1002F photoresist onto commercially-available track-etch microporous polyester membranes and pattern microwells into the photoresist layer that expose the pores in the underlying membrane is detailed. These films can be micropatterned with features as small as 25  $\mu\text{m}$ , with the potential to achieve an even higher resolution. This fabrication process does not appear to destabilize the membrane micropores, meaning that macromolecules can easily traverse the membrane and enter or exit the microwells. Preservation of the micropores allows MDCK cells to grow and polarize in the wells. These results are the first known report of photopatterning microwells directly atop track-etch membranes for cell culture, and hold promise in growth of microcolonies of polarized cells for drug screening applications and studies of fundamental cell processes.

## 4.5 Figures and Tables

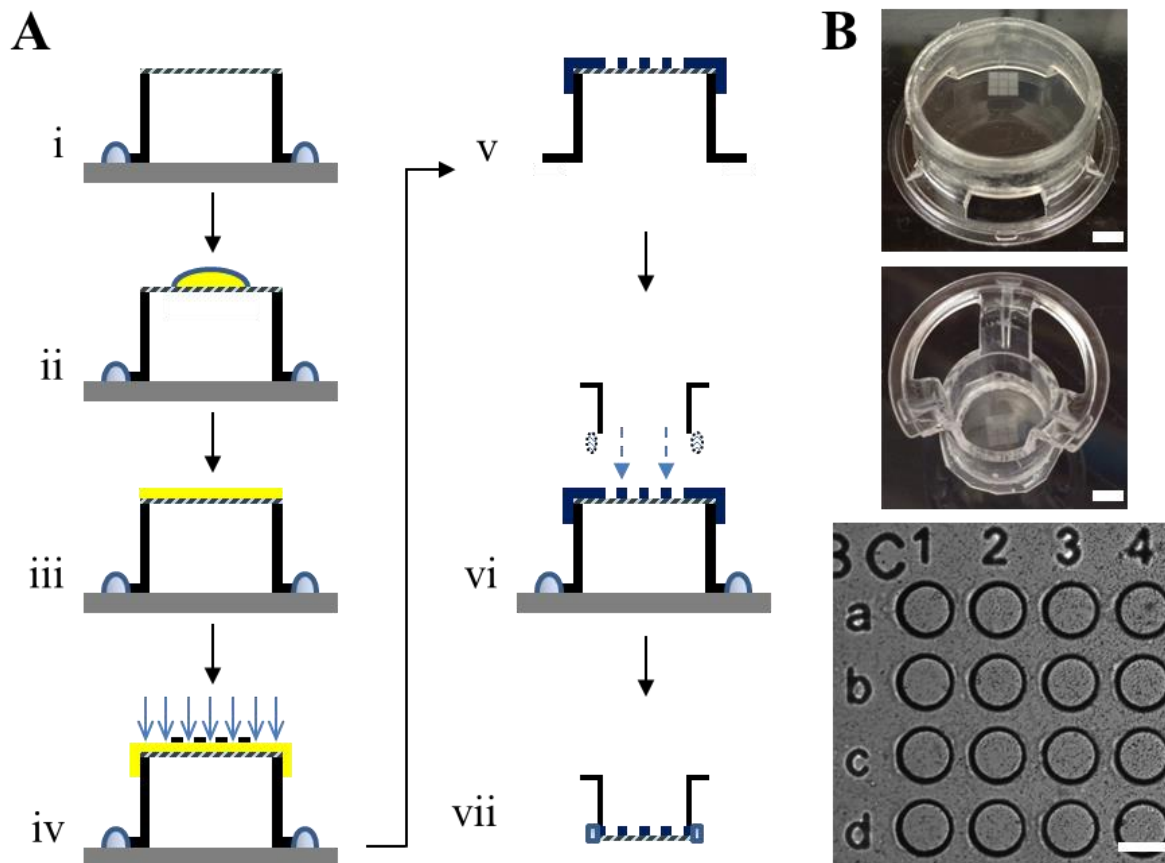


**Figure 4.1.** Fabrication and release of photoresist-micropatterned track-etch membranes. (A) Fabrication and release protocol. Photoresist films are micropatterned directly atop a commercially-available track-etch membrane attached to a polystyrene cassette. The cassette (with membrane attached) is inverted and attached to a glass slide using a PDMS mortar layer. After deposition of a small amount of photoresist (ii), the assembly is spin coated to distribute the photoresist into a film across the membrane (iii). After UV exposure through a patterned photomask (iv) and subsequent development, microwells are patterned atop the membrane (v). Attachment of a smaller cassette directly onto the membrane (vi) and trimming of excess membrane material and photoresist film yields a freestanding track-etch membrane with microwells patterned into the photoresist layer bonded to it above (vii). (B) Photograph showing the microwell pattern atop the track-etch membrane at step (v) (top panel) and step (vii) (middle panel) in (A) at left; lower panel shows brightfield micrograph of microwells patterned into a photoresist layer bonded to an underlying track-etch membrane. Pores give the membrane a finely speckled appearance. Scale bars (top to bottom): 4 mm, 4 mm, 100  $\mu\text{m}$ .

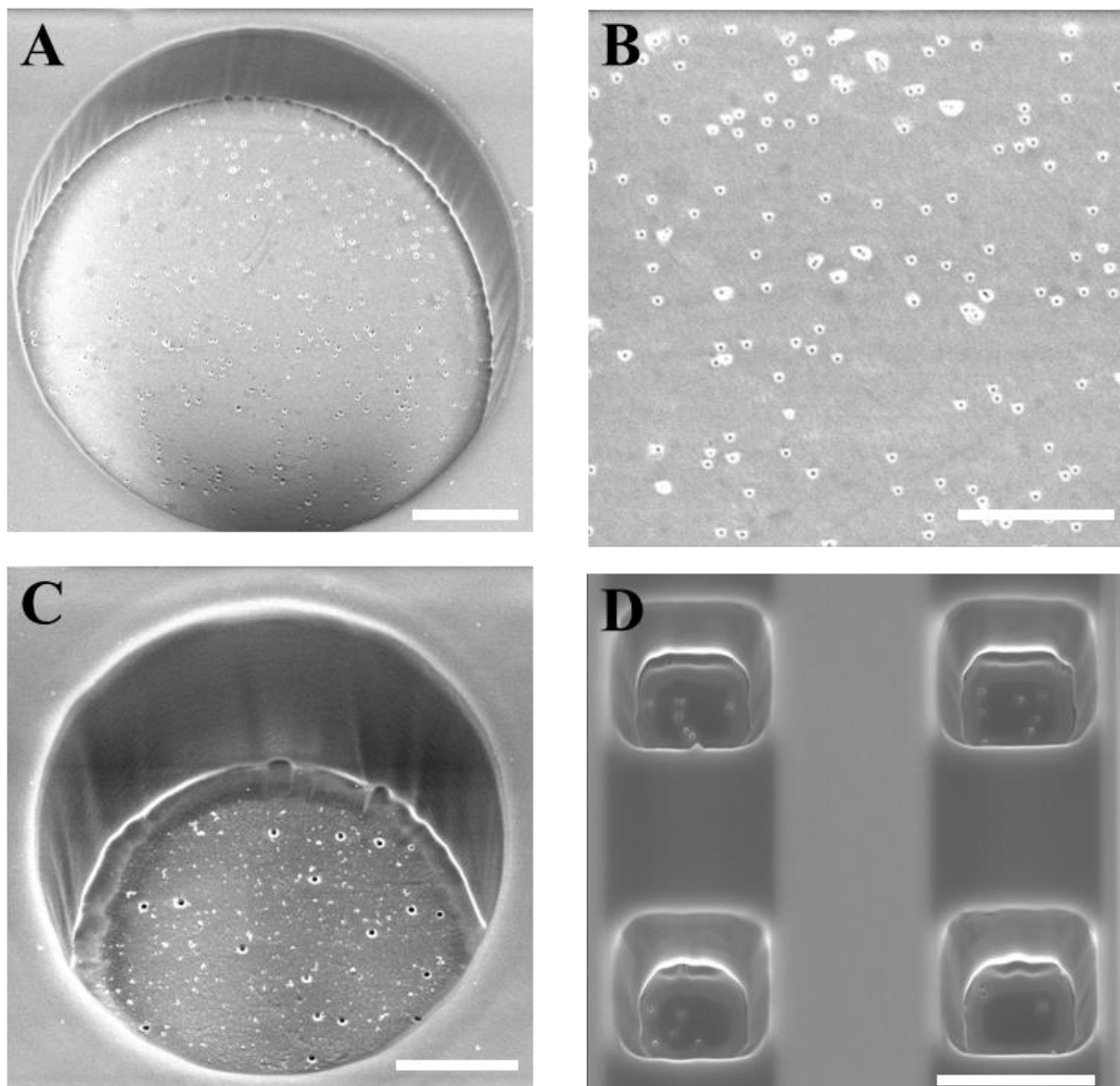


**Figure 4.2.** Imaging of track-etch membranes micropatterned with photoresist. Scanning electron microscopy was used to assess pore structure and stability after completion of the microfabrication process. (A-B) A microwell 100  $\mu\text{m}$  in diameter (A) and a magnified view of its pores (B). (C-D) Microwells with diameter of 40  $\mu\text{m}$  (C) and side length of 25  $\mu\text{m}$  (D). Microwells in (D) were patterned into photoresist 48  $\mu\text{m}$  thick (aspect ratio 1.8:1). Scale bars: (A) 25  $\mu\text{m}$ ; (B) 15  $\mu\text{m}$ ; (C) 10  $\mu\text{m}$ ; (D) 25  $\mu\text{m}$ .

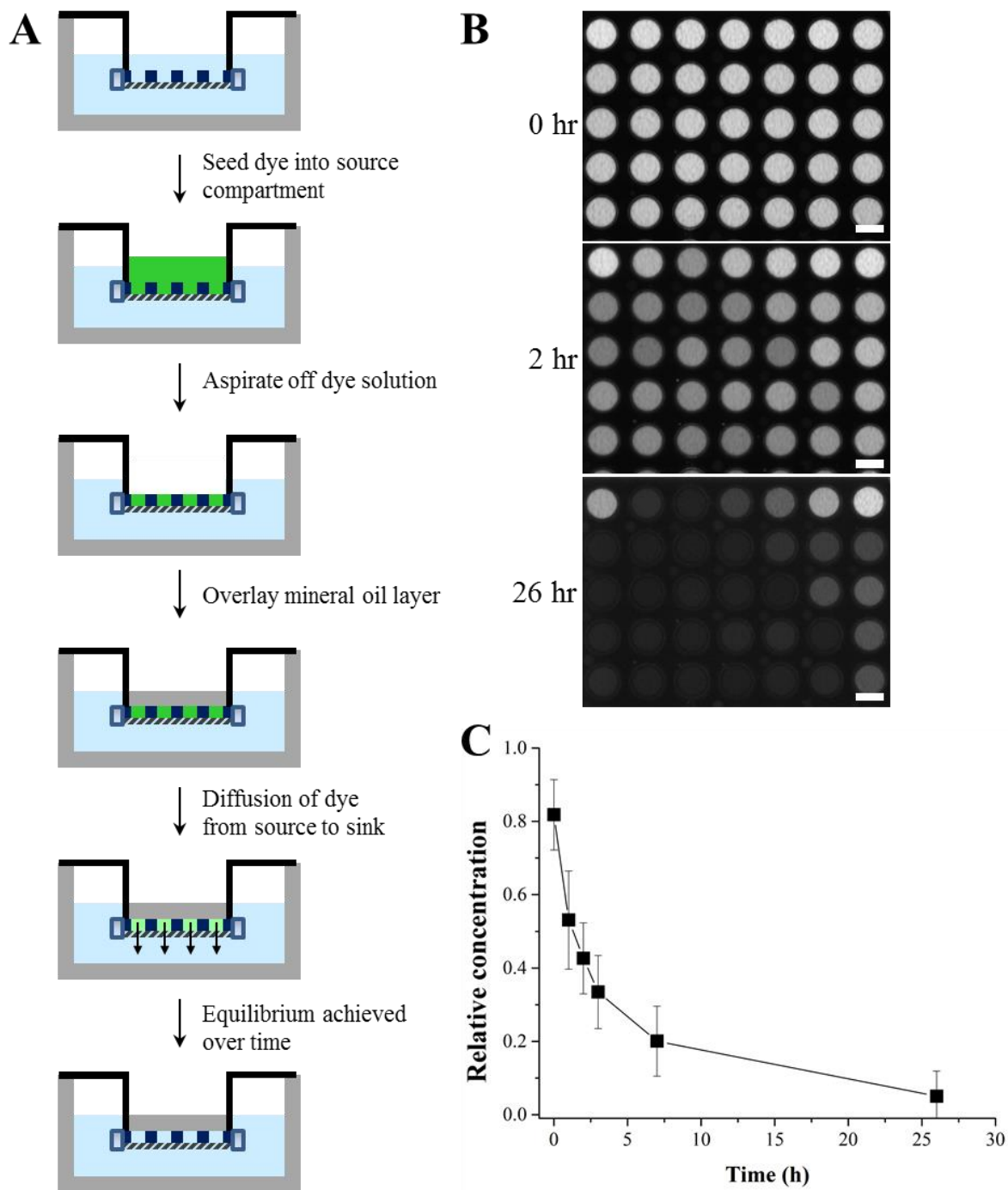


**Figure 4.3.** Verification of pore patency via solute diffusion. (A) Workflow diagram for assessing pore patency via diffusion of FITC-dextran 70 kDa. Images of the microwell array are taken at regular intervals to determine dextran concentration in the microwell spaces. Retention of dextran in the microwell space suggests pores in that microwell space are not patent. (B) Fluorescence micrographs for one region of the microwell array at the indicated timepoints. Scale bars: 100  $\mu\text{m}$ . (C) Quantitation of FITC-dextran 70 kDa concentration in the microwell spaces. Data are presented as mean  $\pm$  SD for  $n = 70$  microwells.

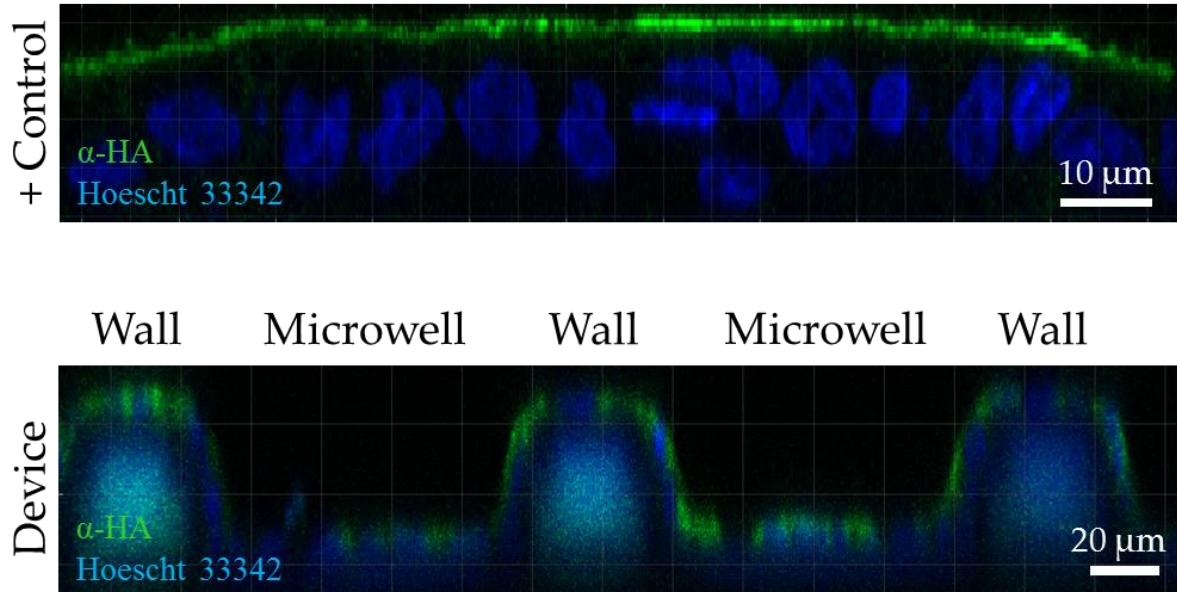


**Figure 4.4.** Polarization of MDCK cells grown on photoresist-patterned track-etch membranes. MDCK II cells expressing HA-tagged human P2Y<sub>2</sub> receptor were seeded into microwells 100 μm in diameter patterned atop polyester track-etch membranes with pores 400 nm in diameter. Cells were also seeded atop identical track-etch membranes that had not been micropatterned. The P2Y<sub>2</sub> receptor is normally sorted to the apical membrane in polarized epithelial cells. After seven days of culture, cells were fixed and immunostained against the HA epitope to mark the cellular locations where the P2Y<sub>2</sub> receptor was found. Green fluorescence indicates staining for the HA-tagged P2Y<sub>2</sub> receptor; Hoescht 33342 was used to counterstain cell nuclei in blue. The upper panel shows an *xz* cross-sectional confocal fluorescence micrograph of cells grown atop a control permeable support lacking a micropattern; the lower panel shows cells grown in microwells patterned atop track-etch membranes. Scale bars: 10 (top panel) and 20 (bottom panel) μm, respectively.

**Table 4.1** Process conditions for micropatterning track-etch membranes with 1002F photoresist.

Photoresist	1002F-10	1002F-50	1002F-50
Spin step 1 (rpm / seconds)	500 / 10	500 / 10	500 / 10
Spin step 2 (rpm / seconds)	1000 / 30	2500 / 30	3000 / 30
Soft bake (65°C) <sup>a</sup>	3 h	6 h	4 h
UV exposure (mJ / cm <sup>2</sup> )	450	450	450
Post-exposure bake (65°C) <sup>a</sup>	3 h	6 h	4 h
Develop (min)	7	7	7
Maximum resolution (μm) <sup>b</sup>	25	25	25
Thickness (μm)	20	45	30

<sup>a</sup> Note the use of hours instead of minutes soft- and post-exposure baking steps.

<sup>b</sup> These were the lowest resolutions that were tested. Features with smaller sizes might be possible to micropattern, given sufficient optimization.

## 4.6 REFERENCES

1. D. M. Bryant, and K. E. Mostov. "From cells to organs: building polarized tissue." *Nat Rev Mol Cell Biol.* **2008**, *9*, 887-901.
2. C. Yeaman, K. K. Grindstaff, and W. J. Nelson. "New perspectives on mechanisms involved in generating epithelial cell polarity." *Physiol Rev.* **1999**, *79*, 73-98.
3. K. E. Mostov, M. Verges, and Y. Altschuler. "Membrane traffic in polarized epithelial cells." *Curr Opin Cell Biol.* **2000**, *12*, 483-90.
4. S. C. Wolff, A. D. Qi, T. K. Harden, and R. A. Nicholas. "Polarized expression of human P2Y receptors in epithelial cells from kidney, lung, and colon." *Am J Physiol Cell Physiol.* **2005**, *288*, C624-32.
5. A. C. Paz, J. Soleas, J. C. Poon, D. Trieu, T. K. Waddell, and A. P. McGuigan. "Challenges and opportunities for tissue-engineering polarized epithelium." *Tissue Eng Part B Rev.* **2014**, *20*, 56-72.
6. L. G. Johnson, K. G. Dickman, K. L. Moore, L. J. Mandel, and R. C. Boucher. "Enhanced Na<sup>+</sup> transport in an air-liquid interface culture system." *Am J Physiol.* **1993**, *264*, L560-5.
7. M. J. Whitcutt, K. B. Adler, and R. Wu. "A biphasic chamber system for maintaining polarity of differentiation of cultured respiratory tract epithelial cells." *In Vitro Cell Dev Biol.* **1988**, *24*, 420-8.
8. L. G. Dobbs, M. S. Pian, M. Maglio, S. Dumars, and L. Allen. "Maintenance of the differentiated type II cell phenotype by culture with an apical air surface." *American Journal of Physiology - Lung Cellular and Molecular Physiology.* **1997**, *273*, L347-L354.
9. L. Jain, X.-J. Chen, S. Ramosevac, L. A. Brown, and D. C. Eaton. "Expression of highly selective sodium channels in alveolar type II cells is determined by culture conditions." *American Journal of Physiology - Lung Cellular and Molecular Physiology.* **2001**, *280*, L646-L658.
10. M. Yamaya, W. E. Finkbeiner, S. Y. Chun, and J. H. Widdicombe. "Differentiated structure and function of cultures from human tracheal epithelium." *Am J Physiol.* **1992**, *262*, L713-24.
11. M. L. Kovarik, P. C. Gach, D. M. Ornoff, Y. Wang, J. Balowski, L. Farrag, and N. L. Allbritton. "Micro total analysis systems for cell biology and biochemical assays." *Anal Chem.* **2012**, *84*, 516-40.

12. J. Y. Park, S. Takayama, and S. H. Lee. "Regulating microenvironmental stimuli for stem cells and cancer cells using microsystems." *Integr Biol.* **2010**, *2*, 229-40.
13. M. Nikkhah, F. Edalat, S. Manoucheri, and A. Khademhosseini. "Engineering microscale topographies to control the cell-substrate interface." *Biomaterials.* **2012**, *33*, 5230-46.
14. I. Y. Wong, S. N. Bhatia, and M. Toner. "Nanotechnology: emerging tools for biology and medicine." *Genes Dev.* **2013**, *27*, 2397-408.
15. M. L. Kovarik, D. M. Ornoff, A. T. Melvin, N. C. Dobes, Y. Wang, A. J. Dickinson, P. C. Gach, P. K. Shah, and N. L. Allbritton. "Micro total analysis systems: fundamental advances and applications in the laboratory, clinic, and field." *Anal Chem.* **2013**, *85*, 451-72.
16. J. Voldman, M. L. Gray, and M. A. Schmidt. "Microfabrication in biology and medicine." *Annual review of biomedical engineering.* **1999**, *1*, 401-25.
17. N. Li, A. Tourovskaia, and A. Folch. "Biology on a chip: microfabrication for studying the behavior of cultured cells." *Crit Rev Biomed Eng.* **2003**, *31*, 423-88.
18. J. Shim, T. F. Bersano-Begey, X. Zhu, A. H. Tkaczyk, J. J. Linderman, and S. Takayama. "Micro- and nanotechnologies for studying cellular function." *Current topics in medicinal chemistry.* **2003**, *3*, 687-703.
19. M. L. Yarmush, and K. R. King. "Living-cell microarrays." *Annual review of biomedical engineering.* **2009**, *11*, 235-57.
20. B. D. Ratner, and S. J. Bryant. "Biomaterials: where we have been and where we are going." *Annual review of biomedical engineering.* **2004**, *6*, 41-75.
21. P. Zorlutuna, N. Annabi, G. Camci-Unal, M. Nikkhah, J. M. Cha, J. W. Nichol, A. Manbachi, H. Bae, S. Chen, and A. Khademhosseini. "Microfabricated biomaterials for engineering 3D tissues." *Adv Mater.* **2012**, *24*, 1782-804.
22. G. M. Whitesides, E. Ostuni, S. Takayama, X. Jiang, and D. E. Ingber. "Soft lithography in biology and biochemistry." *Annual review of biomedical engineering.* **2001**, *3*, 335-73.
23. B. D. Gates, Q. Xu, M. Stewart, D. Ryan, C. G. Willson, and G. M. Whitesides. "New approaches to nanofabrication: molding, printing, and other techniques." *Chem Rev.* **2005**, *105*, 1171-96.
24. D. Huh, B. Matthews, A. Mammoto, M. Montoya-Zavala, H. Hsin, and D. Ingber. "Reconstituting Organ-Level Lung Functions on a Chip." *Science.* **2010**, *328*, 1662-1668.

25. H. J. Kim, D. Huh, G. Hamilton, and D. E. Ingber. "Human gut-on-a-chip inhabited by microbial flora that experiences intestinal peristalsis-like motions and flow." *Lab Chip*. **2012**, *12*, 2165-74.
26. K. J. Jang, and K. Y. Suh. "A multi-layer microfluidic device for efficient culture and analysis of renal tubular cells." *Lab Chip*. **2010**, *10*, 36-42.
27. K. J. Jang, A. P. Mehr, G. A. Hamilton, L. A. McPartlin, S. Chung, K. Y. Suh, and D. E. Ingber. "Human kidney proximal tubule-on-a-chip for drug transport and nephrotoxicity assessment." *Integrative Biology*. **2013**, *5*, 1119-29.
28. A. C. Paz, S. Javaherian, and A. P. McGuigan. "Tools for micropatterning epithelial cells into microcolonies on transwell filter substrates." *Lab Chip*. **2011**, *11*, 3440-8.
29. Y. S. Torisawa, B. Mosadegh, S. P. Cavnar, M. Ho, and S. Takayama. "Transwells with Microstamped Membranes Produce Micropatterned Two-Dimensional and Three-Dimensional Co-Cultures." *Tissue Eng Part C Methods*. **2010**.
30. D. Gallego-Perez, N. Higuera-Castro, R. K. Reen, M. Palacio-Ochoa, S. Sharma, L. J. Lee, J. J. Lannutti, D. J. Hansford, and K. J. Gooch. "Micro/nanoscale technologies for the development of hormone-expressing islet-like cell clusters." *Biomed Microdevices*. **2012**, *14*, 779-89.
31. B. Lu, D. Zhu, D. Hinton, M. Humayun, and Y.-C. Tai. "Mesh-supported submicron parylene-C membranes for culturing retinal pigment epithelial cells." *Biomed Microdevices*. **2012**, *14*, 659-667.
32. R. Truckenmuller, S. Giselbrecht, C. van Blitterswijk, N. Dambrowsky, E. Gottwald, T. Mappes, A. Rolletschek, V. Saile, C. Trautmann, K. F. Weibezahn, and A. Welle. "Flexible fluidic microchips based on thermoformed and locally modified thin polymer films." *Lab Chip*. **2008**, *8*, 1570-9.
33. P. Apel. "Track etching technique in membrane technology." *Radiat Meas*. **2001**, *34*, 559-566.
34. P. Apel, A. Schulz, R. Spohr, C. Trautmann, and V. Vutsadakis. "Track size and track structure in polymer irradiated by heavy ions." *Nucl Instrum Meth B*. **1998**, *146*, 468-474.
35. A. Folch, B. H. Jo, O. Hurtado, D. J. Beebe, and M. Toner. "Microfabricated elastomeric stencils for micropatterning cell cultures." *J Biomed Mater Res*. **2000**, *52*, 346-53.

36. D. M. Ornoff, Y. Wang, and N. L. Allbritton. "Characterization of freestanding photoresist films for biological and MEMS applications." *J Micromech Microeng.* **2013**, *23*, 025009.
37. C. E. Wilkes, J. W. Summers, C. A. Daniels, and M. T. Berard. *PVC handbook*. Hanser: Munich ; Cincinnati. 2005. 723 p.
38. A. K. Van der Vegt, and L. E. Govaert, Polymeren van keten tot kunststof. VSSD,: Delft, 2005; p. 1 online resource (279 p. <http://www.mylibrary.com?id=73089>).
39. P. K. Shah, M. R. Hughes, Y. Wang, C. E. Sims, and N. L. Allbritton. "Scalable synthesis of a biocompatible, transparent and superparamagnetic photoresist for microdevice fabrication." *J Micromech Microeng.* **2013**, *23*.

## **Ch. 5 Conclusions and Future Directions**

### **5.1 Overall summary and conclusions**

In summary, work detailed in this dissertation has directly led to the development of three novel microscale technology platforms that, having now been characterized, are poised for both immediate and long-term applications in the bioMEMS fields.

#### **5.1.1 Freestanding 1002F photoresist films**

Chapter 2 demonstrates that the photoresist 1002F can be micropatterned with good replication of a master using UV photolithography and released without damage from the fabrication substrate in a matter of hours, all without the need for an underlying sacrificial layer. 1002F photoresist films are shown to be mechanically resilient, have low autofluorescence, require only basic UV photolithography to micropattern, and can be made with through-holes with dimensions much smaller than those of other materials typically used in microfabrication. While 1002F microstrainers, featuring both microwells and an underlying pore layer, are impractical for use with primary AT1 cells, these 1002F films hold outstanding potential in forming the overall structure of freestanding microwell arrays in which to grow primary AT1 cells. Even so, freestanding photoresist films can be used as stencils for material deposition, as patterned supports for cell culture, and as platforms to interrogate single cells within a monolayer. Thus, freestanding photoresist films have

potential in future chemical and biological applications and particularly as lab-on-a-foil devices.

### **5.1.2 Chitosan-bottomed microwell arrays**

Chapter 3 presented the development of a microfabricated cellular analysis platform to enable high-throughput study of cellular heterogeneity in response to user-defined and dynamically controlled cell stimulation. This platform features an array of microscale wells, formed via the first reported co-fabrication of a photoresist film with chitosan to form a freestanding array of microwells bound by a semi-permeable hydrogel layer. After seeding cells into the chitosan-bottomed microwells, deposition of a layer of inert mineral oil allows physical confinement of clonally expanding cells, preventing cellular migration and reducing biochemical crosstalk that might confound results while maintaining a user's chemical access to the cells. Use of this platform will enable future high-throughput studies of the diversity in cellular biochemistry and genetics. In addition, the observation of a limited number of primary AT2 cells spreading out over the microwell surface and adopting an AT1-like molecular phenotype suggests the potential of this platform, after optimization, for growth of primary AT1 cells.

### **5.1.3 Photoresist-based micropatterning of polyester track-etch membranes**

Chapter 4 details a reliable strategy to spin coat even layers of 1002F photoresist onto commercially-available track-etch microporous polyester membranes and pattern microwells in a photoresist layer with the membrane pores exposed in the microwells. The ability to micropattern features as small as 25  $\mu\text{m}$ , with the potential to achieve an even higher resolution, was demonstrated. This fabrication process does not appear to destabilize the membrane micropores, meaning that macromolecules can easily traverse the membrane and

enter or exit the microwells. Preservation of the micropores allows MDCK cells to grow and polarize in the wells. These results are the first known report of photopatterning microwells directly atop track-etch membranes for cell culture, and hold promise in growth of microcolonies of polarized cells for drug screening applications and studies of fundamental cell processes.

## **5.2 Anticipated future work**

### **5.2.1 Freestanding 1002F photoresist films**

Development of freestanding photoresist films, presented in Chapter 2, described the novelty of fabricating microwell patterns into photoresist films and then releasing the patterned films from the fabrication substrate. Ironically, the novelty of this method – the release of the intact photoresist films – was sufficiently characterized and future work will instead center around refinement of the patterning process and novel applications for this technology. A future direction that can be immediately investigated concerns the ability to fabricate small features into the photoresist film. In practice, the fabrication of features smaller than 10  $\mu\text{m}$  has been technically difficult. Significant optimization of the UV exposure energy and post-exposure bake and development times was needed in order to prevent excessive tapering of the pore through the depth of the film, while at the same time preventing premature detachment of the entire film during development. In those instances in which films detached, it was theorized that the exposure energy was too low, resulting in a very thin layer of photoresist lying just above the fabrication substrate that was not fully exposed and which therefore dissolved during development, causing film detachment. Therefore, use of a UV exposure system offering a greater degree of collimation or

alternatives to conventional UV photolithography such as microscope projection photolithography, focused ion beam (FIB) milling, deep reactive ion etching (DRIE), or electron beam lithography might be explored to fabricate smaller pores.

Based on the demonstrated capability of 1002F single-pore films to load single cells with exogenous molecules, an additional longer-term future direction for such a platform lies in testing the permeability of single cells, as they exist in a monolayer, to exogenously supplied agents – drugs, hormones, *etc.* An additional application might be a pharmacologically-based study or mapping of the gap junction networks within a monolayer of cells, based on the radial spreading of an exogenous agent such as calcein AM that is loaded into a monolayer cell connected to other cells via gap junctions.

### **5.2.2 Chitosan-bottomed microwell arrays**

Based on results of diffusion experiments, the chitosan films fabricated in the manner described in Chapter 3 were found to have a molecular exclusion limit of  $16200 \pm 6300$  Da. While this cutoff is sufficiently high to allow for diffusion of some serum growth factors (such as insulin, amino acids, or vitamins) into the microwells and to thus maintain viability and growth of entrapped Ba/F3 cells, it is unknown whether other cell types will require larger protein growth factors that are not able to diffuse across the chitosan layer. Therefore, an immediate direction for further work will entail modifying the chitosan film so as to increase its permeability.

One advantage many microtechnologies have over conventional traditional platforms is the ability to recover cells of interest in post-analytical steps. As it currently exists, the chitosan platforms would be amenable to micropipetting to recover cells of interest. However, technology developed in the Allbritton Lab allows for cells to be arrayed on

polystyrene micrafts and release of individual rafts with a microneedle release system for subsequent collection and expansion.<sup>1</sup> One strategy to recover cells from chitosan microwells might be to adapt the microneedle release system to create holes in the chitosan membrane that allow cells to fall through the membrane and into a collection vessel below.

### **5.2.3 Track-etch membranes micropatterned with an overlying photoresist layer**

The results of Chapter 4 suggest that low-temperature processing conditions can be used to micropattern 1002F photoresist atop polyester track-etch membranes. Anecdotal evidence from collaborators suggests that primary bronchial epithelial cells exhibit different degrees of differentiation (mainly ciliogenesis) when grown on polyester versus PTFE membranes, despite similar average pore size and ECM coating. Thus, expanding the micropatterning protocol to allow successful micropatterning of PTFE fiber membranes will be a logical next step and will add micropatterned PTFE membranes alongside polyester membranes in the available toolkit.

As shown in Figure 4.4, MDCK cells could be shown to adopt a polarized phenotype when grown in microwells patterned atop commercially-available polyester track-etch membranes. While these cells were polarized, as demonstrated by distribution of HA-tagged P2Y<sub>2</sub> receptor only to the apical membrane surface, cells nonetheless were shown to migrate out of the microwells. In a protocol for cell growth atop agarose-patterned track-etch membranes, Paz *et al.* aspirated apical fluid once cells had settled into the wells; the report that included this step did not note cell migration out of the well spaces. Replicating this protocol will be a logical step for immediate future work as a manuscript describing this platform is prepared. Longer-term, the ability of MDCK cells to successfully polarize in the microwells of this platform opens the door to numerous future studies of the fundamental

processes involved in cell polarization. By providing a customizable cell culture platform, micropatterned track-etch membranes offer potential to begin addressing these processes.

#### **5.2.4 Adaptation of technology prototypes for specific study of primary AT1 cells**

Consideration can now be given to the original biological problem that motivated the work described in this dissertation. While AT1 surrogates were used to assess compatibility with each stage of device development, the author was required to direct time and effort first to fully characterizing these platforms. As mentioned in Chapter 1, section 4, this was so that, armed with a complete knowledge of the characteristics of the device, results of later experiments with primary AT1 cells could be properly interpreted.

A full characterization having been achieved, experiments with primary AT1 or AT1-like cells can now begin in earnest. The first general step will involve a precise tailoring of the device for consistent and reproducible culture of cells with AT1 morphological and physiological characteristics. The diameter of AT1 cells in culture is usually between 50-100  $\mu\text{m}$ , and so the devices presented here easily satisfy that requirement. Next, an ECM coating that promotes consistent spreading of cells (either primary AT1 or AT2) into an AT1-like morphology should be identified. As mentioned above, components of the alveolar basement membrane include laminin, fibronectin, and collagen types I and VI.<sup>2</sup>

As surface optimization is proceeding, a microelectrodes experimental setup should be constructed. Because conventional Ussing chambers distribute current over the entire area of a permeable culture support, use of micropatterned devices in conventional Ussing chambers might result in concentration of current flow across cells. To avoid this, a microelectrode approach will be considered to determine whether or not single or small discrete numbers of AT1 cells grown in microwells spontaneously develop a potential

difference across their membranes, an indicator of active ion transport. Determining whether this potential difference is affected by ion transport inhibitors will be a key experiment.

### **5.3 Potential for future therapies for and insights into ARDS**

Over the long term, the successful transition of these microdevices to the study of AT1 cells has the potential to significantly affect the clinical standard of care for patients with diseases that lead to flooding of the alveolar space, most commonly pulmonary edema and ARDS. Most directly, the microdevices stand to enable an improved understanding of the mechanisms and regulation of ion and fluid transport by AT1 cells, and the role of AT1 cells in fluid clearance from the overall alveolus. A direct consequence of understanding the mechanisms and regulatory pathways might be the identification of strategies, most likely but not necessarily pharmacologic in nature, to potentiate ion and fluid transport out of the alveolar space.

A useful model for employing such strategies to potentiate fluid clearance out of the alveolus can be found in a seminal clinical study describing the benefits of early goal-directed therapy in patients with severe sepsis.<sup>3</sup> Adaptation of this strategy for ARDS might take the form of clinical guidelines that recommend the early administration, either intravenously or inhalationally, of ion transport potentiator drugs in clinical cases, *e.g.* sepsis, with potential to develop ARDS.

Clinically, the first and most direct question that can be addressed with alveolar ion transport potentiation strategies is whether or not the reversal – or at least the attenuation – of alveolar fluid flooding can improve patient oxygenation status and avoid the need for respiratory support via mechanical ventilation, which brings a host of potential

complications. While studies suggest that mortality from ARDS is due to end-organ failure and not from respiratory failure, this finding suggests only that current ventilation strategies are sufficient for oxygenation: in the absence of ventilator use, patient oxygenation would be expected to be severely reduced.<sup>4</sup> Thus, a primary clinical goal of ion transport potentiators would not be to further improve the oxygenation that comes from ventilator use, but to avoid the need for a ventilator in the first place.

A second and pressing clinical goal would be to reduce alveolar basement membrane disruption and hyaline membrane formation. Study of the clinical and pathological course of ARDS suggests, interestingly, that while the alveolar spaces experience significant flooding in the first 24-48 hours of the clinical course, by day 3 this fluid has been resorbed.<sup>5-6</sup> However, by the time this spontaneous resorption has occurred, hyaline membrane formation is already in full swing, necessitating further ventilator support.<sup>5-6</sup> A question that can be addressed by the early reversal of alveolar fluid accumulation is whether rapid removal of alveolar fluid early in the clinical course might stave off hyaline membrane formation and avert further pathological progression of the disease.

A third way that fluid clearance strategies can have benefit is in investigating the role that alveolar fluid flooding plays in ARDS progression in settings of different etiologies. For example, sepsis is the most common cause of ARDS, but likely originates due to a disruption of the alveolar-capillary barrier that begins on the endothelial or pulmonary microcirculatory side, not within the alveolus.<sup>7</sup> By contrast, aspiration syndromes, inhalation of toxic gases, and near-drowning are all alternative ARDS etiologies that originate on the epithelial or airspace side.<sup>7</sup> Determination of the role of fluid accumulation and early fluid removal might yield results that would fundamentally differentiate treatment schemes for ARDS developed

from a circulatory versus a respiratory side. For example, fluid accumulation might be found to play a more minor role to inflammation in cases of sepsis – in which anti-inflammatory and anticoagulation treatments might be more effective – compared to cases of toxic inhalational injury, which might benefit from more aggressive potentiation of fluid clearance due to the relatively greater damage to epithelial versus endothelial cells.

Additionally, the potentiation of alveolar fluid clearance could yield potentially critical information about ARDS pathophysiology, especially concerning the role of inflammation. While both ARDS and pulmonary edema are circulation-sided causes of alveolar flooding, the lack of hyaline membrane formation in patients with pulmonary edema suggests some role for a pro-inflammatory immune response in the comparatively worse clinical course and prognosis of ARDS relative to pulmonary edema.<sup>8-9</sup> Additionally, in pulmonary edema alveoli are flooded with a transudative fluid most similar to plasma, while alveoli in ARDS are flooded with fluid that is more exudative in nature, similar to serum. Comparing clinical courses and outcomes in patients with pulmonary edema versus ARDS in response to ion and fluid clearance potentiators would provide even greater insight into ARDS pathophysiology that could open up avenues for even more treatment options.

## 5.4 REFERENCES

1. Y. Wang, C. Phillips, W. Xu, J. H. Pai, R. Dhopeswarkar, C. E. Sims, and N. Allbritton. "Micromolded arrays for separation of adherent cells." *Lab Chip*. **2010**, *10*, 2917-24.
2. C. A. Vaccaro, and J. S. Brody. "Structural features of alveolar wall basement membrane in the adult rat lung." *J Cell Biol*. **1981**, *91*, 427-37.
3. E. Rivers, B. Nguyen, S. Havstad, J. Ressler, A. Muzzin, B. Knoblich, E. Peterson, and M. Tomlanovich. "Early goal-directed therapy in the treatment of severe sepsis and septic shock." *New England Journal of Medicine*. **2001**, *345*, 1368-77.
4. A. D. Bersten, C. Edibam, T. Hunt, and J. Moran. "Incidence and mortality of acute lung injury and the acute respiratory distress syndrome in three Australian States." *Am J Respir Crit Care Med*. **2002**, *165*, 443-8.
5. A.-L. A. Katzenstein, and F. B. Askin. *Surgical pathology of non-neoplastic lung disease*. Saunders: Philadelphia. 1982. 430 p.
6. J. F. Tomashefski, Jr. "Pulmonary pathology of the adult respiratory distress syndrome." *Clin Chest Med*. **1990**, *11*, 593-619.
7. M. D. Siegel. Acute respiratory distress syndrome: Epidemiology, pathophysiology, pathology, and etiology in adults *UpToDate* [Online], 2014. [http://www.uptodate.com/contents/acute-respiratory-distress-syndrome-epidemiology-pathophysiology-pathology-and-etiology-in-adults?source=related\\_link](http://www.uptodate.com/contents/acute-respiratory-distress-syndrome-epidemiology-pathophysiology-pathology-and-etiology-in-adults?source=related_link) (accessed May 31, 2014).
8. D. Pinto, and R. Kociol. Pathophysiology of cardiogenic pulmonary edema *UpToDate* [Online], 2012. [http://www.uptodate.com/contents/pathophysiology-of-cardiogenic-pulmonary-edema?source=search\\_result&search=Pathophysiology+of+cardiogenic+pulmonary+edema&selectedTitle=1%7E58](http://www.uptodate.com/contents/pathophysiology-of-cardiogenic-pulmonary-edema?source=search_result&search=Pathophysiology+of+cardiogenic+pulmonary+edema&selectedTitle=1%7E58) (accessed March 17, 2013).
9. W. S. Colucci. Treatment of acute decompensated heart failure: Components of therapy *UpToDate* [Online], 2014. [http://www.uptodate.com/contents/treatment-of-acute-decompensated-heart-failure-components-of-therapy?source=search\\_result&search=cardiogenic+pulmonary+edema&selectedTitle=2~63](http://www.uptodate.com/contents/treatment-of-acute-decompensated-heart-failure-components-of-therapy?source=search_result&search=cardiogenic+pulmonary+edema&selectedTitle=2~63) (accessed May 31, 2014).